

DESIGNING SINTER RESISTANT MONOMETALLIC AND BIMETALLIC NANOMATERIALS FOR CATALYSIS

A Thesis Submitted to the College of Graduate and Postdoctoral Studies
In Partial Fulfillment of the Requirements for the Degree of

Doctor of Philosophy

In the Department of Chemistry
University of Saskatchewan
Saskatoon

By

Sudheesh Kumar V

PERMISSION TO USE

In presenting this thesis/dissertation in partial fulfillment of the requirements for a Postgraduate degree from the University of Saskatchewan, I agree that the Libraries of this University may make it freely available for inspection. I further agree that permission for copying of this thesis/dissertation in any manner, in whole or in part, for scholarly purposes may be granted by the professor or professors who supervised my thesis/dissertation work or, in their absence, by the Head of the Department or the Dean of the College in which my thesis work was done. It is understood that any copying or publication or use of this thesis/dissertation or parts thereof for financial gain shall not be allowed without my written permission. It is also understood that due recognition shall be given to me and to the University of Saskatchewan in any scholarly use which may be made of any material in my thesis/dissertation.

Requests for permission to copy or to make other uses of materials in this thesis/dissertation in whole or part should be addressed to:

Head of the Department of Chemistry

University of Saskatchewan

Saskatoon, Saskatchewan S7N 5C9

Canada

OR

Dean College of Graduate and Postdoctoral Studies

University of Saskatchewan

105 Administration Place

Saskatoon, Saskatchewan S7N 5A2

Canada

ABSTRACT

A major concern associated with the use of noble metal nanoparticles and clusters for catalysis is stability. Stabilizing ligands are used to prevent the agglomeration of nanoparticles synthesized under ambient conditions. However, these ligands may block the active sites on the metal surface. Typically, high-temperature heat treatment (550 °C-650 °C) is required for the complete removal of ligands from catalysts, which leads to the sintering of particles to form larger particles. Sintering occurs during heat treatment processes because of the increased mobility of the nanomaterials and can lead to catalyst deactivation as the surface area of the catalytic nanoparticles decreases. Many studies have focused on improving the thermal stability of nanoparticle catalysts by protecting them with metal oxide shells. However, protective shells can also make it harder for substrates to diffuse to the surface and react, thus creating mass-transfer issues. The main focus of this thesis is synthesizing sinter-resistant metallic and bimetallic catalysts.

In Chapter 1, a detailed description of activation processes and methods for enhancing the thermal stability of nanomaterials are provided. Chapter 2 details how a protective silica shell with a thickness of 40 nm enhances the thermal stability of Au₂₅(MUA)₁₈ clusters (MUA=mercaptoundecanoic acid). The morphology of the resulting Au catalysts before and after calcination at temperatures up to 650 °C was analyzed by TEM and Extended X-ray Absorption Fine Structure Spectroscopy (EXAFS) analyses, which showed that the Au catalysts are much more stable to sintering compared to un-encapsulated clusters. However, mass transfer issues associated with the silica shell were also observed. Chapter 3 shows that Atomic Layer Deposition can be an effective method to control the shell thickness of alumina overlayers using Au₂₅(MUA)₁₈ and Au₂₅(DDT)₁₈ (DDT=dodecanethiol) clusters. TEM and EXAFS analysis were used to study the structural changes before and after thermal treatment. 20 cycles of alumina coating are required to improve the thermal stability of Au catalysts made from Au₂₅(MUA)₁₈ clusters. In Chapter 4, the sintering behavior of Au₂₅(MPTS)₁₈ (MPTS=3-mercaptopropyl)trimethoxysilane) clusters on mesoporous silica supports under oxygen atmosphere (1 Pa) was studied by an *in situ* TEM technique. Particle migration and coalescence was found to be the more dominant mechanism for the sintering of monodisperse Au₂₅(MPTS)₁₈ clusters on the mesoporous silica support. *In situ* TEM studies showed that the mobility of the particles increases as the calcination temperature increases. Further TEOS treatment helped to reduce the mobility of Au nanoparticles by forming silica overcoats and the resulting materials showed excellent sinter-resistance up to 550 °C. The stability of TEOS

treated Au₂₅(MPTS)₁₈/mesoporous silica catalysts were also confirmed by EXAFS analysis. In Chapter 5, the galvanic replacement reaction was employed for synthesizing bimetallic catalysts from silica encapsulated Ag nanoparticles. During the activation process at 650 °C, Ag nanoparticles were fragmented into smaller particles with an average size of 2.2 ± 1.0 nm and well dispersed in a silica matrix. These activated Ag clusters were then used as a sacrificial template for galvanic replacement reactions using Pd salts. Liquid cell *in situ* X-ray absorption analysis was utilized to monitor the galvanic replacement reaction of Ag@silica with Pd precursors. Finally, Chapter 6 focuses on the synthesis of the encapsulation of atom-precise Pd clusters in silica for use as catalysts for methane combustion reactions. Catalytic activity studies for methane combustion reactions using encapsulated and non-encapsulated Pd clusters show that encapsulated clusters were much more active for methane oxidation than their non-encapsulated counterparts.

ACKNOWLEDGMENTS

I would like to acknowledge my supervisor Dr. Robert W. J. Scott for his valuable guidance for the patience, guidance, encouragement, and advice throughout my Ph. D program. I would like to thank my advisory committee Dr. Stephen Urquhart, Dr. Ingrid Pickering and Dr. Jafar Soltan for their valuable suggestions and guidance throughout my PhD degree.

My sincere thanks to the University of Saskatchewan and the Department of Chemistry for giving an opportunity to continue my Ph.D. program. Over the period of my Ph.D., I have been teaching several labs in the department. The support and feedback from Dr. Alex Bartole-Scott have been very helpful in improving my presentation skills; I sincerely acknowledge her support. Thanks also go to Dr. Adrian Clark for providing an opportunity to teach 115 labs. I am grateful to all the faculty members; particularly, to Dr. Timothy Kelly for providing me access to his lab.

I would like to thank all the past and present Scott group members, Dr. Atal Shivhare, Dr. Mahesh Gangishetty, Dr. Yali Yao, Vy Phung, Kazeem Sulaiman, Maryam Alyari, William Barrett, and Brandon Chivers. I would like to thank my wife Dr. Anjali for her support and encouragement to finish my Ph.D. program. I would also like to thank beamline scientists and their associates at Canadian Light Source, particularly Dr. Ning Chen, Dr. Weifeng Chen, and Dr. Yongfeng Hu.

DEDICATIONS

I would like to dedicate this thesis to my supervisor Prof. W. J. Robert Scott and my family

TABLE OF CONTENTS

PERMISSION TO USE	ii
ABSTRACT.....	iii
ACKNOWLEDGMENTS.....	v
DEDICATION.....	vi
TABLE OF CONTENTS.....	vii
LIST OF TABLES.....	xi
LIST OF FIGURES.....	xii
LIST OF SCHEMES.....	xviii
LIST OF ABBREVIATIONS.....	xix

CHAPTER 1

1. Introduction	1
1.1 Catalysis by nanomaterials	1
1.2 Classification of nanomaterials.....	2
1.3 Ligand protected clusters.....	3
1.4 Atom-precise Au clusters.....	5
1.5. Characterization of Au ₂₅ (SR) ₁₈ clusters.....	6
1.6. Catalysis by Au ₂₅ (SR) ₁₈ clusters and importance of activation process in catalysis.....	9
1.6.1. Thermal approaches.....	12
1.6.2. Chemical approaches.....	17
1.6.2.1. Oxidation (using O ₃ , TBHP, <i>etc.</i>)	17
1.6.2.2. Reduction (using LiBH ₄ , NaBH ₄ , <i>etc.</i>).....	18
1.6.3. Light-induced approaches.....	20
1.7. Methods of controlling sintering upon activation of clusters.....	21
1.8. Characterization.....	25
1.8.1. Environmental Transmission Electron Microscope (TEM).....	25
1.8.2. X-ray Absorption Spectroscopy (XAS).....	26
1.8.2.1. X-ray Absorption Near Edge Structure (XANES).....	28

1.8.2.2. Extended X-ray Absorption Fine Structure (EXAFS).....	28
1.8.2.3. Single shell fitting.....	30
1.8.3 X-ray Photoelectron Spectroscopy (XPS).....	33
1.9 Research Objectives.....	34
1.10 Organization and Scope.....	36
1.11 References.....	38

CHAPTER 2

2. Synthesis of sinter resistant Au@silica catalysts derived from Au₂₅ clusters.....	51
2.1. Abstract.....	52
2.2. Introduction	52
2.3. Materials and Methods.....	54
2.3.1. Materials.....	54
2.3.2. Synthesis of Au ₂₅ (MUA) ₁₈ clusters.....	54
2.3.3. Synthesis of silica encapsulated Au ₂₅ (SR) ₁₈ clusters.....	55
2.3.4. Synthesis of Au ₂₅ (MUA) ₁₈ clusters on silica spheres (control sample).....	56
2.3.5. Characterization.....	56
2.3.6. Catalytic activity for 4-nitrophenol reduction.....	57
2.3.7. Styrene epoxidation.....	57
2.4. Results and Discussion.....	57
2.5. Conclusions.....	69
2.6. References.....	70

CHAPTER 3

3. Thermal Stability of Alumina Overcoated Au₂₅ Clusters for Catalysis.....	75
3.1. Abstract.....	76
3.2. Introduction	76
3.3. Materials and Methods.....	78
3.3.1. Materials.....	78
3.3.2. Synthesis of Au ₂₅ (MUA) ₁₈ clusters	78

3.3.3.	Synthesis of Au ₂₅ (DDT) ₁₈ clusters.....	78
3.3.4.	Atomic layer deposition over Au ₂₅ (MUA) ₁₈ /Al ₂ O ₃ and Au ₂₅ (DDT) ₁₈ /Al ₂ O ₃	79
3.3.5.	Characterization	79
3.3.6.	Catalytic activity for 4-nitrophenol reduction reaction.....	80
3.4.	Results and Discussion.....	80
3.5.	Conclusions	90
3.6.	References	92

CHAPTER 4

4.	Probing the Thermal Stability of (3-mercaptopropyl) trimethoxysilane protected Au₂₅ clusters by <i>in situ</i> Transmission Electron Microscopy.....	97
4.1.	Abstract.....	98
4.2.	Introduction.....	98
4.3.	Materials and Methods.....	100
4.3.1.	Materials.....	100
4.3.2.	Synthesis of Au ₂₅ (MPTS) ₁₈ clusters	100
4.3.3.	Synthesis of SBA-15.....	101
4.3.4.	Synthesis of thin overlayer of Au ₂₅ (MPTS) ₁₈ clusters on SBA-15.....	101
4.3.5.	Characterization.....	102
4.4.	Results and discussion.....	102
4.5.	Conclusions.....	117
4.6.	References.....	118

CHAPTER 5

5.	Galvanic synthesis of Ag-Pd bimetallic catalysts from Ag clusters dispersed in a silica.....	125
5.1.	Abstract.....	126
5.2.	Introduction.....	126
5.3.	Materials and Methods.....	128
5.3.1.	Materials.....	128
5.3.2.	Synthesis of Ag encapsulated with silica catalysts.....	128

5.3.3.	Synthesis of Ag-Pd@SiO ₂ bimetallic catalysts by galvanic exchange with Pd precursor.....	129
5.3.4.	Synthesis of Pd@SiO ₂ catalysts.....	129
5.3.5.	Characterization.....	130
5.3.6.	Catalytic activity for 3-hexyne-1-ol hydrogenation	131
5.4.	Results and discussion.....	131
5.5.	Conclusions.....	138
5.6.	References.....	140

CHAPTER 6

6.	Activation of silica encapsulated Pd_m(MUA)_n clusters for catalysis.....	146
6.1.	Abstract.....	147
6.2.	Introduction.....	147
6.3.	Materials and Methods.....	149
6.3.1.	Materials.....	149
6.3.2.	Synthesis of Pd _m (MUA) _n clusters.....	149
6.3.3.	Synthesis of silica encapsulated Pd _m (MUA) _n clusters	149
6.3.4.	Synthesis of Pd _m (MUA) _n clusters on silica spheres	150
6.3.5.	Characterization.....	150
6.3.6.	Catalytic activity for the methane combustion reaction.....	151
6.4.	Results and discussion.....	151
6.5.	Conclusions.....	159
6.6.	References.....	160

CHAPTER 7

7.	Conclusions.....	164
7.1.	Summary and Conclusions.....	164
7.2.	Future Outlook.....	166
7.2.1.	Synthesis of metal clusters encapsulated with hollow silica sphere...	167
7.2.2.	Synthesis of ligand-free catalysts via a top-down approach.....	168
7.3.	References	170

LIST OF TABLES

Table 2.1: EXAFS fitting parameters of as synthesized Au ₂₅ (MUA) ₁₈ @SiO ₂ clusters.....	62
Table 2.2: EXAFS fitting parameters of Au ₂₅ @SiO ₂ clusters calcined at different temperatures.....	65
Table 2.3: Rate constants k (min ⁻¹) for 4-nitrophenol reduction reaction	66
Table 2.4: Conversion (%) and TONs for styrene epoxidation reactions over 24 h.....	69
Table 3.1: EXAFS fitting parameters of as-synthesized 20c-Al ₂ O ₃ /Au/Al ₂ O ₃	86
Table 3.2: EXAFS fitting parameters of 10c-Al ₂ O ₃ /Au/Al ₂ O ₃ and 20c-Al ₂ O ₃ /Au/Al ₂ O ₃ materials calcined at two different temperatures.....	88
Table 3.3: Rate constant k (min ⁻¹) for 4-nitrophenol reduction reaction.....	90
Table 4.1: EXAFS fitting parameters of as-synthesized TEOS-treated Au ₂₅ (MPTS) ₁₈ clusters on SBA-15.....	104
Table 4.2: EXAFS fitting parameters of untreated and TEOS-treated Au ₂₅ (MPTS) ₁₈ /SBA-15 materials calcined at different temperatures.....	110
Table 5.1: EXAFS fitting parameters of Ag-Pd@SiO ₂ catalyst.....	137
Table 5.2: The catalytic activity for 3-hexyne-1-ol hydrogenation reaction.....	138
Table 6.1: EXAFS fitting parameters Pd _m (MUA) _n @SiO ₂ materials as synthesized and calcined at different temperatures.....	155
Table 6.2: CO chemisorption analysis and catalytic activity for methane combustion reaction of 0.5-Pd@SiO ₂ and 2.0-Pd@SiO ₂ catalysts calcined at 650 °C.....	159

LIST OF FIGURES

Figure 1.1: Geometric and electronic structure of nanoparticle, cluster and a single atom.....	3
Figure 1.2: Schematic representation of Brust-Shiffrin synthesis of MPCs clusters.....	4
Figure 1.3: a) Step like UV-Vis absorption features of $\text{Au}_{25}(\text{SR})_{18}^-$ clusters and b) orbital level energy diagram for a model compound: $\text{Au}_{25}(\text{SH})_{18}^-$	7
Figure 1.4: a) The icosahedral Au_{13} core (left), the core is protected with six $\text{Au}_2(\text{SR})_3$ staple motifs (middle), and the full structure of $\text{Au}_{25}(\text{SR})_{18}$ clusters including TOA (tetraoctylammonium) counter ion (Au: Yellow, S: Red, TOA: Blue, C: Black, and H: White).....	8
Figure 1.5: Simulated FT-EXAFS spectra of $\text{Au}_{25}(\text{SR})_{18}$ clusters. The simulation was done by averaging the EXAFS spectra from all representative Au sites of Au_{25} (k : 3–14.5 \AA^{-1} , k^1 weighted). The spectrum was phase-corrected using the Au–S peak.....	9
Figure 1.6: Activation of $\text{Au}_{25}(\text{SR})_{18}$ clusters over different metal oxides for CO oxidation. A) CO activity over different metal oxides as a function of temperature for unactivated clusters and B) CO activity on ceria supports as a function of different activation conditions.....	10
Figure 1.7: Rate constant for the reduction of 4-nitrophenol using carbon-supported $\text{Au}_{25}(\text{SC}_8\text{H}_9)_{18}$ MPC catalysts thermally treated at different temperatures.....	11
Figure 1.8: Au L_3 edge EXAFS spectra in R space of $\text{Au}_{25}(\text{SR})_{18}$ clusters on carbon supports after heating in air (plotted with no phase shift correction).....	14
Figure 1.9: Thiolate ligand migration to ceria support during the calcination process.....	16
Figure 1.10: Soft oxidative removal of thiolates from Au clusters using peroxide oxidants...	18
Figure 1.11: Illustration of enhanced catalytic activity in selective oxidation reaction with supported ultrasmall organothiolate-protected $\text{Au}_{25}(\text{SR})_{18}$ clusters catalysts by mild chemical stripping of their surface ligands.....	19
Figure 1.12: Illustration of the <i>in situ</i> transformation of Au clusters to Au nanoparticles on nanoporous titania nanotube arrays.....	21

Figure 1.13: Illustration of Au ₂₅ (SR) ₁₈ clusters (a) encapsulated in and (b) impregnated onto a ZIF-8 metal-organic framework.....	24
Figure 1.14: Schematics of environmental TEM set-up featuring differential pumping, dedicated apertures, and pole pieces, b) sample holder with gas inlet, and c) A heating coil centered on the SiN _x window of the TEM grid.....	26
Figure 1.15: X-ray absorption measurements: (a) An incident beam of monochromatic X-rays of intensity I ₀ passes through a sample of thickness t, and the transmitted beam has intensity I _t , and (b) a diagram showing the ionization of a 1s core electron.....	26
Figure 1.16: Absorption of X-rays as a function of photon energy E=hv by a) a free atom and b) by atoms in a lattice.....	29
Figure 1.17: a) Experimental X-ray absorption spectra of Au nanoparticles. The free-atom absorption coefficient (red line) and jump at the edge energy are indicated b) extracted EXAFS signal with a k ² weighting, c) the Fourier-transformed EXAFS signal, d) a first shell fit to the EXAFS spectra using a fcc Au model.....	32
Figure 1.18: XPS spectra of Pd 3d _{3/2} and Pd 3d _{5/2} peaks for a) PdCl ₂ -TiO ₂ b) PdO-TiO ₂ and Reduced Pd-TiO ₂ . Reproduced with permission 118. Copy right (2015), Institute of Physics Science.....	34
Figure 2.1: UV-Vis spectra of Au ₂₅ (MUA) ₁₈ clusters.....	58
Figure 2.2: a) & b) TEM images of as synthesized Au ₂₅ (MUA) ₁₈ clusters.....	59
Figure 2.3: TEM images of Au ₂₅ /SiO ₂ catalysts a) as-synthesized, b) calcined at 250 °C and c) calcined at 650 °C.....	59
Figure 2.4: TEM images of Au ₂₅ @SiO ₂ calcined at a) 250 °C, b) 350 °C, c) 450 °C, d) 550 °C, e) and f) 650 °C (inset; enlarged image).....	60
Figure 2.5: Histogram of Au@SiO ₂ catalysts calcined at different temperatures.....	61
Figure 2.6: Au L ₃ edge EXAFS fitting in a) k space and b) phase-corrected R space of as synthesized Au ₂₅ (MUA) ₁₈ @SiO ₂ clusters	62
Figure 2.7: Au-L ₃ edge EXAFS data in phase corrected R-space of Au ₂₅ @SiO ₂ catalysts calcined at different temperatures.....	63

Figure 2.8: Au-L ₃ edge EXAFS fitting data in k (left) and R-space of Au@SiO ₂ calcined at a ₁ &a ₂) 250 °C, b ₁ &b ₂) 350 °C, c ₁ &c ₂) 450 °C, d ₁ &d ₂) 550 °C, and e ₁ &e ₂) 650 °C.....	64
Figure 2.9: Catalytic activity for 4-nitrophenol reduction reaction over Au@SiO ₂ calcined at a) 250 °C, b) 350 °C, c) 450 °C, d) 550 °C, and e) 650 °C, and f) Plot of ln[Ct]/[C ₀] as a function of reaction time in min.....	66
Figure 2.10: Plot of first shell coordination number of Au@SiO ₂ catalysts vs rate constant for 4-nitrophenol reduction reaction and calcination temperature.....	67
Figure 2.11: Catalytic activity for 4-nitrophenol reduction reaction over Au/SiO ₂ calcined at a) 250°C, and b) 650°C.....	68
Figure 3.1: TEM images of as-synthesized a) Au ₂₅ (MUA) ₁₈ /Al ₂ O ₃ , b) Au ₂₅ (DDT) ₁₈ /Al ₂ O ₃ , and c) 10c-Al ₂ O ₃ /Au ₂₅ (MUA) ₁₈ /Al ₂ O ₃ and d)10c-Al ₂ O ₃ /Au ₂₅ (DDT) ₁₈ /Al ₂ O ₃	81
Figure 3.2: TEM images of Au ₂₅ (MUA) ₁₈ samples on Al ₂ O ₃ calcined at a) 250 °C, b) 650 °C; 5c-Al ₂ O ₃ /Au(MUA)/Al ₂ O ₃ calcined at c) 250 °C, d) 650 °C; 10c-Al ₂ O ₃ /Au(MUA)/Al ₂ O ₃ calcined at e) 250, f) 650 °C; and 20c-Al ₂ O ₃ /Au(MUA)/Al ₂ O ₃ calcined at g) 250 °C, h) 650°C.....	82
Figure 3.3: Histograms of a) Au(MUA)/Al ₂ O ₃ , b) 5c-Al ₂ O ₃ /Au(MUA)/Al ₂ O ₃ , c) 10c-Al ₂ O ₃ /Au(MUA)/Al ₂ O ₃ , and d) 20c-Al ₂ O ₃ /Au(MUA)/Al ₂ O ₃ catalysts calcined at different temperatures	83
Figure 3.4: TEM images of 10c-Al ₂ O ₃ /Au ₂₅ (DDT) ₁₈ /Al ₂ O ₃ calcined at a) 250 °C, and b) 650°C.....	84
Figure 3.5: Au L ₃ edge EXAFS fitting data in k and R space of as-synthesized 20c-Al ₂ O ₃ /Au/Al ₂ O ₃	85
Figure 3.6: Au L ₃ edge EXAFS fitting data in phaseshift corrected-k(left) and R space of 10c-Al ₂ O ₃ /Au/Al ₂ O ₃ calcined at a) & b) 250°C and c) & d) 650°C.....	87
Figure 3.7: Au L ₃ edge EXAFS fitting data in phaseshift corrected-k (left) and R space of 20c-Al ₂ O ₃ /Au/Al ₂ O ₃ calcined at a) & b) 250 °C and c) & d) 650 °C.....	87

Figure 3.8: 4-Nitrophenol reduction reaction over catalyst calcined at 250 °C a) Au(MUA)/Al ₂ O ₃ b) 10c-Al ₂ O ₃ /Au(MUA)/Al ₂ O ₃ c) 20c-Al ₂ O ₃ /Au(MUA)/Al ₂ O ₃ and d) Plot of ln[Ct]/[C ₀] as a function of reaction time in min.....	89
Figure 3.9: 4-Nitrophenol reduction reaction over catalyst calcined at 650 °C a) Au(MUA)/Al ₂ O ₃ b) 10c-Al ₂ O ₃ /Au(MUA)/Al ₂ O ₃ c) 20c-Al ₂ O ₃ /Au(MUA)/Al ₂ O ₃ and d) Plot of ln[Ct]/[C ₀] as a function of reaction time in min.....	90
Figure 4.1: a) UV-Vis spectra and b) TEM images of Au ₂₅ (MPTS) ₁₈ clusters.....	103
Figure 4.2: Au L ₃ edge EXAFS fitting (not phase corrected) in a) k space and b) R space of as-synthesized TEOS-treated Au ₂₅ (MPTS) ₁₈ clusters on SBA-15.....	104
Figure 4.3: TEM images of Au ₂₅ (MPTS) ₁₈ /SBA-15. a) as synthesized, b) calcined at 250 °C, c) 450 °C, and d) 650 °C for 3 h.....	105
Figure 4.4: TEM images of TEOS/Au ₂₅ (MPTS) ₁₈ /SBA-15. a) as-synthesized, b) calcined at 250 °C, c) 450 °C, and d) 650 °C for 3 h.....	106
Figure 4.5: XRD spectra of a) Au ₂₅ (MPTS) ₁₈ /SBA b) TEOS/Au ₂₅ (MPTS) ₁₈ /SBA	107
Figure 4.6: Au L ₃ edge EXAFS fitting in phase-corrected R-space of a) TEOS/Au ₂₅ (MPTS) ₁₈ /SBA-15 materials at different temperatures b) Au ₂₅ (MPTS) ₁₈ /SBA-15 at 250 °C and 650 °C.....	108
Figure 4.7: Au L ₃ edge EXAFS fitting in phase-corrected k (left) space and R (right) space of Au ₂₅ (MPTS) ₁₈ /SBA calcined a) & b) at 250 °C and c) & d) at 650 °C.....	109
Figure 4.8: Au L ₃ edge EXAFS fitting in phase-corrected k (left) and R (right) space of TEOS/Au ₂₅ (MPTS) ₁₈ /SBA catalysts calcined at a) & b) 250 °C c) & d) 350 °C e) & f) 450 °C g) & h) 550 °C and i) & j) 650 °C.....	111
Figure 4.9: The sequence of <i>in situ</i> TEM heating images of Au ₂₅ (MPTS) ₁₈ clusters on the SBA-15 at 550 °C in every 8 s. The trajectory of individual Au particles is indicated by blue line.....	113
Figure 4.10: The sequence of <i>in situ</i> TEM heating images of Au ₂₅ (MPTS) ₁₈ /SBA-15 sample were collected at 650 °C in every 2 s. The trajectory of a Au particle (particle in a blue circle) is indicated by blue line.....	114

Figure 4.11: The sequence of <i>in situ</i> TEM heating images of TEOS/Au ₂₅ (MPTS) ₁₈ /SBA-15 samples at a) 50 °C, b) 250 °C, c) 350 °C, d) 450 °C, e) 550 °C, and f) 650 °C.....	116
Figure 4.12: The sequence of <i>in situ</i> TEM heating TEOS/Au ₂₅ (MPTS) ₁₈ /SBA-15 at 650 °C in every 8 s (except image f).	116
Figure 5.1: UV-Vis spectra of Ag Nanotriangle	132
Figure 5.2: BET surface area of Ag@SiO ₂ materials after calcination at 650 °C.....	132
Figure 5.3: a) TEM image of a) as-synthesized Ag NP's b) as-synthesized Ag@SiO ₂ , c) Ag@SiO ₂ calcined at 650 °C, and d) Ag-Pd@SiO ₂ sample after galvanic exchange.....	133
Figure 5.4: a) Ag 3d XPS spectra of Ag@SiO ₂ , b) Ag 3d XPS spectra of Ag-Pd@SiO ₂ and c) Pd 3d XPS spectra of Ag-Pd@SiO ₂	134
Figure 5.5: Pd L ₃ -edge XANES spectra of K ₂ PdCl ₄ before and after the addition of Ag@silica.....	135
Figure 5.6: $\chi(k)$ vs k^2 plots of EXAFS spectra of Ag-Pd@SiO ₂ at a) Ag-K edge b) Pd-K edge.....	136
Figure 5.7: EXAFS fitting data of Ag-Pd@SiO ₂ a), Pd K edge in k space b), Pd K edge in R sapce, and c), Ag K edge in k space d), Ag K edge in R space.....	137
Figure 6.1: a) UV-Vis spectra of Pd _m (MUA) _n clusters b) TGA of Pd _m (MUA) _n clusters.....	152
Figure 6.2: a) TEM image of Pd _m (MUA) _n clusters b) as-synthesized Pd(MUA) _n @ SiO ₂ , and c) Pd@SiO ₂ calcined at 250 °C.d) Pd@SiO ₂ calcined at 650 °C.....	152
Figure 6.3: TEM images of a) Pd/SiO ₂ samples b) calcined at 250 °C c) calcined at 650 °C	153
Figure 6.4: BET- Surface area analysis of silica encapsulated Pd _m (MUA) _n clusters.....	153
Figure 6.5: Pd K-edge EXAFS spectra in R space of Pd _m (MUA) _n @SiO ₂ catalysts calcined at different temperatures.....	154
Figure 6.6: Pd K-edge EXAFS fitting data of Pd _m (MUA) _n @SiO ₂ in a) R-space and b) k-space. Pd K-edge EXAFS fitting data of Pd _m (MUA) _n @SiO ₂ calcined at 250 °C in c) R-space and d) k-space.....	156
Figure 6.7: a) Unit cell of Pd-O, grey and red circles represent Pd and O, respectively, and Pd	

K-edge EXAFS spectra in b) R-space and c) k-space of Pd@SiO₂ catalysts calcined at 650 °C
.....157

Figure 6.8: Methane combustion reaction over Pd@SiO₂ and Pd/SiO₂ catalysts.....158

Figure 7.1: a) TEM image of a) as-synthesized Au-Ag@SiO₂ b) Ag 3d XPS spectra of Au-Ag@SiO₂ and c) Au 4f spectra of Au-Ag@SiO₂.....169

LIST OF SCHEMES

Scheme 2.1: General scheme for the synthesis of silica encapsulated $\text{Au}_{25}(\text{MUA})_{18}$ clusters.....	55
Scheme 3.1: Schematic illustration of alumina deposition over $\text{Au}_{25}(\text{MUA})_{18}/\text{Al}_2\text{O}_3$. Colour scheme: red circles, methyl groups, light blue Al, dark purple O, and dark blue H.....	84
Scheme 4.1: Schematic representation of experimental setup to introduce moisture to the ethanolic- TEOS solution for silica coating.....	101
Scheme 6.1: Silica encapsulation of $\text{Pd}_m(\text{MUA})_n$ clusters.....	150

\

LIST OF ABBREVIATIONS

ALD: Atomic Layer Deposition

CN: Coordination Number

CLS: Canadian Light Source

CVD: Chemical vapour deposition

DDT: Dodecanethiol

DMA: Dimethylamine

DMF: *N, N*-dimethylformamide

ESCA: Electron Spectroscopy for Chemical Analysis

ESI: Electron Spray Ionization

EXAFS: Extended X-Ray Absorption Fine Structure

HXMA: Hard X-ray Microanalysis Beamline

MALDI: Matrix-Assisted Laser Desorption Ionization

MHA: 16-Mercaptohexadecanoic acid

MIL-101: $\text{Cr}_3\text{F}(\text{H}_2\text{O})_2\text{O}(1,4\text{-benzenedicarboxylate})_3$

MOF: Metal-Organic Framework

MPC: Monolayer-Protected Cluster

MPTS: (3-mercaptopropyl) trimethoxysilane

MUA: Mercaptoundecanoic acid

NMR: Nuclear Magnetic Resonance

OR: Ostwald Ripening

PMC: Particle Migration and Coalescence

PVP: Poly(N-vinylpyrrolidone)

SBA-15: Santa Barbara Amorphous (silica)

SPR: Surface Plasmon Resonance

STEM: Scanning Transmission Electron Microscopy

SXRMB: Soft X-ray Micro Characterization Beamline

TBHP: Tert-butyl hydroperoxide

TEM: Transmission Electron Microscopy

TEOS: Tetraethylorthosilicate

TGA: Thermogravimetric Analysis

THF: Tetrahydrofuran

TMA: Trimethylaluminum

TOAB: Tetraoctylammonium Bromide

XAS: X-ray Absorption Spectroscopy

XANES: X-ray Absorption Near Edge Structure

XPS: X-Ray Photoelectron Spectroscopy

XRD: X-Ray Diffraction

ZIF-8: Zn(2-methylimidazole)₂

CHAPTER 1

1. Catalysis by nanomaterials

Catalysis plays an important role in industry because most chemical reactions occur on the surface of catalysts. Homogeneous and heterogeneous catalysts are two major classifications of catalysts. Since the catalyst and substrate are in the same phase, recycling of homogeneous catalysts is an important issue in large-scale production of chemicals. Heterogeneous catalysts offer an advantage that products are easily separated from the catalyst since both catalysts and reactants are in different phases. However, heterogeneous catalysts sometimes show lesser activity or selectivity than homogeneous counterparts.¹ Nanocatalysis has emerged as a subfield from the nanoscience that offers a unique solution to overcome all the limitations associated with the homogeneous and heterogeneous catalytic systems. Nanocatalysis can bridge the gap between homogeneous and heterogeneous catalysis, preserving the desirable attributes of both systems.

The word “nano” refers to very small objects that have at least one dimension in the nanoscale range (1-100 nm) of size. Nanoparticles have specific physical and chemical properties that are intermediate between those of the atomic element from which they are composed and bulk materials. It is observed that a strong relationship exists between catalytic activity and properties of nanomaterials due to factors such as surface to volume ratio, geometric surface rearrangements (surface atom arrangements and under-coordinated atoms), electronic interactions between atoms, and quantum size effects.²⁻³ Precious metal nanoparticles including Ag, Au, Pd, Pt, Rh, and Ru have been found to be active for many industrial reactions.⁴ Among these metals, Au has been attracted tremendous research attention since the discovery of its catalytic properties.

In the 1970s, Au nanoparticles were found to be promising low-temperature catalysts for CO oxidation.⁵ Au nanoparticles that are below 5 nm in size are an efficient catalyst for CO oxidation at low temperatures (-77 °C). Since discovering the excellent activity for CO oxidation at low temperatures, Au catalysis has been a hotspot for research. Haruta *et al.* investigated the catalytic activity of Au catalysts supported on various oxides for selective catalytic reduction of NO_x to N₂ by hydrocarbons such as propane, propene, ethane, and ethene and reported Au/Al₂O₃ is most active for the reduction reaction.⁶ Following the pioneering

study of Haruta, groups have explored the catalytic activity of Au for many reactions.⁷⁻⁹ Recently Au catalysts have been commercialized in China for the synthesis of vinyl chloride by acetylene hydrochlorination.¹⁰ Although factors such as metal-support interactions, the nature of the support, the nature of stabilizing ligands, and particle shape affect the catalytic activity, the size of the Au nanoparticles plays a major role in the catalysis; generally, catalytic activity increases as the size of the particle decreases.¹¹ Due to the excellent activity, chemical stability, availability, and lower price compared to Pt and Rh, Au can be a good replacement for industrial applications. However, the major challenge of using Au as a catalyst is sintering. Au nanoparticle catalysts tend to deactivate at moderate temperature (250 °C) due to the agglomeration of clusters, which restricts the use of Au systems as catalysts in industry. Synthesis of sinter-resistant Au nanoparticle catalysts remains an elusive research goal in the field.

1.2. Classification of nanomaterials

Based on the relative size of the materials, nanomaterials are often classified into nanoparticles and clusters.¹² Colloidal particles that are 2-100 nm in size are commonly known as nanoparticles, while colloids that are below 2 nm in size are often referred to as clusters. As shown in Figure 1.1, the electronic properties of materials vary with their size. Nanoparticles have properties between bulk materials with continuous energy states and clusters which have discrete energy levels. Electronic properties are drastically changed from nanoparticles to clusters due to the loss of overlapping atomic orbitals.¹³ Below 2 nm-sized metal clusters exhibit quantum confinement effects such as the disappearance of surface plasmon resonance (SPR) bands and emergence of HOMO-LUMO transitions. Specifically, Au nanoparticles show SPR bands due to the collective oscillation of electrons in the conduction band.¹⁴ As UV-visible radiation passes through the nanoparticles in solution, the electron density in the particle is polarized to one surface and oscillates in resonance with the frequency of incident radiation causing a standing oscillation. Resonance conditions depend on the size, shape, and dielectric constant of the metal nanoparticle and surrounding material.

Nanoparticles and clusters are often prepared by the reduction of metal precursors in the presence of capping agents such as polymers, amines, and surfactants that stabilize the nanoparticles from agglomeration. Stabilization in colloids is achieved by either electrostatic or steric stabilization.¹⁵ Electrostatic repulsion between the particles is due to the formation of an electrical double layer created by the adsorption of charged species on the nanoparticle

surface. This kind of stabilization is generally provided by means of ionic surfactants. Steric stabilization is often achieved by the adsorption of macromolecules to the surface of metal nanoparticles that inhibit the agglomeration of nanoparticles in solution. A shell is formed via metal-ligand interactions that provide stability to the colloidal system.

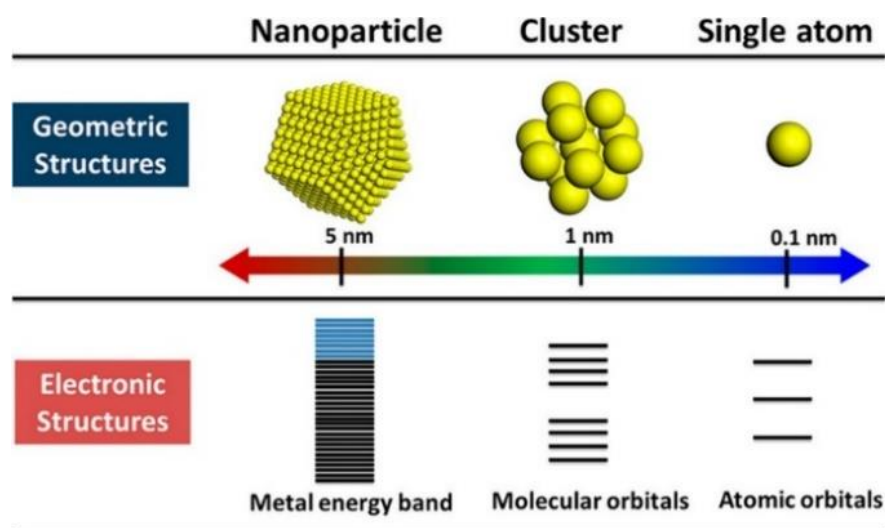


Figure 1.1: Geometric and electronic structures of nanoparticles, clusters, and a single atom. Reprinted with permission from reference 12. Copyright 2018, American Chemical Society.

1.3. Ligand protected Au clusters

Metal clusters are an important class of materials due to their unique properties that differ from both bulk and atomic scale.¹³ Noble metals with sizes in the nanoscale, also commonly referred to as nanoclusters, or simply as clusters, generally show excellent catalytic activity due to their enhanced surface-to-volume ratio which leads to more active sites, as well as having modified surface geometries and tremendously different electronic properties as compared to bulk materials and nanoparticles. Naked metal clusters are typically unstable in solution, and their synthesis becomes feasible when protected with small, strongly-bound ligands such as thiolates, carbenes, phosphenes, and selenolates.¹² The stability of clusters is often achieved by a core-shell morphology, in which core with a certain number of metal atoms is protected by a shell that consists of metal-ligand staple motifs. The type of ligand, among other factors, influences reaction conditions for the successful synthesis of ligand protected metal clusters. Although clusters protected with other ligands are included, the emphasis below is on different forms of thiolate-protected metal clusters.

Among metal clusters, Au monolayer protected clusters have been extensively studied. After the first report of $\text{Au}_{11}(\text{SCN})_3(\text{PPh}_3)_7$ clusters in 1969, many research efforts have been made resulting in the development of a variety of Au clusters.¹⁶⁻²² A detailed crystallographic study of $\text{Au}_{11}(\text{SCN})_3(\text{PPh}_3)_7$ clusters indicated that one Au central atom is surrounded by ten gold atoms that are attached to one ligand each. In 1981 Schmid *et al.* introduced a method for synthesizing $\text{Au}_{55}[\text{P}(\text{C}_6\text{H}_5)_3]_{12}\text{Cl}_6$ clusters.²³ Brust and coworkers first reported a biphasic method in 1994 for synthesizing thiolate-based monolayer-protected clusters.²⁴⁻²⁵ As shown in Figure 1.2, the metal precursor is dissolved in an aqueous solution and transferred into the organic phase using phase transfer agents such as tetraoctylammonium bromide. In the second step, Au (III) salts in toluene are converted into Au(I) species by reacting with thiol stabilizers. Finally, the Au(I) species are reduced by adding an excess of NaBH_4 . These Au clusters were found to be relatively polydisperse in nature, and the size of the clusters could be tuned, to some extent, by changing the Au: thiol ratio and type of thiol used. In seminal work, Schaff and coworkers isolated a series of clusters ranging in size from ~1.4 to ~1.9 nm by fractional crystallization or column chromatography.²⁶⁻²⁷ Palmer *et al.* made a detailed study of $\text{Au}_{55}[\text{P}(\text{C}_6\text{H}_5)_3]_{12}\text{Cl}_6$ clusters using aberration-corrected scanning transmission electron microscopy (STEM) combined with simulation of STEM images.²⁸⁻²⁹ The results indicated that the $\text{Au}_{55}[\text{P}(\text{C}_6\text{H}_5)_3]_{12}\text{Cl}_6$ samples contained clusters with different crystal structures as well as clusters containing between 30-60 Au atoms. Due to sample polydispersity and the uncertain surface structure of monolayer protected clusters, structure-activity relationships in catalysis for such clusters could not be well explained.³⁰ To reveal an atomic level understanding of such a relationship, a model catalyst with monodisperse and well-defined structure is required. For fundamental studies on the size effect in catalysis, it is crucial to prepare monodisperse clusters.

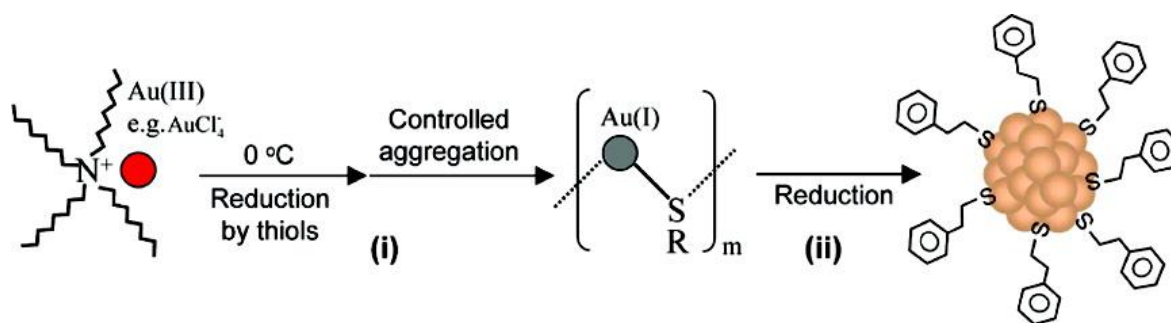


Figure 1.2: Schematic representation of the Brust-Shiffrin synthesis of Au clusters. Reprinted with permission from reference 24). Copyright 2008, American Chemical Society.

1.4. Atom-precise Au clusters

The demand for monodisperse catalysts resulted in the development of a new class of materials, known as atom-precise clusters. Atom-precise clusters can be used as model catalysts to explore structure-activity relationships in catalysis because they have a well-defined structure. Atom-precise clusters are highly monodisperse, stable, structurally well-defined, and generally designated as M_xL_y , where x is the number of metal atoms, and y is the number of protecting ligands (L) in the cluster composition. Organic ligands such as thiols, acetylene, carbenes, phosphines, and selenolates provide stability to the Au core under ambient conditions. In recent years, tremendous research has focused on the ability to synthesize monodisperse, atom-precise metal clusters by optimizing the synthesis conditions such as solvent, metal to ligand ratio, temperature, reducing agent, and purification and separation strategies.³⁰⁻³⁶

Thiolate protected clusters are widely studied due to strong sulfur-metal interactions that enable good stability in solution, facile synthesis, and controlled cluster compositions as well as functionalization of stable clusters. In this thesis, I focus on the synthesis of thiolate protected clusters. Thiolate protected clusters are generally represented by their exact formula $Au_n(SR)_m$, where n and m are the respective numbers of metal atoms and thiolate ligands (SR). Such clusters can be synthesized via “bottom-up” and “top-down” synthetic strategies. Top-down approaches involve the breaking of a bulk material into nanostructures by the use of physical process such as lithographic techniques,³⁷⁻³⁸ ball milling,³⁹ pulse laser vaporization,⁴⁰ or chemical etching.⁴¹ Chemical etching is the most simple method to synthesize Au clusters from larger structures. Zhou *et al.* synthesized Au_8 clusters by breaking apart Au nanorods under sonication in H_2O .⁴¹ The bottom-up approach involves the reduction of a metal precursor using a reducing agent followed by nucleation of zerovalent metal clusters. Various modified Brust-Schiffrin methods are representative of the bottom-up synthetic strategy. Many reports on the synthesis, characterization, and applications of atom-precise thiolate-protected Au clusters such as $Au_{144}(SR)_{60}$,⁴² $Au_{102}(SR)_{44}$,⁴³ $Au_{38}(SR)_{24}$,⁴⁴ and $Au_{25}(SR)_{18}$,⁴⁵ can be found in the literature.

Among these clusters, $Au_{25}(SR)_{18}^-$ clusters have attracted tremendous research attention because of their reproducible syntheses and high stability. In 2004, Murray and coworkers synthesized well-dispersed Au clusters using a modified Brust procedure and mislabelled it as $Au_{38}(SCH_2CH_2Ph)_{24}$.⁴⁶ Later, they investigated the structural details of these clusters with the

use of electron spray ionization mass spectrometry and correctly identified them as $\text{Au}_{25}(\text{SCH}_2\text{CH}_2\text{Ph})_{18}$ clusters.⁴⁷ The first report for the high yield synthesis of phenylethanethiol protected Au_{25} clusters was documented by Jin and coworkers in 2008.²⁴ In a typical procedure, Au (III) in aqueous solution is transformed into organic phase (toluene) with aid of tetraoctylammonium (TOA) bromide. The solution is cooled down to 0 °C, followed by the addition of phenylethanethiol. At this point the colour of the solution turns from orange to colorless that indicate the reduction of Au (III) to Au (I). Then the Au:SR (I) intermediate is reduced by addition of an ice-cold NaBH_4 solution. It is observed that temperature greatly affects the kinetics of cluster synthesis. Several alternative methods have been reported for the synthesis of Au_{25} clusters with different types of ligands.⁴⁸⁻⁵¹ Initially, it was believed that TOA cations simply acted as a phase transfer agent that helps metal precursor to transfer from aqueous to organic phase. Later single-phase synthetic studies show that TOA has a special role in the stability of the clusters, as it acts as a counter ion for the negative charge on the Au_{25} clusters.⁵²

1.5. Characterization of $\text{Au}_{25}(\text{SR})_{18}$ clusters¹

Atom-precise metal clusters have unique absorption behavior in the visible region of light, due to their discrete electronic structures.⁵³⁻⁵⁴ As a result, specific clusters show multiple features across the entire visible range in their optical absorption spectra that are defined by their core structures, and thus UV-Vis spectroscopy can be used as a facile technique, or fingerprint, to follow cluster speciation in solution. Since the position of absorption bands vary with cluster size, this technique can be used to reveal the structural integrity of clusters. For example, $\text{Au}_{25}(\text{SR})_{18}$ clusters show three distinct adsorption bands at 400 nm, 450 nm, and 680 nm which are shown in Figure 1.3.⁵⁵ The peak at 680 nm is attributed to the HOMO-LUMO transition, which is essentially an intraband ($\text{sp} \leftarrow \text{sp}$) transition. The second peak at 450 nm arises from the intraband ($\text{sp} \leftarrow \text{sp}$) and interband ($\text{sp} \leftarrow \text{d}$) transitions. The last one appears at 400 nm and corresponds to interband ($\text{sp} \leftarrow \text{d}$) transitions.

¹ Some of the material has been published in *Nanoscale Adv.*⁶⁹

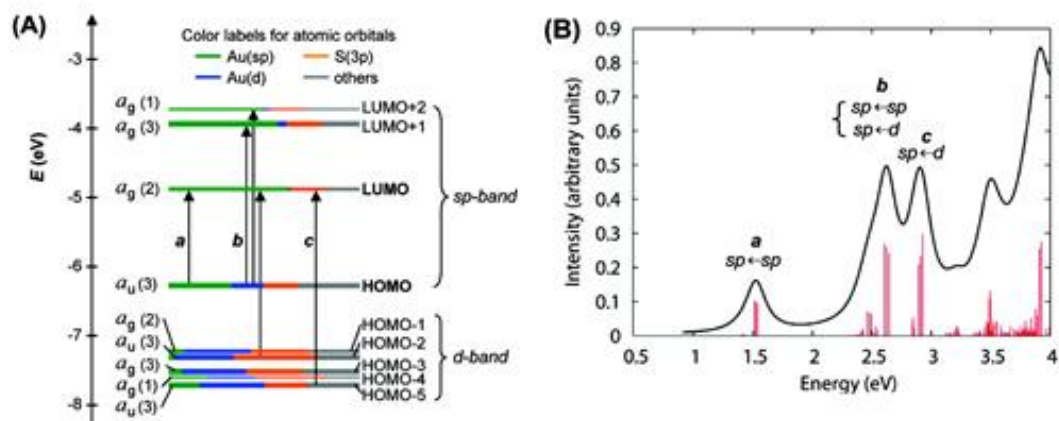


Figure 1.3: a) Step like UV-Vis absorption features of $\text{Au}_{25}(\text{SR})_{18}^-$ clusters and b) orbital level energy diagram for a model compound: $\text{Au}_{25}(\text{SH})_{18}^-$. Reprinted with permission from reference 55. Copyright 2008, American Chemical Society.

Mass spectrometry has been used in many cases to precisely follow the masses and charges on clusters. Ionization methods in mass spectrometry such as matrix-assisted laser desorption ionization (MALDI) and electron spray ionization (ESI) have allowed for determinations of the exact formulae of ligand-protected clusters, particularly in the absence of single-crystal X-ray crystallography data.^{42-44, 56} In recent years, many structures have been solved by single-crystal crystallography, and core-shell morphologies are often seen, wherein the Au core has certain geometrical structures that give unique physicochemical properties to the whole cluster, and Au-thiolate staples cap the core structure.⁵⁷ Murray *et al.* and Jin *et al.* independently reported the crystal structure of $\text{Au}_{25}(\text{SR})_{18}$ clusters, which comprise an icosahedral Au_{13} core which is capped by six dimeric $\text{Au}_2(\text{SR})_3$ staple motifs anchored on 12 out of 20 facets of the icosahedral core which is shown in Figure 1.4.^{52, 55} The Au_{25} clusters exhibit stability against degradation in solution and thiol etching. Figure 1.4 shows a single-crystal structure of the $\text{Au}_{25}(\text{SR})_{18}$ clusters; the formation of a core-shell morphology can be seen in which 13 atoms are in the central core which is capped with metal-thiolate staples.

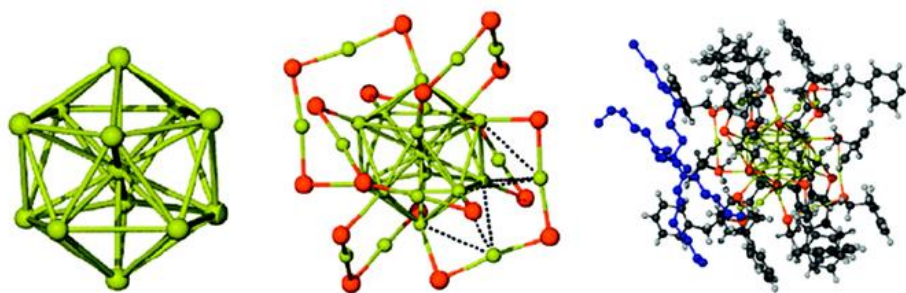


Figure 1.4: The icosahedral Au_{13} core (left), the core is protected with six $\text{Au}_2(\text{SR})_3$ staple motifs (middle), and the full structure of $\text{Au}_{25}(\text{SR})_{18}$ clusters including TOA (tetraoctylammonium) counter ion (Au: Yellow, S: Red, TOA: Blue, C: Black, and H: White). Reprinted with permission from reference 52. Copyright 2008, American Chemical Society.

Extended X-ray absorption fine structure (EXAFS) spectroscopy is another valuable tool that has been used to follow the structure of various supported and non-supported metal clusters. Based on the crystal structure, Zhang and coworkers demonstrated an atomic model of $\text{Au}_{25}(\text{SR})_{18}$ clusters for EXAFS fitting.⁵⁸ As shown in Figure 1.5, the structure of $\text{Au}_{25}(\text{SR})_{18}$ clusters is divided into several distinct bonding domains. The first prominent peak at approximately $\sim 2.3 \text{ \AA}$ is due to Au-S first shell scattering. The first Au-Au contribution is observed at $\sim 2.8 \text{ \AA}$, is due to the interatomic distance between the central Au atom of icosahedral core and the 12 surface Au atoms, and some interactions of adjacent surface Au atoms. The second Au-Au interaction consists of a bond ($\sim 2.95 \text{ \AA}$) between the adjacent atoms on the surface of the icosahedral core. The last peak appears at $\sim 3.15 \text{ \AA}$, which is due to the surface-staple Au-Au interactions.

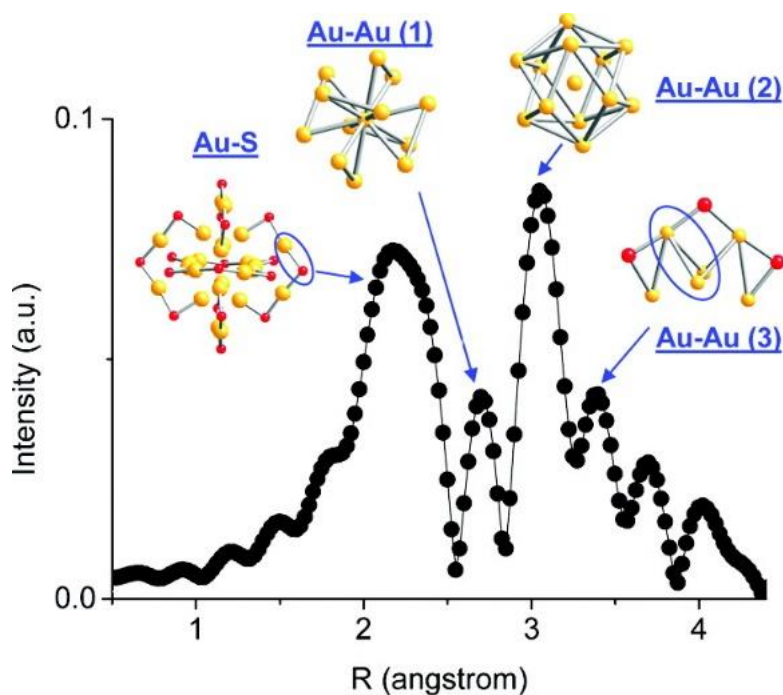


Figure 1.5: Simulated FT-EXAFS spectra of $\text{Au}_{25}(\text{SR})_{18}$ clusters. The simulation was done by averaging the EXAFS spectra from all representative Au sites of Au_{25} (k : 3–14.5 \AA^{-1} , k^1 weighted). The spectrum was phase-corrected using the Au–S peak. Reprinted with permission from ref 58. Copyright 2011, American Chemical Society.

1.6. Catalysis by $\text{Au}_{25}(\text{SR})_{18}$ clusters and importance of activation process in catalysis

$\text{Au}_{25}(\text{SR})_{18}$ clusters have been found to be an effective catalyst for various oxidation and reduction reactions such as cyclohexane oxidation, styrene epoxidation, hydrogenation of α , β -unsaturated ketones/aldehydes, and 4-nitrophenol reduction reactions.⁵⁹ Ceria-supported Au_{25} clusters have shown moderate catalytic activity for carbon monoxide oxidation at room temperature.⁶⁰ The influence of thiolate ligands around Au_{25} clusters on porous carbon nanosheets for benzyl alcohol oxidation was studied by Yoskamtorn *et al.*⁶¹ They observed that thiolate ligands act as a site-blocking agent that suppresses the catalytic activity. The catalysts with thiolate ligands did not exhibit any catalytic activity, while the thiolate-free Au_{25} clusters showed 84% conversion to benzaldehyde. Our group and several other groups have observed that Au clusters are an effective catalyst for styrene oxidation reactions.^{62–63} Glutathione-stabilized $\text{Au}_{25}(\text{SR})_{18}$ clusters on hydroxyapatite were found to be capable of catalyzing selective styrene to styrene oxide reactions using tert-butyl hydroperoxide (TBHP) as an oxidant.⁶³ After heating for 12 h at 80 °C in toluene, the reaction yielded styrene oxide (92%) as the major product. Zhu

et al. showed that $\text{Au}_{25}(\text{SR})_{18}$ (in the form of free clusters or supported clusters) is an effective catalyst for styrene oxidation in the presence of oxygen.⁶⁴ The reaction was performed at 80–100 °C for 12–24 h producing benzaldehyde as a major product using the atom-precise Au clusters as the catalyst. They observed that the size of the cluster plays an important role in styrene epoxidation reaction, and found that $\text{Au}_{25}(\text{SR})_{18}$ clusters on SiO_2 are more catalytically active than $\text{Au}_{38}(\text{SR})_{24}$ and $\text{Au}_{144}(\text{SR})_{60}$ clusters on the same support when O_2 is used as the oxidant. This result indicates that $\text{Au}_{25}(\text{SR})_{18}$ clusters on silica are capable for activating oxygen, which is key step in the oxidation reaction. Nie *et al.* examined the catalytic activity of phenylethanethiolate-stabilized $\text{Au}_{25}(\text{SR})_{18}$ clusters on different oxide supports for CO oxidation and found that optimal CO oxidation catalysts were generated using ceria supports and activation at 150 °C under oxygen, as seen in Figure 1.6.⁶⁰ Interestingly, pretreated catalysts showed excellent activity for CO oxidation, as the CO conversion starts at *ca.* 40 °C and reaches 100 % conversion at approximately 80 °C.

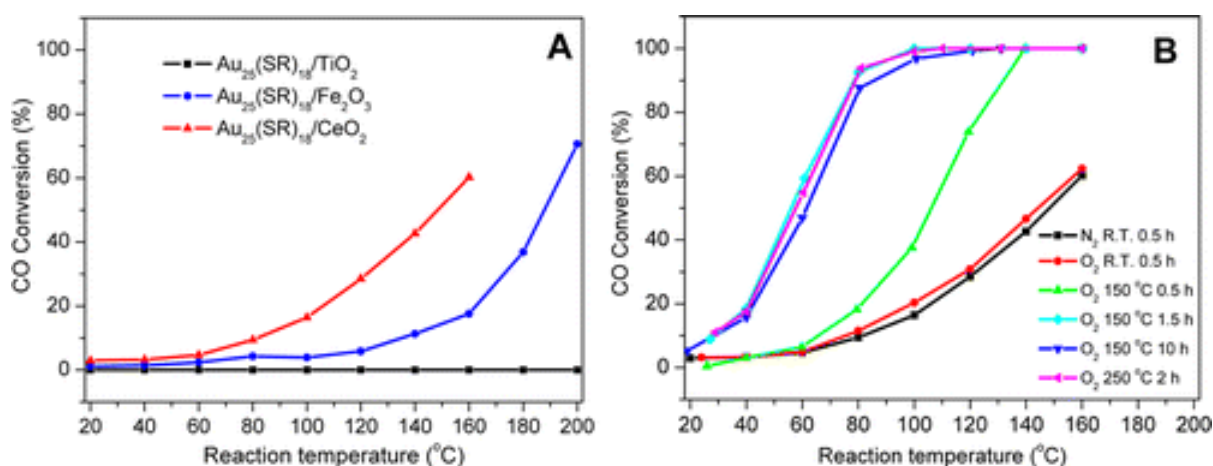


Figure 1.6: Activation of $\text{Au}_{25}(\text{SR})_{18}$ clusters over different metal oxides for CO oxidation. A) CO activity over different metal oxides as a function of temperature for unactivated clusters and B) CO activity on ceria supports as a function of different activation conditions. Reproduced with permission from ref 60. Copyright 2012, American Chemical Society.

$\text{Au}_{25}(\text{SR})_{18}$ catalysts were found to be an active catalyst for the hydrogenation of α , β -unsaturated ketones to α , β -unsaturated alcohols at 0 °C.⁶⁵ Zhu *et al.* investigated the catalytic activity of $\text{Au}_{25}(\text{SR})_{18}$ clusters for the hydrogenation of benzalacetone.⁶⁶ The reaction was carried out at 0 °C under a hydrogen atmosphere for 3 h and yielded 22% conversion with 100% selectivity towards the α , β -unsaturated alcohol. Yamamoto *et al.* investigated the catalytic activity of glutathione protected Au_{25} clusters for 4-nitrophenol reduction and showed that they had much better catalytic activity than larger *N,N*-dimethylformamide (DMF)-

stabilized Au nanoclusters.⁶⁷ Our group studied the impact of chain length of ligands in the catalytic activity for 4-nitrophenol reduction reaction using three different $\text{Au}_{25}(\text{SR})_{18}$ clusters, including $\text{Au}_{25}(\text{SC}_8\text{H}_9)_{18}$, $\text{Au}_{25}(\text{SC}_6\text{H}_{13})_{18}$, and $\text{Au}_{25}(\text{SC}_{12}\text{H}_{25})_{18}$.⁵¹ The lower rate constant measured for $\text{Au}_{25}(\text{SC}_{12}\text{H}_{25})_{18}$ clusters was explained by the increased mass transfer issue associated with longer chain length of thiol ligands. In another study, carbon-supported $\text{Au}_{25}(\text{SC}_8\text{H}_9)_{18}$ clusters were found to be capable of catalyzing the 4-nitrophenol reduction to 4-aminophenol.⁶⁸ Thermal calcination at 250 °C led to the removal of thiolate ligands and resulted in enhancement in the catalytic activity as shown in Figure 1.7. However, deactivation of the catalyst was observed after higher temperatures due to cluster sintering.

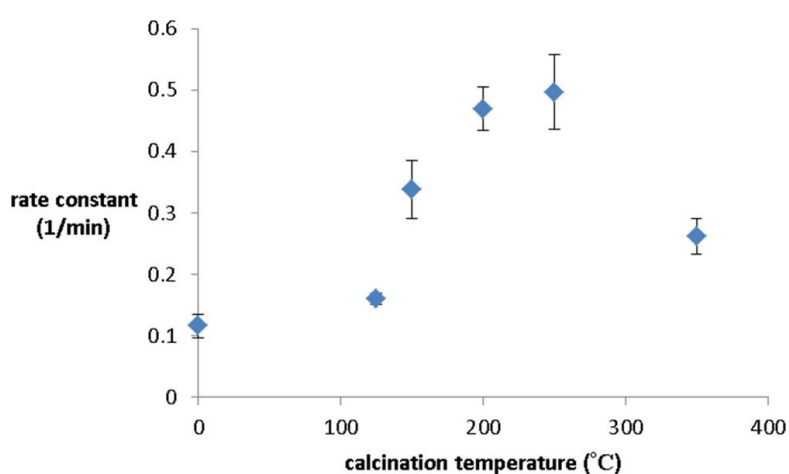


Figure 1.7: Rate constant for the reduction of 4-nitrophenol using carbon-supported $\text{Au}_{25}(\text{SC}_8\text{H}_9)_{18}$ catalysts thermally treated at different temperatures. Reprinted with permission from ref 68. Copyright 2013, American Chemical Society.

Several studies have shown the capping ligand around the clusters can influence the activity and/or selectivity of ligand-protected metal clusters in catalytic reactions. Typically, it is desirable to have partial or complete ligand removal to enhance mass transport of reactants to the surface metal atoms, and thus allow higher catalytic activity. Common procedures entail immobilization of metal clusters onto support materials, followed by removal of ligands using a variety of activation strategies. The method of immobilization and activation must be carefully chosen to avoid compromise of the unique structure of the synthesized metal clusters. The challenge is to minimize cluster aggregation and sintering upon removal of protecting ligands from clusters loaded on solid supports.

1.6.1 Thermal approaches¹

One of the simplest approaches to activate atom-precise clusters involves the removal of ligands off metal surfaces by thermal calcination in air, which leads to the oxidation of ligands from the metal surface. However, in order to efficiently carry out such calcinations, it is important to be able to follow both the removal of the oxidized ligands and possible growth of the resulting activated clusters by sintering. In addition, in the case of some metal systems, it is possible that metal sulfide or oxide formation can occur during the calcination process.

Much early work towards understanding the thermal stability of thiolate-stabilized atom-precise clusters was carried out by Jin and coworkers, who examined the relative stability of Au-S binding modes in $\text{Au}_{25}(\text{SR})_{18}$ (SR = glutathionate) clusters by NMR and optical spectroscopy.⁷⁰ They found that ligands directly attached to the 13 atom Au core were more stable to thermal removal under nitrogen than the six thiolate ligands that were in the center of the staple motifs; the staple-thiolates were removed at temperatures of 160 °C while the rest of the thiolates were stable until 180 °C. Significantly, they noted that these changes occurred even in the absence of any detectable mass loss by thermogravimetric (TGA) analysis, which suggested that while the thiolates were removed from the Au surface, the ligands were still present in the final sample. This is important as it shows that TGA analyses themselves are not sufficient proof of structural integrity in such systems. Jin and coworkers subsequently did TGA analyses of $\text{Au}_{25}(\text{SCH}_2\text{CH}_2\text{Ph})_{18}$, $\text{Au}_{38}(\text{SCH}_2\text{CH}_2\text{Ph})_{24}$, and $\text{Au}_{144}(\text{SCH}_2\text{CH}_2\text{Ph})_{60}$ clusters.⁶⁴ They showed that all the cluster samples begin to lose mass at a temperature around 200 °C and all ligands were removed by *ca.* 250 °C. The same group also studied the thermal decomposition of $\text{Au}_{144}(\text{SR})_{60}$ clusters with various thiolate ligands.²¹ TGA results revealed that Au_{144} clusters protected by thiolate ligands with longer chains showed slightly higher stability, *i.e.*, $\text{Au}_{144}(\text{SC}_4\text{H}_9)_{60}$, $\text{Au}_{144}(\text{SC}_5\text{H}_{11})_{60}$, and $\text{Au}_{144}(\text{SC}_6\text{H}_{13})_{60}$ begin to show mass losses at 178 °C, 195 °C, and 205 °C, respectively.

Nie *et al.* observed that mild heating in the presence of an oxidative gas (O_2) followed by the calcination under reductive gases (CO or H_2) at 80 °C was more effective for the activation of $\text{Au}_{144}(\text{SR})_{60}/\text{CeO}_2$ catalysts.⁶⁶ Tsukuda and coworkers examined the activation of $\text{Au}_{25}(\text{SR})_{18}$ clusters on hydroxyapatite supports, and showed that clusters activated at 300 °C could be used for the selective oxidation of styrene to styrene oxide.⁶³ At this temperature, all thiolate ligands were removed from the sample as evidenced by the mass loss in the system. However, a slight increase in cluster size (1.4 nm) was noted in the activated catalyst. The $\text{Au}_{25}(\text{SR})_{18}$ clusters on

hydroxyapatite were found to be an effective catalyst for styrene epoxidation reactions.⁶³ The activated clusters showed 100% conversion and 92% selectivity towards styrene epoxide using tertbutylhydroperoxide (TBHP) as an oxidant in toluene at 80 °C. In other work, the same group synthesized hydroxyapatite-supported Au_n clusters (*n* = 10, 18, 25, and 39) and investigated the selective oxidation of cyclohexane to cyclohexanol and cyclohexanone.⁷¹ The glutathione protected Au_n clusters were deposited onto the support and then calcined at 300 °C for 2 h *in vacuo*. XPS and elemental analysis revealed the complete removal of glutathione ligands from the catalysts. During the calcination process, there was no significant change in cluster size as evidenced by TEM. The optimal cluster size for catalysis was found to be in the 39 Au atom range.

X-ray absorption spectroscopy can be a valuable technique to follow cluster integrity upon calcination of supported-cluster materials. In an early study, Gaur *et al.* synthesized titania-supported Au₃₈(SC₁₂H₂₅)₂₄ clusters and activated the samples by calcination at 400 °C under a H₂/He flow for 1 h.⁷² EXAFS analysis of catalysts before and after calcination gave clear evidence for the removal of thiols from the Au surface, as a peak due to Au-S interatomic distance was observed around 2.3 Å in untreated and dried (100 °C for 1 h) catalysts, while the Au-S contribution was completely absent after thermal treatment. However, significant cluster sintering was seen in this system as the average Au particle size increased from 1.7 ± 0.2 nm to 3.9 ± 0.96 nm. Subsequently, our group reported a very careful study of the activation of phenylethanethiolate- and hexanethiolate-stabilized Au₂₅(SR)₁₈ clusters on carbon supports.⁶⁸ Samples were calcined for 1.5 h in air at temperatures of 125 °C, 150 °C, 200 °C, and 250 °C and analyzed by EXAFS Au-L₃ edge analysis. Figure 1.8 shows the Au L₃ edge EXAFS results for the phenylethanethiolate system. Results showed that the thiolate ligands start to be removed from the Au surface at 125 °C and were nearly completely removed from the Au surface at 250 °C. Importantly, no mass loss was seen in the TGA data until 150 °C. During the activation process, peaks due to Au-S species just below 2 Å slowly disappear, which indicates the removal of thiolate ligands. This disappearance of the Au-S peaks is accompanied by a growth in the first shell Au-Au peaks in the 2.5 to 3.0 Å region. EXAFS modelling shows that the coordination number (CN) of the Au-Au first shell contribution increases from 6.3(5) to 10.1(5) as the calcination temperature increased from 125 °C to 250 °C, which was strong evidence of Au cluster sintering. TEM images similarly showed that average particle sizes increased from 1.3 ± 0.1 nm to 1.9 ± 1.1 nm. Maximum activity for 4-nitrophenol reduction with NaBH₄ was seen for clusters activated at 250 °C.

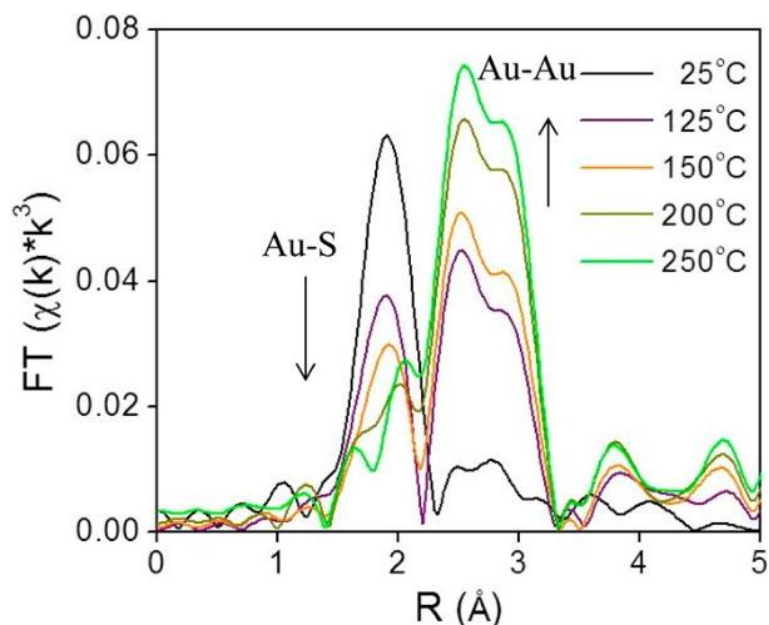


Figure 1.8: Au L₃ edge EXAFS spectra in R space of Au₂₅(SR)₁₈ clusters on carbon supports after heating in air (plotted with no phase shift correction). Reprinted with permission from ref 68. Copyright 2013, American Chemical Society.

Wu *et al.* subsequently reported the activation of Au₂₅(SR)₁₈ clusters on ceria rods for CO oxidation.⁷³ They noted that the thiolate ligands were a “double-edged sword” for CO oxidation as they blocked CO adsorption sites on Au while also being important to retain cluster integrity. Careful IR studies of CO adsorbed to activated cluster surfaces showed that partially cationic (δ^+) Au sites at the Au/ceria interface were likely the major catalytic site for CO oxidation, and only appeared after calcination of the Au₂₅(SR)₁₈ clusters on ceria at temperatures of 150 °C and beyond. They also speculated that thiolate on-off dynamic states might be responsible for catalytic behavior in solution phase studies. Tsukuda and coworkers also showed that some ligand removal was essential for liquid phase aerobic oxidations of benzyl alcohol on Au₂₅ clusters supported on carbon nanosheet supports.⁶¹ They removed thiols by calcination under vacuum at temperatures between 400 °C and 500 °C, and found that ligands were increasingly removed at higher temperatures with little to no growth in cluster sizes. Interestingly, they found that Au clusters that were unactivated had no activity, while those that still had some residual thiolates were selective catalysts for the oxidation of benzyl alcohol to benzaldehyde, and samples in which all thiolates were removed gave a much broader distribution of products (including benzoic acid and benzyl benzoate). The use of higher-temperature removal of thiols under vacuum needs to be investigated with other supports and thiolates to see if it is a general route to thiolate removal without significant cluster sintering. A number of groups have also

examined the role of the support on the resulting stability of Au clusters after activation. Yan and colleagues examined the activation of 6-mercaptohexanoic acid protected $\text{Au}_{25}(\text{SR})_{18}$ clusters on various supports, and found that after calcination under nitrogen at 300 °C, no significant size growth of the clusters were seen on hydroxyapatite and Degussa P25 titania supports, while significant sintering of the clusters was seen on activated carbon, graphene oxide, and silica supports.⁷⁴ They postulated that the increased stability in the two systems was due to stronger interactions of the clusters with the supports in those cases, though it is not clear whether this result may be partially due to the use of 6-mercaptohexanoic acid ligands used in this system. Garcia *et al.* examined the activation of $\text{Au}_{25}(\text{SR})_{18}$ and $\text{Au}_{144}(\text{SR})_{60}$ clusters over titania and silica supports, and found that Au_{144} clusters were more stable to sintering than the smaller Au_{25} clusters, and both systems were more stable on silica supports.⁷⁵

While most research attention has been on the stability of metal clusters upon thiolate removal, very little work has focused on the fate of the removed ligands. This can be significant as oxidized ligands may still be present in the system after calcination, and thus can potentially modify the catalytic behaviour of the system. Zhang *et al.* examined the activation of $\text{Au}_{38}(\text{SR})_{24}$ clusters on alumina and ceria supports in air and inert atmospheres.⁷⁶ Cationic Au sites were observed on Au_{38} /ceria samples calcined at 300 °C by Au L_3 edge XAS, whereas these sites were absent using analogous alumina supports. They also noted a two-step mass loss by TGA in air that was absent for samples heated under inert atmosphere, which was possibly due to the different binding modes of the thiolates in the staples and core, respectively. In addition, upon using the resulting activated catalysts as cyclohexane oxidation catalysts, cyclohexanethiol was observed as one of the products, which suggested that thiolate byproducts are still present on the support surface after activation. In a follow-up study, Zhang *et al.* also observed the ligand migration from $\text{Au}_{38}(\text{SR})_{24}$ clusters to the ceria support after thermal treatments (Figure 1.9).⁷⁷ Sulfur K-edge XANES analysis clearly showed that thiolate migration not only leads to the formation of active sites on the Au surface but also leaves sulfur species such as disulfides, sulfites, and sulfates on the support. Recent work from the same group has noted the presence of SO_x species on the surface of the support during reactions.⁷⁸ It was noted that the presence of these species can potentially limit the role of redox active supports in catalytic reactions. That being said, Alkmukhlifi *et al.* showed that while low levels of sulfates are present on inorganic support surfaces after the oxidation of supported thiolate-stabilized Au nanoparticles at 340 °C, the resulting catalysts are still active oxidation catalysts for hydrocarbon oxidations even with the sulfate present.⁷⁹

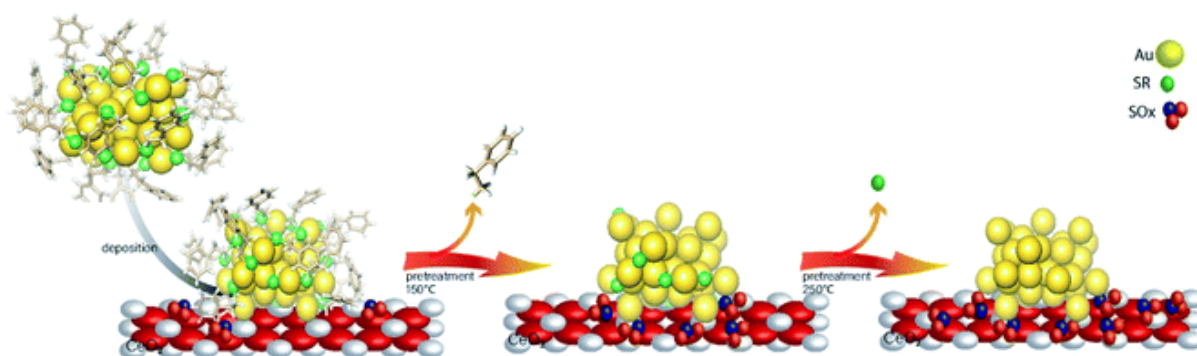


Figure 1.9: Thiolate ligand migration to ceria support during the calcination process.

Reprinted with permission from ref 77. Copyright 2018, John Wiley and Sons.

While most of the above discussion has focused on thiolate-stabilized systems, there have also been significant examples of thermally activated clusters using other ligand systems. The relative stability of $\text{Au}_{25}(\text{SeC}_8\text{H}_{17})_{18}$ vs. $\text{Au}_{25}(\text{SC}_8\text{H}_{17})_{18}$ clusters during thermal calcination was explored by Kurashige *et al.*⁸⁰ The TGA curve starts to show mass losses at 136 °C for selenolate and 165 °C for thiolate ligands, which indicates selenolate ligands begin to oxidize at a lower temperature than those of thiolate-protected clusters. A number of groups have studied the activation of phosphine-stabilized clusters for catalysis. Tsukuda and coworkers investigated the catalytic performance of triphenylphosphine-protected Au_{11} clusters on mesoporous silica for benzyl alcohol oxidation.⁸¹ The phosphine ligands were removed by calcination at 200 °C for 2 h before the catalytic study. Wu *et al.* showed that Au_{22} clusters stabilized with six diphenylphosphine ligands ($\text{Au}_{22}(\text{L})_6$) can oxidize CO without any ligand removal as evidenced by EXAFS and IR adsorption spectroscopy.⁸² They noted that uncoordinated Au sites in the intact clusters were able to absorb CO and activate oxygen. Wan and coworkers synthesized Au_{38} clusters with two different ligands $\text{Au}_{38}(\text{L})_{20}(\text{Ph}_3\text{P})_4$ ($\text{L} = \text{PhC}\equiv\text{C}$ and 3-methylbenzenethiol) and studied the ligand effect on catalysis.⁸³ In TGA analysis, the complete removal of thiolate ligands was observed at 250-300 °C, whereas $\text{PhC}\equiv\text{C}$ ligands were removed completely at 400 °C. This result indicates that the phenylethynyl ligand is much more stable than the 3-methylbenzenethiol ligand during the thermal activation process. Anderson *et al.* published several papers examining the activation of various $\text{Au}_n(\text{PPh}_3)_y$ (with $n = 8, 9, 11, 101$) clusters on titania nanoparticles by low temperature calcinations.⁸⁴⁻⁸⁵ They found that partial cluster sintering was seen after removal of phosphines at 200 °C heating under air. However, washing with toluene at 100 °C was shown to remove some of the phosphines with little to no aggregation of the clusters. Nakayama and coworkers

similarly synthesized $[\text{Au}_9(\text{PPh}_3)_8](\text{NO}_3)_3$ clusters and deposited them onto titania nanosheets.⁸⁶ The activation of the clusters was achieved by the calcination at 200 °C for 20 min under high vacuum. In XPS analysis, the P 2p_{3/2} peak disappeared after the thermal activation process which indicated the PPh₃ ligands were removed from the system. However, tremendous cluster sintering, as evidenced by atomic force microscopy, was seen after phosphine removal.

1.6.2. Chemical approaches¹

1.6.2.1. Oxidation (using O₃, TBHP, *etc.*)

While oxidative calcinations under air have been noted in the above section, a number of groups have examined alternative oxidants for cluster activation. Ozone exposure was found to be an effective method for the removal of stabilizing ligands from TiO₂ supported Au₁₃[PPh₃]₄[S(CH₂)₁₁CH₃]₄ clusters.⁸⁷ Ligand removal was achieved by flowing ozone (0.15% in oxygen) over the supported Au₁₃ clusters at a rate 1 ml/min for 1 h at room temperature. Both XPS and EXAFS analysis gave clear evidence for removal of ligands. This method provided considerable advantages over thermal treatment (400 °C for 2 h), which led to the particle size growth from 0.8 to 2.7 nm, whereas the post-ozone treated sample showed an average particle size of 1.2 nm. Hutchison and coworkers reported a slow oxidation process that precisely controls the exposure of the ligand shell to dilute ozone treatment, followed by the removal of oxidized ligand by soaking in water.⁸⁸ This strategy retains Au core sizes but suffers from incomplete removal of the ligand.

Peroxides have also been shown to be effective oxidizing agents for ligand removal. Kilmartin *et al.* observed that a strong oxidizing agent like TBHP could be used to generate active Au catalysts from silica supported Au₆[(Ph₂P-*o*-tolyl)₆](NO₃)₂ clusters.⁸⁹ While samples that were pre-calcined at 300 °C showed significant activity for the oxidation of benzyl alcohol with the peroxide, they noted that unactivated samples also began to be quite active after an induction period. Samples were heated up to 95 °C in benzyl alcohol in the presence of the peroxide, and gradual loss of the phosphine was observed over the first several hours of the reaction by Au L₃ edge EXAFS. In early studies, several groups reported that unactivated thiolate-stabilized Au clusters were active for the oxidation of styrene with peroxides such as TBHP and oxygen gas.^{64, 90} However, Dreier *et al.* noted that Au₂₅(SR)₁₈ clusters are not stable in the presence of peroxides under catalytic conditions, and control studies showed that mononuclear Au thiolate species that are removed from the cluster surface are likely the active

catalyst.⁹¹ Poisoning experiments were done using phosphine additives as they noted Au(I) phosphine systems were not typically active styrene oxidation catalysts. Similarly, Zhang *et al.* used TBHP to activate mercaptoalkanoic acid-stabilized Au₂₅(SR)₁₈ clusters that were supported on hydroxyapatite, as shown in Figure 1.10.⁹² They noted that mercaptoalkanoic acid thiolates could be removed from the clusters as disulfide and sulfonate species at temperatures as low as 50 °C, while mercaptobenzoic acid ligands were not as easily removed. Significantly, the activation of the clusters using peroxide oxidants led to no significant increase in cluster sizes. Thus, the resulting activated clusters were much more active styrene and benzyl alcohol oxidation catalysts than clusters that were thermally calcined at 300 °C.

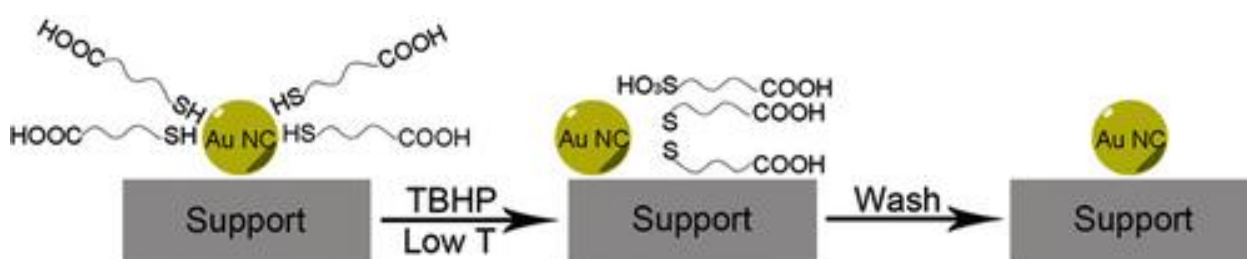


Figure 1.10: Soft oxidative removal of thiolates from Au clusters using peroxide oxidants. Reprinted with permission from ref 92. Copyright 2015, John Wiley and Sons.

1.6.2.2. Reduction (using LiBH₄, NaBH₄, *etc.*)¹

Another possible method to remove thiolates from metal cluster surfaces is to chemically reduce the thiolates from the surface, presumably as free thiols. This can be done, somewhat counterintuitively, using the same types of reducing agents used to make such clusters to begin with; *i.e.* using borohydride reducing agents. Typically, during syntheses, a large excess of thiol ligands are usually present in the reaction mixture, and any possible thiolate reduction and desorption events are counterbalanced by the presence of large amounts of free thiol in solution. Both our group and others have shown that desorption of thiols occurs on purified Au-thiolate clusters in the presence of large excess NaBH₄ concentrations. Dasog *et al.* showed that the Au–thiolate bonds can be completely removed by concentrated strong reducing agents such as sodium borohydride, and the growth of monolayer-protected Au clusters (Au MPCs) can be controlled by changing the MPC:reducing agent ratio.⁹³ Studies using alkanethiolate ligands with different chain lengths revealed that the immersion time for complete removal of thiols from Au surfaces becomes shorter when the chain length decreased. Ansar and coworkers demonstrated that removal of thiols from Au thiolate-stabilized nanoparticles could be

achieved through thiolate displacement by NaBH_4 .⁹⁴ They analyzed the kinetics of the thiolate removal from the Au surface by time-resolved UV-Vis measurements, and found that thiols could be completely removed using 25 mM NaBH_4 for 10 min at room temperature. It was found that the rate of desorption can be accelerated by increasing the concentration of reducing agent.

Asefa and coworkers demonstrated that NaBH_4 treatments of $\text{Au}_{25}(\text{SCH}_2\text{CH}_2\text{Ph})_{18}$ and $\text{Au}_{144}(\text{SCH}_2\text{CH}_2\text{Ph})_{60}$ clusters on mesoporous silica supports leads to an improvement in catalytic activity for styrene oxidation reactions, which was also attributed to the removal of thiolate ligands from the Au surface (Figure 1.11).⁹⁵ Our group studied the stability of $\text{Au}_{25}(\text{SR})_{18}$ and larger $\text{Au}_{\sim 180}(\text{SC}_6\text{H}_{13})_{\sim 100}$ clusters in high concentrations of NaBH_4 .⁵¹ Interestingly, $\text{Au}_{25}(\text{SR})_{18}$ clusters in solution retained their structural integrity after NaBH_4 treatments, whereas the larger cluster samples grew in size due to thiolate removal. However, the $\text{Au}_{25}(\text{SR})_{18}$ clusters could be used as recyclable catalysts for the reduction of nitrophenol with NaBH_4 . In further work, we studied the advantages of chemical reduction treatments compared to thermal treatment for the activation of $\text{Au}_{25}(\text{SR})_{18}$ clusters on alumina supports.⁹⁶ Thiolate ligands were removed partially by treating alumina supported $\text{Au}_{25}(\text{SC}_8\text{H}_9)_{18}$ clusters with excess LiBH_4 or LiAlH_4 solutions. It was noted that some thiolate removal was seen by Au L_3 edge EXAFS upon depositing the clusters on the alumina supports, which explains why the thiolates on supported clusters may be more easily removed than from clusters in solution. For samples calcined at 250 °C for 1.3 h in air, the supported clusters grew to an average size of ~ 1.8 nm, while in contrast, cluster growth was inhibited when BH_4^- reducing agents were used to remove ligands. Similarly, we have shown bimetallic AuPd clusters could be activated on alumina supports by LiBH_4 treatment with little to no growth of cluster size.²²

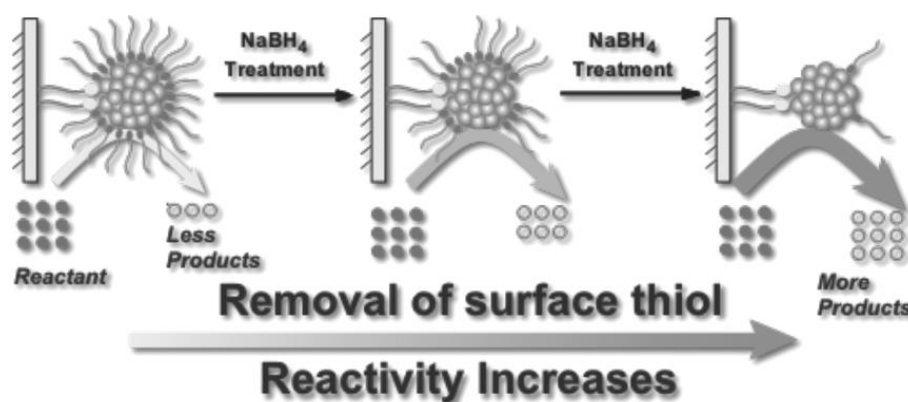


Figure 1.11: Illustration of enhanced catalytic activity for selective oxidation reactions with supported organothiolate-protected $\text{Au}_{25}(\text{SR})_{18}$ clusters catalysts by mild chemical stripping of

their surface ligands. Reprinted with permission from ref 95. Copyright 2014, John Wiley and Sons.

1.6.3. Light-induced approaches¹

One area of intense research involving Au catalysts involves the design of photocatalytically active materials by supporting Au clusters and/or nanoparticles on redox active metal oxide supports such as titania.⁹⁷⁻¹⁰⁰ A number of groups noted that one could take advantage of the dye-like HOMO-LUMO transitions in Au₂₅(SR)₁₈ clusters to enhance visible light absorption for solar cell or photocatalytic applications.^{45,101} Yu *et al.* showed that unactivated phenylethanethiolate-stabilized Au₂₅(SR)₁₈ clusters on nanocrystalline titania can be used for the photocatalytic degradation of methyl orange.⁴⁵ They noted that visible light could lead to the excitation of clusters followed by the transfer of excited electrons to the conduction band of titania, or alternatively, by the activation of oxygen by excited electrons in the LUMO of the clusters to form singlet oxygen. In the meantime, photogenerated holes in the HOMO can lead to the formation of hydroxyl radicals in aqueous solutions. Addition of a singlet oxygen quencher, l-histidine, led to a large decrease in activity. While the clusters were not activated before the reaction, there was no detail provided on whether the thiolates present on the clusters remained intact during the photocatalytic process.

Subsequent work by Liu and coworkers demonstrated that glutathione ligands were removed from *ca.* 1.5 nm Au clusters supported on TiO₂ nanotubes by simulated solar light irradiation.¹⁰² A 300 W Xe arc lamp with a AM 1.5 cutoff filter and band-pass light filter ($\lambda > 420$ nm) was used as the light source. The complete transformation of Au_x clusters to Au nanoparticles was observed after 10 h of light illumination. The proposed mechanism for the transformation of Au clusters to Au nanoparticles under visible light irradiation involved photogenerated electrons in the clusters which enhances the reduction of Au(I) on the staple motifs to the metallic state. In addition, they noted that ligand removal may be facilitated by *in situ* formed active species such as hydroxyl radicals, superoxide radicals, and holes during the irradiation process. A similar report of light-induced cluster aggregation was reported by Liu and Xu for TiO₂-supported Au₂₅(SR)₁₈ clusters during the solar light irradiation using a 150 W Xe lamp.¹⁰³ The thiolate ligand underwent an oxidation process which facilitates the transformation of Au₂₅ clusters to larger Au nanoparticles, as shown in Figure 1.12. The average Au nanoparticle sizes grew from *ca.* 1.3 nm to 3 nm, 7 nm, 10 nm, and 15 nm after irradiation for 1, 5, 8, and 72 h, respectively. Both hydroxyl and superoxide radicals were

detected by electron spin resonance analysis under simulated solar light irradiation. Thus, the reaction between photogenerated electrons and oxygen/water molecules leads to the formation of active intermediates such as hydroxyl/superoxide radicals which are responsible for the oxidative attack on the thiolate ligands. XPS studies of the sample before and after light irradiation gave clear evidence for the removal of thiolate ligands via the presence of sulfonate residues after illumination.

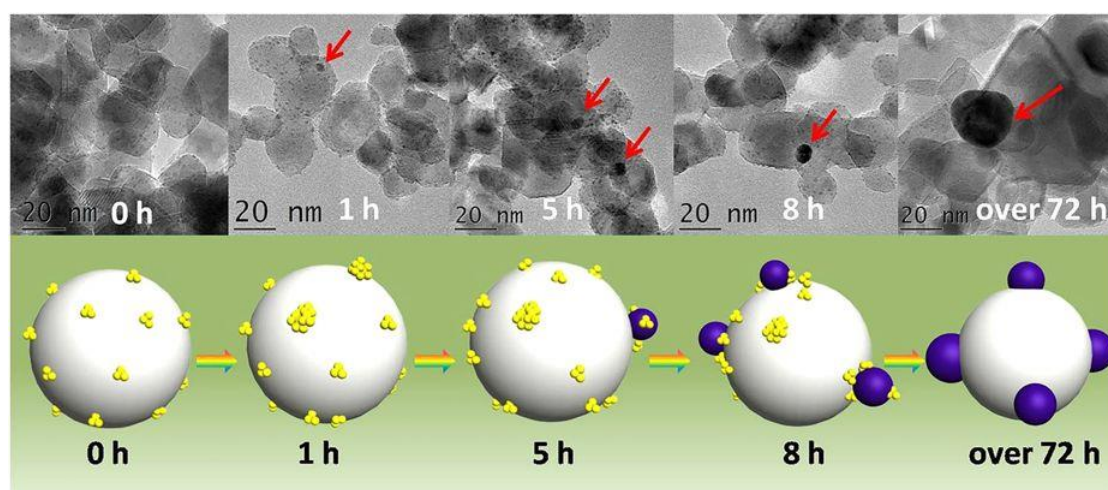


Figure 1.12: Illustration of the *in situ* light-induced transformation of Au clusters to Au nanoparticles on nanoporous titania nanotube arrays. Reprinted with permission from ref 103. Copyright 2016, Nature Publishing Group.

1.7. Methods of controlling sintering upon activation of clusters¹

Sintering is the loss of active surface area due to the agglomeration of nano-sized materials. As noted in the last section, sintering can be problematic in many scenarios that involve activating atom-precise clusters by using calcination and oxidation approaches, although some control of sintering was generated by selective removal of only some thiolate ligands from these systems or use of supports that promote strong support/cluster interactions. However, many important industrial reactions such as reforming of hydrocarbons, methane combustion reactions, and automobile exhaust control are carried out at higher temperatures (*i.e.* above 600 °C), and since many noble metal cluster and nanoparticle systems lack stability at such temperatures, industrial applications of such catalysts may be limited without further sintering control.

Encapsulation with metal oxide shells is a straightforward way of stabilizing metal nanoparticles towards sintering. This strategy involves the isolation of metal nanoparticles with

a porous metal oxide shell such as silica, alumina, titania, or zirconia. For example, Somorjai and coworkers demonstrated that Pt nanoparticle sintering could be prevented by encapsulating Pt nanoparticles with silica shells which showed remarkable thermal stability even up to 750 °C.¹⁰⁴ Silica shells with an average thickness of 17 nm were grown by sol-gel chemistry via the hydrolysis and condensation of tetraethylorthosilicate (TEOS) on tetradecyltrimethylammonium bromide protected Pt nanoparticles. However, the mass transfer issues associated with the metal oxide shell can be problematic in catalysis. Even though some metal oxide shells are porous, they may block certain amounts of active sites on the surface of the catalyst. To overcome this mass transfer issue, Schüth and coworkers demonstrated another strategy to synthesize high-temperature stable Au nanoparticle catalysts with a yolk-shell structure.¹⁰⁵ Au nanoparticles were encapsulated with silica shell followed by a thin layer of zirconia using sol-gel chemistry. Finally, a yolk-shell structure around Au nanoparticles was created via selective etching of the inner silica layer.

There have only been a few examples of attempts to control sintering of atom-precise cluster by growing shells of metal oxides and other materials around the clusters.^{50, 106} Samanta and coworkers showed that embedding arrays of multiple Au clusters (<2 nm) in a silica matrix could improve the thermal stability, in which clusters were encapsulated by silica.¹⁰⁶ After calcination at 250 °C the size of the particle could be maintained below 3 nm. Chen *et al.* reported an alternative method to improve the thermal stability of Au clusters growing silica shells over Au₂₅[SC₃H₆Si(OCH₃)₃]₁₈ clusters.¹⁰⁷ Au clusters were deposited on a silica core, and further layers were added by the hydrolysis of TEOS. The resulting materials showed improved sinter-resistance, with average particle sizes of 2.0 ± 0.6 nm and 2.2 ± 0.5 nm after calcination at 400 and 600 °C, respectively. A fraction of > 4 nm Au nanoparticles was seen at the higher calcination temperature as some Au nanoparticles were able to escape the silica shells, and as a result the resulting samples calcined at 600 °C showed slightly lower activity for 4-nitrophenol reduction than seen for samples calcined at 400 °C.

Another method to improve sintering control is to isolate clusters within two-dimensional mesoporous materials. In an early example, Dai and colleagues showed that Au₂₅(SR)₁₈ and Au₁₄₄(SR)₆₀ clusters could be stabilized towards sintering by incorporating them into mesoporous silica that was coated with CuO.¹⁰⁸ Clusters on pure mesoporous silica showed tremendous sintering after calcination at 300 °C, whereas those that were deposited onto CuO intermediate layers had an average size of 1.7 ± 0.2 nm after calcination at the same temperature. Similar results were obtained for Co₃O₄ overlayers on silica. Control studies of clusters deposited on similar oxides on non-porous silica supports showed poorer sintering resistance; thus while ordered porous

silica templates themselves cannot mitigate sintering, they can improve the resistance of systems that have a secondary stabilization mechanism; in this case, a metal oxide that allows for strong cluster/support interactions. Several groups have examined the use of thiol tethers on the surface of porous silica materials to anchor Au clusters, followed by activation. For example, Das *et al.* showed that 3-mercaptopropyltrimethoxysilane (MPTS) could be anchored onto mesoporous SBA-15 silica, which allowed for efficient anchors of Au₂₅(SR)₁₈ and Au₁₄₄(SR)₆₀ clusters. This was followed by activation of the clusters by partial chemical removal of thiolates by NaBH₄.⁹⁵ Similarly, Zheng *et al.* showed that porous silica spheres decorated with MPTS could capture Au clusters. The resulting materials showed moderate sinter resistance when samples were activated under H₂ atmosphere at 350 °C.¹⁰⁹

Xu and coworkers reported a method to improve the photostability of glutathione protected Au clusters on silica spheres using branched polyethylenimine for surface modification.¹¹⁰ The structural integrity of Au clusters was preserved after 10 h light irradiation (420 nm), likely because the surface modification prevents the glutathione ligands from oxidizing. An additional coating with a titania shell further improved the photostability of these clusters. Sintering of glutathione protected clusters could be eliminated to some extent by encapsulation within a metal-organic framework, which has been reported by Xiong and coworkers.¹¹¹ Xu and coworkers reported that hydroxyl groups on the surface of titania have a critical role in the stability of Au clusters during the light irradiation process.¹¹² Hydroxyl radicals could be created by the interaction of surface hydroxyl groups and photogenerated holes, which leads to the decomposition of protecting ligands around the cluster, resulting in clusters sintering to form Au nanoparticles. It was observed that the replacement of the hydroxyl groups with fluoride ions enhanced the photostability of the clusters.

Physical confinement within metal-organic frameworks (MOFs) provides a novel strategy for improving the thermal stability of clusters. Zhu and coworkers detailed the synthesis of Au₁₁(PPh₃)₈Cl₂ and Au₁₃Ag₁₂(PPh₃)₁₀Cl₈ clusters inside ZIF-8 (Zn(2-methylimidazole)₂) and MIL-101 (Cr₃F(H₂O)₂O(1,4-benzenedicarboxylate)₃) templates.¹¹³ The authors noted that not all of the clusters were encapsulated in the MOF; a fraction of the clusters formed on the MOF surface. The systems could be activated for catalysis at 150 °C, however moderate sintering was observed after calcination of the MOF/cluster composites at temperatures of 200 °C and beyond. In further work, the same group demonstrated an electrostatic attraction strategy to incorporate [Au₁₂Ag₃₂(SR)₃₀]⁴⁻, [Ag₄₄(SR)₃₀]⁴⁻, and [Ag₁₂Cu₂₈(SR)₃₀]⁴⁻ nanoclusters within ZIF-8, ZIF-67, and manganese hexacyanoferrate hydrate frameworks by a cation exchange strategy.¹¹⁴ Similarly, Rosi and coworkers showed that cationic Au₁₃₃(SR)₅₂ clusters could be incorporated

into the surface of MOF crystals by cation exchange.¹¹⁵ However, the thermal stability of these systems was not analyzed in either of these publications. Luo *et al.* reported an approach for improving the thermal stability by embedding glutathione-stabilized $\text{Au}_{25}(\text{SR})_{18}$ clusters in a ZIF-8 metal-organic framework, as shown in Figure 1.13.¹¹⁶ Two nanocomposites were synthesized by incorporating clusters either inside or outside of the framework. Au clusters were encapsulated into the framework via ‘coordination assisted self-assembly’ or alternatively decorated on the MOF surface by impregnation of clusters onto the surface of the framework. After calcination at 300 °C in a nitrogen atmosphere, both systems did not show notable aggregation and maintained the dispersity of Au clusters in or on the MOF. For the comparison of the properties of these two systems, the catalytic activity for the 4-nitrophenol reduction reaction was studied. $\text{Au}_{25}(\text{SR})_{18}$ clusters within the MOF showed lesser activity than those on the surface of the MOF, which is likely due to mass-transfer issues of the substrate accessing clusters within the MOF.

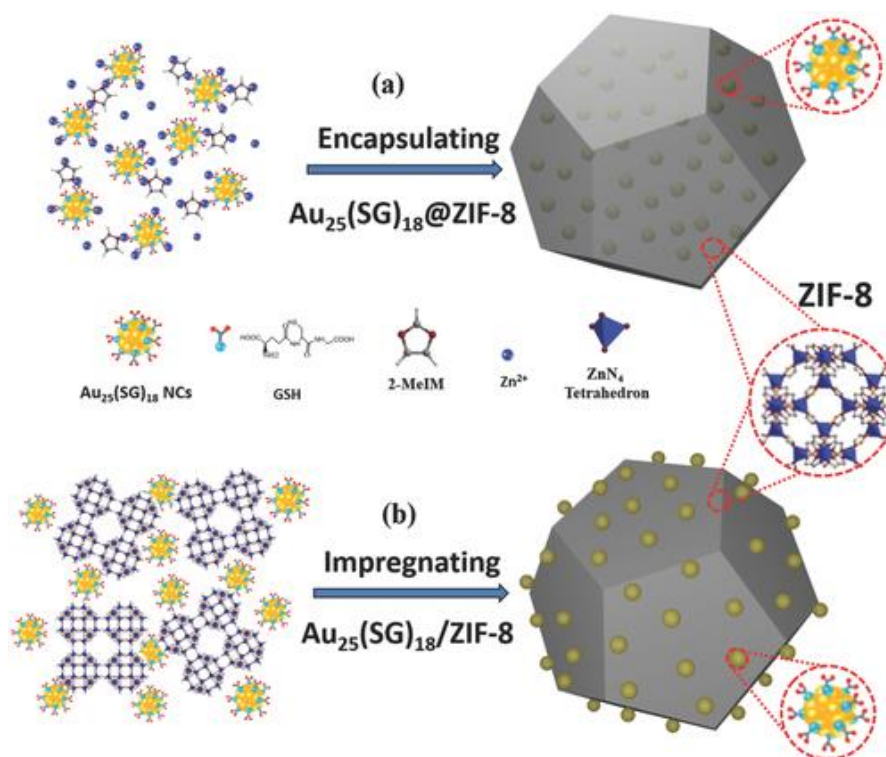


Figure 1.13: Illustration of $\text{Au}_{25}(\text{SR})_{18}$ clusters (a) encapsulated in and (b) impregnated onto a ZIF-8 metal organic framework. Reproduced with permission 116. Copyright 2018, John Wiley and Sons.

1.8. Characterization

1.8.1. Environmental Transmission Electron Microscopy (TEM)

Transmission electron microscopy has been widely used to measure the size of nanomaterials with high magnification and resolution. Briefly, an electron gun at the top produces a high-intensity source of electrons (100-300 keV) which pass through an aperture to give a parallel beam of electrons. The electron beam is focused into the sample by a condenser lens and transmitted electrons are collected by a digital camera. As the attenuation of the beam depends on the density and the thickness of the sample, the transmitted electrons form a two-dimensional projection of the sample, which is subsequently magnified by the electron optics to produce the so-called bright field image. A dark field image can also be obtained from the diffracted electron beams, which are slightly off angle from the transmitted beam.

Conventional TEM requires high vacuum ($\geq 10^{-6}$ torr) within the specimen chamber to eliminate the energy loss of electrons due to the collision with gas atoms. This means conventional TEMs have limitations for observing material changes during experimental conditions, and thus images are typically obtained under vacuum at ambient temperatures. It is desirable to have a TEM instrument that is capable of allowing the observation of real-time changes to catalysts during catalytic experiments. Environmental TEM offers real-time monitoring of structural changes of samples under the reaction conditions, and thus can lead to information concerning the mechanism of sintering.¹¹⁷⁻¹¹⁸ The schematics of an environmental TEM used in this thesis is shown in Figure 1.14. Generally, there are two ways to maintain the gaseous environment vicinity of the sample, i) to modify the entire column with a differential pumping system or ii) to use a specially designed sample cell that allows a thin gaseous environment above the sample. Adding a differential pumping system to the entire TEM column is expensive; however, this approach has several advantages as it allows for high-resolution imaging, sample tilting, and sample heating. The gas is restricted near the specimen through pressure-controlled apertures, and a differential pumping design can help retain the vacuum in other parts of the column. In the second approach, windows have to be designed for the sample cell with significant thickness to maintain the gaseous environment around the sample; this often limits the resolution of the image. The sample holder is specially designed to introduce different gaseous mixtures into the sample chamber via an injection nozzle.

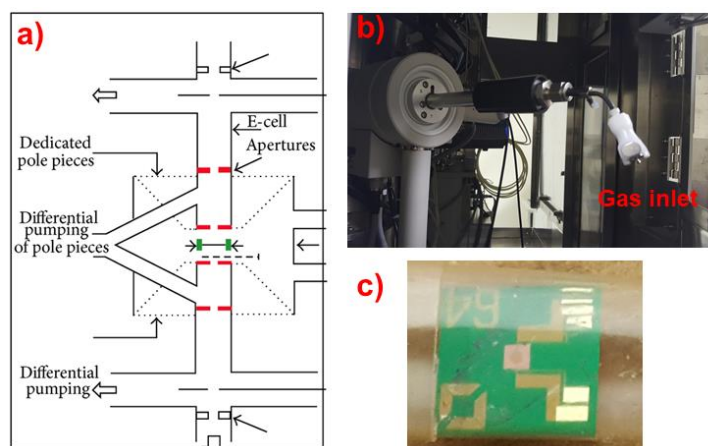


Figure 1.14: Schematics of environmental TEM set-up featuring differential pumping, dedicated apertures, and pole pieces, b) sample holder with gas inlet, and c) A heating coil centered on the SiN_x window of the TEM grid.¹¹⁸

1.8.2. X-ray Absorption Spectroscopy (XAS)

X-ray absorption spectroscopy (XAS) has become a fairly common technique to probe the oxidation state and local structure of materials.¹¹⁹ XAS involves the excitation of an electron from its bound state to higher levels when X-rays with energy $h\nu$ pass through a material. If the energy of an incident photon is higher than the binding energy of an electron, absorption occurs, and there is a sharp rise in the absorption coefficient, which is known as the absorption edge. The edges are named according to the principle quantum number of the electron that is excited. According to the Beer-Lambert law, the absorption coefficient is related to sample thickness (t), and the intensity of incident photon (I_0) and the transmitted photon (I_t) which is shown in Figure 1.15.

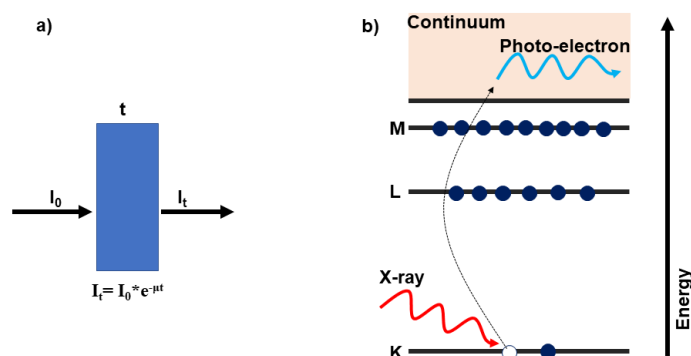


Figure 1.15: X-ray absorption measurements: (a) An incident beam of monochromatic X-rays of intensity I_0 passes through a sample of thickness t , and the transmitted beam has

intensity I_t , and (b) a diagram showing the ionization of a 1s core electron. Figure adapted from reference 119.

The absorption coefficient is a smooth function of photon energy and varies with the following parameters: sample density (ρ), the atomic number (Z), the atomic mass (A), and the X-ray energy (E), as shown in Equation 1.1:

$$\mu = \rho Z^4 / AE^3 \quad (1.1)$$

XAS measures the energy dependence of the X-ray absorption coefficient $\mu(E)$ at and above the absorption edge; it can be measured in either transmission mode or fluorescence mode. In transmission mode, the absorption coefficient is directly measured by measuring the intensity of incident and transmitted photons which are given by Equation 1.2:

$$\mu(E) = \log(I_0/I_t) \quad (1.2)$$

X-ray fluorescence is a result of the relaxation of core electrons to a deeper core hole by emitting an X-ray with definite energy. Since the fluorescence X-ray energies observed are characteristic of the specific elements, they can be used to identify the absorbing atom and to quantify concentration. Auger processes are another process of relaxation, in which an electron drops from a higher level into a core hole and a second electron is excited to the continuum. In the soft X-ray regime (<2 keV), the Auger effect is more dominant for the relaxation of an electron, while X-ray fluorescence is more likely to occur in the hard X-ray regime. Fluorescence mode can be used to analyze samples with low concentrations and/or samples being interrogated at low-energy edges. Thus, X-ray fluorescence can be used as an alternative to transmission measurements, using Equation 1.3:

$$\mu(E) \propto (I_f/I_0) \quad (1.3)$$

XAS is mainly divided into two regions; X-ray Absorption Near-Edge Structure (XANES) and Extended X-ray Absorption Fine Structure (EXAFS). The XANES region includes the vicinity of the absorption edge that includes the pre-edge, absorption edge, and all the features within ~ 50 eV above the absorption edge. The XANES region provides information about the chemical state of the element including oxidation state and local geometry. The EXAFS region consists of all the features in the spectrum beyond ~ 50 eV past the absorption edge and provides information about structural parameters of the local environment of atoms including interatomic distances, coordination numbers, and structural and thermal disorder of

neighbouring atoms. As EXAFS analyses do not require the samples to have long-range order, this technique can be applicable to amorphous samples, complex molecules, solid solutions, and crystalline materials.

1.8.2.1. X-ray Absorption Near-Edge Structure (XANES)

XANES spectroscopy refers to the region which lies vicinity of the absorption edge, about 10 eV below the edge and 50 eV above the edge. XANES spectra mainly deal with the excitation of an electron from a bound state to higher unoccupied bands. The XANES spectra consist of three parts; a pre-edge region, an absorption edge, and a post edge region. The pre-edge region arises due to the electronic excitations to empty bound states that are spin-forbidden and can provide information about the local geometry around an absorbing atom and can be influenced by the oxidation state and bonding characteristics. The absorption edge is sensitive to the oxidation state of the element and is caused by the excitation of electrons to higher energy levels. In this thesis, two absorption edges, the K and L₃ edges, were analyzed. K edge represents the excitation of an electron from a 1s state to (n+1)p orbitals while the L₃ edge represents the 2p_{3/2}→nd transition. As the oxidation state of the element increases, the absorption edge typically shifts to higher energy. The post edge region originates due to the multiple scattering of photoelectrons with low kinetic energy and can provide information about interatomic distances and coordination numbers.¹²⁰

1.8.2.2. Extended X-ray Absorption Fine Structure (EXAFS)

When an isolated atom is irradiated with X-rays of energy $h\nu$, the photoelectron wave propagates as an undisturbed wave. As shown in Figure 1.16, the absorption of X-rays by an atom results in a sharp rise in the absorption coefficient. The X-ray absorption spectrum shows an edge corresponding to the binding energy of the electron energy levels in the atom. If the atom is bound in a lattice, the absorption is modulated by neighboring atoms and gives a fine structure. As the photoelectron has both particle and wave character, it can be scattered back from the neighboring atom. This situation is illustrated in Figure 1.16b. These outgoing and backscattered waves can interfere constructively and destructively, which leads to an oscillating wave known as the fine structure. The amount of interference varies with amplitude and phase of the backscattered wave. This oscillation above the edge is known as the Extended X-ray Absorption Fine Structure (EXAFS); it can be extend up to 1000 eV beyond the

absorption edge. As the oscillation arises from the backscattering by the neighboring atoms, it provides information about the local structure around the absorbing atom.

The oscillatory part of the signal $\chi(E)$ is determined by normalizing the absorption coefficient $\mu(E)$ by the edge step, $\Delta\mu_0(E)$, and subtracting the smooth isolated-atom background function $\mu_0(E)$, as shown in Equation 1.4:

$$\chi(E) = [\mu(E) - \mu_0(E)] / \Delta\mu_0(E) \quad (1.4)$$

Since the photoelectron has wave character, the EXAFS function can be expressed as a function of wavenumber (k) using Equation 1.5:

$$k = \sqrt{2m_e(E - E_0) / \hbar^2} \quad (1.5)$$

where E_0 is the absorption edge energy (determined by either at the middle of absorption edge jump or at the first inflection point), \hbar is the Planck's constant and m_e is mass of the electron.

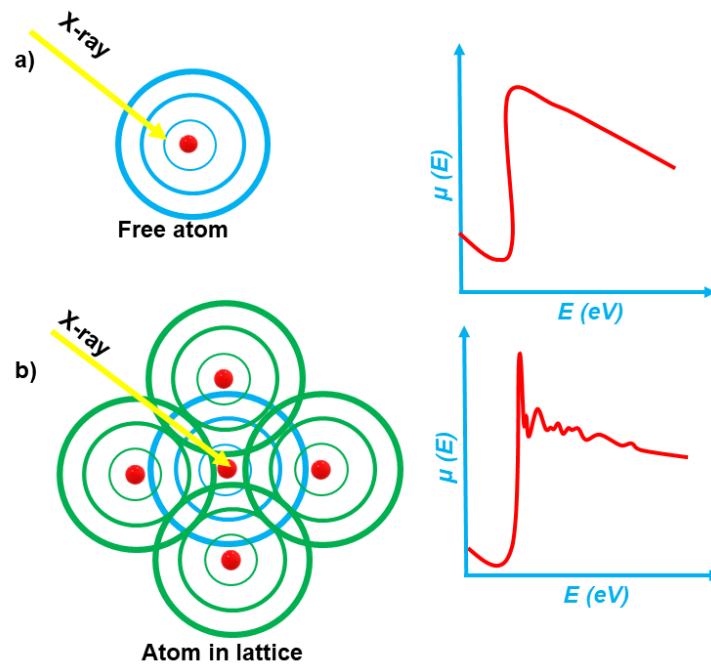


Figure 1.16: Absorption of X-rays as a function of photon energy $E=h\nu$ by a) a free atom and b) by atoms in a lattice. The blue circle represents the photoelectron wave and the green circle represents backscattered wave from neighboring atoms. Figure adapted from reference 119.

The EXAFS $\chi(k)$ signal contains a sum of all contributions arising from all the scattering paths, which can be described using Equation 1.6:

$$\chi(k) = \sum_j S_0^2 N_j \frac{|f_j(k)|}{kR_j^2} e^{-2R_j/\lambda(k)} e^{-2\sigma_j^2 k^2} \sin\left(2kR_j + \delta_c(k) + \delta_j(k)\right) \quad (1.6)$$

Here, S_0^2 is amplitude reduction factor which is caused by the relaxation of all other electrons in the absorbing atom to the core hole, N_j represents the coordination number or the degeneracy of a particular scattering path J, and f_j represents the scattering amplitude. The term $e^{-2R_j/\lambda(k)}$ is due to inelastic losses in the scattering process. The term $\lambda(k)$ is the mean free path of the ejected photoelectron from the absorber atom. The term $e^{-2\sigma_j^2 k^2}$ accounts for the k dependent dampening of the EXAFS wave. The dampening of the wave occurs at a higher k range due to positional and thermal disorder which is designated by the symbol σ . The terms $\delta_c(k)$ and $\delta_j(k)$ represent the phase shift due to the central atom and the phase shift due to the neighboring atoms respectively. The interatomic distance that is observed in the EXAFS spectrum is typically a little smaller than the actual interatomic distance (theoretical value) which is due to the phase shift. This phase shift is caused by the interaction of photoelectron with the positively charged nucleus of the absorber atom and neighboring atoms, resulting in energy losses and lengthening its wavelength. The average interatomic distance between the neighboring atoms is inversely proportional to the frequency of the EXAFS oscillation. The amplitude of each EXAFS wave depends on the coordination number and the backscattering power of neighboring atoms.

1.8.2.3. Single shell fitting

EXAFS is an excellent tool to determine interatomic distances and coordination numbers. To extract the structural parameters, a procedure is followed that consists of converting raw absorption spectra into normalized EXAFS oscillations. In this step, the EXAFS signal, $\chi(k)$ is normalized at the edge from 0 to 1. Then the energy of the photoelectron is converted to the wave vector k using Equation 1.5. The y-axis of the k-space data is multiplied by k^n ($n = 1, 2, 3$) in order to magnify the dampened EXAFS oscillations at higher k values. The EXAFS signal consists of sum of all the sinusoidal waves with different frequencies that correspond to the different types of neighbors of the absorbing atom and absorber-scatter distances. Fourier transformation of the k-space data can be used to separate the EXAFS contributions from different coordination shells. This technique provides a photoelectron scattering profile as a function of the radial distance from the absorber. In such a radial distribution function, the positions of peaks correspond to the interatomic distance while the size of the peaks is related to the coordination number.

As shown in Equation 1.6, the EXAFS equation consists of several variables in which some variables ($f_j(k)$, $\delta_c(k)$, $\delta_j(k)$, $\lambda(k)$, and R_0) are calculated theoretically and the remaining five variables (S_0^2 , N_j , σ_j^2 , ΔR , and E_0) need to be modelled experimentally. The term N_j provides the number of backscattering atoms at a distance R_j which is highly correlated to the EXAFS signal. The vibrational motions and static disorder of the scattering atoms cause the damping of the EXAFS signal at higher k . The effect of this disorder is accounted by the term σ_j . ΔR is defined as the difference between first neighbor distance from the model and fitted distance. The term, ΔE_0 , is defined as a change in energy from the theoretical data and is used to align the energy scale of the theoretical spectrum to match the measured spectrum. To extract the information about the local structure of absorbing atom, the resulting R-space spectra is fitted with a suitable model. A theoretical spectrum which is created from a model is used to fit the experimental EXAFS signal. All variables such as N_j , σ_j^2 , ΔR and E_0 can be extracted after fitting the amplitude reduction factor that is obtained from a reference compound. In the example below in Figure 1.17, the result of modelling the experimental data using a fcc Au model results in a first shell Au-Au distance of $R=2.851(6) \text{ \AA}$, a coordination number (CN) of $12.0(4)$, a mean square disorder of $\sigma^2=0.0082(9) \text{ \AA}^2$ and a shift in E_0 of $4.7(6) \text{ eV}$. The CN provides information about the average size of nanoparticles. Unlike TEM, it does not provide the particle size of individual particles, rather EXAFS CNs measure the average CN of all-absorbing atoms in the sample. An atom in bulk fcc materials such as Au, Pt, Pd, etc. has 12 first shell neighboring atoms. The local CN for surface atoms is below 12 because a large number of neighboring atoms are missing on the surface. As the particle size decreases, a greater percentage of the total atoms in a particle are on the surface, and thus the average CN will drop. EXAFS spectra of nanoparticles less than 5 nm in size will be discussed in the following chapters.

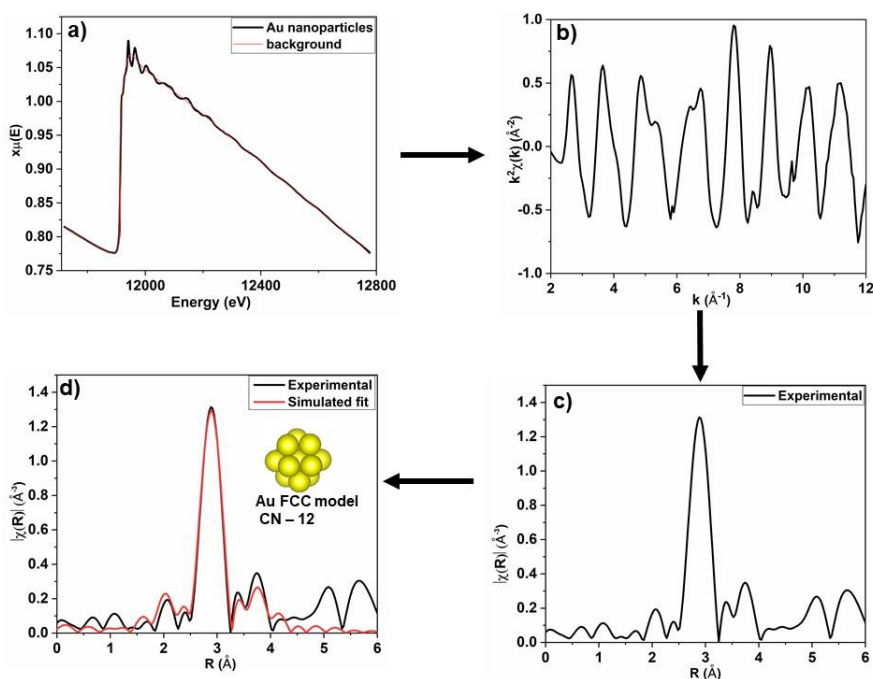


Figure 1.17: a) Experimental X-ray absorption spectra of Au nanoparticles. The free-atom absorption coefficient (red line) and jump at the edge energy are indicated b) extracted EXAFS signal with a k^2 weighting, c) the Fourier-transformed EXAFS signal, d) a first shell fit to the EXAFS spectra using a fcc Au model (data was collected at the Canadian Light Source for Chapter 4).

At this point, it is worth to mention the goodness of fit and how the best fit and uncertainties are determined in the refinement. The R factor is often used to gauge how close the experimental data to the theoretical model overlap, and it is interpreted as a percentage misfit or, equivalently, as a numerical evaluation of how closely the fitted function overplots the data. The R-value for a good fit in which a correct model is used to model the data is typically found to be below 0.02 (2 %). Reduced chi-square is another statistic used to measure the goodness of fit and it is more appropriate to compare two fitting results against the data set. It is a useful parameter to determine whether a fit is improved by adding additional paths or fit. In principle, it is highly desirable to have unity for reduced chi-square (*i.e.* lower values are better). Along with the reduced chi-square and R factors, some other fitting parameters need to be considered. The value of the amplitude reduction factor (S_0^2) should typically be between 0.7 and 1. The mean square disorder (σ^2) should be a positive value and less than 0.01 if a fit is to be meaningful. The value for ΔE_0 more than 10 eV is not acceptable, as this would typically involve a shift of the k-space wave by a period. Finally, the number of variables that can be fit depends on the quality of the data, and ideally a minimal amount of variables should be

modelled such that a low correlation between the parameters is obtained. For an acceptable fit, the correlation between (ΔE_0 and R, N, and S_0^2) parameters should typically be less than 85%.

1.8.3. X-ray Photoelectron Spectroscopy (XPS)

X-ray photoelectron spectroscopy which is also referred to as Electron Spectroscopy for Chemical Analysis (ESCA), is widely used surface analytical technique.¹²¹ XPS gives direct information on the oxidation state of the components of a materials. XPS wide scan spectra of a material includes peaks of various elements (except H and He). Since the area under these peaks are related to the amount of each element, XPS is useful to analyze the elemental composition.

XPS is based on the photoelectric effect. When a surface of materials is irradiated by X-rays with energy $h\nu$, core level electrons are excited. The electron is released with a certain kinetic energy E_k , that is directly related to the binding energy E_b . This process is described by Einstein equation (1.7).

$$E_k = h\nu - E_b - \phi \quad (1.7)$$

Where, ν is the frequency of exciting radiation and ϕ is the work function of the material, a factor that corrects for the electrostatic environment in which the electron is formed and measured, and E_b is the binding energy. Routinely used X-ray sources are Mg K_α (1253.6 eV) and Al K_α (1486.6 eV). The ejected photoelectrons are directed to an electron energy analyzer through the electron lens and separated based on their kinetic energy. Following the energy separation and analysis, photoelectrons are detected by electron multiplier tubes, multichannel plates, or anode electrodes.

In XPS, the number of photoelectrons of a given energy, $N(E)$, is measured as a function of their binding energy. In a XPS spectrum, each peak at a specific binding energy is representative of a specific element present in the material. Since the binding energy of an electron is strongly influenced by a screening of the nuclear charge, XPS offers information that enables the identification of atoms of an element in different chemical environments. Figure 1.18 shows the XPS spectrum of different Pd species.¹²² Two Pd 3d peaks are seen for the $3d_{5/2}$ and $3d_{3/2}$ states due to the spin-orbit coupling. Metallic Pd has peaks at ~ 334.9 eV and ~ 340.4 eV corresponding to the binding energy of Pd $3d_{5/2}$ and Pd $3d_{3/2}$. The spectrum clearly shows that the binding energy of Pd atom is strongly influenced by the electron-withdrawing

nature of the adjacent atom. In PdO, the binding energy of Pd 3d_{5/2} is shifted to ~336.5 eV. In PdCl₂, the Pd atom is in the next most electron-withdrawing environment and shifted to ~337.9 eV.

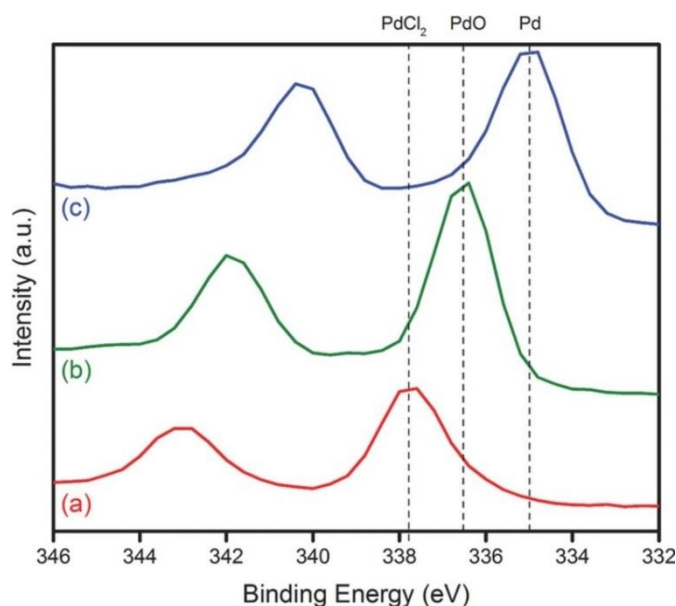


Figure 1.18: XPS spectra of Pd 3d_{3/2} and Pd 3d_{5/2} peaks for a) PdCl₂-TiO₂ b) PdO-TiO₂ and Reduced Pd-TiO₂. Reproduced with permission from ref 122. Copyright 2015, Institute of Physics Science.

1.9. Research Objectives

Our group has previously focused on the synthesis of atom-precise clusters and showed that the complete removal of stabilizing ligands could be achieved by thermal treatments.^{68, 96} Previous results indicated that carbon-supported Au₂₅(SR)₁₈ clusters were subject to sintering under moderate temperatures (250 °C), and that stabilizing ligands need to be removed for improving the accessibility of catalytic sites to reaction substrate. The catalytic activity studies for 4-nitrophenol reduction reactions over thermally treated catalysts at different temperatures indicated that activation improves the catalytic performance. However, this activation process often leads to the sintering of metal clusters and a loss of active surface area.

A major goal of this research work is the synthesis of sinter resistant Au and Pd catalysts and analysis of the thermal stability of these materials by both TEM and EXAFS techniques. The first research objective was to synthesize a core-shell catalyst by growing silica shells around the Au₂₅ clusters using sol-gel chemistry. Others have shown that carboxylic acid groups on the surface of particles readily interact with silica precursors which can allow the formation of silica coatings around nanomaterials.¹²³ Here Au₂₅(MUA)₁₈ clusters were chosen

as a starting precursor for the silica encapsulation step. In order to show that there is an advantage to encapsulating the clusters, a control catalyst with similar Au loading was also synthesized by depositing $\text{Au}_{25}(\text{MUA})_{18}$ clusters onto silica spheres. The thermal stability of both catalysts was analyzed by TEM and EXAFS before and after the high-temperature heat treatment (650 °C for 3 h). Styrene epoxidation reactions and the 4-nitrophenol reduction reactions was used as a model reactions to monitor the catalytic activity. The results of this study are documented in Chapter 2.

A mass transfer issue associated with the silica shell was noticed in the encapsulated catalysts. Although silica has a porous nature, it reduces the accessibility of substrate to the active sites on the Au surface. In Chapter 3, our objective was to control the thickness of the shell to minimize mass transfer issues. Atomic layer deposition is a versatile technique to create a metal oxide shell with controlled thickness. Previous studies indicate that the nature of ligands has a significant role in the effectiveness of ALD growth. $\text{Au}_{25}(\text{MUA})_{18}$ and $\text{Au}_{25}(\text{DDT})_{18}$ (DDT – dodecanethiol) clusters were chosen for alumina ALD coatings, as the carboxylic acid groups of the $\text{Au}_{25}(\text{MUA})_{18}$ clusters are expected to readily react with the trimethylaluminum ALD precursor and thus allow the alumina coating over the clusters. The DDT-protected clusters should act as an inhibitor for the ALD coating, and thus alumina deposition should only occur around the Au_{25} clusters for this system. To study the effect of thickness on the thermal stability, catalysts were synthesized by 5, 10, and 20 cycles of alumina deposition over $\text{Au}_{25}(\text{MUA})_{18}$ clusters. Both TEM and EXAFS were employed to examine the thermal stability of these catalysts and the 4-nitrophenol reduction reaction was used as a model catalytic reaction.

To design a thermally stable catalyst, it is highly desirable to understand the mechanism of the sintering. It has been reported that both particle migration and coalescence and/or Ostwald ripening mechanisms are responsible for the sintering of nanoparticles.¹²⁴ The third part of the research objective, detailed in Chapter 4, involves monitoring the mechanism of aggregation of Au clusters. An environmental *in situ* TEM technique was utilized to probe the sintering behavior of Au_{25} clusters on mesoporous silica (SBA-15) during thermal treatment up to 650 °C. A bifunctional ligand, (3-mercaptopropyl)trimethoxysilane (MPTS), was employed as a stabilizing ligand for the Au_{25} clusters as it is expected to provide for stronger metal-support interactions.

In the last two chapters, the research objectives focused on the synthesis of Pd based clusters, as Pd is a very common catalytic metal. Two different routes to do this were attempted. It is highly desirable to synthesize ligand-free clusters that enable one to avoid necessary activation process. In Chapter 5, the research objective was to synthesize ligand-free clusters via a top-down approach. This study was a follow up on previous work that showed the formation of Ag clusters dispersed in a silica matrix by breaking up larger triangular Ag nanoparticles upon calcination in air.¹²⁵ I hypothesized that Pd based catalysts could then be synthesized by galvanic replacement of Pd precursors with the naked-Ag clusters dispersed in the silica matrix. The reduction of Pd precursors with Ag clusters in a silica shell was monitored by Pd-L₃ edge XAS analysis at the Canadian Light Source. TEM, XPS, and EXAFS spectroscopy were used to analyze the morphology and local structure of the catalysts. The objectives of Chapter 6 was to synthesize silica encapsulated Pd_m(MUA)_n clusters using a similar route used for Au clusters in Chapter 2. Here the methane combustion reaction was chosen as a model reaction to explore the role of silica coating in catalytic activity and sintering.

1.10. Organization and Scope

This Ph.D. thesis describes the synthesis of sinter resistant Au and Pd based catalysts. It is divided into seven chapters. Parts of Chapter 1, and Chapters 2 and 3 are based on articles already published in different journals with minor formatting changes. Chapter 4, 5, and 6 are manuscripts to be submitted in the near future. This introduction chapter gives a brief introduction about atom-precise clusters, especially Au₂₅(SR)₁₈ clusters. This chapter also discusses the importance of activation of clusters in catalysis, methods used for activation of clusters and an overview of the main characterization techniques used in this thesis. Part of the first chapter incorporates parts of a recent review that focuses on the recent establishment of several methodologies for the activation of metal clusters. Approaches for synthesizing sinter resistant catalysts are also discussed in the first chapter. Chapters 2, 3, and 4 describe several strategies including silica encapsulation, atomic layer deposition, and immobilization with bifunctional ligands for improving the thermal stability of Au₂₅ cluster catalysts during the thermal activation process. Chapter 2 focuses on the synthesis of sinter-resistant Au clusters encapsulated inside silica spheres that are formed by sol-gel chemistry. The thermal stability and catalytic activity of the silica-encapsulated clusters was compared with non-encapsulated clusters on top of silica particles. Chapter 3 focuses on the effect of atomic layer deposition of alumina over Au clusters. In Chapter 4, an *in situ* TEM technique was used to monitor the

mechanism of sintering of Au₂₅ clusters on a silica support. A bifunctional ligand, MPTS, provides a strong metal catalyst-support interaction that minimizes the mobility of clusters on the catalyst support. An environmental *in situ* TEM technique was utilized to probe the sintering behavior of the Au₂₅ clusters on mesoporous silica (SBA-15) during thermal treatment up to 650 °C. Chapter 5 describes the galvanic replacement method for the synthesis of bimetallic clusters starting with ligand free-Ag clusters dispersed in a silica matrix. Here we synthesized a Pd based catalyst from activated silica-encapsulated Ag cluster catalysts. Chapter 6 describes the direct synthesis of thiolate-stabilized Pd clusters, and encapsulation of the Pd clusters in silica, followed by activation. The thermal stability and catalytic activity for methane oxidation of silica-coated catalysts and non-coated catalysts were studied. Finally, in Chapter 7, I summarize all the conclusions of this thesis, and suggest possible avenues of future work that could be done in this area.

1.11. References

- (1) Astruc, D.; Lu, F.; Aranzaes, J. R. Nanoparticles as Recyclable Catalysts: The Frontier between Homogeneous and Heterogeneous Catalysis. *Angew. Chem. Int. Edit.* **2005**, *44*, 7852-7872.
- (2) Chen, M. S.; Goodman, D. W. Structure–Activity Relationships in Supported Au Catalysts. *Catal. Today* **2006**, *111*, 22-33.
- (3) Zhang, Q.; Wang, H. Facet-Dependent Catalytic Activities of Au Nanoparticles Enclosed by High-Index Facets. *ACS Catal.* **2014**, *4*, 4027-4033.
- (4) Caulton, K. G.; Thomas, M. G.; Sosinsky, B. A.; Muetterties, E. L. Metal Clusters in Catalysis: Hydrocarbon Reactions. *Proc. Natl. Acad. Sci.* **1976**, *73*, 4274-4276.
- (5) Haruta, M.; Yamada, N.; Kobayashi, T.; Iijima, S. Gold Catalysts Prepared by Coprecipitation for Low-Temperature Oxidation of Hydrogen and of Carbon monoxide. *J. Catal.* **1989**, *115*, 301-309.
- (6) Ueda, A.; Haruta, M. Nitric Oxide Reduction with Hydrogen, Carbon Monoxide, and Hydrocarbons over Gold Catalysts. *Gold Bull.* **1999**, *32*, 3-11.
- (7) Ousmane, M.; Liotta, L. F.; Carlo, G. D.; Pantaleo, G.; Venezia, A. M.; Deganello, G.; Retailleau, L.; Boreave, A.; Giroir-Fendler, A. Supported Au Catalysts for Low-Temperature Abatement of Propene and Toluene, as Model VOCs: Support Effect. *Appl. Catal. B: Environ.* **2011**, *101*, 629-637.
- (8) Li, Q.; Zhang, Y.; Chen, G.; Fan, J.; Lan, H.; Yang, Y. Ultra-Low-Gold Loading Au/CeO₂ Catalysts for Ambient Temperature CO Oxidation: Effect of Preparation Conditions on Surface Composition and Activity. *J. Catal.* **2010**, *273*, 167-176.
- (9) Widmann, D.; Liu, Y.; Schüth, F.; Behm, R. J. Support Effects in the Au-Catalyzed CO Oxidation – Correlation between Activity, Oxygen Storage Capacity, and Support Reducibility. *J. Catal.* **2010**, *276*, 292-305.
- (10) Malta, G.; Kondrat, S. A.; Freakley, S. J.; Davies, C. J.; Lu, L.; Dawson, S.; Thetford, A.; Gibson, E. K.; Morgan, D. J.; Jones, W.; Wells, P. P.; Johnston, P.; Catlow, C. R. A.; Kiely, C. J.; Hutchings, G. J. Identification of Single-Site Gold Catalysis in Acetylene Hydrochlorination. *Science.* **2017**, *355*, 1399-1403.

- (11) Tsunoyama, H.; Sakurai, H.; Tsukuda, T. Size Effect on the Catalysis of Gold Clusters Dispersed in Water for Aerobic Oxidation of Alcohol. *Chem. Phys. Lett.* **2006**, *429*, 528-532.
- (12) Liu, L.; Corma, A. Metal Catalysts for Heterogeneous Catalysis: From Single Atoms to Nanoclusters and Nanoparticles. *Chem. Rev.* **2018**, *118*, 4981-5079.
- (13) Eberhardt, W. Clusters as New Materials. *Surf. Sci.* **2002**, *500*, 242-270.
- (14) and, S. L.; ElSayed, M. A. Optical Properties and Ultrafast Dynamics of Metallic Nanocrystals. *Annu. Rev. Phys. Chem.* **2003**, *54*, 331-366.
- (15) Studart, A. R.; Amstad, E.; Gauckler, L. J. Colloidal Stabilization of Nanoparticles in Concentrated Suspensions. *Langmuir* **2007**, *23*, 1081-1090.
- (16) McPartlin, M.; Mason, R.; Malatesta, L. Novel Cluster Complexes of Gold(0)–Gold(I). *J. Chem. Soc., Chem. Commun.* **1969**, *7*, 334-334.
- (17) Weare, W. W.; Reed, S. M.; Warner, M. G.; Hutchison, J. E. Improved Synthesis of Small ($d_{\text{CORE}} \approx 1.5$ nm) Phosphine-Stabilized Gold Nanoparticles. *J. Am. Chem. Soc.* **2000**, *122*, 12890-12891.
- (18) Zeng, C.; Chen, Y.; Kirschbaum, K.; Appavoo, K.; Sfeir, M. Y.; Jin, R. Structural Patterns at all Scales in a Nonmetallic Chiral Au₁₃₃(SR)₅₂ Nanoparticle. *Sci. Adv.* **2015**, *1*, 1-6.
- (19) Gutrath, B. S.; Opperl, I. M.; Presly, O.; Beljakov, I.; Meded, V.; Wenzel, W.; Simon, U. [Au₁₄(PPh₃)₈(NO₃)₄]: An Example of a New Class of Au(NO₃)-Ligated Superatom Complexes. *Angew. Chem. Int. Edit.* **2013**, *52*, 3529-3532.
- (20) Shibu, E. S.; Radha, B.; Verma, P. K.; Bhyrappa, P.; Kulkarni, G. U.; Pal, S. K.; Pradeep, T. Functionalized Au₂₂ Clusters: Synthesis, Characterization, and Patterning. *ACS Appl. Mater. Inter.* **2009**, *1*, 2199-2210.
- (21) Qian, H.; Jin, R. Ambient Synthesis of Au₁₄₄(SR)₆₀ Nanoclusters in Methanol. *Chem. Mater.* **2011**, *23*, 2209-2217.
- (22) Shivhare, A.; Scott, R. W. J. Au₂₅ Clusters as Precursors for the Synthesis of AuPd Bimetallic Nanoparticles with Isolated Atomic Pd-Surface Sites. *Mol. Catal.* **2018**, *457*, 33-40.

- (23) Schmid, G.; Pfeil, R.; Boese, R.; Bandermann, F.; Meyer, S.; Calis, G. H. M.; Van der Velden, J. W. A. Au₅₅[P(C₆H₅)₃]₁₂Cl₆ -A Gold cluster of Unusual Size. *Chem. Ber.* **1981**, *114*, 3634-3642.
- (24) Zhu, M.; Lanni, E.; Garg, N.; Bier, M. E.; Jin, R. Kinetically Controlled, High-Yield Synthesis of Au₂₅ Clusters. *J. Am. Chem. Soc.* **2008**, *130*, 1138-1139.
- (25) Brust, M.; Walker, M.; Bethell, D.; Schiffrin, D. J.; Whyman, R. Synthesis of Thiol-Derivatised Gold Nanoparticles in a Two-Phase Liquid-Liquid System. *J. Chem. Soc., Chem. Commun.* **1994**, *7*, 801-802.
- (26) Alvarez, M. M.; Khoury, J. T.; Schaaff, T. G.; Shafigullin, M.; Vezmar, I.; Whetten, R. L. Critical Sizes in the Growth of Au Clusters. *Chem. Phys. Lett.* **1997**, *266*, 91-98.
- (27) Schaaff, T. G.; Knight, G.; Shafigullin, M. N.; Borkman, R. F.; Whetten, R. L. Isolation and Selected Properties of a 10.4 kDa Gold:Glutathione Cluster Compound. *J. Phys. Chem. B* **1998**, *102*, 10643-10646.
- (28) Wang, Z. W.; Palmer, R. E. Experimental Evidence for Fluctuating, Chiral-Type Au₅₅ Clusters by Direct Atomic Imaging. *Nano Lett.* **2012**, *12*, 5510-5514.
- (29) Jian, N.; Stapelfeldt, C.; Hu, K. J.; Fröba, M.; Palmer, R. E. Hybrid Atomic Structure of the Schmid Cluster Au₅₅(PPh₃)₁₂Cl₆ Resolved by Aberration-Corrected STEM. *Nanoscale* **2015**, *7*, 885-888.
- (30) Chakraborty, I.; Pradeep, T. Atomically Precise Clusters of Noble Metals: Emerging Link between Atoms and Nanoparticles. *Chem. Rev.* **2017**, *117*, 8208-8271.
- (31) Pichugina, D. A.; Kuz'menko, N. E.; Shestakov, A. F. Ligand-Protected Gold Clusters: the Structure, Synthesis and Applications. *Russ. Chem. Rev.* **2015**, *84*, 1114-1144.
- (32) Du, Y.; Sheng, H.; Astruc, D.; Zhu, M. Atomically Precise Noble Metal Nanoclusters as Efficient Catalysts: A Bridge between Structure and Properties. *Chem. Rev.* **2019**, *120*, 526-622.
- (33) Qian, H.; Zhu, M.; Wu, Z.; Jin, R. Quantum Sized Gold Nanoclusters with Atomic Precision. *Acc. Chem. Res.* **2012**, *45*, 1470-1479.

- (34) Jin, R.; Zeng, C.; Zhou, M.; Chen, Y. Atomically Precise Colloidal Metal Nanoclusters and Nanoparticles: Fundamentals and Opportunities. *Chem. Rev.* **2016**, *116*, 10346-10413.
- (35) Weerawardene, K. L. D. M.; Häkkinen, H.; Aikens, C. M. Connections Between Theory and Experiment for Gold and Silver Nanoclusters. *Annu. Rev. Phys. Chem.* **2018**, *69*, 205-229.
- (36) Yuan, X.; Dou, X.; Zheng, K.; Xie, J. Recent Advances in the Synthesis and Applications of Ultrasmall Bimetallic Nanoclusters. *Part. Part. Syst. Char.* **2015**, *32*, 613-629.
- (37) Liu, J.; Lee, T.; Janes, D. B.; Walsh, B. L.; Melloch, M. R.; Woodall, J. M.; Reifenberger, R.; Andres, R. P. Guided Self-Assembly of Au Nanocluster Arrays Electronically Coupled to Semiconductor Device Layers. *Appl. Phys. Lett.* **2000**, *77*, 373-375.
- (38) Kadossov, E.; Cabrini, S.; Burghaus, U. Adsorption Kinetics and Dynamics of CO on Silica Supported Au Nanoclusters-Utilizing Physical Vapor Deposition and Electron Beam Lithography. *J. Mol. Catal. A-Chem.* **2010**, *321*, 101-109.
- (39) Ishida, T.; Kinoshita, N.; Okatsu, H.; Akita, T.; Takei, T.; Haruta, M. Influence of the Support and the Size of Gold Clusters on Catalytic Activity for Glucose Oxidation. *Angew. Chem. Int. Edit.* **2008**, *47*, 9265-9268.
- (40) Hu, C. W.; Kasuya, A.; Wawro, A.; Horiguchi, N.; Czajka, R.; Nishina, Y.; Saito, Y.; Fujita, H. Gold Clusters Deposited on Highly Oriented Pyrolytic Graphite by Pulse Laser Ablation and Liquid Metal Ion Source. *Mater. Sci. Eng. A* **1996**, *217-218*, 103-107.
- (41) Zhou, R.; Shi, M.; Chen, X.; Wang, M.; Chen, H. Atomically Monodispersed and Fluorescent Sub-Nanometer Gold Clusters Created by Biomolecule-Assisted Etching of Nanometer-Sized Gold Particles and Rods. *Chem. Eur. J.* **2009**, *15*, 4944-4951.
- (42) Jensen, K. M. Ø.; Juhas, P.; Tofanelli, M. A.; Heinecke, C. L.; Vaughan, G.; Ackerson, C. J.; Billinge, S. J. L. Polymorphism in Magic-Sized Au₁₄₄(SR)₆₀ Clusters. *Nat. Commun.* **2016**, *7*, 11859-11865.
- (43) Mednikov, E. G.; Dahl, L. F. Crystallographically Proven Nanometer-Sized Gold Thiolate Cluster Au₁₀₂(SR)₄₄: Its Unexpected Molecular Anatomy and Resulting Stereochemical and Bonding Consequences. *Small* **2008**, *4*, 534-537.

- (44) Weerawardene, K. L. D. M.; Guidez, E. B.; Aikens, C. M. Photoluminescence Origin of Au₃₈(SR)₂₄ and Au₂₂(SR)₁₈ Nanoparticles: A Theoretical Perspective. *J. Phys. Chem. C* **2017**, *121*, 15416-15423.
- (45) Yu, C.; Li, G.; Kumar, S.; Kawasaki, H.; Jin, R. Stable Au₂₅(SR)₁₈/TiO₂ Composite Nanostructure with Enhanced Visible Light Photocatalytic Activity. *J. Phys. Chem. Lett.* **2013**, *4*, 2847-2852.
- (46) Donkers, R. L.; Lee, D.; Murray, R. W. Synthesis and Isolation of the Molecule-like Cluster Au₃₈(PhCH₂CH₂S)₂₄. *Langmuir* **2004**, *20*, 1945-1952.
- (47) Tracy, J. B.; Crowe, M. C.; Parker, J. F.; Hampe, O.; Fields-Zinna, C. A.; Dass, A.; Murray, R. W. Electrospray Ionization Mass Spectrometry of Uniform and Mixed Monolayer Nanoparticles: Au₂₅[S(CH₂)₂Ph]₁₈ and Au₂₅[S(CH₂)₂Ph]_{18-x}(SR)_x. *J. Am. Chem. Soc.* **2007**, *129*, 16209-16215.
- (48) Agrachev, M.; Antonello, S.; Dainese, T.; Gascón, J. A.; Pan, F.; Rissanen, K.; Ruzzi, M.; Venzo, A.; Zoleo, A.; Maran, F. A Magnetic Look into the Protecting Layer of Au₂₅ Clusters. *Chem. Sci.* **2016**, *7*, 6910-6918.
- (49) Kurashige, W.; Yamazoe, S.; Yamaguchi, M.; Nishido, K.; Nobusada, K.; Tsukuda, T.; Negishi, Y. Au₂₅ Clusters Containing Unoxidized Tellurolates in the Ligand Shell. *J. Phys. Chem. Lett.* **2014**, *5*, 2072-2076.
- (50) Habeeb Muhammed, M. A.; Pradeep, T. Au₂₅@SiO₂: Quantum Clusters of Gold Embedded in Silica. *Small* **2011**, *7*, 204-208.
- (51) Shivhare, A.; Ambrose, S. J.; Zhang, H.; Purves, R. W.; Scott, R. W. J. Stable and recyclable Au₂₅ clusters for the reduction of 4-nitrophenol. *Chem. Commun.* **2013**, *49*, 276-278.
- (52) Heaven, M. W.; Dass, A.; White, P. S.; Holt, K. M.; Murray, R. W. Crystal Structure of the Gold Nanoparticle [N(C₈H₁₇)₄][Au₂₅(SCH₂CH₂Ph)₁₈]. *J. Am. Chem. Soc.* **2008**, *130*, 3754-3755.
- (53) Aikens, C. M. Origin of Discrete Optical Absorption Spectra of M₂₅(SH)₁₈⁻ Nanoparticles (M = Au, Ag). *J. Phys. Chem. C* **2008**, *112*, 19797-19800.

- (54) Aikens, C. M. Electronic and Geometric Structure, Optical Properties, and Excited State Behavior in Atomically Precise Thiolate-Stabilized Noble Metal Nanoclusters. *Acc. Chem. Res.* **2018**, *51*, 3065-3073.
- (55) Zhu, M.; Aikens, C. M.; Hollander, F. J.; Schatz, G. C.; Jin, R. Correlating the Crystal Structure of A Thiol-Protected Au₂₅ Cluster and Optical Properties. *J. Am. Chem. Soc.* **2008**, *130*, 5883-5885.
- (56) Dainese, T.; Antonello, S.; Bogialli, S.; Fei, W.; Venzo, A.; Maran, F. Gold Fusion: From Au₂₅(SR)₁₈ to Au₃₈(SR)₂₄, the Most Unexpected Transformation of a Very Stable Nanocluster. *ACS Nano* **2018**, *12*, 7057-7066.
- (57) Nasaruddin, R. R.; Chen, T.; Yan, N.; Xie, J. Roles of Thiolate Ligands in the Synthesis, Properties and Catalytic Application of Gold Nanoclusters. *Coord. Chem. Rev.* **2018**, *368*, 60-79.
- (58) MacDonald, M. A.; Chevrier, D. M.; Zhang, P.; Qian, H.; Jin, R. The Structure and Bonding of Au₂₅(SR)₁₈ Nanoclusters from EXAFS: The Interplay of Metallic and Molecular Behavior. *J. Phys. Chem. C* **2011**, *115*, 15282-15287.
- (59) Li, G.; Jin, R. Atomically Precise Gold Nanoclusters as New Model Catalysts. *Acc. Chem. Res.* **2013**, *46*, 1749-1758.
- (60) Nie, X.; Qian, H.; Ge, Q.; Xu, H.; Jin, R. CO Oxidation Catalyzed by Oxide-Supported Au₂₅(SR)₁₈ Nanoclusters and Identification of Perimeter Sites as Active Centers. *ACS Nano* **2012**, *6*, 6014-6022.
- (61) Yoskamtorn, T.; Yamazoe, S.; Takahata, R.; Nishigaki, J. I.; Thivasasith, A.; Limtrakul, J.; Tsukuda, T. Thiolate-Mediated Selectivity Control in Aerobic Alcohol Oxidation by Porous Carbon-Supported Au₂₅ Clusters. *ACS Catal.* **2014**, *4*, 3696-3700.
- (62) Sudheeshkumar, V.; Shivhare, A.; Scott, R. W. J. Synthesis of Sinter-Resistant Au@silica Catalysts Derived from Au₂₅ Clusters. *Catal. Sci. Technol.* **2017**, *7*, 272-280.
- (63) Liu, Y.; Tsunoyama, H.; Akita, T.; Tsukuda, T. Efficient and Selective Epoxidation of Styrene with TBHP Catalyzed by Au₂₅ Clusters on Hydroxyapatite. *Chem. Commun.* **2010**, *46*, 550-552.

- (64) Zhu, Y.; Qian, H.; Jin, R. An Atomic-Level Strategy for Unraveling Gold Nanocatalysis from the Perspective of Au_n(SR)_m Nanoclusters. *Chem. Eur. J.* **2010**, *16*, 11455-11462.
- (65) Zhu, Y.; Qian, H.; Drake, B. A.; Jin, R. Atomically Precise Au₂₅(SR)₁₈ Nanoparticles as Catalysts for the Selective Hydrogenation of α,β -Unsaturated Ketones and Aldehydes. *Angew. Chem. Int. Edit.* **2010**, *49*, 1295-1298.
- (66) Li, W.; Ge, Q.; Ma, X.; Chen, Y.; Zhu, M.; Xu, H.; Jin, R. Mild Activation of CeO₂-Supported Gold Nanoclusters and Insight into the Catalytic Behavior in CO Oxidation. *Nanoscale* **2016**, *8*, 2378-2385.
- (67) Yamamoto, H.; Yano, H.; Kouchi, H.; Obora, Y.; Arakawa, R.; Kawasaki, H. N,N-Dimethylformamide-Stabilized Gold Nanoclusters as a Catalyst for the Reduction of 4-nitrophenol. *Nanoscale* **2012**, *4*, 4148-4154.
- (68) Shivhare, A.; Chevrier, D. M.; Purves, R. W.; Scott, R. W. J. Following the Thermal Activation of Au₂₅(SR)₁₈ Clusters for Catalysis by X-ray Absorption Spectroscopy. *J. Phys. Chem. C* **2013**, *117*, 20007-20016.
- (69) Sudheeshkumar, V.; Sulaiman, K. O.; Scott, R. W. J. Activation of Atom-Precise Clusters for Catalysis. *Nanoscale Adv.* **2020**, *2*, 55-69.
- (70) Wu, Z.; Jin, R. Stability of the Two Au–S Binding Modes in Au₂₅(SG)₁₈ Nanoclusters Probed by NMR and Optical Spectroscopy. *ACS Nano* **2009**, *3*, 2036-2042.
- (71) Liu, Y.; Tsunoyama, H.; Akita, T.; Xie, S.; Tsukuda, T. Aerobic Oxidation of Cyclohexane Catalyzed by Size-Controlled Au Clusters on Hydroxyapatite: Size Effect in the Sub-2 nm Regime. *ACS Catal.* **2011**, *1*, 2-6.
- (72) Gaur, S.; Miller, J. T.; Stellwagen, D.; Sanampudi, A.; Kumar, C. S. S. R.; Spivey, J. J. Synthesis, Characterization, and Testing of Supported Au Catalysts Prepared from Atomically-Tailored Au₃₈(SC₁₂H₂₅)₂₄ clusters. *Phys. Chem. Chem. Phys.* **2012**, *14*, 1627-1634.
- (73) Wu, Z.; Jiang, D. E.; Mann, A. K. P.; Mullins, D. R.; Qiao, Z. A.; Allard, L. F.; Zeng, C.; Jin, R.; Overbury, S. H. Thiolate Ligands as a Double-Edged Sword for CO Oxidation on CeO₂ Supported Au₂₅(SCH₂CH₂Ph)₁₈ Nanoclusters. *J. Am. Chem. Soc.* **2014**, *136*, 6111-6122.

- (74) Fang, J.; Li, J.; Zhang, B.; Yuan, X.; Asakura, H.; Tanaka, T.; Teramura, K.; Xie, J.; Yan, N. The Support Effect on the Size and Catalytic Activity of Thiolated Au₂₅ Nanoclusters as Precatalysts. *Nanoscale* **2015**, *7*, 6325-6333.
- (75) García, C.; Pollitt, S.; van der Linden, M.; Truttmann, V.; Rameshan, C.; Rameshan, R.; Pittenauer, E.; Allmaier, G.; Kregsamer, P.; Stöger-Pollach, M.; Barrabés, N.; Rupprechter, G. Support Effect on the Reactivity and Stability of Au₂₅(SR)₁₈ and Au₁₄₄(SR)₆₀ nanoclusters in liquid phase cyclohexane oxidation. *Catal. Today* **2018**, *336*, 174-185.
- (76) Zhang, B.; Kaziz, S.; Li, H.; Hevia, M. G.; Wodka, D.; Mazet, C.; Bürgi, T.; Barrabés, N. Modulation of Active Sites in Supported Au₃₈(SC₂H₄Ph)₂₄ Cluster Catalysts: Effect of Atmosphere and Support Material. *J. Phys. Chem. C* **2015**, *119*, 11193-11199.
- (77) Zhang, B.; Sels, A.; Salassa, G.; Pollitt, S.; Truttmann, V.; Rameshan, C.; Llorca, J.; Olszewski, W.; Rupprechter, G.; Bürgi, T.; Barrabés, N. Ligand Migration from Cluster to Support: A Crucial Factor for Catalysis by Thiolate-protected Gold Clusters. *ChemCatChem* **2018**, *10*, 5372-5376.
- (78) Zhang, B.; García, C.; Sels, A.; Salassa, G.; Rameshan, C.; Llorca, J.; Hradil, K.; Rupprechter, G.; Barrabés, N.; Bürgi, T. Ligand and Support Effects on the Reactivity and Stability of Au₃₈(SR)₂₄ Catalysts in Oxidation Reactions. *Catal. Commun.* **2019**, *130*, 105768-105774.
- (79) Almukhlifi, H. A.; Burns, R. C. Gold Nanoparticles on Metal Oxide Surfaces Derived from n-Alkanethiolate-Stabilized Gold Nanoparticles; Investigations of the Adsorption Mechanism and Sulfate Formation During Subsequent Thermolysis. *Appl. Catal. A-Gen.* **2015**, *502*, 174-187.
- (80) Kurashige, W.; Yamaguchi, M.; Nobusada, K.; Negishi, Y. Ligand-Induced Stability of Gold Nanoclusters: Thiolate versus Selenolate. *J. Phys. Chem. Lett.* **2012**, *3*, 2649-2652.
- (81) Liu, Y.; Tsunoyama, H.; Akita, T.; Tsukuda, T. Preparation of ~1 nm Gold Clusters Confined within Mesoporous Silica and Microwave-Assisted Catalytic Application for Alcohol Oxidation. *J. Phys. Chem. C* **2009**, *113*, 13457-13461.
- (82) Wu, Z.; Hu, G.; Jiang, D. E.; Mullins, D. R.; Zhang, Q. F.; Allard, L. F.; Wang, L. S.; Overbury, S. H. Diphosphine-Protected Au₂₂ Nanoclusters on Oxide Supports Are Active for Gas-Phase Catalysis without Ligand Removal. *Nano Lett.* **2016**, *16*, 6560-6567.

- (83) Wan, X. K.; Wang, J. Q.; Nan, Z. A.; Wang, Q. M. Ligand Effects in Catalysis by Atomically Precise Gold Nanoclusters. *Sci. Adv.* **2017**, *3*, 1-7.
- (84) Anderson, D. P.; Alvino, J. F.; Gentleman, A.; Qahtani, H. A.; Thomsen, L.; Polson, M. I. J.; Metha, G. F.; Golovko, V. B.; Andersson, G. G. Chemically-Synthesised, Atomically-Precise Gold Clusters Deposited and Activated on Titania. *Phys. Chem. Chem. Phys.* **2013**, *15*, 3917-3929.
- (85) Anderson, D. P.; Adnan, R. H.; Alvino, J. F.; Shipper, O.; Donoeva, B.; Ruzicka, J.-Y.; Al Qahtani, H.; Harris, H. H.; Cowie, B.; Aitken, J. B.; Golovko, V. B.; Metha, G. F.; Andersson, G. G. Chemically Synthesised Atomically Precise Gold Clusters Deposited and Activated on Titania. Part II. *Phys. Chem. Chem. Phys.* **2013**, *15*, 14806-14813.
- (86) Al Qahtani, H. S.; Higuchi, R.; Sasaki, T.; Alvino, J. F.; Metha, G. F.; Golovko, V. B.; Adnan, R.; Andersson, G. G.; Nakayama, T. Grouping and Aggregation of Ligand Protected Au₉ Clusters on TiO₂ Nanosheets. *RSC Adv.* **2016**, *6*, 110765-110774.
- (87) Menard, L. D.; Xu, F.; Nuzzo, R. G.; Yang, J. C. Preparation of TiO₂-Supported Au Nanoparticle Catalysts from a Au₁₃ Cluster Precursor: Ligand Removal Using Ozone Exposure Versus a Rapid Thermal Treatment. *J. Catal.* **2006**, *243*, 64-73.
- (88) Elliott, E. W.; Glover, R. D.; Hutchison, J. E. Removal of Thiol Ligands from Surface-Confinned Nanoparticles without Particle Growth or Desorption. *ACS Nano* **2015**, *9*, 3050-3059.
- (89) Kilmartin, J.; Sarip, R.; Grau-Crespo, R.; Di Tommaso, D.; Hogarth, G.; Prestipino, C.; Sankar, G. Following the Creation of Active Gold Nanocatalysts from Phosphine-Stabilized Molecular Clusters. *ACS Catal.* **2012**, *2*, 957-963.
- (90) Liu, J.; Krishna, K. S.; Losovyj, Y. B.; Chattopadhyay, S.; Lozova, N.; Miller, J. T.; Spivey, J. J.; Kumar, C. S. S. R. Ligand-Stabilized and Atomically Precise Gold Nanocluster Catalysis: A Case Study for Correlating Fundamental Electronic Properties with Catalysis. *Chem. Eur. J.* **2013**, *19*, 10201-10208.
- (91) Dreier, T. A.; Andrea Wong, O.; Ackerson, C. J. Oxidative Decomposition of Au₂₅(SR)₁₈ Clusters in a Catalytic Context. *Chem. Commun.* **2015**, *51*, 1240-1243.

- (92) Zhang, B.; Fang, J.; Li, J.; Lau, J. J.; Mattia, D.; Zhong, Z.; Xie, J.; Yan, N. Soft, Oxidative Stripping of Alkyl Thiolate Ligands from Hydroxyapatite-Supported Gold Nanoclusters for Oxidation Reactions. *Chem. Asian. J.* **2016**, *11*, 532-539.
- (93) Dasog, M.; Hou, W.; Scott, R. W. J. Controlled Growth and Catalytic Activity of Gold Monolayer Protected Clusters in Presence of Borohydride Salts. *Chem. Commun.* **2011**, *47*, 8569-8571.
- (94) Ansar, S. M.; Ameer, F. S.; Hu, W.; Zou, S.; Pittman, C. U.; Zhang, D. Removal of Molecular Adsorbates on Gold Nanoparticles Using Sodium Borohydride in Water. *Nano Lett.* **2013**, *13*, 1226-1229.
- (95) Das, S.; Goswami, A.; Hesari, M.; Al-Sharab, J. F.; Mikmeková, E.; Maran, F.; Asefa, T. Reductive Deprotection of Monolayer Protected Nanoclusters: An Efficient Route to Supported Ultrasmall Au Nanocatalysts for Selective Oxidation. *Small* **2014**, *10*, 1473-1478.
- (96) Shivhare, A.; Scott, R. W. J. Following the Thermal and Chemical Activation of Supported Au Clusters Using X-ray Absorption Spectroscopy. *RSC Adv.* **2016**, *6*, 62579-62584.
- (97) Sarina, S.; Waclawik, E. R.; Zhu, H. Photocatalysis on Supported Gold and Silver Nanoparticles under Ultraviolet and Visible Light Irradiation. *Green Chem.* **2013**, *15*, 1814-1833.
- (98) Peiris, S.; McMurtrie, J.; Zhu, H.-Y. Metal Nanoparticle Photocatalysts: Emerging Processes for Green Organic Synthesis. *Catal. Sci. Technol.* **2016**, *6*, 320-338.
- (99) Khan, M. E.; Khan, M. M.; Cho, M. H. Recent Progress of Metal-Graphene Nanostructures in Photocatalysis. *Nanoscale* **2018**, *10*, 9427-9440.
- (100) Li, G.; Wang, Y.; Mao, L. Recent Progress in Highly Efficient Ag-based Visible-Light Photocatalysts. *RSC Adv.* **2014**, *4*, 53649-53661.
- (101) Chen, Y. S.; Choi, H.; Kamat, P. V. Metal-Cluster-Sensitized Solar Cells. A New Class of Thiolated Gold Sensitizers Delivering Efficiency Greater Than 2%. *J. Am. Chem. Soc.* **2013**, *135*, 8822-8825.
- (102) Xiao, F. X.; Zeng, Z.; Hsu, S.-H.; Hung, S. F.; Chen, H. M.; Liu, B. Light-Induced In Situ Transformation of Metal Clusters to Metal Nanocrystals for Photocatalysis. *ACS Appl. Mater. Inter.* **2015**, *7*, 28105-28109.

- (103) Liu, S.; Xu, Y. J. Photo-induced Transformation Process at Gold Clusters-Semiconductor Interface: Implications for the Complexity of Gold Clusters-Based Photocatalysis. *Sci. Rep-UK*. **2016**, *6*, 1-7.
- (104) Joo, S. H.; Park, J. Y.; Tsung, C. K.; Yamada, Y.; Yang, P.; Somorjai, G. A. Thermally Stable Pt/Mesoporous Silica Core-Shell Nanocatalysts for High-Temperature Reactions. *Nat. Mater.* **2008**, *8*, 126-135.
- (105) Arnal, P. M.; Comotti, M.; Schüth, F. High-Temperature-Stable Catalysts by Hollow Sphere Encapsulation. *Angew. Chem. Int. Edit.* **2006**, *45*, 8224-8227.
- (106) Samanta, A.; Dhar, B. B.; Devi, R. N. Ultrasmall Gold Cluster Arrays Encapsulated in Silica Nanospheres: Applications in Fluorescence Imaging and Catalysis. *J. Phys. Chem. C* **2012**, *116*, 1748-1754.
- (107) Chen, H.; Liu, C.; Wang, M.; Zhang, C.; Li, G.; Wang, F. Thermally Robust Silica-Enclosed Au₂₅ Nanocluster and its Catalysis. *Chinese J. Catal.* **2016**, *37*, 1787-1793.
- (108) Ma, G.; Binder, A.; Chi, M.; Liu, C.; Jin, R.; Jiang, D. E.; Fan, J.; Dai, S. Stabilizing Gold Clusters by Heterostructured Transition-Metal Oxide-Mesoporous Silica Supports for Enhanced Catalytic Activities for CO Oxidation. *Chem. Commun.* **2012**, *48*, 11413-11415.
- (109) Zheng, Y.; Zhang, X.; Yao, Y.; Chen, X.; Yang, Q. Ultra-Small Au Nanoparticles Stabilized by Silica Hollow Nanospheres for Styrene Oxidation with Oxygen. *RSC Adv.* **2015**, *5*, 105747-105752.
- (110) Weng, B.; Lu, K. Q.; Tang, Z.; Chen, H. M.; Xu, Y. J. Stabilizing Ultrasmall Au Clusters for Enhanced Photoredox Catalysis. *Nat. Commun.* **2018**, *9*, 1543-1557.
- (111) Cui, X.; Wang, J.; Liu, B.; Ling, S.; Long, R.; Xiong, Y. Turning Au Nanoclusters Catalytically Active for Visible-Light-Driven CO₂ Reduction through Bridging Ligands. *J. Am. Chem. Soc.* **2018**, *140*, 16514-16520.
- (112) Weng, B.; Zhang, J.; Shi, Z. F.; Tang, Z.; Zheng, L. S.; Xu, Y. J. Improving the Photostability of Ultrasmall Au Clusters via a Combined Strategy of Surface Engineering and Interfacial Modification. *Langmuir* **2019**, *35*, 5728-5736.

- (113) Liu, L.; Song, Y.; Chong, H.; Yang, S.; Xiang, J.; Jin, S.; Kang, X.; Zhang, J.; Yu, H.; Zhu, M. Size-Confined Growth of Atom-Precise Nanoclusters in Metal–Organic Frameworks and their Catalytic Applications. *Nanoscale* **2016**, *8*, 1407-1412.
- (114) Sun, L.; Yun, Y.; Sheng, H.; Du, Y.; Ding, Y.; Wu, P.; Li, P.; Zhu, M. Rational Encapsulation of Atomically Precise Nanoclusters into Metal–Organic Frameworks by Electrostatic Attraction for CO₂ Conversion. *J. Mater. Chem. A* **2018**, *6*, 15371-15376.
- (115) Liu, C.; Zeng, C.; Luo, T. Y.; Merg, A. D.; Jin, R.; Rosi, N. L. Establishing Porosity Gradients within Metal–Organic Frameworks Using Partial Postsynthetic Ligand Exchange. *J. Am. Chem. Soc.* **2016**, *138*, 12045-12048
- (116) Luo, Y.; Fan, S.; Yu, W.; Wu, Z.; Cullen, D. A.; Liang, C.; Shi, J.; Su, C. Fabrication of Au₂₅(SG)₁₈–ZIF-8 Nanocomposites: A Facile Strategy to Position Au₂₅(SG)₁₈ Nanoclusters Inside and Outside ZIF-8. *Adv. Mater.* **2018**, *30*, 1-9.
- (117) Petkov, N. In Situ Real-Time TEM Reveals Growth, Transformation and Function in One-Dimensional Nanoscale Materials: From a Nanotechnology Perspective. *ISRN Nanotechnology* **2013**, *2013*, 21-28.
- (118) Jinschek, J. R. Advances in the Environmental Transmission Electron Microscope (ETEM) for Nanoscale in situ Studies of Gas–Solid Interactions. *Chem. Commun.* **2014**, *50*, 2696-2706.
- (119) Neville, M.; Fundamentals in XAFS, Consortium for Advanced Radiation Sources; University of Chicago: Chicago, IL, **2004**.
- (120) Baker, M. L.; Mara, M. W.; Yan, J. J.; Hodgson, K. O.; Hedman, B.; Solomon, E. I. K- and L-edge X-ray Absorption Spectroscopy (XAS) and Resonant Inelastic X-ray Scattering (RIXS) Determination of Differential Orbital Covalency (DOC) of Transition Metal Sites. *Coord Chem Rev* **2017**, *345*, 182-208.
- (121) Seyama, H.; Soma, M.; Theng, B. K. G. Chapter 2.5 - X-Ray Photoelectron Spectroscopy. Elsevier. **2013**, *5*, 161-176.
- (122) Miller, A.; Yu, L.; Blickensderfer, J.; Akolkar, R. Electrochemical Copper Metallization of Glass Substrates Mediated by Solution-Phase Deposition of Adhesion-Promoting Layers. *J. Electrochem. Soc.* **2015**, *162*, 630-634.

- (123) Zhang, Y.; Kong, X.; Xue, B.; Zeng, Q.; Liu, X.; Tu, L.; Liu, K.; Zhang, H. A Versatile Synthesis Route for Metal@SiO₂ Core–Shell Nanoparticles Using 11-Mercaptoundecanoic Acid as Primer. *J. Mater. Chem. C* **2013**, *1*, 6355-6363.
- (124) Hansen, T. W.; DeLaRiva, A. T.; Challa, S. R.; Datye, A. K. Sintering of Catalytic Nanoparticles: Particle Migration or Ostwald Ripening? *Acc. Chem. Res.* **2013**, *46*, 1720-1730.
- (125) Gangishetty, M. K.; Scott, R. W. J.; Kelly, T. L. Thermal Degradation Mechanism of Triangular Ag@SiO₂ Nanoparticles. *Dalton Trans.* **2016**, *45*, 9827-9834.

CHAPTER 2

Synthesis of Sinter-Resistant Au@Silica Catalysts Derived from Au₂₅ Clusters

In this work, the thermal stability of silica-encapsulated Au₂₅(MUA)₁₈ clusters made by sol-gel chemistry is discussed. Both TEM and EXAFS studies showed that encapsulation improves the stability towards sintering during the activation process. Also, the activity of the resulting materials for 4-nitrophenol reduction and styrene epoxidation reactions was monitored.

This chapter is a near-verbatim copy of work published in *Catal. Sci. Technol.* **2017**, 2, 272-280. All the experimental work in this article was performed by myself. Some preliminary EXAFS analysis was done with the assistance of Dr. Atal Shivhare. The first draft of the manuscript was written by myself and it was revised by Prof. Robert Scott prior to publication.

2.1. Abstract

Gold clusters exhibit remarkable catalytic activity for many reactions such as carbon monoxide oxidation, alcohol, alkene, and hydrocarbon oxidations, and reduction reactions at low temperatures. However, several previous studies show that Au clusters undergo problematic sintering at temperatures above 250 °C, which makes them unsuitable catalysts for high-temperature oxidation reactions. Here we report the coating of Au₂₅(MUA)₁₈ clusters (where MUA=mercaptoundecanoic acid) by silica to produce sinter-resistant Au@SiO₂ catalysts. The structure of the resulting materials before and after calcination at temperatures up to 650 °C was followed by TEM and Extended X-ray Absorption Fine Structure Spectroscopy (EXAFS) analyses, which showed that the Au@SiO₂ catalysts created were much more stable to sintering compared to control materials; with average particles sizes of 2.2 nm after calcination at 250 °C and just over 3 nm after calcination at 650 °C. In addition, we explored the activity of the resulting materials for the 4-nitrophenol reduction and styrene epoxidation reactions; results clearly showed that the Au surfaces are accessible for reactants and that the kinetics of 4-nitrophenol reduction was directly related to the dispersion of the Au particles, as measured via the first shell Au-Au coordination numbers by EXAFS. Styrene epoxidation results show that the Au@SiO₂ materials have excellent activity and recyclability.

2.2. Introduction

Gold catalysts, especially below 2 nm in size, have attracted much attention in catalysis owing to their well-understood structures and broad catalytic activity.¹⁻⁵ Several theoretical studies have shown that small clusters (Au₁₄, Au₂₅, Au₂₈, Au₃₈, etc.) can dissociate molecular oxygen by transferring electron charge to $2\pi^*$ of dioxygen,⁶⁻⁷ which is a crucial step in oxidation reactions. For example, ceria supported Au₂₅ clusters have shown moderate catalytic activity for carbon monoxide oxidation at room temperature.⁸ A number groups have shown that Au₂₅(SR)₁₈ (in the form of free clusters or supported clusters) are effective catalysts for oxidation and reduction reactions at moderate temperatures.⁹⁻¹⁰ However, activation of pre-synthesized clusters without destroying their integrity remains a significant challenge in the field. Many groups have shown that Au catalysts showed sintering and corresponding drops in activity for supported-Au catalysts after heating at moderate temperatures.¹¹⁻¹² For example, Haruta *et al.* observed that the Au supported on TiO₂ catalyst calcined at 500 °C showed lesser catalytic activity for CO oxidation than the catalyst calcined at 200 °C, due to sintering of Au clusters at higher calcination temperatures.¹³ The melting point of metals decreases with

particle size,¹⁴ and most metals show significant surface mobility and sintering when approaching their Tammann temperature (half the melting point of a metal, in K).¹⁵ Thermal stability of catalysts is crucial because many industrially important reactions, such as hydrocracking,¹⁶ partial oxidation,¹⁷ and complete combustion¹⁸ are carried out at higher temperatures of 300 °C to 600 °C. Thus due to their thermal instability, application of Au catalysts in industry is restricted.

Previously our group studied the thermal stability of Au₂₅(SC₃H₉)₁₈ clusters on carbon supports by EXAFS and TEM analysis which showed that at temperatures above 200 °C, thiol stabilizers start to decompose and Au clusters begin to sinter.¹⁹ The size of the Au clusters increased up to 1.9 nm and 2.1 nm after heating at 250 °C and 350 °C for 1.5h, respectively. Other groups have shown similar results on a variety of supports, particularly at high loadings.²⁰⁻²¹ Zhu *et al.* carried out thermogravimetric analysis (TGA) studies which showed that Au_n(SR)_m begins to lose its stabilizing ligands at 200 °C and decomposes completely at 250 °C.²⁰ Sintering in nanoparticle catalysts is mainly due to the agglomeration of small particles owing to their mobility on supports at a higher temperature. The agglomeration of Au (and other metal) nanoparticles can be prevented by a number of strategies. One popular strategy is to encapsulate the nanoparticles with a metal oxide shell (either core@shell or yolk@shell structures),²²⁻²³ overcoating with metal oxides via atomic vapour deposition,²⁴ or spatially isolating them in mesoporous silica²⁵ or MOF frameworks.²⁶

Nearly all attempts to make core@shell or yolk@shell clusters have involved much larger nanoparticles, which have lower metal surface areas and thus are less practical for catalysis. Two previous attempts have been made to encapsulate Au clusters with a silica shell.²⁷⁻²⁸ Pradeep *et al.* previously synthesized glutathione-protected Au₂₅ clusters encapsulated with silica shell, with many clusters embedded in a silica matrix, but did not study the thermal stability of the resulting materials.²⁷ Nandini *et al.* synthesized silica colloids containing many *ca.* 1.5 nm Au clusters stabilized by mercaptoalkylammonium chloride stabilizers.²⁸ However, while the resulting particles were catalytically active for H₂O₂ oxidation of a peroxidase substrate, the Au clusters were found to undergo significant sintering at 250 °C thermal treatments, with 90% of the particles above 3 nm in size.

In this paper, we synthesized Au₂₅(MUA)₁₈ clusters and then encapsulated the clusters with silica shells. The thermal stability of the resulting materials was probed by TEM and EXAFS analysis. TEM images of Au@SiO₂ catalysts revealed that majority of the particles are still less

than 2 nm in size after calcination at 650 °C, although there is some minor sintering of particles to 2-4 nm in size which is due to agglomeration of multiple Au₂₅(MUA)₁₈ clusters in single silica particles. In order to show that the Au clusters are much more sinter-resistant in the silica matrix, we coated Au₂₅(MUA)₁₈ clusters onto silica spheres and calcined at two different temperatures (250 °C and 650 °C) and compared the samples and their catalytic activity with Au₂₅@SiO₂ catalysts. There were dramatic differences in the catalytic activity of silica-encapsulated vs. the non-encapsulated clusters, which was due to the tremendous sintering seen for non-encapsulated clusters. For encapsulated clusters, only a small reduction of the catalytic activity for 4-nitrophenol reduction reaction over Au₂₅@SiO₂ catalysts was seen upon increased calcination temperature, which correlates well with the slight increase in EXAFS first shell Au-Au coordination numbers. Styrene epoxidation reactions using Au₂₅@SiO₂ particles show that materials calcined at 250 °C retain excellent activity and strong recyclability, while materials calcined at 650 °C significantly outperform their non-encapsulated counterparts

2.3. Materials and Methods

2.3.1. Materials

Hydrogen tetrachloroaurate (III) trihydrate (HAuCl₄·3H₂O, 99.9% on metal basis, Aldrich), 11-mercaptoundecanoic acid (MUA, 95%, Sigma-Aldrich), tetraoctylammonium bromide (TOAB, 98%, Aldrich), sodium borohydride (NaBH₄, 98%, EMD), tetraethylorthosilicate (TEOS, 98%, Aldrich), 4-nitrophenol (PNP, 99%, Alfa Aesar), tert-butyl hydroperoxide (TBHP, 70 wt% in H₂O, Sigma-Aldrich), acetonitrile (CH₃CN, 99.9% Fischer Scientific), and styrene (99%, Sigma-Aldrich) were used as received. Ammonia (30%), tetrahydrofuran (THF, high purity) and ethanol (100%) were purchased from EMD, Fischer Scientific and Commercial Alcohol respectively. Milli-Q water was used for synthesis

2.3.2. Synthesis of Au₂₅(MUA)₁₈ clusters

The synthetic procedure for Au₂₅(MUA)₁₈ clusters has been documented previously by our group.²⁹ In a typical synthesis, TOAB (333.5 mg, 1.2 eq) was added to HAuCl₄·3H₂O solution (200.0 mg) in 20 ml THF in a round bottom flask. The solution was stirred until it turned from yellow to orange-red. After that MUA (545.9 mg, 5 eq in 5 mL THF) was added to the flask and the solution was stirred until it became colourless. The solution was then cooled using an ice bath followed by the addition of ice-cold NaBH₄ (75.66 mg, 4 eq. in 2 mL water) dropwise

and the solution was monitored using UV-Vis spectroscopy. The addition of NaBH_4 was continued until the characteristic absorption peaks of $\text{Au}_{25}(\text{MUA})_{18}$ clusters were seen by UV-Vis spectroscopy. The solution was then centrifuged at 10,000 rpm for 2 min, and the precipitate of larger particles was discarded. The remaining $\text{Au}_{25}(\text{MUA})_{18}$ cluster solution in THF was then cooled in an ice bath and additional NaBH_4 (28.38 mg, 1.5 eq in 2 mL water) was added dropwise until a brown precipitate was obtained. The residue was centrifuged and washed with THF twice, followed by re-dissolution in water. $\text{Au}_{25}(\text{MUA})_{18}$ clusters were precipitated out with a few drops of dilute acetic acid with an approximate pH of 3. The precipitate was washed with water twice and redissolved in THF. One drop of NaBH_4 (1.5 eq in 2 mL water) was added to the THF solution, which re-precipitated out $\text{Au}_{25}(\text{MUA})_{18}$ clusters. The precipitate was then collected using centrifugation and washed with THF. 10 mg of dried $\text{Au}_{25}(\text{SR})_{18}$ clusters were dispersed in Millipore water (6 mL) and diluted with 25 mL ethanol.

2.3.3. Synthesis of silica encapsulated $\text{Au}_{25}(\text{MUA})_{18}$ clusters

The silica encapsulation strategy is depicted in Scheme 2.1. In order to minimize the formation of multiple clusters in a single silica shell, 1.0 ml of the above $\text{Au}_{25}(\text{MUA})_{18}$ cluster solution was diluted with 10 mL ethanol. Then the diluted $\text{Au}_{25}(\text{MUA})_{18}$ clusters and ammonia (1.0 mL) were added to a solution of TEOS (10 μL) in ethanol (10 mL) dropwise under moderate stirring. After 12 h of stirring, the silica encapsulated clusters are labeled as $\text{Au}_{25}@\text{SiO}_2$ in this manuscript for brevity. The $\text{Au}_{25}@\text{SiO}_2$ materials were dried at 100 $^\circ\text{C}$ and then calcined at different temperatures 250 $^\circ\text{C}$, 350 $^\circ\text{C}$, 450 $^\circ\text{C}$, 550 $^\circ\text{C}$, and 650 $^\circ\text{C}$ for 3 h in a stream of air, to give the resulting $\text{Au}@\text{SiO}_2$ materials.



Scheme 2.1: General scheme for the synthesis of silica encapsulated $\text{Au}_{25}(\text{MUA})_{18}$ clusters.

2.3.4. Synthesis of Au₂₅(MUA)₁₈ clusters on silica spheres (control samples)

Synthesis of silica spheres: To synthesize silica spheres, we followed the same procedure as above, without Au₂₅(MUA)₁₈ clusters. In a typical synthesis, 6 mL water is diluted with 25 mL ethanol, and then 1 mL of a water/ethanol mixture is added into the vial and the whole mixture was diluted with 10 mL ethanol. Then this very diluted water/ethanol mixture and ammonia (1 mL) was added to the TEOS (10 μ L) and ethanol (10 mL) solution dropwise under moderate stirring. The solution was then kept stirring for 12 h, then collected by centrifugation and washed several times with ethanol and water.

Deposition of Au₂₅(MUA)₁₈ clusters on silica spheres: 1.0 ml of the aqueous Au₂₅(MUA)₁₈ cluster solution was added to the dried silica sphere sample and stirred. After 2 h stirring, the solvent was evaporated using a rotary evaporator followed by drying on a Schlenk line apparatus. The metal loading was maintained as 2.0 wt% Au. Au₂₅(MUA)₁₈ clusters supported on silica spheres were dried at 100 °C and then calcined at two different temperatures 250 °C and 650 °C for 3 h in a stream of air. The non-encapsulated catalysts have been labeled as Au₂₅/SiO₂.

2.3.5. Characterization

UV-Vis absorption spectra of the Au₂₅(MUA)₁₈ clusters were analyzed using a Varian Cary 50 Bio UV-Vis Spectrometer. The morphology of the Au₂₅@SiO₂ materials was analyzed by a HT7700 TEM operating at 100 kV. The size of 200 particles was measured for each sample using ImageJ software to calculate average particle sizes and standard deviations and create size distribution histograms.³⁰ Extended X-ray Absorption Fine Structure (EXAFS) spectroscopic analysis was performed at HXMA beamline 061D-1 (energy range 5-30 keV, resolution 1×10^{-4} $\Delta E/E$) at the Canadian Light Source. The storage ring electron energy and ring current were 2.9 GeV and 250mA, respectively. All data was collected in transmission mode. The energy for the Au-L₃ edge (11919 eV) was selected by using a Si (111) double crystal monochromator with Rh-coated 100 nm long KB mirror. Higher harmonics were removed by detuning the double crystal monochromator. Data fitting was carried out using the Demeter software package.³¹ In order to fit the data, the amplitude reduction factor was fixed at 0.9 for all the data, which was the value obtained from fitting of the Au foil data. Metal loadings of Au₂₅@SiO₂ and Au₂₅/SiO₂ were analyzed by a Varian Spectra AA 55 Atomic Absorption Spectroscope. Nitrogen adsorption/desorption isotherms were collected by using a

Micromeritics ASAP2020 system (Norcross GA). The BET model was used to calculate the specific surface area of catalysts.

2.3.6. Catalytic activity for 4-nitrophenol reduction

2.0 mL of 0.10 mM 4-nitrophenol and 1.0 mg Au₂₅@SiO₂ were mixed in a quartz cuvette and the UV-Vis spectra were collected. After adding ice cold 0.5 mL 0.1 M NaBH₄ in water to the cuvette, the spectrum was analysed immediately, to get the initial concentration of 4-nitrophenolate, and the progress of the reaction was monitored at 2 min time intervals. Catalytic results were reproduced several times for each sample, with errors <5%.

2.3.7. Styrene epoxidation

Catalytic tests were carried out in a 100 mL round bottom flask fitted with a reflux condenser. 20 mg catalyst, 920 µL styrene, and 2.0 mL of the TBHP solution were added to 5.0 mL acetonitrile and then kept for stirring for 24 h at 82 °C.³² The substrate to Au mole ratio is 3920:1. Products were analysed by a gas chromatograph (7890A, Agilent Technologies) equipped with a HP-5 column using a flame ionization detector. For recyclability tests, the catalyst was removed from the catalytic mixture by centrifugation, washed with acetone, and dried at 50 °C before reuse.

2.4. Results and discussion

UV-Vis absorption studies of the as-synthesized Au₂₅(MUA)₁₈ clusters in water/ethanol mixtures show three peaks at 680 nm, 446 nm, and 398 nm which are attributed to HOMO – LUMO transitions as shown in Figure 2.1.³³ The UV-Vis spectra give clear evidence for the formation of Au₂₅ clusters. Previously we have also used MALDI-MS analysis to further strengthen this assignment.²⁹ The clusters were copiously purified by taking advantage of the poor solubility of the carboxylate-terminated clusters in THF in basic conditions as well as poor solubility in water under acidic conditions. TEM images of the Au₂₅(MUA)₁₈ clusters show cluster cores with a size of ca. 1 nm in agreement with previous results.³⁴

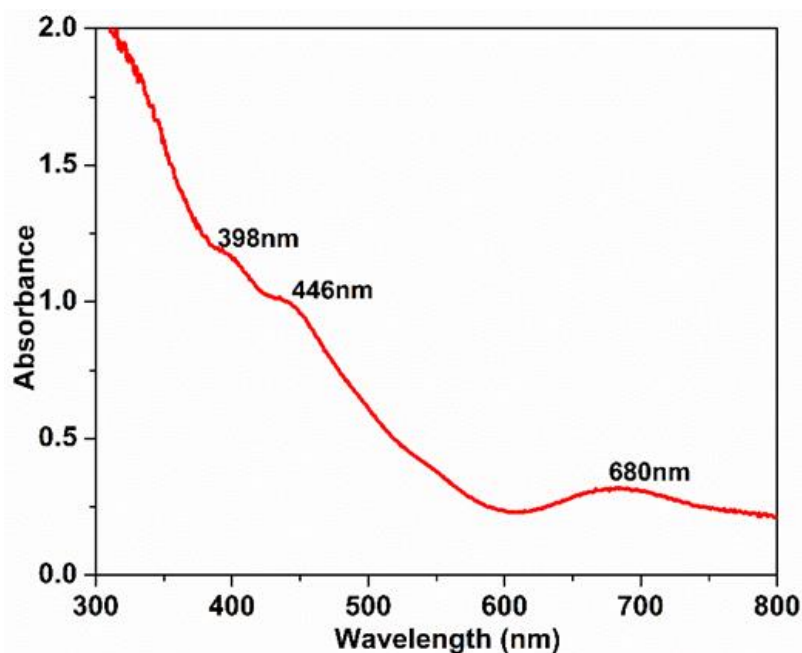


Figure 2.1: UV-Vis spectra of Au₂₅(MUA)₁₈ clusters.

The Au₂₅(MUA)₁₈ clusters were then coated with silica via sol-gel synthesis using NH₃ as a catalyst. Au₂₅ cluster solutions were significantly diluted before silica coating to minimize the number of clusters per silica sphere in the final materials and control the final metal loading. Figure 2.2 shows TEM images of the as-synthesized silica coated Au₂₅(MUA)₁₈ clusters. The TEM images suggest that the clusters are encapsulated in the silica matrix, stronger evidence for encapsulation comes from comparisons of calcinations of encapsulated clusters vs. control samples shown below. It should be noted that many silica spheres contain multiple clusters, although some particles seem to have only a single Au₂₅(MUA)₁₈ cluster. From TEM analysis, the average silica sphere diameter is 40 nm and clusters are *ca.* 1.1 ± 0.3 nm in size (the slightly larger sizes are likely an artifact of the inability to focus on each individual particle in the three-dimensional silica spheres, causing some particles to appear larger as they are out of focus). The Au loading in silica matrix was maintained as 2.0 wt% which was confirmed by Atomic Absorption Spectroscopy (AAS). Control samples were also made which consisted of Au₂₅(MUA)₁₈ clusters decorated on the surface of silica spheres, as shown in Figure 2.3a.

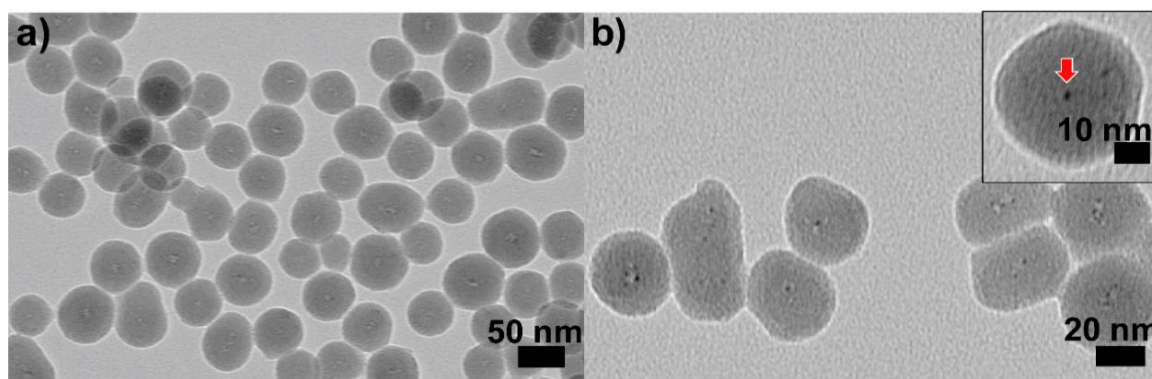


Figure 2.2: a) & b) TEM images of as-synthesized $\text{Au}_{25}(\text{MUA})_{18}$ clusters (inset of b); enlarged image).

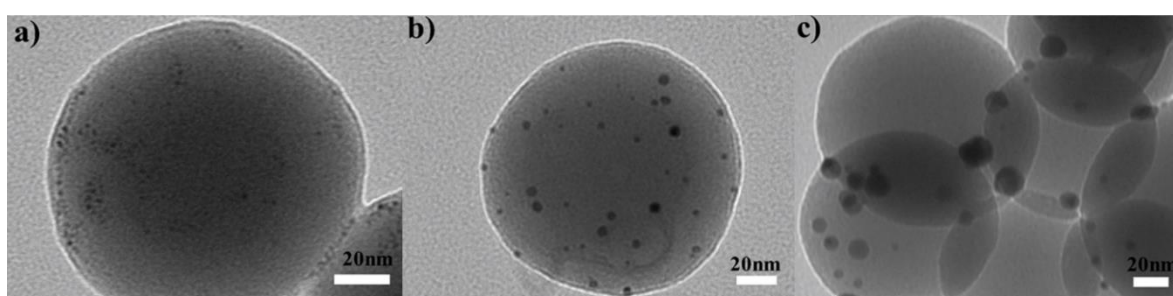


Figure 2.3: TEM images of $\text{Au}_{25}/\text{SiO}_2$ catalysts a) as-synthesized, b) calcined at 250 °C and c) calcined at 650 °C.

A major issue with many Au systems is the propensity for Au clusters or nanoparticles to sinter at moderate calcination temperatures; previous studies have shown that temperatures of at least 250 °C are needed to remove thiol stabilizers from the Au cluster surfaces, with even higher temperatures needed to completely oxidize the disulphide biproducts.¹⁹ To investigate the sinter-resistance of the $\text{Au}_{25}@\text{SiO}_2$ catalysts, they were calcined at temperatures up to 650 °C followed by TEM analysis. Figure 2.4 shows TEM images of the samples upon sintering at temperatures between 250 °C and 650 °C; very little growth in the average particle size was seen (2.2 ± 1.0 nm at 250 °C and 3.2 ± 2.0 nm at 650 °C). Particle size histograms showed a high population of <2 nm sized particles even after calcination at higher temperatures (Figure 2.5a). As shown in Figures 2.3b and 2.3c, control samples consisting of $\text{Au}_{25}(\text{MUA})_{18}$ clusters on the surface of silica spheres showed a much greater degree of sintering, with average particle sizes of 3.2 ± 1.7 nm at 250 °C and 15.5 ± 10.0 nm at 650 °C. The particle size histogram for the non-encapsulated control samples is shown in Figure 2.5b, and is quite distinct from the $\text{Au}@\text{SiO}_2$ histogram in Figure 2.5a, with a number of particles > 6 nm in size even after calcination at 250 °C, and nearly all particles > 5 nm in size after calcination at 650 °C. Thus,

it is quite evident that the encapsulation of the Au₂₅ clusters in silica greatly promotes their stability to sintering at higher temperatures.

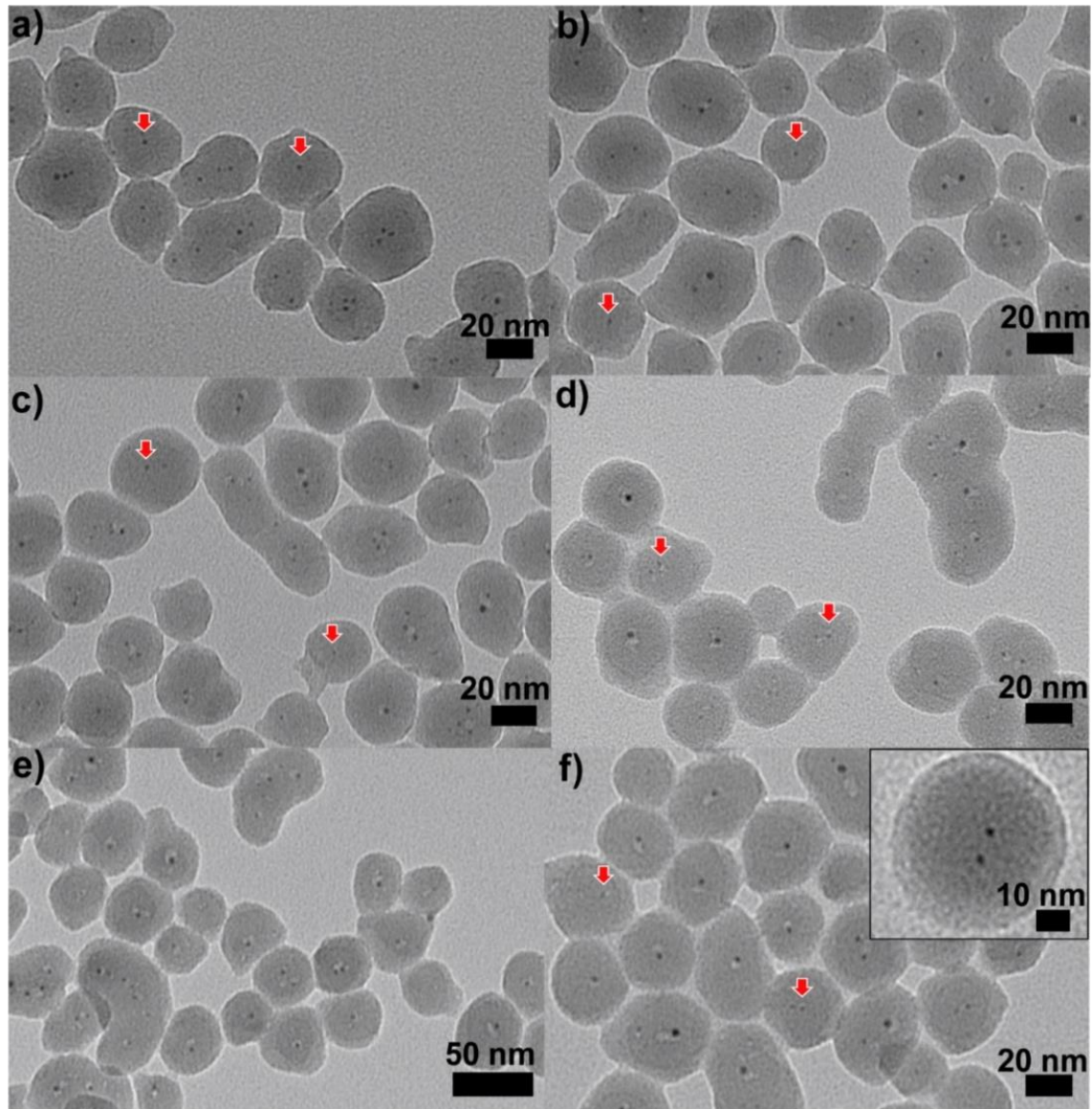


Figure 2.4: TEM images of Au₂₅@SiO₂ calcined at a) 250 °C, b) 350 °C, c) 450 °C, d) 550 °C, e) and f) 650 °C (inset; enlarged image).

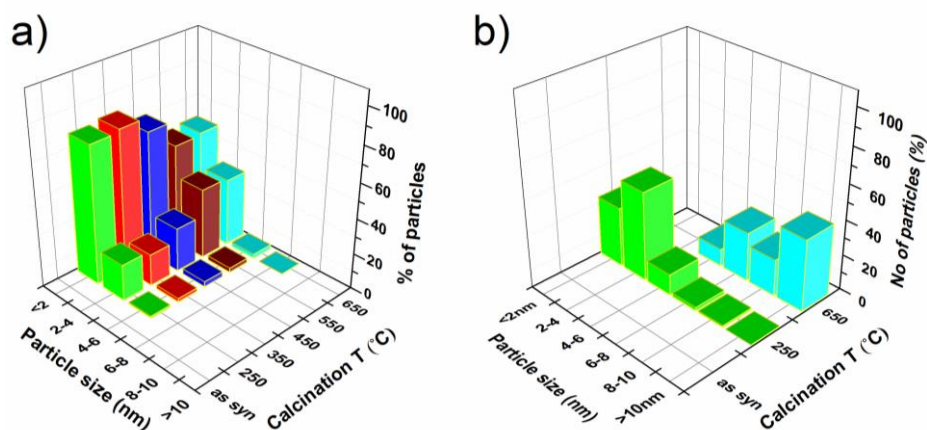


Figure 2.5: Histogram of Au@SiO₂ catalysts calcined at different temperatures.

The Au₂₅@SiO₂ materials were also examined by nitrogen adsorption/desorption isotherms. The BET surface area of the catalyst increased from 23 m²/g to 70 m²/g after calcination at 250 °C; we believe the resulting porosity was caused by the removal of some of the MUA as well as residual solvent from the silica spheres. Importantly, the silica spheres have some porosity, which may allow for catalytic accessibility of the Au clusters.

To further understand changes to the Au clusters before and after calcination, Au L₃-edge EXAFS analysis was carried out in transmission mode on the Hard X-ray Microanalysis beamline (HXMA) at the Canadian Light Source (CLS). Figure 2.6 shows the Au L₃ edge EXAFS k-space and phase-corrected R-space spectra of the as-synthesized Au₂₅(MUA)₁₈@SiO₂ clusters prior to calcination. The black line represents the experimental Fourier Transformed EXAFS spectra, and the red line represents the simulated EXAFS fit for Au₂₅(MUA)₁₈ clusters. Others have previously collected X-ray crystallographic data of Au₂₅(SR)₁₈ clusters which have shown that they consist of a core-shell morphology, in which the core is composed of an Au₁₃ icosahedron, in which the central atom is surrounded by 12 Au atoms while the shell consists of six S-Au-S-Au-S staple motifs.³⁵ Twelve out of the twenty faces of the icosahedron are surrounded by six staple motifs, with sulfur atoms directly attached to 12 Au atoms of the icosahedron core. A multishell fitting approach which has previously been documented by Zhang's group was used to fit the Au-S and three Au-Au contributions of the clusters.³⁶ In order to fit the data, we first fit the Au-S contribution by using Au-S model data obtained from the standard Au₂₅(SR)₁₈ structure.³⁶⁻³⁷ After fitting the parameters for Au-S contribution, we fixed those values followed by fitting all first shell Au-Au coordination modes (there are three Au-Au first shell interactions: the first two involve Au atoms in core and the third involves Au staple atoms). Coordination number (CN) values for all Au-Au

contributions were fixed based on the crystal structure of the clusters. The final EXAFS fitting parameters are shown in Table 2.1. The Au-S bond length was found to be 2.31(1) Å which matches well with crystallographic data of Au₂₅L₁₈ clusters in which L=phenylethanethiol.³⁸ For the Au first shell fit the Au-Au (core) R value of 2.76(2) Å is attributed to the distance between the central Au atom and the surface Au atom of the icosahedron core, and some short bonds between adjacent surface Au atoms. Second Au-Au contribution is observed at 2.91(6) Å that is due to the bond distance between the 12 surface Au atoms of the icosahedron (Au-Au(surf)). The last Au-Au bond length, 3.32(1) Å is attributed to the distance between the surface Au atoms and the staple Au atoms. These values agree well with those seen for other Au clusters,¹⁹ and thus, the EXAFS data fitting clearly shows that the basic core structure of Au₂₅(MUA)₁₈ clusters are similar to that of Au₂₅ clusters using other thiolate ligands.

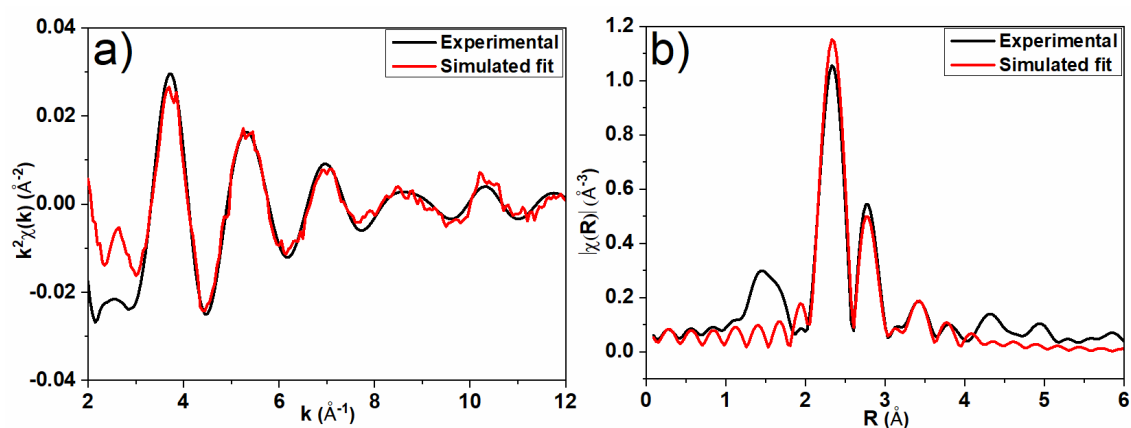


Figure 2.6: Au L₃ edge EXAFS fitting in a) k space and b) phase-corrected R space of as synthesized Au₂₅(MUA)₁₈@SiO₂ clusters.

Table 2.1: EXAFS fitting parameters of as synthesized Au₂₅(MUA)₁₈@SiO₂ clusters

Type	CN	R/Å	σ ² /Å ²	E _o Shift(eV)	R (%)
Au-S	1.3	2.31(1)	0.001(1)	2.5(3)	1.9
Au-Au(core)	1.44	2.76(2)	0.002(2)	2.5(3)	
Au-Au(surf)	1.92	2.91(6)	0.01(1)	2.5(3)	
Au-Au(staple)	2.88	3.32(1)	0.01(1)	2.5(3)	

The Au₂₅@SiO₂ materials calcined at different temperatures were also analyzed by EXAFS spectroscopy at the Au L₃ edge. Phase-corrected R-space EXAFS spectra are shown in Figure 2.7, while fitted data are found in Table 2.2. Individual k and phase-corrected R space spectra of Au₂₅@SiO₂ calcined at different temperatures are shown in Figure 2.8. Au-S contributions are seen around 2.3 Å, while Au-Au contributions are present between 2.8 Å and 3.2 Å. An fcc Au model was used for fitting the single shell Au-Au fit, as some growth in cluster sizes was seen which prevented the use of the previous Au₂₅ model. After calcination at 250 °C, an Au-S contribution was not observed in the data, which suggests that thiol stabilizers are completely removed from the gold surface, which is consistent with previous work using other thiolate ligands.¹⁹ After calcination at 250 °C, the first shell coordination number for the Au-Au (N_{Au-Au}) contribution is 9.6(7) which suggest that the average number of atoms per particle is ~300, which works out to a *ca.* 2.1 nm average particle size.³⁹ As many of the silica spheres contain multiple Au clusters, this is consistent with some sintering of clusters within silica spheres, and is also consistent with TEM analysis above. EXAFS data suggest that on average *ca.* 12 clusters sinter together by 250 °C. As the calcination temperature increases, the average N_{Au-Au} slightly increases and the N_{Au-Au} of catalysts calcined at 350 °C, 450 °C, 550 °C, and 650 °C are 9.8(7), 10.0(7), 10.2(7), and 10.5(6), respectively, which suggests that the average number of atoms in the Au particles grows slowly at higher calcination temperatures. Thus, EXAFS results suggest that there is some sintering within particles, albeit from TEM analyses there are still a large number of <2 nm particles at 650 °C.

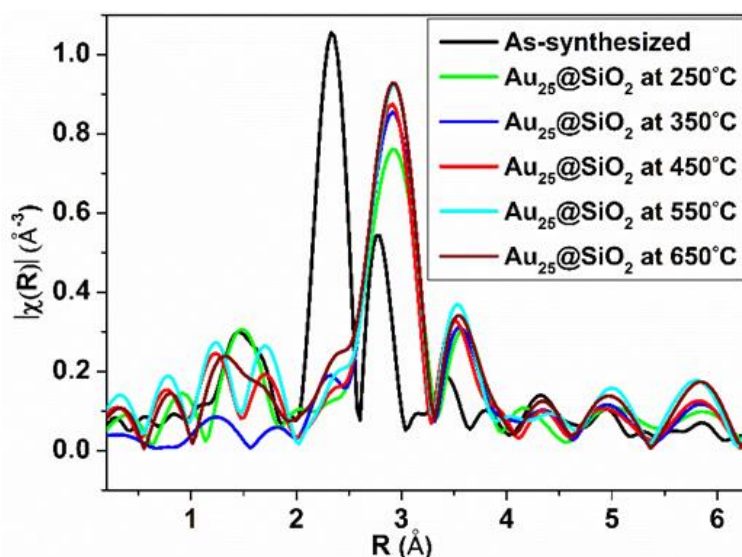


Figure 2.7: Au-L₃ edge EXAFS data in phase-corrected R-space of Au₂₅@SiO₂ catalysts calcined at different temperatures.

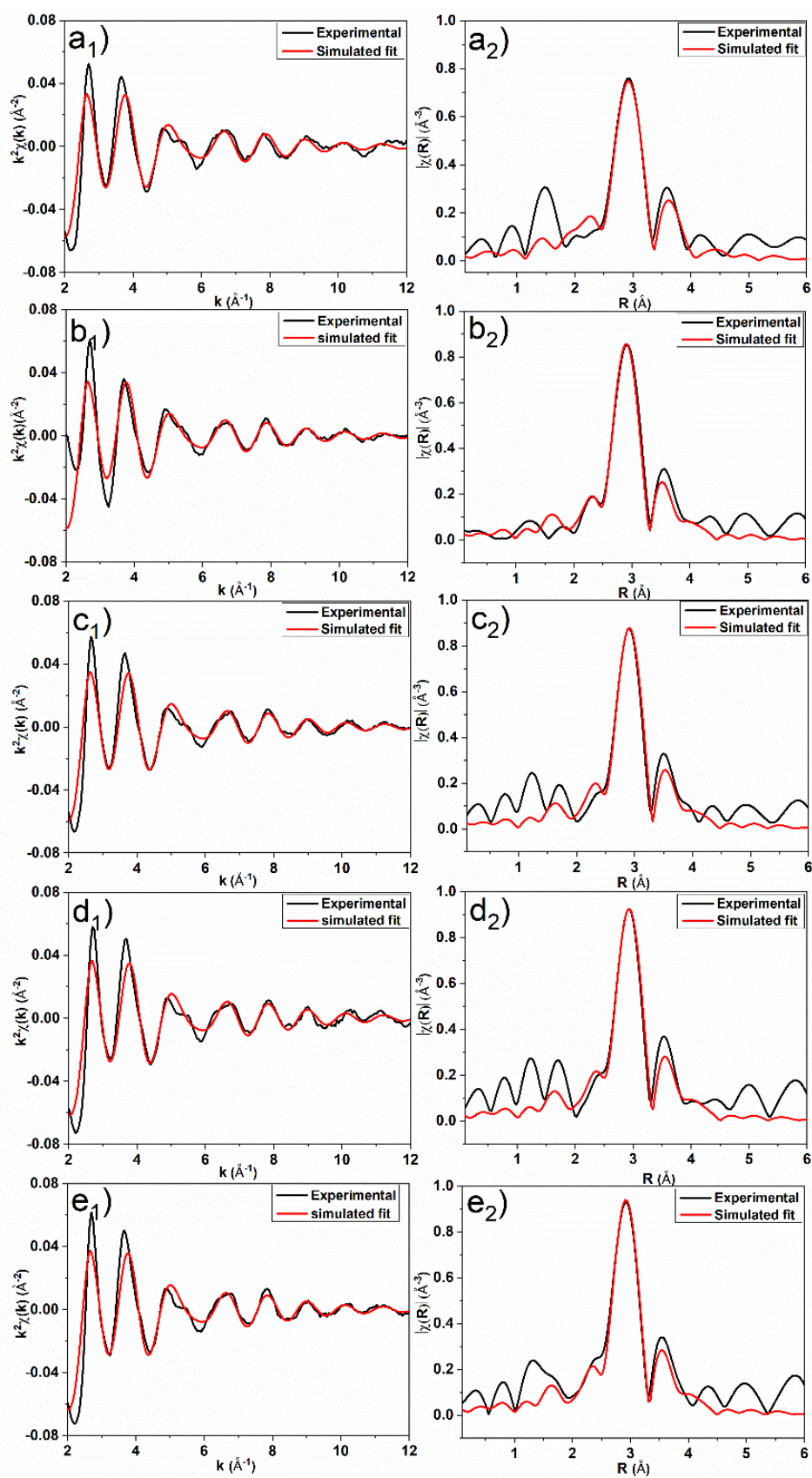


Figure 2.8: Au-L₃ edge EXAFS fitting data in k- (left) and R-space of Au@SiO₂ calcined at a₁&a₂) 250 °C, b₁&b₂) 350 °C, c₁&c₂) 450 °C, d₁&d₂) 550 °C, and e₁&e₂) 650 °C.

Table 2.2 : EXAFS fitting parameters of Au₂₅@SiO₂ clusters calcined at different temperatures.

Catalyst	CN (Au-Au)	R/ Å	σ^2 /Å ²	E ₀ Shift (eV)	R (%)
Au ₂₅ @SiO ₂ calcined at 250 °C	9.6(7)	2.84(1)	0.010(2)	6.1(8)	1.8
Au ₂₅ @SiO ₂ calcined at 350 °C	9.8(7)	2.843(8)	0.010(1)	5.7(7)	1.3
Au ₂₅ @SiO ₂ calcined at 450 °C	10.0(7)	2.851(7)	0.009(1)	5.6(7)	1.7
Au ₂₅ @SiO ₂ calcined at 550 °C	10.2(7)	2.860(8)	0.009(1)	6.7(7)	1.8
Au ₂₅ @SiO ₂ calcined at 650 °C	10.5(6)	2.856(6)	0.009(1)	6.5(5)	1.5

One of the major concerns upon coating clusters or nanoparticles with silica overlayers is whether or not the metal surfaces are still catalytically accessible. To probe whether the Au clusters could be accessed prior to and after sintering the Au₂₅@SiO₂ materials, the materials were probed as catalysts for the reduction of 4-nitrophenol. The catalytic activity for the 4-nitrophenol reduction reaction is an excellent gauge of the catalytically accessible surface area of metallic catalysts.⁴⁰ A typical UV-Vis spectra reaction profile is shown in Figure 2.9; the original solution has a peak at 317 nm which corresponds to 4-nitrophenol.⁴¹ After adding NaBH₄ to the solution, the peak shifted to 400 nm which indicates the deprotonation of 4-nitrophenol to form nitrophenolate. The intensity of peak due to 4-nitrophenolate decreased as a function of time and a new peak appeared at 300 nm, which has been previously attributed to the formation of 4-aminophenol.⁴² In the absence of Au₂₅@SiO₂ catalysts, no activity for nitrophenol reduction was seen. Table 2.3 shows the rate constants for 4-nitrophenolate reduction reactions, which are calculated using pseudo-first-order kinetics.⁴³⁻⁴⁴ All materials showed a linear relationship between $\ln[C_t]/[C_0]$ and reaction time (min), as shown in Figure 2.9f. As the calcination temperature increases, the rate constants for the 4-nitrophenol reduction reaction was slightly reduced from $1.1 \times 10^{-1} \text{ min}^{-1}$ at 250 °C to $1.78 \times 10^{-2} \text{ min}^{-1}$ at 650 °C, which is likely due to the small increase in Au particle size, and thus decrease in catalytically available surface area. Figure 2.10 shows the correlation of reaction rate constant with the coordination number of Au as determined by EXAFS at each calcination temperature; a strong relationship was seen between $N_{\text{Au-Au}}$ and the rate constant for 4-nitrophenol reduction. There is a drop in activity beyond calcination temperatures of 350 °C that cannot be explained by

coordination number changes alone; this may be due to partial condensation of the silica matrix which leads to mass-transfer issues.

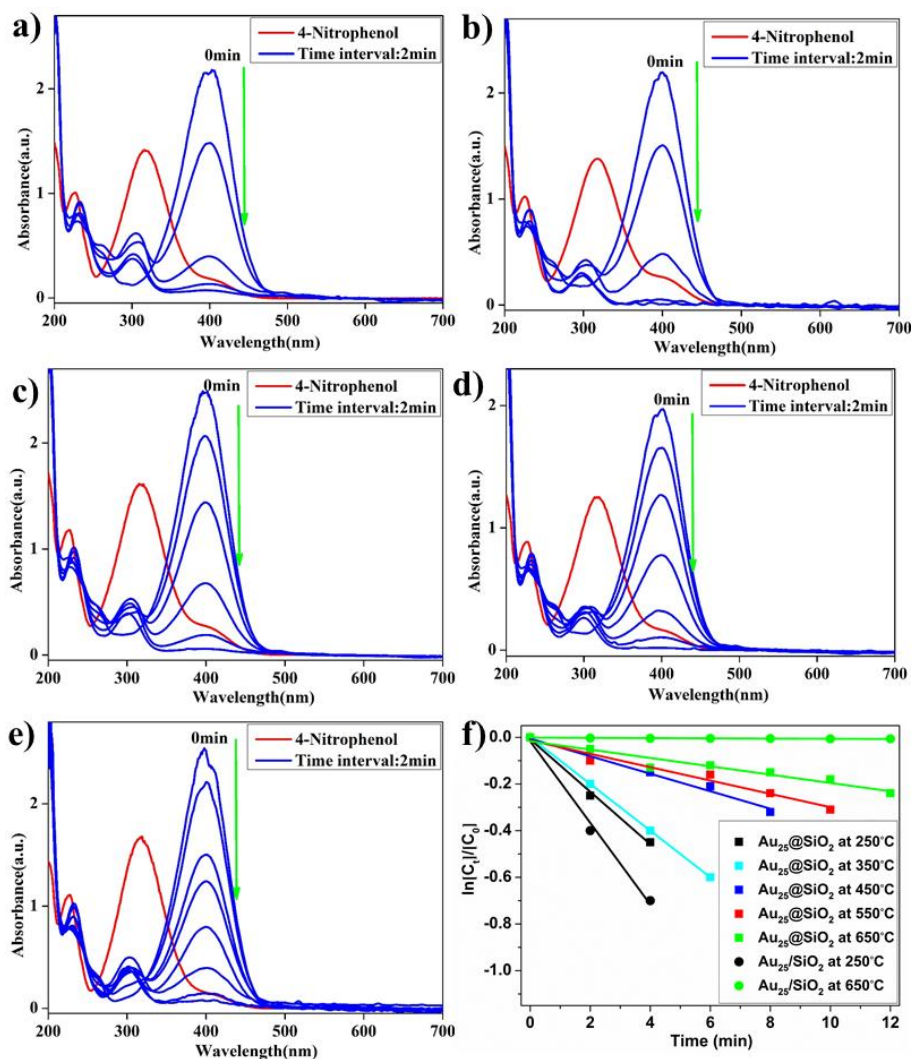


Figure 2.9: Catalytic activity for 4-nitrophenol reduction reaction over Au@SiO₂ calcined at a) 250 °C, b) 350 °C, c) 450 °C, d) 550 °C, and e) 650 °C, and f) Plot of $\ln[C_t]/[C_o]$ as a function of reaction time in min.

Table 2.3: Rate constants k (min⁻¹) for 4-nitrophenol reduction reaction

Catalyst	k (min ⁻¹)
Au ₂₅ @SiO ₂ calcined at 250 °C	1.1×10^{-1}
Au ₂₅ @SiO ₂ calcined at 350 °C	1.0×10^{-1}
Au ₂₅ @SiO ₂ calcined at 450 °C	3.75×10^{-2}
Au ₂₅ @SiO ₂ calcined at 550 °C	2.80×10^{-2}
Au ₂₅ @SiO ₂ calcined at 650 °C	1.78×10^{-2}
Au ₂₅ /SiO ₂ calcined at 250 °C	1.75×10^{-1}
Au ₂₅ /SiO ₂ calcined at 650 °C	4.82×10^{-4}

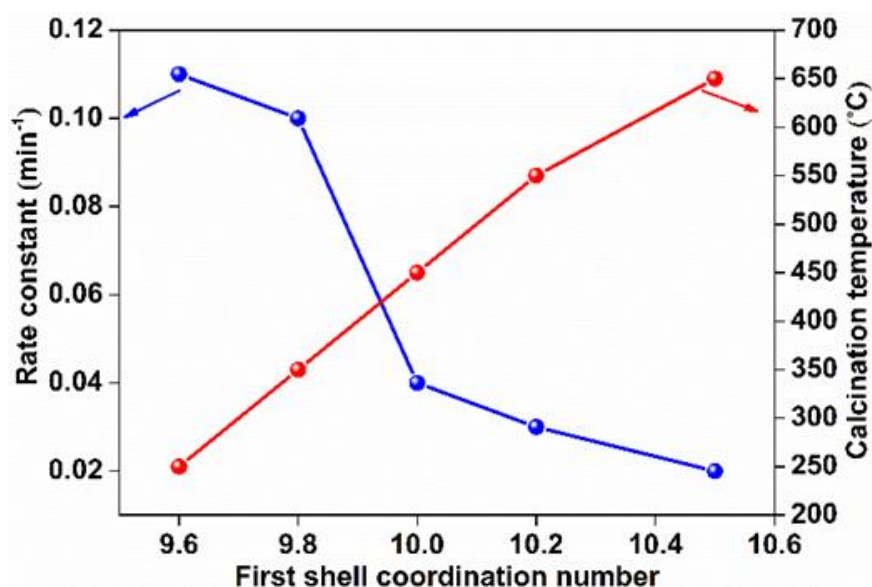


Figure 2.10: Plot of first shell coordination number of Au@SiO₂ catalysts vs rate constant for 4-nitrophenol reduction reaction and calcination temperature.

Control samples in which silica spheres were decorated with Au₂₅(MUA)₁₈ clusters on the surface, followed by calcination at 250 °C and 650 °C were also examined (Figure 2.11). The encapsulated clusters (*e.g.* Au₂₅@SiO₂) showed a slightly lower activity than the Au₂₅/SiO₂ control samples upon calcination at 250 °C; this is likely due to mass transfer issues caused by the silica shell.⁴⁵ The rate constant for the control samples for 4-nitrophenol reduction dropped from $1.75 \times 10^{-1} \text{ min}^{-1}$ for samples treated at 250 °C to $4.82 \times 10^{-4} \text{ min}^{-1}$ for samples treated at 650 °C, which was due to the tremendous sintering of Au clusters on the surface of the silica support as shown earlier by TEM. The Au₂₅@SiO₂ sample calcined at 650 °C had a rate constant that was over 35 times that of the control samples treated at the same temperature. Thus, this cluster encapsulation strategy allows for the formation of well-dispersed, supported-Au catalysts that can withstand high temperature operating and/or calcination conditions. We do note that for mild catalytic reactions such as CO oxidation, Au₂₅ clusters can be activated under mild thermal conditions without significant adverse sintering of the Au cluster catalysts.⁴⁶

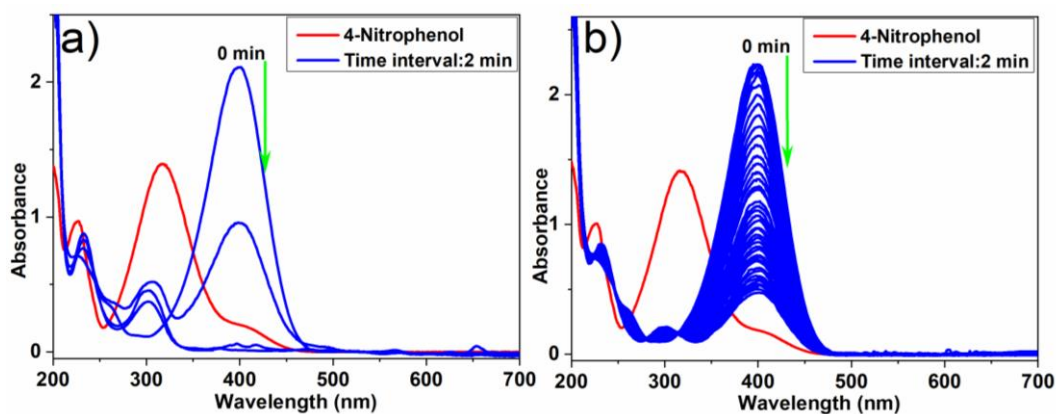


Figure 2.11: Catalytic activity for 4-nitrophenol reduction reaction over Au/SiO₂ calcined at a) 250 °C, and b) 650 °C.

Results for styrene epoxidation reactions over Au₂₅@SiO₂ and Au₂₅/SiO₂ catalysts calcined at two different temperatures (250 °C and 650 °C) are shown in Table 2.4. The Au₂₅@SiO₂ catalyst calcined at 250 °C catalyst showed 70.0% conversion for this reaction, with a selectivity towards styrene oxide (SO) of 92.3% (the other product is benzaldehyde (BA)). This is higher than selectivities seen for larger Au particles,³² but in line with that reported for Au₂₅ clusters supported on hydroxyapatite (HAP) by others.⁴⁷ After calcination at 650 °C, conversion was slightly reduced to 62.3% with similar selectivity for SO, which is consistent with the drop in catalytic activity seen in the 4-nitrophenol reduction reactions above due to the slightly lower surface area of catalysts calcined at higher temperatures. Recyclability of Au₂₅@SiO₂ catalysts calcined at 250 °C was investigated; after five cycles the catalyst showed the same activity for the reaction. This is significant, as others have shown that Au clusters supported on HAP or silica showed slight deactivation over multiple cycles.²⁰ Au₂₅@SiO₂ catalysts calcined at 250 °C and 650 °C had average turnover frequencies (TOFs) of 116±9 h⁻¹ and 103±10 h⁻¹, respectively. These catalysts also show excellent catalytic activity for the styrene epoxidation reaction, in line with the best results in the literature.^{32,47-49} For example, Tsukada *et al.* reported that Au₂₅/HAP had an average TOF of 114 h⁻¹.⁴⁷ Wu *et al.* demonstrated that silica supported Au nanoparticles with average particle size 6.4 nm had an average TOF of 99.4 h⁻¹.³² Non-encapsulated catalysts (Au₂₅/SiO₂) calcined at 250 °C had a slightly higher conversion of styrene, with very slightly higher selectivity for styrene oxide (>93%); however, conversions dropped to 15.1% upon calcination of the control samples at 650 °C. These results are also consistent with 4-nitrophenol reduction results, such that non-encapsulated catalysts show slightly higher activities at moderate calcination temperatures due to the absence of mass-transfer issues, while higher calcination temperatures lead to tremendous sintering and a

corresponding loss of catalyst surface area and activity. In order to compare TONs of the catalysts, we also took total surface Au atoms into account. When accounting for the relative surface areas; samples calcined at 650 °C showed higher adjusted TONs compared to Au₂₅@SiO₂ calcined at 250 °C. This may be due to the removal of disulphide by-products from the catalyst at higher temperatures.

Table 2.4: Conversion (%) and TONs for styrene epoxidation reactions over 24 h.

Catalyst	Conversion %	Selectivity		TON
		SO(%)	BA(%)	
Au ₂₅ @SiO ₂ calcined at 250 °C	70.0	92.3	7.6	2800
Au ₂₅ @SiO ₂ calcined at 650 °C	62.3	91.8	8.3	2500
Au ₂₅ /SiO ₂ calcined at 450 °C	75.6	93.7	6.3	3000
Au ₂₅ /SiO ₂ calcined at 550 °C	15.1	93.4	6.6	600

TON= Moles of reactant converted / moles of Au

2.5. Conclusions

Herein we have synthesized silica encapsulated Au₂₅(MUA)₁₈ clusters, followed by calcination to give active catalysts which have minimal sintering of the Au clusters. To the best of our knowledge, sinter-resistant Au₂₅(MUA)₁₈ clusters encapsulated with silica shells have not been documented elsewhere. Even after calcination at 650 °C, the majority of the particles are below 2 nm. Catalytic studies for 4-nitrophenolate reduction reaction and styrene epoxidation reactions over the catalysts show that the active sites on the gold surface are accessible to the reactants. As the calcination temperature increases, the rate constant of the reaction slightly decreased, which is likely due to the increased coordination number of gold atoms, as individual clusters within the silica spheres sinter to form slightly larger particles. Finally, Au₂₅@SiO₂ catalysts calcined at 250 °C showed remarkable catalytic activity, selectivity and recyclability for styrene epoxidation reactions.

2.6. References

- (1) Zhu, Y.; Qian, H.; Drake, B. A.; Jin, R. Atomically Precise Au₂₅(SR)₁₈ Nanoparticles as Catalysts for the Selective Hydrogenation of α,β -Unsaturated Ketones and Aldehydes. *Angew. Chem. Int. Edit.* **2010**, *49*, 1295-1298.
- (2) Sreedhala, S.; Sudheeshkumar, V.; Vinod, C. P. Oxidation Catalysis by Large Trisuboctahedral Gold Nanoparticles: Mind the Step! *Catal. Today.* **2015**, *244*, 177-183.
- (3) Lopez-Acevedo, O.; Kacprzak, K. A.; Akola, J.; Häkkinen, H. Quantum Size Effects in Ambient CO Oxidation Catalysed by Ligand-Protected Gold Clusters. *Nat. Chem.* **2010**, *2*, 329-334.
- (4) Haruta, M.; Daté, M. Advances in the Catalysis of Au Nanoparticles. *Appl. Catal. A: Gen.* **2001**, *222*, 427-437.
- (5) Zhao, Y.; Mpela, A.; Enache, D. I.; Taylor, S. H.; Hildebrandt, D.; Glasser, D.; Hutchings, G. J.; Atkins, M. P.; Scurrill, M. S. Study of Carbon Monoxide Hydrogenation Over Supported Au Catalysts. *Stud. Surf. Sci. Catal.* **2007**, *1*, 141-151.
- (6) Yoon, B.; Häkkinen, H.; Landman, U. Interaction of O₂ with Gold Clusters: Molecular and Dissociative Adsorption. *J. Phys. Chem. A* **2003**, *107*, 4066-4071.
- (7) Sanchez, A.; Abbet, S.; Heiz, U.; Schneider, W. D.; Häkkinen, H.; Barnett, R. N.; Landman, U. When Gold Is Not Noble: Nanoscale Gold Catalysts. *J. Phys. Chem. A* **1999**, *103*, 9573-9578.
- (8) Nie, X.; Qian, H.; Ge, Q.; Xu, H.; Jin, R. CO Oxidation Catalyzed by Oxide-Supported Au₂₅(SR)₁₈ Nanoclusters and Identification of Perimeter Sites as Active Centers. *ACS Nano.* **2012**, *6*, 6014-6022.
- (9) Zhu, Y.; Qian, H.; Zhu, M.; Jin, R. Thiolate-Protected Au_n Nanoclusters as Catalysts for Selective Oxidation and Hydrogenation Processes. *Adv. Mater.* **2010**, *22*, 1915-1920.
- (10) Shivhare, A.; Ambrose, S. J.; Zhang, H.; Purves, R. W.; Scott, R. W. J. Stable and Recyclable Au₂₅ Clusters for the Reduction of 4-nitrophenol. *Chem. Commun.* **2013**, *49*, 276-278.

- (11) Yang, C.M.; Kalwei, M.; Schüth, F.; Chao, K. J. Gold Nanoparticles in SBA-15 Showing Catalytic Activity in CO Oxidation. *Appl. Catal. A: Gen.* **2003**, *254*, 289-296.
- (12) Veith, G. M.; Lupini, A. R.; Rashkeev, S.; Pennycook, S. J.; Mullins, D. R.; Schwartz, V.; Bridges, C. A.; Dudney, N. J. Thermal Stability and Catalytic Activity of Gold Nanoparticles Supported on Silica. *J. Catal.* **2009**, *262*, 92-101.
- (13) Boccuzzi, F.; Chiorino, A.; Manzoli, M.; Lu, P.; Akita, T.; Ichikawa, S.; Haruta, M. Au/TiO₂ Nanosized Samples: A Catalytic, TEM, and FTIR Study of the Effect of Calcination Temperature on the CO Oxidation. *J. Catal.* **2001**, *202*, 256-267.
- (14) Buffat, P.; Borel, J. P. Size Effect on the Melting Temperature of Gold Particles. *Phys. Rev.* **1976**, *13*, 2287-2298.
- (15) Lu, J.; Fu, B.; Kung, M. C.; Xiao, G.; Elam, J. W.; Kung, H. H.; Stair, P. C. Coking- and Sintering-Resistant Palladium Catalysts Achieved Through Atomic Layer Deposition. *Science* **2012**, *335*, 1205-1208.
- (16) Park, K. C.; Ihm, S. K. Comparison of Pt/zeolite Catalysts for n-hexadecane Hydroisomerization. *Appl. Catal. A: Gen.* **2000**, *203*, 201-209.
- (17) Bharadwaj, S. S.; Schmidt, L. D. Catalytic Partial Oxidation of Natural Gas to Syngas. *Fuel Process. Technol.* **1995**, *42*, 109-127.
- (18) Deutschmann, O.; Maier, L. I.; Riedel, U.; Stroemman, A. H.; Dibble, R. W. Hydrogen Assisted Catalytic Combustion of Methane on Platinum. *Catal. Today* **2000**, *59*, 141-150.
- (19) Shivhare, A.; Chevrier, D. M.; Purves, R. W.; Scott, R. W. J. Following the Thermal Activation of Au₂₅(SR)₁₈ Clusters for Catalysis by X-ray Absorption Spectroscopy. *J. Phys. Chem. C.* **2013**, *117*, 20007-20016.
- (20) Zhu, Y.; Qian, H.; Jin, R. An Atomic-Level Strategy for Unraveling Gold Nanocatalysis from the Perspective of Au_n(SR)_m Nanoclusters. *Chem. Eur. J.* **2010**, *16*, 11455-11462.
- (21) Martin, J. E.; Odinek, J.; Wilcoxon, J. P.; Anderson, R. A.; Provencio, P. Sintering of Alkanethiol-Capped Gold and Platinum Nanoclusters. *J. Phys. Chem. B* **2003**, *107*, 430-434.

- (22) Joo, S. H.; Park, J. Y.; Tsung, C. K.; Yamada, Y.; Yang, P.; Somorjai, G. A. Thermally Stable Pt/Mesoporous Silica Core–Shell Nanocatalysts for High-Temperature Reactions. *Nature Mater.* **2009**, *8*, 126-131.
- (23) Wang, S.; Zhang, M.; Zhang, W. Yolk–Shell Catalyst of Single Au Nanoparticle Encapsulated within Hollow Mesoporous Silica Microspheres. *ACS Catal.* **2011**, *1*, 207-211.
- (24) Cao, A.; Lu, R.; Vesper, G. Stabilizing Metal Nanoparticles for Heterogeneous Catalysis. *Phys. Chem. Chem. Phys.* **2010**, *12*, 13499-13510.
- (25) Song, H.; Rioux, R. M.; Hoefelmeyer, J. D.; Komor, R.; Niesz, K.; Grass, M.; Yang, P.; Somorjai, G. A. Hydrothermal Growth of Mesoporous SBA-15 Silica in the Presence of PVP-Stabilized Pt Nanoparticles: Synthesis, Characterization, and Catalytic Properties. *J. Am. Chem. Soc.* **2006**, *128*, 3027-3037.
- (26) Lu, G.; Li, S.; Guo, Z.; Farha, O. K.; Hauser, B. G.; Qi, X.; Wang, Y.; Wang, X.; Han, S.; Liu, X.; DuChene, J. S.; Zhang, H.; Zhang, Q.; Chen, X.; Ma, J.; Loo, S. C. J.; Wei, W. D.; Yang, Y.; Hupp, J. T.; Huo, F. Imparting Functionality to a Metal–Organic Framework Material by Controlled Nanoparticle Encapsulation. *Nature Chem.* **2012**, *4*, 310-316.
- (27) Habeeb Muhammed, M. A.; Pradeep, T. Au₂₅@SiO₂: Quantum Clusters of Gold Embedded in Silica. *Small* **2011**, *7*, 204-208.
- (28) Samanta, A.; Dhar, B. B.; Devi, R. N. Ultrasmall Gold Cluster Arrays Encapsulated in Silica Nanospheres: Applications in Fluorescence Imaging and Catalysis. *J. Phys. Chem. C* **2012**, *116*, 1748-1754.
- (29) Shivhare, A.; Wang, L.; Scott, R. W. J. Isolation of Carboxylic Acid-Protected Au₂₅ Clusters Using a Borohydride Purification Strategy. *Langmuir.* **2015**, *31*, 1835-1841.
- (30) Liu, X.; Atwater, M.; Wang, J.; Huo, Q. Extinction Coefficient of Gold Nanoparticles with Different Sizes and Different Capping Ligands. *Colloids Surf. B.* **2007**, *58*, 3-7.
- (31) Ravel, B.; Newville, M. ATHENA, ARTEMIS, HEPHAESTUS: Data Analysis for X-ray Absorption Spectroscopy Using IFEFFIT. *J. Synchrotron Radiat.* **2005**, *12*, 537-541.
- (32) Liu, J.; Wang, F.; Qi, S.; Gu, Z.; Wu, G. Highly Selective Epoxidation of Styrene over Gold–Silica Catalysts via One-pot Synthesis: Synthesis, Characterization, and Catalytic Application. *New J. Chem.* **2013**, *37*, 769-774.

- (33) Lu, Y.; Chen, W. Sub-nanometre Sized Metal Clusters: from Synthetic Challenges to the Unique Property Discoveries. *Chem. Soc. Rev.* **2012**, *41*, 3594-3623.
- (34) Wu, Z.; Suhan, J.; Jin, R. One-pot Synthesis of Atomically Monodisperse, Thiol-Functionalized Au₂₅ Nanoclusters. *J. Mater. Chem.* **2009**, *19*, 622-626.
- (35) Akola, J.; Walter, M.; Whetten, R. L.; Häkkinen, H.; Grönbeck, H. On the Structure of Thiolate-Protected Au₂₅. *J. Am. Chem. Soc.* **2008**, *130*, 3756-3757.
- (36) MacDonald, M. A.; Chevrier, D. M.; Zhang, P.; Qian, H.; Jin, R. The Structure and Bonding of Au₂₅(SR)₁₈ Nanoclusters from EXAFS: The Interplay of Metallic and Molecular Behavior. *J. Phys. Chem. C* **2011**, *115*, 15282-15287.
- (37) Simms, G. A.; Padmos, J. D.; Zhang, P. Structural and Electronic Properties of Protein/Thiolate-Protected Gold Nanocluster with “Staple” Motif: A XAS, L-DOS, and XPS study. *J. Chem. Phys.* **2009**, *131*, 214703-214708.
- (38) Zhu, M.; Aikens, C. M.; Hollander, F. J.; Schatz, G. C.; Jin, R. Correlating the Crystal Structure of A Thiol-Protected Au₂₅ Cluster and Optical Properties. *J. Am. Chem. Soc.* **2008**, *130*, 5883-5885.
- (39) Fritsche, H. G.; Benfield, R. E. Exact Analytical Formulae for Mean Coordination Numbers in Clusters. *Z. Phys. D At. Mol. Clusters* **1993**, *26*, 15-17.
- (40) Wunder, S.; Polzer, F.; Lu, Y.; Mei, Y.; Ballauff, M. Kinetic Analysis of Catalytic Reduction of 4-Nitrophenol by Metallic Nanoparticles Immobilized in Spherical Polyelectrolyte Brushes. *J. Phys. Chem. C* **2010**, *114*, 8814-8820.
- (41) Dong, F.; Guo, W.; Park, S. K.; Ha, C. S. Controlled Synthesis of Novel Cyanopropyl Polysilsesquioxane Hollow Spheres Loaded with Highly Dispersed Au Nanoparticles for Catalytic Applications. *Chem. Commun.* **2012**, *48*, 1108-1110.
- (42) Kuroda, K.; Ishida, T.; Haruta, M. Reduction of 4-nitrophenol to 4-aminophenol over Au Nanoparticles Deposited on PMMA. *J. Mol. Catal. A: Chem.* **2009**, *298*, 7-11.
- (43) Schrunner, M.; Polzer, F.; Mei, Y.; Lu, Y.; Haupt, B.; Ballauff, M.; Gödel, A.; Drechsler, M.; Preussner, J.; Glatzel, U. Mechanism of the Formation of Amorphous Gold Nanoparticles within Spherical Polyelectrolyte Brushes. *Macromol. Chem. Phys.* **2007**, *208*, 1542-1547.

- (44) Baruah, B.; Gabriel, G. J.; Akbashev, M. J.; Booher, M. E. Facile Synthesis of Silver Nanoparticles Stabilized by Cationic Polynorbornenes and Their Catalytic Activity in 4-Nitrophenol Reduction. *Langmuir*. **2013**, *29*, 4225-4234.
- (45) Lee, J.; Park, J. C.; Song, H. A Nanoreactor Framework of a Au@SiO₂ Yolk/Shell Structure for Catalytic Reduction of p-Nitrophenol. *Adv. Mater.* **2008**, *20*, 1523-1528.
- (46) Wu, Z.; Jiang, D. E.; Mann, A. K. P.; Mullins, D. R.; Qiao, Z. A.; Allard, L. F.; Zeng, C.; Jin, R.; Overbury, S. H. Thiolate Ligands as a Double-Edged Sword for CO Oxidation on CeO₂ Supported Au₂₅(SCH₂CH₂Ph)₁₈ Nanoclusters. *J. Am. Chem. Soc.* **2014**, *136*, 6111-6122.
- (47) Liu, Y.; Tsunoyama, H.; Akita, T.; Tsukuda, T. Efficient and Selective Epoxidation of Styrene with TBHP Catalyzed by Au₂₅ Clusters on Hydroxyapatite. *Chem. Commun.* **2010**, *46*, 550-552.
- (48) Patil, N. S.; Jha, R.; Uphade, B. S.; Bhargava, S. K.; Choudhary, V. R. Epoxidation of Styrene by Anhydrous t-butyl hydroperoxide over Gold Supported on Al₂O₃, Ga₂O₃, In₂O₃ and Tl₂O₃. *Appl. Catal. A: Gen.* **2004**, *275*, 87-93.
- (49) Jin, Y.; Wang, P.; Yin, D.; Liu, J.; Qiu, H.; Yu, N. Gold Nanoparticles Stabilized in a Novel Periodic Mesoporous Organosilica of SBA-15 for Styrene Epoxidation. *Microporous Mesoporous Mater.* **2008**, *111*, 569-576.

CHAPTER 3

Thermal Stability of Alumina-Overcoated Au₂₅ Clusters for Catalysis

In this work, the effect of thin layers of alumina over Au₂₅(MUA)₁₈ and Au₂₅(DDT)₁₈ clusters using Atomic Layer Deposition (ALD) is discussed. Results on alumina-overcoated Au₂₅(MUA)₁₈ and Au₂₅(DDT)₁₈ clusters show that the carboxylic acid groups at the surface of the clusters are necessary for complete ALD coating of the clusters. Furthermore, EXAFS and TEM analysis clearly showed that 20 cycle-coated Au₂₅(MUA)₁₈ clusters are much more sinter-resistant than the 10-cycle coated clusters.

This chapter is a near-verbatim copy of work published in ACS Appl. Nano Mater. **2018**, 1, 6904-6911. All the experimental work in this article was performed by myself. Atomic Layer Deposition work was done in the laboratory of Xueliang Sun at Western University and carried out by Dr. Andrew Lushington. The first draft of the manuscript was written by myself and it was revised by Prof. Robert Scott prior to publication.

3.1. Abstract

One of the prevalent difficulties in using supported Au cluster or nanoparticle catalysts for applications is the ease at which such systems sinter at even moderate temperatures and conditions. Herein we demonstrate a stabilization strategy involving atomic layer deposition (ALD) of alumina overlayers onto supported gold clusters which greatly alleviates high-temperature sintering. Control over both the number of cycles (5, 10, and 20) of alumina deposition over Au₂₅ clusters and the surface chemistry of the clusters themselves were found to be important for optimal stabilization. TEM and EXAFS analyses showed that Au₂₅ clusters using 11-mercaptoundecanoic acid stabilizers with 20 cycles of alumina-overcoating via ALD showed remarkable thermal stability, with particle sizes growing only slightly to *ca.* 2.5 nm after calcination at 650 °C. However, such stabilization does come with a cost; at moderate temperatures 10 cycle alumina-coated catalysts showed better catalytic activity for 4-nitrophenol reduction reaction than 20 cycle alumina-coated catalysts which is likely due to increased mass transfer resistance associated with the protective shell.

3.2. Introduction

Gold catalysts supported on reducible and non-reducible metal oxides have been studied for many reactions, including low-temperature CO oxidation, partial oxidation of hydrocarbons, and reduction of nitrogen oxides.¹⁻³ One important conclusion that has arisen from previous studies with Au catalysts is that Au nanoparticles have remarkable size-dependent catalytic activity, with Au particles below 4 nm having strong catalytic activity and particles greater than 6 nm being nearly inactive.⁴⁻⁶ Thiol stabilized gold clusters with sizes in the 1 nm range (such as [Au₂₅(SR)₁₈]) have been shown to be model catalysts for many oxidation and reduction reactions at moderate temperatures.⁷⁻⁹ However, Au clusters/nanoparticles rapidly sinter under reaction conditions and/or thermal activation treatment and form larger particles.¹⁰ Due to this limitation, the commercialization of supported-gold catalysts has been restricted to low-temperature applications.

Several methods, such as chemical vapour deposition (CVD),¹¹ grafting of amines onto nanoparticles,¹² dendrimer encapsulation,¹³ and encapsulation by the sol-gel method,¹⁴⁻¹⁵ have been reported to help alleviate sintering of metal clusters and nanoparticles. Previously, we documented that silica encapsulated Au₂₅(MUA)₁₈ clusters showed significant sinter-resistance up to 650°C, and that the resulting catalysts still showed good activity and recyclability for

styrene epoxidation reactions.¹⁵ However mass transfer issues associated with the protective silica shell were problematic. Chemical vapour deposition (CVD) is a thin film deposition involving the reaction of gas phase precursors at or near the vicinity of the substrate.¹⁶ Atomic layer deposition (ALD) is a self-limiting, multi-step gas phase CVD technique which provides a unique method for depositing ultra-thin films on surfaces. In the ALD process, growth progresses layer by layer by sequential alternating pulse of gas precursors. During each half cycle, the gas precursor is pulsed into reaction chamber for certain time to allow the precursor to react with the substrate, which allows the fabrication of thin films with precise thickness control, high uniformity, and excellent conformality.¹⁷⁻²² In contrast to other methods, ALD is a non-line of sight technique, capable of coating high surface area materials in a conformal manner.¹⁸ For example, Ma *et al.* reported that silica overcoating by ALD over Au (~5 nm)/TiO₂ catalysts could enhance the thermal stability of the nanoparticles.²³ Smaller Au particles were successfully coated by ALD of silica whereas larger particles were non-coated or incompletely coated. Feng *et al.* reported that 16 cycles of alumina overcoating (one cycle consisting of trimethylaluminum exposure followed by water exposure) on Pd nanoparticles (1-2 nm) by ALD prevented the sintering of the Pd particles after heating to 500 °C for 6 h in argon flow.²⁴ In addition, they observed that the catalytic activity for methanol decomposition dropped when over 16 cycles of ALD alumina coatings were used, presumably due to mass-transfer issues. Stair *et al.* observed that 45 cycles of alumina deposition over Pd/Al₂O₃ were required to maintain the size of Pd nanoparticles at 2.8 ± 0.46 nm at high temperatures and long reaction times (675 °C for 1700 min).²⁵

In this work, the ALD technique was utilized to create protective overlayers of alumina over supported-Au₂₅ clusters. To probe the critical role of carboxyl groups on the surface of mercaptoundecanoic acid (MUA) ligands in the ALD process, the thermal stability of alumina-overcoated dodecanethiolate-stabilized Au₂₅ clusters were compared with that of alumina-overcoated Au₂₅(MUA)₁₈ clusters. Results showed that tremendous sintering was observed at 650 °C in the absence of carboxylic acid groups, while the Au₂₅(MUA)₁₈ system showed dramatically improved stability. The structure of the resulting materials before and after calcination at temperatures up to 650 °C was analyzed by TEM and extended X-ray absorption fine structure (EXAFS) spectroscopy analyses, which showed that the alumina-overcoated Au₂₅(MUA)₁₈ clusters were much more stable to sintering compared to control materials. The catalytic activity of the clusters was examined via a model nitrophenolate reduction reaction. Catalysts with 20 cycles of alumina overcoating were found to effectively mitigate the sintering

of clusters, albeit while introducing mild mass-transfer concerns at moderate calcination temperatures.

3.3. Materials and Methods

3.3.1. Materials

Hydrogen tetrachloroaurate(III) trihydrate ($\text{HAuCl}_4 \cdot 3\text{H}_2\text{O}$, 99.9% on metal basis, Aldrich), 11-mercaptoundecanoic acid (MUA, 95%, Sigma Aldrich), dodecanethiol (DDT, 98%, Sigma Aldrich), tetraoctylammonium bromide (TOAB, 98%, Aldrich), sodium borohydride (NaBH_4 , 98%, EMD), 4-nitrophenol (PNP, 99%, Alfa Aesar) alumina (Al_2O_3 , pore size 58 Å, Sigma Aldrich) and trimethylaluminum, (TMA, 98%, Strem), were used as received. Tetrahydrofuran (THF, high purity) was purchased from EMD. Milli-Q water was used for ALD synthesis.

3.3.2. Synthesis of $\text{Au}_{25}(\text{MUA})_{18}$ clusters

$\text{Au}_{25}(\text{MUA})_{18}$ clusters were synthesized by using an existing procedure that has been published by our group.²⁶ Briefly, $\text{HAuCl}_4 \cdot 3\text{H}_2\text{O}$ (200 mg) and TOAB (1.2 equiv.) were added to 20 ml THF. The solution kept for stirring until it turned from yellow to orange-red. After the addition of MUA (5 equiv. in 5 mL THF), the solution was stirred until it became colorless. The solution was then cooled using an ice bath followed by the addition of ice cold NaBH_4 (4 equiv. in 2 mL water) dropwise and the solution was monitored using UV-Vis spectroscopy. The addition of NaBH_4 was continued until the characteristic UV-Vis absorption peaks of $\text{Au}_{25}(\text{MUA})_{18}$ clusters were observed. Larger nanoparticles were then removed by centrifugation at 10,000 rpm for 2 min. $\text{Au}_{25}(\text{MUA})_{18}$ clusters were precipitated out with further NaBH_4 (1.5 equiv. in 2 mL water) addition. The residue was then centrifuged and washed with THF twice, followed by dissolution in water. $\text{Au}_{25}(\text{MUA})_{18}$ clusters were precipitated out with a few drops of dilute acetic acid with an approximate pH of 3. The precipitate was washed with water twice and dissolved in THF.

$\text{Au}_{25}(\text{MUA})_{18}$ clusters were deposited on alumina by the following procedure: 200 mg of alumina was added to the $\text{Au}_{25}(\text{MUA})_{18}$ solution and stirred for 2 h. After stirring, $\text{Au}_{25}(\text{MUA})_{18}/\text{Al}_2\text{O}_3$ catalysts were dried by solvent evaporation.

3.3.3. Synthesis of $\text{Au}_{25}(\text{DDT})_{18}$ clusters

To the solution of $\text{HAuCl}_4 \cdot 3\text{H}_2\text{O}$ (500 mg) in THF (50 mL), TOAB (1.2 equiv.), and 1-dodecanethiol (5 equiv.) were added.²⁷ The resulting solution was stirred until it became clear followed by the addition of ice-cold NaBH_4 (10 equiv. in 10 ml H_2O). The solution was stirred

at room temperature for 4 days. The solid was then collected by the evaporation of solvent and washed with an ethanol/water mixture three times, followed by redissolution in THF. The alumina-supported $\text{Au}_{25}(\text{DDT})_{18}$ clusters were synthesized in a similar way as the procedure using $\text{Au}_{25}(\text{MUA})_{18}$ clusters above.

3.3.4. Atomic Layer Deposition of Alumina over $\text{Au}_{25}(\text{MUA})_{18}/\text{Al}_2\text{O}_3$ and $\text{Au}_{25}(\text{DDT})_{18}/\text{Al}_2\text{O}_3$

Atomic layer deposition was carried out by sequential exposure of trimethylaluminum (TMA) and deionized water at room temperature. ALD films were deposited using a commercial cross flow-type hot-wall ALD reactor (Arradiance Gemstar-8) using TMA and deionized Milli-Q water. All precursors were evaporated with an external reservoir held at room temperature. Argon (99.999% Praxair) was used as both a carrier and purge gas. Thiolate protected Au clusters were loaded into a boat and placed in the ALD chamber that was pumped down to ~50 mTorr. All depositions were conducted at 60 °C using a 50 ms pulse of TMA and 50 ms pulse of water separated by a 60 s purge of argon at a flow rate of 20 sccm. Alumina-overcoated samples were prepared using 5, 10, and 20 cycles of TMA/ H_2O . For brevity, catalysts prepared by different cycles (5, 10, and 20) of ALD coating are designated as 5c- $\text{Al}_2\text{O}_3/\text{Au}(\text{MUA})/\text{Al}_2\text{O}_3$, 10c- $\text{Al}_2\text{O}_3/\text{Au}(\text{MUA})/\text{Al}_2\text{O}_3$, and 20c- $\text{Al}_2\text{O}_3/\text{Au}(\text{MUA})/\text{Al}_2\text{O}_3$, respectively, whereas the sample prior to ALD deposition is designated as $\text{Au}(\text{MUA})/\text{Al}_2\text{O}_3$. The 10c- $\text{Al}_2\text{O}_3/\text{Au}_{25}(\text{DDT})_{18}/\text{Al}_2\text{O}_3$ catalysts were prepared using 10 cycles of alumina deposition on $\text{Au}_{25}(\text{DDT})_{18}/\text{Al}_2\text{O}_3$. All samples were then dried at 100 °C. Further calcinations were carried out at two different temperatures (250 °C and 650 °C) for 3 h in air.

3.3.5. Characterization

A Varian Cary 50 Bio UV-Vis Spectrometer was used to collect UV-Vis absorption spectra of the $\text{Au}_{25}(\text{MUA})_{18}$ clusters. The morphology of the ALD-coated $\text{Au}_{25}/\text{Al}_2\text{O}_3$ materials was analysed by a HT7700 TEM operating at 100 kV. ImageJ software was used to measure the size of 200 particles for particle size distribution histograms.²⁸ Extended X-ray Absorption Spectra Fine Structure (EXAFS) spectroscopic analysis was performed on the HXMA beamline 061D-1 (energy range 5-30 keV, resolution $1 \times 10^{-4} \Delta E/E$) at the Canadian Light Source. The storage ring electron energy and ring current were 2.9 GeV and 250 mA, respectively. All data was collected in fluorescence mode using a 32 element detector. The energy for the Au- L_3 edge (11919 eV) was selected by using a Si (111) double crystal monochromator with a Rh-coated 100 nm long KB mirror. Higher harmonics were removed

by detuning the double crystal monochromator. Data analysis and EXAFS fitting was carried out using the Demeter software package.^{30,35} An amplitude reduction factor of 0.86 was obtained from fitting of the Au foil. The coordination number of calcined Au cluster samples were determined by keeping this amplitude reduction factor fixed.

3.3.6. Catalytic activity for 4-nitrophenol reduction

2.0 mL of 0.10 mM 4-nitrophenol and 2.0 mg ALD-coated Au₂₅/Al₂O₃ were mixed in a quartz cuvette. After adding 0.5 mL of ice-cold 0.10 M NaBH₄ in water to the cuvette, the sample was analyzed by UV-Vis spectroscopy immediately, to get the initial concentration of 4-nitrophenolate, and the progress of the reaction was monitored at 2 min time intervals.

3.4. Results and Discussion

Au₂₅(SC₁₀H₂₀COOH)₁₈ (Au₂₅(MUA)₁₈) clusters and Au₂₅(SC₁₂H₂₅)₁₈ (Au₂₅(DDT)₁₈) clusters were synthesized according to aforementioned procedures.²⁶⁻²⁷ The formation of Au₂₅ clusters was verified by UV-Vis spectra which showed three peaks at 399 nm, 446 nm, and 680 nm which are characteristic of the HOMO-LUMO transitions of the Au₂₅ clusters.²⁹⁻³⁰ Previously we analyzed the MALDI-TOF spectra of Au₂₅(MUA)₁₈ clusters which gave clear evidence for the formation of Au₂₅(MUA)₁₈ clusters.²⁶ TEM images of the as-synthesized Au₂₅(MUA)₁₈/Al₂O₃ and Au₂₅(DDT)₁₈/Al₂O₃ materials before and after ALD deposition are shown in Figure 3.1. The average particle size of the Au₂₅(MUA)₁₈/Al₂O₃ and Au₂₅(DDT)₁₈/Al₂O₃ materials were measured to be 1.4 ± 0.1 nm and 1.5 ± 0.1 nm respectively. The average particle size of both samples was retained after 10 cycles of alumina deposition. The particle sizes in these samples are slightly larger than the sizes of the pristine clusters deposited on carbon films (~ 1.1 nm), the slight size increase is likely an artefact due to imperfect focusing of all clusters in the 3D materials.

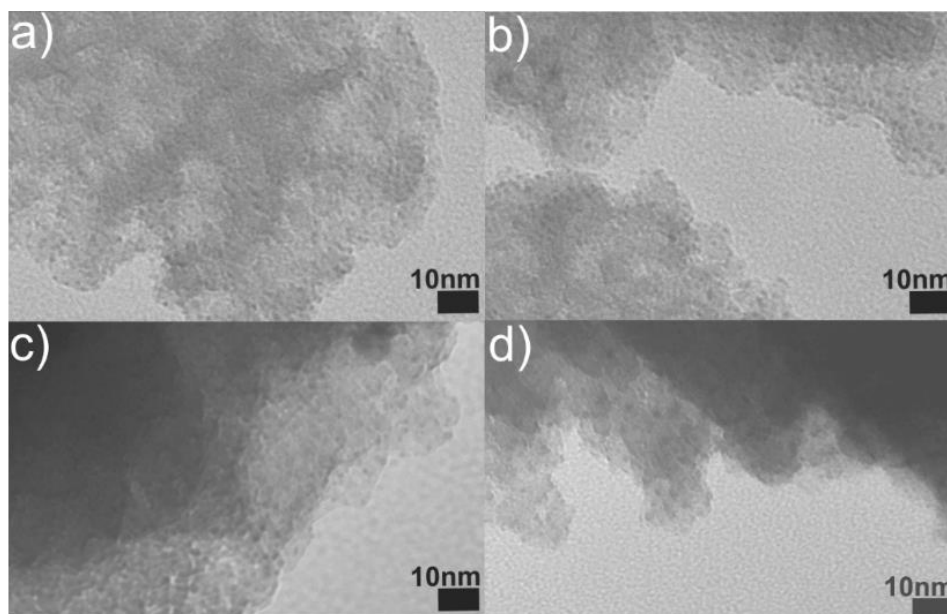


Figure 3.1: TEM images of as-synthesized a) $\text{Au}_{25}(\text{MUA})_{18}/\text{Al}_2\text{O}_3$, b) $\text{Au}_{25}(\text{DDT})_{18}/\text{Al}_2\text{O}_3$, c) $10\text{c-Al}_2\text{O}_3/\text{Au}_{25}(\text{MUA})_{18}/\text{Al}_2\text{O}_3$, and d) $10\text{c-Al}_2\text{O}_3/\text{Au}_{25}(\text{DDT})_{18}/\text{Al}_2\text{O}_3$.

Overlayers of alumina were grown onto the $\text{Au}_{25}(\text{MUA})_{18}/\text{Al}_2\text{O}_3$ and $\text{Au}_{25}(\text{DDT})_{18}/\text{Al}_2\text{O}_3$ materials by ALD using sequential pulses of trimethylaluminum (TMA) and H_2O . The Au particle sizes of alumina-overcoated samples of $\text{Au}_{25}(\text{MUA})_{18}$ clusters with 5, 10, and 20 alumina ALD cycles, followed by calcination, were examined by TEM analysis; results are shown in Figure 3.2. Previous work by our group and others has shown that the thiolate ligands in such clusters are not removed until temperatures of *ca.* $125\text{ }^\circ\text{C}$, and typically completely removed by $250\text{ }^\circ\text{C}$.^{7,31} The $\text{Au}(\text{MUA})/\text{Al}_2\text{O}_3$, $5\text{c-Al}_2\text{O}_3/\text{Au}(\text{MUA})/\text{Al}_2\text{O}_3$, $10\text{c-Al}_2\text{O}_3/\text{Au}(\text{MUA})/\text{Al}_2\text{O}_3$, and $20\text{c-Al}_2\text{O}_3/\text{Au}(\text{MUA})/\text{Al}_2\text{O}_3$ catalysts calcined at $250\text{ }^\circ\text{C}$ showed average particle sizes of $7.1 \pm 6.0\text{ nm}$, $2.5 \pm 1.0\text{ nm}$, $1.9 \pm 0.8\text{ nm}$, and $1.8 \pm 0.8\text{ nm}$, respectively. Thus, some growth of the clusters via sintering already occurred at this stage, albeit sintering was mitigated with more cycles of alumina deposition. The $\text{Au}(\text{MUA})/\text{Al}_2\text{O}_3$, $5\text{c-Al}_2\text{O}_3/\text{Au}(\text{MUA})/\text{Al}_2\text{O}_3$, $10\text{c-Al}_2\text{O}_3/\text{Au}(\text{MUA})/\text{Al}_2\text{O}_3$, and $20\text{c-Al}_2\text{O}_3/\text{Au}(\text{MUA})/\text{Al}_2\text{O}_3$ samples calcined at $650\text{ }^\circ\text{C}$ showed average particle sizes of $11.7 \pm 4.0\text{ nm}$, $6.8 \pm 2.8\text{ nm}$, $2.7 \pm 1.6\text{ nm}$, and $2.4 \pm 0.9\text{ nm}$, respectively. This shows that thicker alumina overcoatings can drastically mitigate sintering at higher temperatures. Prior literature suggests that the coatings would only be 1.1 nm and 2.2 nm thick for 10 and 20 cycle alumina ALD coatings.³² We note that we were not able to reproducibly image alumina overcoatings over all the particles, which is likely due to the lack of contrast between the overcoating and support, although some particles exhibit coatings in the expected size range. Particle size histograms of each of the samples are

shown in Figure 3.3. The 10c- $\text{Al}_2\text{O}_3/\text{Au}(\text{MUA})/\text{Al}_2\text{O}_3$ and 20c- $\text{Al}_2\text{O}_3/\text{Au}(\text{MUA})/\text{Al}_2\text{O}_3$ catalysts exhibited tremendous sinter resistance upon calcination in air up to 650 °C.

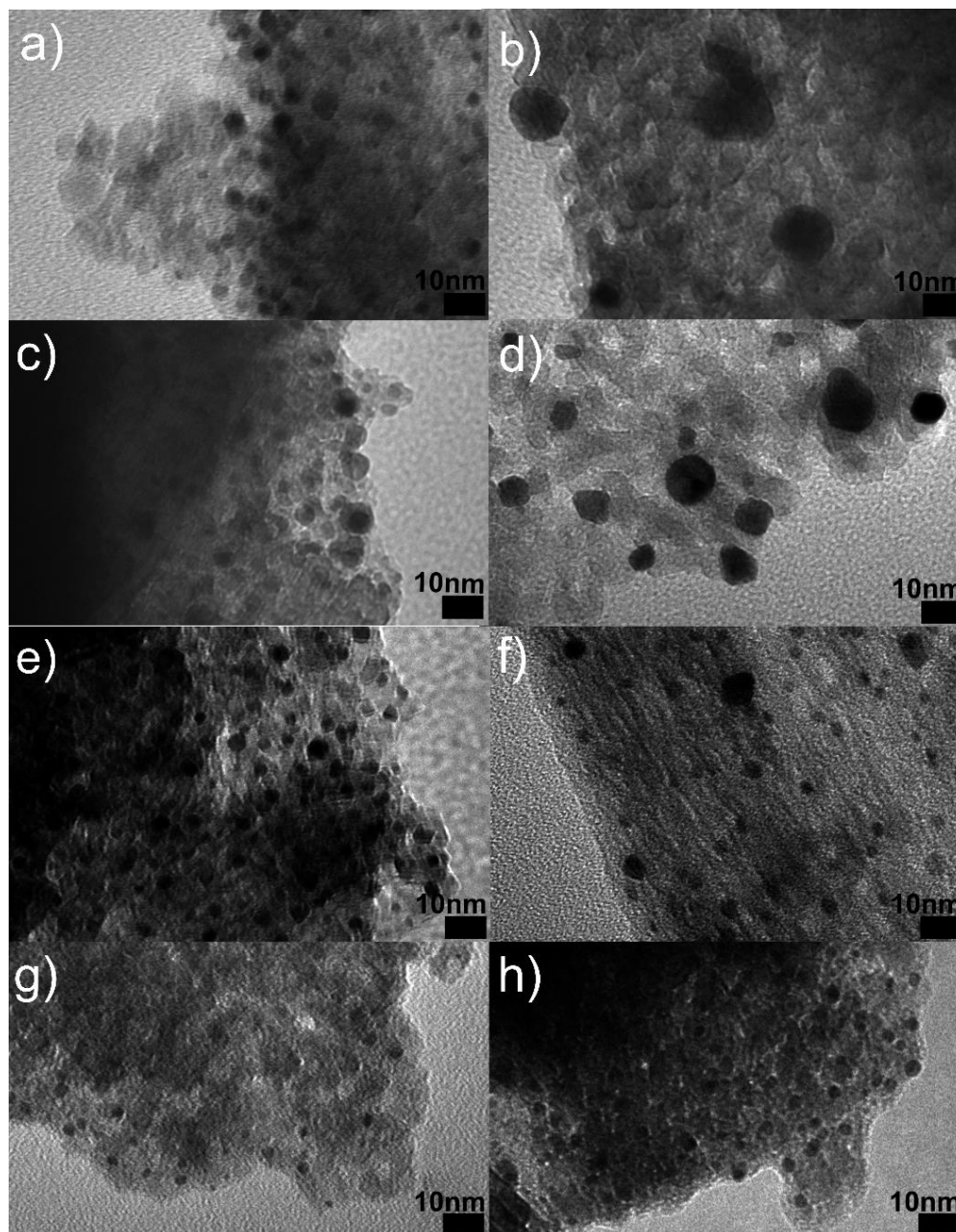


Figure 3.2: TEM images of $\text{Au}_{25}(\text{MUA})_{18}$ samples on Al_2O_3 calcined at a) 250 °C, b) 650 °C; 5c- $\text{Al}_2\text{O}_3/\text{Au}(\text{MUA})/\text{Al}_2\text{O}_3$ calcined at c) 250 °C, d) 650 °C; 10c- $\text{Al}_2\text{O}_3/\text{Au}(\text{MUA})/\text{Al}_2\text{O}_3$ calcined at e) 250, f) 650 °C; and 20c- $\text{Al}_2\text{O}_3/\text{Au}(\text{MUA})/\text{Al}_2\text{O}_3$ calcined at g) 250 °C, h) 650 °C.

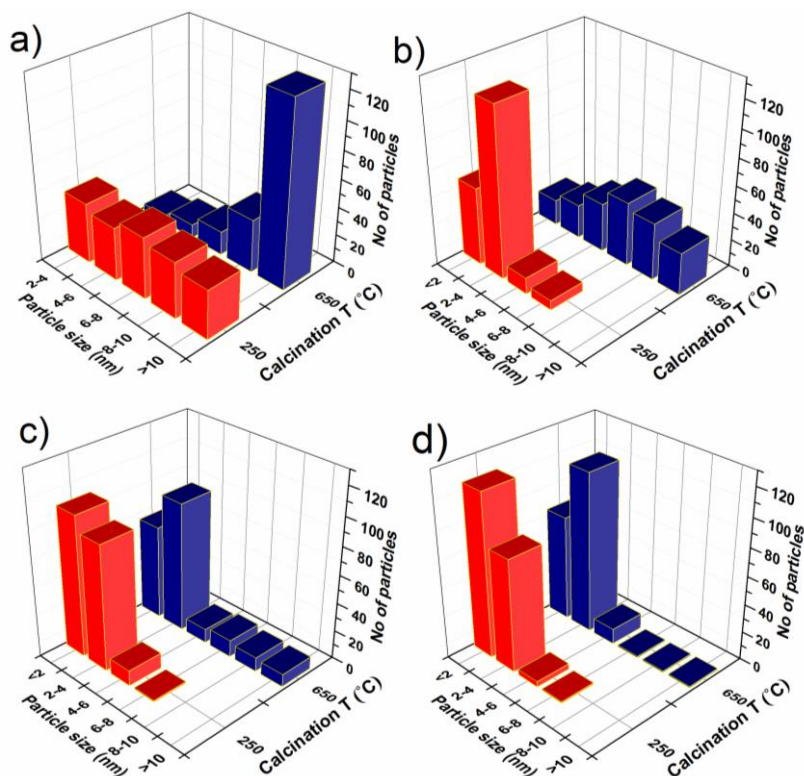


Figure 3.3: Histograms of a) Au(MUA)/Al₂O₃, b) 5c-Al₂O₃/Au(MUA)/Al₂O₃, c) 10c-Al₂O₃/Au(MUA)/Al₂O₃, and d) 20c-Al₂O₃/Au(MUA)/Al₂O₃ catalysts calcined at different temperatures.

We also wanted to understand how important the surface chemistry of the clusters was for effective ALD deposition. Thus, we also examined the thermal stability of 10c-Al₂O₃/Au₂₅(DDT)₁₈/Al₂O₃ materials; TEM images of the resulting materials after calcination at 250 °C and 650 °C are shown in Figure 3.4. The average particle size increased to 2.0 ± 0.8 nm after calcination at 250 °C, and to 5.2 ± 2.1 nm upon calcination at 650 °C. These values are higher than the values seen for comparable Au₂₅(MUA)₁₈ samples above (1.9 ± 0.8 nm and 2.7 ± 1.6 nm for samples calcined at 250 °C and 650 °C, respectively), particularly for the sample calcined at higher temperature. This implies that that insufficient alumina deposition over Au₂₅(DDT)₁₈ clusters occurs, likely due to the lack of functional groups available for anchoring TMA on the dodecanethiol ligands.³³ The moderate stability of the Au₂₅(DDT)₁₈ system at 250 °C may be explained as alumina growth happens around the clusters, thus preventing mild sintering at lower temperatures and partially mitigating sintering at higher temperatures (as compared to uncoated samples). In the Au₂₅(MUA)₁₈ system, on the other hand, the carboxyl groups on the surface of the clusters can allow for anchoring of an alumina overlayer, as shown in Scheme 3.1; indeed, there is precedence in the literature for growing metal oxide films on the surface of carboxylic acid-terminated self-assembled monolayers.³⁴⁻

³⁵ First the TMA can react with surface carboxylic acid group to form $\text{COO-Al}(\text{CH}_3)_2^*$ and CH_4 . Next H_2O is introduced into the reaction chamber which reacts with $-\text{Al}(\text{CH}_3)_2$ to form $-\text{Al}(\text{OH})_2^*$ and CH_4 . This process is then repeated in the next cycle. It is not clear whether this overlayer on $\text{Au}_{25}(\text{MUA})_{18}$ clusters remain completely intact upon removal of the organic thiolate linker in this case; however, results unambiguously show that much greater sinter-resistance is gained in the $\text{Au}_{25}(\text{MUA})_{18}$ system compared to the $\text{Au}_{25}(\text{DDT})_{18}$ system.

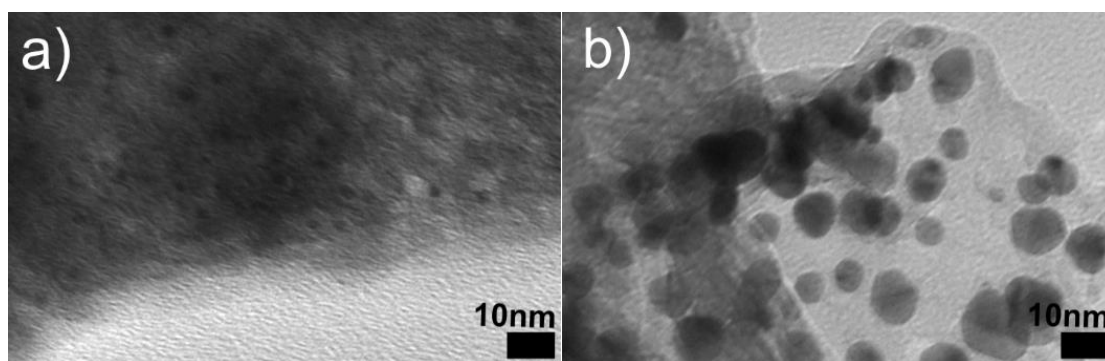
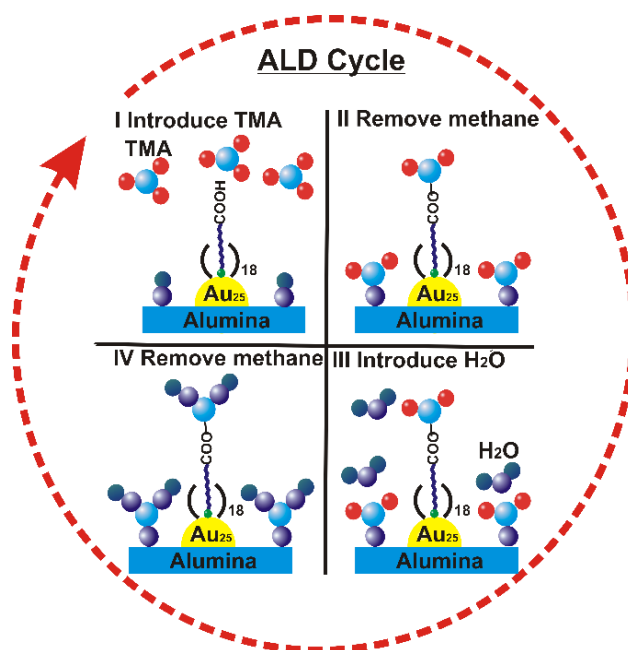


Figure 3.4: TEM images of $10\text{c-Al}_2\text{O}_3/\text{Au}_{25}(\text{DDT})_{18}/\text{Al}_2\text{O}_3$ calcined at a) $250\text{ }^\circ\text{C}$, and b) $650\text{ }^\circ\text{C}$.



Scheme 3.1: Schematic illustration of alumina deposition over $\text{Au}_{25}(\text{MUA})_{18}/\text{Al}_2\text{O}_3$. Colour scheme: red circles: methyl groups, light blue: Al, dark purple: O, and dark blue: H.

To further understand the effects of 10 and 20 cycles coating against sintering, the $\text{Au}_{25}(\text{MUA})_{18}$ samples were also examined by Au L_3 -edge EXAFS spectroscopy in

fluorescence mode on the Hard X-ray Microanalysis beamline (HXMA) at the Canadian Light Source (CLS). Figure 3.5 shows the Au L₃-edge K-space and individual R-space spectra of the as-synthesized Au₂₅(MUA)₁₈ samples coated with 20 layers of alumina prior to calcination. X-ray crystallographic data of Au₂₅(SR)₁₈ clusters has shown that Au₂₅(SR)₁₈ clusters have a core-shell morphology, in which the core is composed of an Au₁₃ icosahedron, in which the central atom is surrounded by 12 Au atoms while the shell consists of six S-Au-S-Au-S staple motifs.³⁶ Twelve out of the twenty faces of the icosahedron are surrounded by six staple motifs, with sulfur atoms directly attached to 12 Au atoms of the icosahedron core. A multishell fitting approach was used to fit the Au-S and three Au-Au contributions of the clusters in the as-synthesized materials.^{31, 37} After fitting the parameters for Au-S contribution, we fixed those values followed by fitting all three first shell Au-Au coordination modes. Coordination number (CN) values for all Au-Au first shell contributions were fixed based on the crystal structure of the clusters. The final EXAFS fitting parameters are shown in Table 3.1. The Au-S bond length was found to be 2.32(1) Å which matches well with crystallographic data of Au₂₅L₁₈ clusters (L=phenylethanethiol). The R-value at 2.82(3) Å represents the distance from central Au atom to the surface Au atom of the icosahedron core and also some short bonds between adjacent surface Au atoms. The second Au-Au interaction at 3.03(4) Å is the bond distance between the 12 surface Au atoms of the icosahedron (Au-Au(surf)). The last Au-Au bond length, 3.31(9) Å represents the distance between the surface Au atoms and the staple Au atoms. These values are in good agreement with literature values for other Au clusters, and thus the EXAFS data fitting clearly shows that the basic core structure of Au₂₅(MUA)₁₈ clusters is retained in the ALD-coated samples prior to calcination.

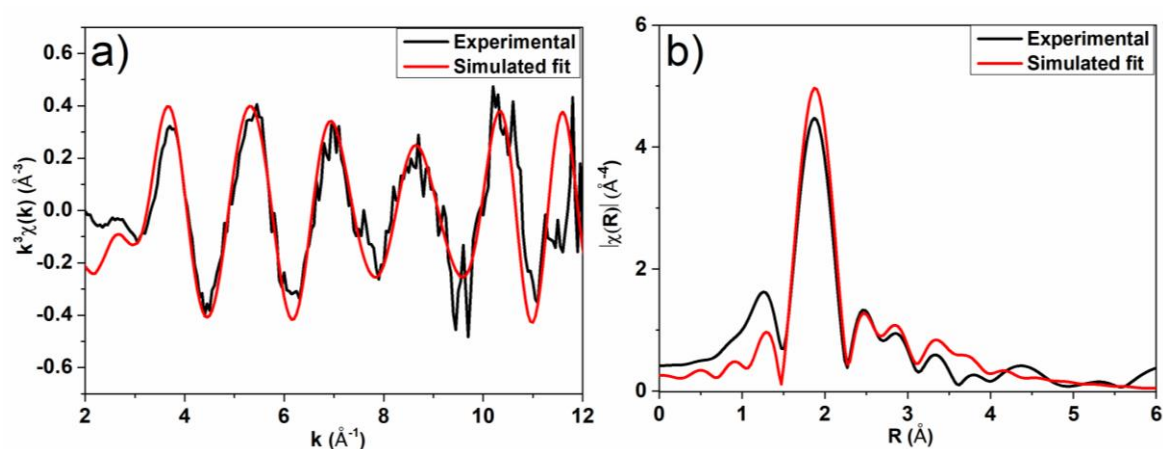


Figure 3.5: Au L₃ edge EXAFS fitting data in k- and R-space of as-synthesized 20c-Al₂O₃/Au/Al₂O₃.

Table 3.1: EXAFS fitting parameters of as-synthesized 20c-Al₂O₃/Au/Al₂O₃.

Type	CN	R/Å	$\sigma^2/\text{Å}^2$	E ₀ Shift(eV)	R (%)
Au-S	1.3	2.32(1)	0.001(1)	8.5(2)	1.8
Au-Au(core)	1.44	2.82(3)	0.003(2)	8.5(2)	
Au-Au(surf)	1.92	3.03(4)	0.004(4)	8.5(2)	
Au-Au(staple)	2.88	3.31(9)	0.02(1)	8.5(2)	

The Fourier-transformed R-space spectra for the 10c-Al₂O₃/Au(MUA)/Al₂O₃, and 20c-Al₂O₃/Au(MUA)/Al₂O₃ samples after calcination at 250 °C and 650 °C are shown in Figure 3.6. Individual k- and R-space spectra of 10c-Al₂O₃/Au(MUA)/Al₂O₃, and 20c-Al₂O₃/Au(MUA)/Al₂O₃ samples calcined at two different temperatures 250 °C, and 650 °C are shown in Figure 3.6 and 3.7 respectively. The Au-S contribution was not observed at 2.3 Å in calcined samples which suggest that the thiolate ligand is removed completely from the Au surface by 250 °C, which is in agreement with previous findings by our group and others.^{7, 15, 38} A fcc Au model was for used for single-shell fitting of the calcined samples.³¹ Fitted EXAFS parameters of all the samples are shown in Table 3.2. In the case of 250 °C-treated 10c-Al₂O₃/Au(MUA)/Al₂O₃ catalysts, the first shell coordination number for the Au-Au (N_{Au-Au}) contribution was found to be 10.4(5) which increased to 11.6(5) after calcination at 650 °C. The average first shell coordination number of 11.6 (compared with 12 for bulk gold) indicates that the average Au particles consist of 10,000 or more atoms with an average particle size of 10 nm.³⁹⁻⁴² As this is significantly larger than the average size seen by TEM, it suggests there are some much larger Au particles in the sample which local TEM analyses do not capture. The first shell coordination number for the Au-Au (N_{Au-Au}) contribution of 20c-Al₂O₃/Au/Al₂O₃ catalysts calcined at 250 °C and 650 °C were found to be 10.2(5) and 10.5(3) respectively. An average co-ordination number of 10.5(3) implies an average particle size of about 2.5 to 3 nm (containing ~1600 atoms).³⁹⁻⁴² This value is in reasonable agreement with TEM data; both TEM and EXAFS studies indicate that catalysts with 20 cycles of alumina deposition showed better sinter resistance than those with 10 cycles of alumina coating.

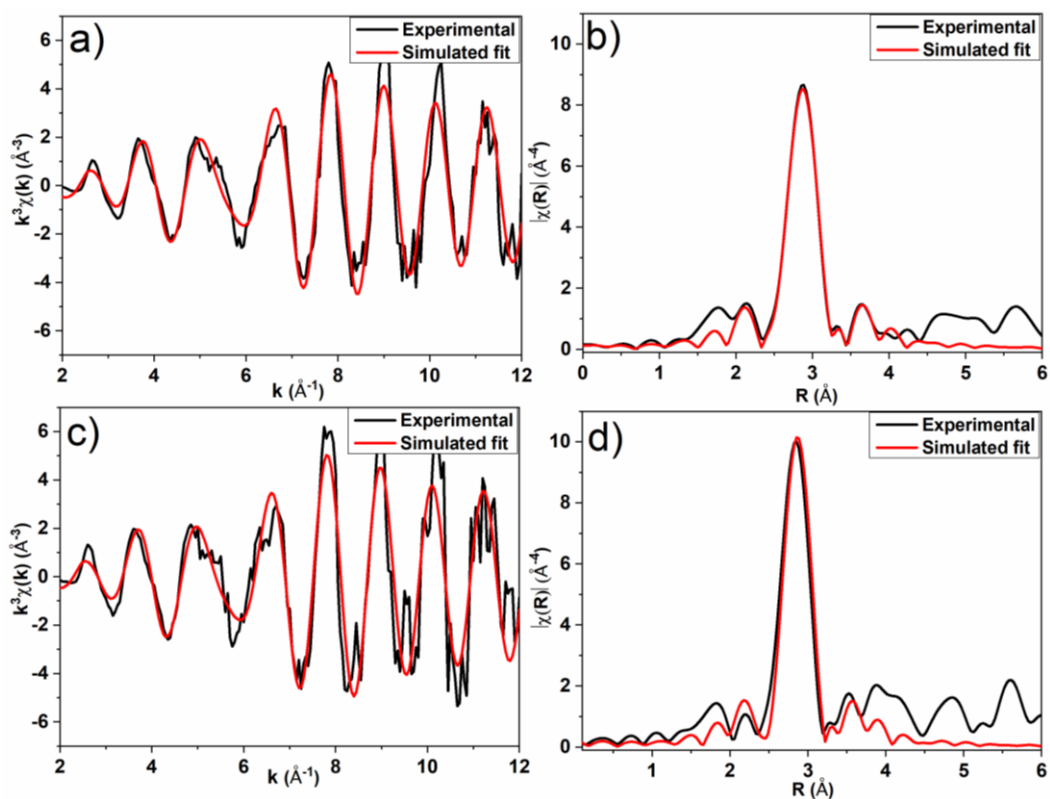


Figure 3.6: Au L₃ edge EXAFS fitting data in phase shift corrected-k (left) and R-space of 10c-Al₂O₃/Au/Al₂O₃ calcined at a) & b) 250 °C, and c) & d) 650 °C.

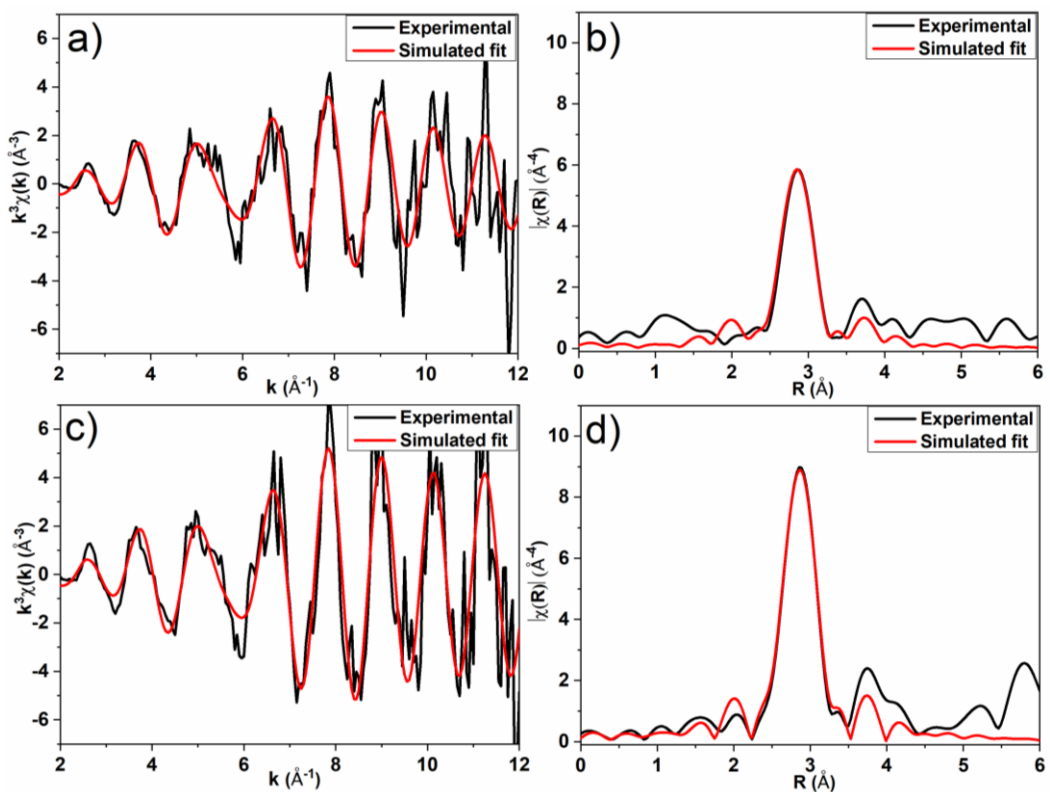


Figure 3.7: Au L₃ edge EXAFS fitting data in phase shift corrected k-(left) and R-space of 20c-Al₂O₃/Au/Al₂O₃ calcined at a) & b) 250 °C, and c) & d) 650 °C.

Table 3.2: EXAFS fitting parameters of 10c-Al₂O₃/Au/Al₂O₃ and 20c-Al₂O₃/Au/Al₂O₃ materials calcined at two different temperatures.

Catalyst	CN	R/Å	σ^2 /Å ²	E ₀ Shift (eV)	R (%)
10c-Al ₂ O ₃ /Au/Al ₂ O ₃ calcined at 250 °C	10.4(5)	2.851(6)	0.0092(9)	4.7(6)	1.1
10c-Al ₂ O ₃ /Au/Al ₂ O ₃ calcined at 650 °C	11.6(5)	2.852(6)	0.0092(7)	3.4(5)	1.0
20c-Al ₂ O ₃ /Au/Al ₂ O ₃ calcined at 250 °C	10.2(5)	2.838(7)	0.010(1)	3.6(6)	1.0
20c-Al ₂ O ₃ /Au/Al ₂ O ₃ calcined at 650 °C	10.5(3)	2.847(4)	0.0081(6)	4.1(4)	1.2

Previously, we reported that Au₂₅(MUA)₁₈ clusters coated with 40 nm silica spheres using sol-gel chemistry also enhanced the thermal stability of Au₂₅(11-MUA)₁₈ clusters and showed similar average coordination number 10.5(6) upon calcination at 650 °C, whereas Au₂₅(MUA)₁₈ clusters on silica spheres are not thermally stable and the average particle size increased to 5.1 ± 3.2 nm after calcination at 650 °C.¹⁵ Similarly, Chen *et al.* found that Au₂₅[SC₃H₆Si(OCH₃)₃]₁₈ clusters embedded in a thick silica matrix were found to undergo moderate sintering at 600 °C and the cluster size increased to 2.2 ± 0.5 nm.⁴³ The ALD results here show that similar stabilization can be gained with much thinner alumina ALD overlayers. Nakayama *et al.* investigated the thermal stability of Au₉ clusters on ALD fabricated amorphous titania. It was found that the height distribution (AFM image) for Au₉ clusters increased from 1.7 ± 0.6 nm to 2.9 ± 1.6 nm after heat treatment at 200 °C under vacuum (10⁻⁴ mbar) for 20 min.⁴⁴ This reinforces the advantage of having carboxylic acid groups on the surface available for ALD overlayer growth.

To probe the effect of ALD alumina overcoats on the catalytic performance of the resulting materials, we carried out 4-nitrophenol reduction reactions over Au(MUA)/Al₂O₃, 10c-Al₂O₃/Au(MUA)/Al₂O₃ and 20c-Al₂O₃/Au(MUA)/Al₂O₃ catalysts calcined at 250 °C. The 4-nitrophenol reduction results are shown in Figure 3.8.⁴⁵ 4-Nitrophenol reductions have been shown by our group and others to be an effective model catalytic reaction to probe the available surface area of Au catalysts.^{27,46} After first adding the NaBH₄ reducing agent, the 4-nitrophenol solution showed a peak at 400 nm which corresponds to the nitrophenolate anion.⁴⁷⁻⁴⁸ The intensity of this peak decreases as a function of time and a new peak appeared at 300 nm which corresponds to the formation of the 4-aminophenol product.⁴⁹ In the absence of Au cluster catalysts, no activity for 4-nitrophenol reduction was observed. The rate constant for

the reaction was calculated using pseudo-first order kinetics; fits for each of the plots are shown in Figure 3.8d and values are shown in Table 3.3.⁵⁰⁻⁵¹ Several samples showed small delay times before catalytic reactions began, which is likely due to the presence of small amounts of oxygen in the system.⁵² 10c-Al₂O₃/Au(MUA)/Al₂O₃ and 20c-Al₂O₃/Au(MUA)/Al₂O₃ catalysts calcined at 250 °C have rate constants for nitrophenol reduction of $1.25 \times 10^{-2} \text{ min}^{-1}$ and $5.71 \times 10^{-3} \text{ min}^{-1}$, respectively, for nitrophenol reduction. The 20 ALD cycle catalyst showed lower activity, though still slightly higher than the uncoated catalyst ($3.70 \times 10^{-3} \text{ min}^{-1}$). This drop in catalytic activity from 10 to 20 cycles of ALD overcoating is not due to the size differences of the particles, but rather is likely due to mass transfer resistance related to the alumina overlayer.²⁴ Previous quartz crystal microbalance studies demonstrated that $\sim 1 \text{ \AA}$ alumina deposition occurs per cycle,^{31,53} thus based on these studies, the 20c-Al₂O₃/Au(MUA)/Al₂O₃ catalysts have a 1 nm greater alumina thickness than 10c-Al₂O₃/Au(MUA)/Al₂O₃ catalysts. The rate constants for 4-nitrophenol reduction reaction over Au(MUA)/Al₂O₃, 10c-Al₂O₃/Au(MUA)/Al₂O₃, and 20c-Al₂O₃/Au(MUA)/Al₂O₃ catalysts calcined at 650 °C were $7.19 \times 10^{-4} \text{ min}^{-1}$, $4.49 \times 10^{-4} \text{ min}^{-1}$ and $3.32 \times 10^{-3} \text{ min}^{-1}$, respectively (Figure 3.9). It is clear that 20c-Al₂O₃/Au(MUA)/Al₂O₃ catalysts calcined at 650 °C are more catalytically active than other two systems, which is likely due to the much smaller particle sizes seen in these samples as evidenced from EXAFS and TEM analyses.

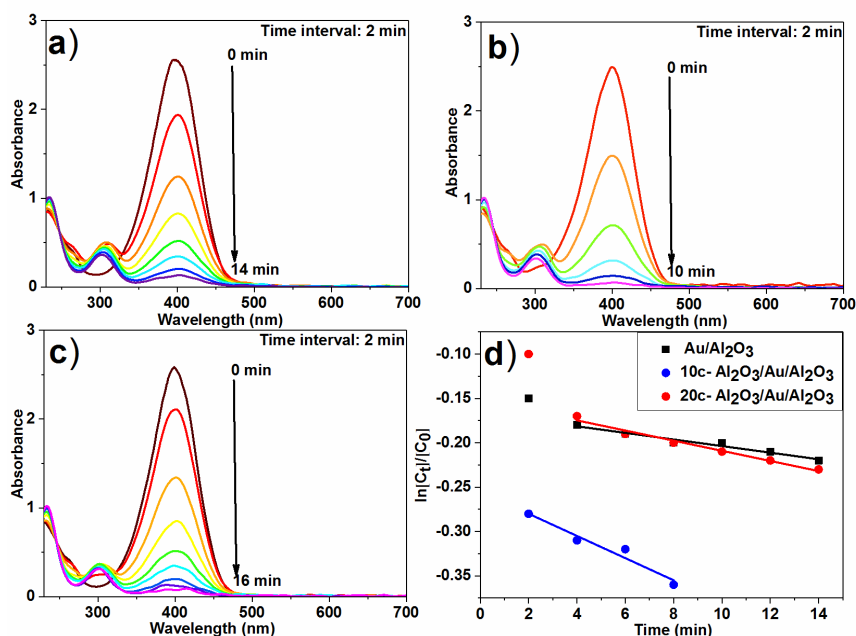


Figure 3.8: 4-Nitrophenol reduction reaction over catalyst calcined at 250 °C, a) Au(MUA)/Al₂O₃, b) 10c-Al₂O₃/Au(MUA)/Al₂O₃, c) 20c-Al₂O₃/Au(MUA)/Al₂O₃, and d) plot of $\ln[C_t]/[C_0]$ as a function of reaction time in min.

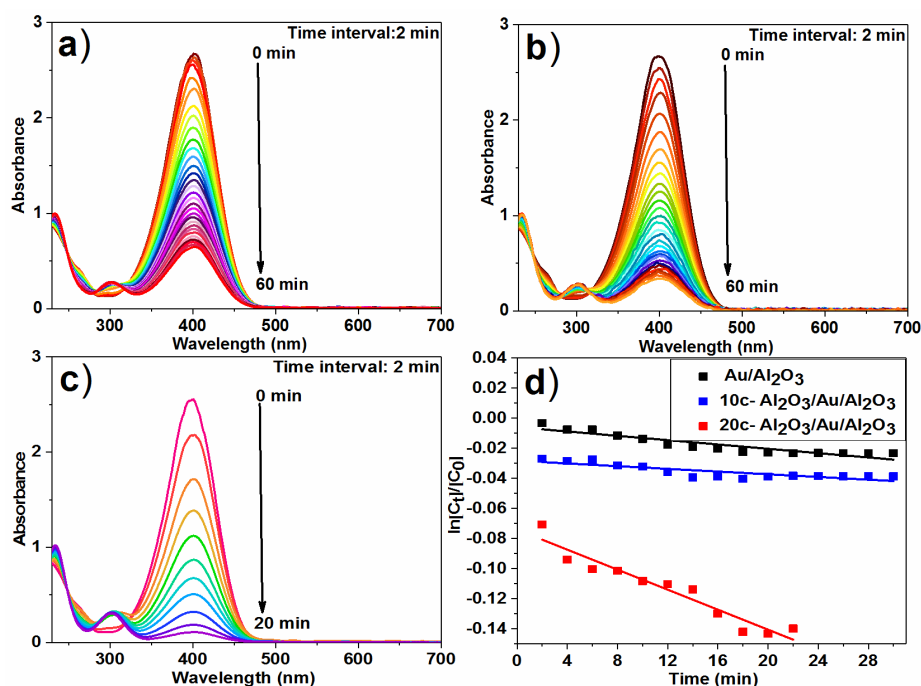


Figure 3.9: 4-Nitrophenol reduction reaction over catalyst calcined at 650 °C, a) Au(MUA)/Al₂O₃, b) 10c-Al₂O₃/Au(MUA)/Al₂O₃, c) 20c-Al₂O₃/Au(MUA)/Al₂O₃, and d) plot of ln[C_t]/[C₀] as a function of reaction time in min.

Table 3.3: Rate constant k (min⁻¹) for 4-nitrophenol reduction reaction.

Catalyst	k (min ⁻¹)*	R ² value
Au(MUA)/Al ₂ O ₃ calcined at 250 °C	$3.70 \times 10^{-3} \pm 0.0003$	0.99
10c-Al ₂ O ₃ /Au(MUA)/Al ₂ O ₃ calcined at 250 °C	$1.25 \times 10^{-2} \pm 0.001$	0.99
20c-Al ₂ O ₃ /Au(MUA)/Al ₂ O ₃ calcined at 250 °C	$5.71 \times 10^{-3} \pm 0.0004$	0.98
Au(MUA)/Al ₂ O ₃ calcined at 650 °C	$7.19 \times 10^{-4} \pm 0.0001$	0.95
10c-Al ₂ O ₃ /Au(MUA)/Al ₂ O ₃ calcined at 650 °C	$4.49 \times 10^{-4} \pm 0.0001$	0.85
20c-Al ₂ O ₃ /Au(MUA)/Al ₂ O ₃ calcined at 650 °C	$3.32 \times 10^{-3} \pm 0.0003$	0.92

3.5. Conclusions

ALD alumina-overcoated Au₂₅(MUA)₁₈/Al₂O₃ samples were synthesized using 5, 10, and 20 cycles of trimethylaluminum/water exposure. Based on TEM and EXAFS analysis, 10 and 20 cycles of alumina overcoating led to much improved stability towards sintering when compared with uncoated catalysts, with 20 cycles of ALD of alumina dramatically improving the sinter resistance of the Au clusters at high temperatures. 10 cycle-alumina ALD coatings of analogous Au₂₅(DDT)₁₈ clusters were less stable to sintering at higher temperatures, likely because alumina coatings could only form around such clusters, while alumina coatings could form on top of the Au₂₅(MUA) samples. 4-Nitrophenol reduction reactions carried out over non-coated, and 10- and 20 cycle-overcoated catalysts showed that the highest rate constants

for samples with 10 cycles of alumina deposition calcined at 250 °C; however, samples with 20 cycles of alumina deposition were much more effective catalysts after calcination at 650 °C.

3.5. References

- 1) Bharadwaj, S. S.; Schmidt, L. D. Catalytic Partial Oxidation of Natural Gas to Syngas. *Fuel Process. Technol.* **1995**, *42*, 109-127.
- (2) Ueda, A.; Oshima, T.; Haruta, M. Reduction of Nitrogen Monoxide with Propene in the Presence of Oxygen and Moisture over Gold Supported on Metal Oxides. *Appl. Catal. B* **1997**, *12*, 81-93.
- (3) Gu, D.; Tseng, J. C.; Weidenthaler, C.; Bongard, H. J.; Spliethoff, B.; Schmidt, W.; Soulimani, F.; Weckhuysen, B. M.; Schüth, F. Gold on Different Manganese Oxides: Ultra-Low-Temperature CO Oxidation over Colloidal Gold Supported on Bulk-MnO₂ Nanomaterials. *J. Am. Chem. Soc.* **2016**, *138*, 9572-9580.
- (4) Yang, C. M.; Kalwei, M.; Schüth, F.; Chao, K.J. Gold Nanoparticles in SBA-15 Showing Catalytic Activity in CO Oxidation. *Appl. Catal. A* **2003**, *254*, 289-296.
- (5) Haruta, M. Size- and Support-Dependency in the Catalysis of Gold. *Catal. Today.* **1997**, *36*, 153-166.
- (6) Valden, M.; Lai, X.; Goodman, D. W. Onset of Catalytic Activity of Gold Clusters on Titania with the Appearance of Nonmetallic Properties. *Science* **1998**, *281*, 1647-1650.
- (7) Nie, X.; Qian, H.; Ge, Q.; Xu, H.; Jin, R. CO Oxidation Catalyzed by Oxide-Supported Au₂₅(SR)₁₈ Nanoclusters and Identification of Perimeter Sites as Active Centers. *ACS Nano.* **2012**, *6*, 6014-6022.
- (8) Antonello, S.; Hesari, M.; Polo, F.; Maran, F. Electron Transfer Catalysis with Monolayer Protected Au₂₅ Clusters. *Nanoscale.* **2012**, *4*, 5333-5342.
- (9) Liu, Y.; Tsunoyama, H.; Akita, T.; Tsukuda, T. Efficient and Selective Epoxidation of Styrene with TBHP Catalyzed by Au₂₅ Clusters on Hydroxyapatite. *Chem. Commun.* **2010**, *46*, 550-552.
- (10) Martin, J. E.; Odinek, J.; Wilcoxon, J. P.; Anderson, R. A.; Provencio, P. Sintering of Alkanethiol-Capped Gold and Platinum Nanoclusters. *J. Phys. Chem. B.* **2003**, *107*, 430-434.
- (11) Choy, K. L. Chemical Vapour Deposition of Coatings. *Prog. Mater. Sci.* **2003**, *48*, 57-170.

- (12) Liu, Y.; Guerrouache, M.; Kebe, S. I.; Carbonnier, B.; Le Droumaguet, B. Gold Nanoparticles-Supported Histamine-Grafted Monolithic Capillaries as Efficient Microreactors for Flow-through Reduction of Nitro-Containing Compounds. *J. Mater. Chem. A*. **2017**, *5*, 11805-11814.
- (13) Boisselier, E.; Diallo, A. K.; Salmon, L.; Ornelas, C.; Ruiz, J.; Astruc, D. Encapsulation and Stabilization of Gold Nanoparticles with “Click” Polyethyleneglycol Dendrimers. *J. Am. Chem. Soc.* **2010**, *132*, 2729-2742.
- (14) Pablo, M. A.; Massimiliano, C.; Ferdi, S. High-Temperature-Stable Catalysts by Hollow Sphere Encapsulation. *Angew. Chem., Int. Ed.* **2006**, *45*, 8224-8227.
- (15) Sudheeshkumar, V.; Shivhare, A.; Scott, R. W. J. Synthesis of Sinter-Resistant Au@silica Catalysts Derived from Au₂₅ Clusters. *Catal. Sci. Technol.* **2017**, *7*, 272-280.
- (16) Mattevi, C.; Kim, H.; Chhowalla, M. A Review of Chemical Vapour Deposition of Graphene on Copper. *J. Mater. Chem.* **2011**, *21*, 3324-3334.
- (17) Puurunen, R. L. Surface Chemistry of Atomic Layer Deposition: A Case Study for the Trimethylaluminum/Water Process. *J. Appl. Phys.* **2005**, *97*, 121301.
- (18) George, S. M. Atomic Layer Deposition: An Overview. *Chem. Rev.* **2010**, *110*, 111-131.
- (19) Knez, M.; Nielsch, K.; Niinisto, L. Synthesis and Surface Engineering of Complex Nanostructures by Atomic Layer Deposition. *Adv. Mater.* **2007**, *19*, 3425-3438.
- (20) Groner, M. D.; Fabreguette, F. H.; Elam, J. W.; George, S. M. Low-Temperature Al₂O₃ Atomic Layer Deposition. *Chem. Mater.* **2004**, *16*, 639-645.
- (21) Wang, X.; Tabakman, S. M.; Dai, H. Atomic Layer Deposition of Metal Oxides on Pristine and Functionalized Graphene. *J. Am. Chem. Soc.* **2008**, *130*, 8152-8153.
- (22) Chen, P.; Mitsui, T.; Farmer, D. B.; Golovchenko, J.; Gordon, R. G.; Branton, D. Atomic Layer Deposition to Fine-Tune the Surface Properties and Diameters of Fabricated Nanopores. *Nano Lett.* **2004**, *4*, 1333-1337.
- (23) Ma, Z.; Brown, S.; Howe, J. Y.; Overbury, S. H.; Dai, S. Surface Modification of Au/TiO₂ Catalysts by SiO₂ via Atomic Layer Deposition. *J. Phys. Chem. C*. **2008**, *112*, 9448-9457.

- (24) Feng, H.; Lu, J.; Stair, P. C.; Elam, J. W. Alumina over-Coating on Pd Nanoparticle Catalysts by Atomic Layer Deposition: Enhanced Stability and Reactivity. *Catal. Lett.* **2011**, *141*, 512-517.
- (25) Lu, J.; Fu, B.; Kung, M. C.; Xiao, G.; Elam, J. W.; Kung, H. H.; Stair, P. C. Coking- and Sintering-Resistant Palladium Catalysts Achieved through Atomic Layer Deposition. *Science*. **2012**, *335*, 1205-1208.
- (26) Shivhare, A.; Wang, L.; Scott, R. W. J. Isolation of Carboxylic Acid-Protected Au₂₅ Clusters Using a Borohydride Purification Strategy. *Langmuir* **2015**, *31*, 1835-1841.
- (27) Shivhare, A.; Ambrose, S. J.; Zhang, H.; Purves, R. W.; Scott, R. W. J. Stable and Recyclable Au₂₅ Clusters for the Reduction of 4-Nitrophenol. *Chem. Commun.* **2013**, *49*, 276-278.
- (28) Liu, X.; Atwater, M.; Wang, J.; Huo, Q. Extinction Coefficient of Gold Nanoparticles with Different Sizes and Different Capping Ligands. *Colloids Surf. B.* **2007**, *58*, 3-7.
- (29) Zhu, M.; Aikens, C. M.; Hollander, F. J.; Schatz, G. C.; Jin, R. Correlating the Crystal Structure of a Thiol-Protected Au₂₅ Cluster and Optical Properties. *J. Am. Chem. Soc.* **2008**, *130*, 5883-5885.
- (30) Heaven, M. W.; Dass, A.; White, P. S.; Holt, K. M.; Murray, R. W. Crystal Structure of the Gold Nanoparticle [N(C₈H₁₇)₄][Au₂₅(SCH₂CH₂Ph)₁₈]. *J. Am. Chem. Soc.* **2008**, *130*, 3754-3755.
- (31) Shivhare, A.; Chevrier, D. M.; Purves, R. W.; Scott, R. W. J. Following the Thermal Activation of Au₂₅(SR)₁₈ Clusters for Catalysis by X-ray Absorption Spectroscopy. *J. Phys. Chem. C.* **2013**, *117*, 20007-20016.
- (32) Whitney, A. V.; Elam, J. W.; Zou, S.; Zinovev, A. V.; Stair, P. C.; Schatz, G. C.; Van Duyne, R. P. Localized Surface Plasmon Resonance Nanosensor: A High-Resolution Distance-Dependence Study Using Atomic Layer Deposition. *J. Phys. Chem. B.* **2005**, *109*, 20522-20528.
- (33) Avila, J. R.; Demarco, E. J.; Emery, J. D.; Farha, O. K.; Pellin, M. J.; Hupp, J. T.; Martinson, A. B. F. Real-Time Observation Of Atomic Layer Deposition Inhibition: Metal Oxide Growth on Self Assembled Alkanethiols. *ACS Appl. Mater. Inter.* **2014**, *6*, 11891-11898.

- (34) Li, M.; Dai, M.; Chabal, Y. J. Atomic Layer Deposition of Aluminum Oxide on Carboxylic Acid-Terminated Self-Assembled Monolayers. *Langmuir*. **2009**, *25*, 1911-1914.
- (35) Lee, B. H.; Lee, K. H.; Im, S.; Sung, M. M. Monolayer-Precision Fabrication of Mixed-Organic–Inorganic Nanohybrid Superlattices for Flexible Electronic Devices. *Org. Electron*. **2008**, *9*, 1146-1153.
- (36) Dainese, T.; Antonello, S.; Gascón, J. A.; Pan, F.; Perera, N. V.; Ruzzi, M.; Venzo, A.; Zoleo, A.; Rissanen, K.; Maran, F. Au₂₅(SEt)₁₈, a Nearly Naked Thiolate-Protected Au₂₅ Cluster: Structural Analysis by Single Crystal X-ray Crystallography and Electron Nuclear Double Resonance. *ACS Nano*. **2014**, *8*, 3904-3912.
- (37) MacDonald, M. A.; Chevrier, D. M.; Zhang, P.; Qian, H.; Jin, R. The Structure and Bonding of Au₂₅(SR)₁₈ Nanoclusters from EXAFS: The Interplay of Metallic and Molecular Behavior. *J. Phys. Chem. C*. **2011**, *115*, 15282-15287.
- (38) Yan, Z.; Huifeng, Q.; Rongchao, J. An Atomic-Level Strategy for Unraveling Gold Nanocatalysis from the Perspective of Au_n(SR)_m Nanoclusters. *Chem. Eur. J*. **2010**, *16*, 11455-11462.
- (39) Ramallo-López, J. M.; Requejo, F. G.; Craievich, A. F.; Wei, J.; Avalos-Borja, M.; Iglesia, E. Complementary Methods for Cluster Size Distribution Measurements: Supported Platinum Nanoclusters in Methane Reforming Catalysts. *J. Mol. Catal. A: Chem*. **2005**, *228*, 299-307.
- (40) Jentys, A. Estimation of Mean Size and Shape of Small Metal Particles by EXAFS. *Phys. Chem. Chem. Phys*. **1999**, *1*, 4059-4063.
- (41) Fritsche, H. G.; Benfield, R. E. Exact Analytical Formulae for Mean Coordination Numbers in Clusters. *Z. Phy. D: At., Mol.Clusters* **1993**, *26*, 15-17.
- (42) Benfield, R. E. Mean Coordination Numbers and the Non-metal-Metal Transition in Clusters. *J. Chem. Soc., Faraday Trans*. **1992**, *88*, 1107-1110.
- (43) Chen, H.; Liu, C.; Wang, M.; Zhang, C.; Li, G.; Wang, F. Thermally Robust Silica-Enclosed Au₂₅ Nanocluster and its Catalysis. *Chin. J. Catal*. **2016**, *37*, 1787-1793.
- (44) Al Qahtani, H. S.; Metha, G. F.; Walsh, R. B.; Golovko, V. B.; Andersson, G. G.; Nakayama, T. Aggregation Behavior of Ligand-Protected Au₉ Clusters on Sputtered Atomic Layer Deposition TiO₂. *J. Phys. Chem. C*. **2017**, *121*, 10781-10789.

- (45) Wunder, S.; Polzer, F.; Lu, Y.; Mei, Y.; Ballauff, M. Kinetic Analysis of Catalytic Reduction of 4-Nitrophenol by Metallic Nanoparticles Immobilized in Spherical Polyelectrolyte Brushes. *J. Phys. Chem. C*. **2010**, *114*, 8814-8820.
- (46) Yang, H.; Nagai, K.; Abe, T.; Homma, H.; Norimatsu, T.; Ramaraj, R. Enhanced Catalytic Activity of Gold Nanoparticles Doped in a Mesoporous Organic Gel Based on Polymeric Phloroglucinol Carboxylic Acid–Formaldehyde. *ACS Appl. Mater. Inter.* **2009**, *1*, 1860-1864.
- (47) Dong, F.; Guo, W.; Park, S. K.; Ha, C. S. Controlled Synthesis of Novel Cyanopropyl Polysilsesquioxane Hollow Spheres Loaded with Highly Dispersed Au Nanoparticles for Catalytic Applications. *Chem. Commun.* **2012**, *48*, 1108-1110.
- (48) Vysakh, A. B.; Babu, C. L.; Vinod, C. P. Demonstration of Synergistic Catalysis in Au@Ni Bimetallic Core–Shell Nanostructures. *J. Phys. Chem. C*. **2015**, *119*, 8138-8146.
- (49) Deng, Y.; Cai, Y.; Sun, Z.; Liu, J.; Liu, C.; Wei, J.; Li, W.; Liu, C.; Wang, Y.; Zhao, D. Multifunctional Mesoporous Composite Microspheres with Well-Designed Nanostructure: A Highly Integrated Catalyst System. *J. Am. Chem. Soc.* **2010**, *132*, 8466-8473.
- (50) Marc, S.; Frank, P.; Yu, M.; Yan, L.; Björn, H.; Matthias, B.; Astrid, G.; Markus, D.; Johannes, P.; Uwe, G. Mechanism of the Formation of Amorphous Gold Nanoparticles within Spherical Polyelectrolyte Brushes. *Macromol. Chem. Phys.* **2007**, *208*, 1542-1547.
- (51) Baruah, B.; Gabriel, G. J.; Akbashev, M. J.; Booher, M. E. Facile Synthesis of Silver Nanoparticles Stabilized by Cationic Polynorbornenes and their Catalytic Activity in 4-Nitrophenol Reduction. *Langmuir*. **2013**, *29*, 4225-4234.
- (52) Menumorov, E.; Hughes, R. A.; Neretina, S. Catalytic Reduction of 4-Nitrophenol: A Quantitative Assessment of the Role of Dissolved Oxygen in Determining the Induction Time. *Nano Lett.* **2016**, *16*, 7791-7797.
- (53) Ott, A. W.; Klaus, J. W.; Johnson, J. M.; George, S. M. Al₃O₃ Thin Film Growth on Si(100) Using Binary Reaction Sequence Chemistry. *Thin Solid Films*. **1997**, *292*, 135-144.

CHAPTER 4

Probing the Thermal Stability of (3-mercaptopropyl)trimethoxysilane-Protected Au₂₅ Clusters by *in situ* Transmission Electron Microscopy

This chapter investigates the synthesis and the thermal stability of (3-mercaptopropyl)trimethoxysilane protected Au₂₅ clusters on SBA-15 supports. An environmental *in situ* TEM technique was utilized to probe the sintering behavior of Au₂₅ clusters on mesoporous silica (SBA-15) during thermal treatment up to 650 °C. It was observed that the particle migration and coalescence mechanism is more dominant at high temperatures and is responsible for particle sintering.

This chapter is a manuscript that is in preparation for publication. The first draft of the manuscript was written by myself. *in situ* TEM analyses were done with the assistance of Dr. Charles Soong and Dr. Stas Dogel at Hitachi.

4.1. Abstract

High-surface-area gold catalysts are promising catalysts for a number of selective oxidation and reduction reactions, but typically suffer catalyst deactivation at higher temperatures. The major reason for catalyst deactivation is sintering, which can be triggered via two mechanisms: particle migration and coalescence, and Ostwald ripening. Herein, we report a direct method to synthesize Au₂₅ clusters stabilized with 3-mercaptopropyltrimethoxysilane (MPTS) ligands. The sintering of Au₂₅(MPTS)₁₈ clusters on mesoporous silica (SBA-15) was monitored by using an environmental *in situ* TEM technique. Results showed that agglomeration of smaller particles was accelerated by increased mobility of particles during heat treatments, while growth of immobile particles occurred via diffusion of atomic species from smaller particles. The mobility of the Au clusters could be alleviated by fabricating overlayers of silica around the clusters. The resulting materials showed tremendous sinter resistance at temperatures up to 650 °C as shown by *in situ* TEM and EXAFS analysis.

4.2. Introduction

Gold was considered a chemically inert and catalytically inactive metal until the 1980s when Huruta and others showed that Au nanoparticles below 5 nm in size supported on metal oxides were active for low-temperature CO oxidation.¹⁻² There is a growing interest in utilizing Au clusters, especially Au₂₅(SR)₁₈ clusters, as ideal model catalysts.³ Au clusters show remarkable catalytic activity for low-temperature catalytic CO oxidation reactions,⁴⁻⁵ oxidation of styrene,⁶⁻⁷ hydrogenation of unsaturated hydrocarbons,⁸⁻⁹ and reduction of 4-nitrophenol.¹⁰⁻¹¹ However, Au clusters are subject to sintering under high-temperature reaction conditions.¹² Immobilization of clusters on metal oxide supports such as silica, alumina, and titania can help to minimize sintering to some extent. Since many industrial reactions such as catalytic methane combustion, reforming of hydrocarbons, and automobile exhaust control exceed 600 °C, industrial applications of Au as a catalyst is restricted.

Catalyst sintering is mainly ascribed to two mechanisms; Ostwald ripening and particle migration and coalescence.¹³ One of the biggest challenges is discriminating between these two mechanisms, particularly when samples have broad size distributions. Ostwald ripening is a thermodynamically driven process than involves dissolution and diffusion of atoms or atomic species from smaller particles to larger particles. As a result, the average size of the particles is increased. The Ostwald ripening mechanism has been observed in several supported metal

nanoparticles such as Au,¹⁴ Pd,¹⁵ and Pt,¹⁶ particularly in the presence of oxidizing chemical species at high temperatures. It should be noted that Ostwald ripening is driven by thermodynamics, and in theory this driving force is absent for perfectly monodisperse clusters,¹⁷ and indeed experimental studies have shown that monodispersity of particles suppresses Ostwald ripening.¹⁸⁻²⁰ Wettergren *et al.* reported that the driving force for the Ostwald ripening mechanism can be eliminated through the size selection of clusters.¹⁸ Monodispersed Pt clusters are found to be more stable than the clusters with two different sizes. In the particle migration and coalescence mechanism, sintering happens due to the Brownian motion of clusters/nanoparticles, followed by the coalescence of adjacent particles. The mobility of small particles increases dramatically at the Tammann temperature, which is the temperature where the surface atoms become mobile.²¹ Particle migration and coalescence mechanisms can often be eliminated by physical confinement of clusters in a metal oxide or metal-organic framework shell.²²

Several methods have been reported to control the particle aggregation and sintering upon calcination. Physical confinement in a metal oxide shell is an efficient strategy to minimize the mobility of metal nanoparticles/clusters and results in enhanced thermal stability.²³⁻²⁶ Previously our group reported that a silica shell with 40 nm thickness enhances the thermal stability of mercaptoundecanoic acid protected Au₂₅ clusters.²⁷ Similarly, we achieved large improvements in thermal stability of Au₂₅(MUA)₁₈ clusters with 10 and 20 cycles of alumina coating via atomic layer deposition.²⁸ However, a mass transfer issue associated with the silica and/or alumina shell was observed in both cases, which is problematic for heterogeneous catalysis. Others have similarly shown that physical confinement within a metal-organic framework offers improved thermal stability for Au clusters, but have also noted that this typically comes with a mass transport cost.²⁹

Another approach for reducing the sintering behavior of catalysts is improvement of metal-support interactions. Strong metal-support interactions at mild temperatures can be achieved by functionalization of the catalyst support with bifunctional ligands with thiolate or amine terminal groups which have been reported by several groups.³⁰⁻³² Several studies showed that 3-mercaptopropyltrimethoxysilane (MPTS) can act as a linker, in which the thiol group strongly adheres to the surface of metal particles and the silane group anchors to silica support through Si-O-Si linkages.³³⁻³⁵ An alternative method for facilitating the metal-support interaction is the impregnation of MPTS stabilized clusters on the catalyst support. MPTS

ligands on the Au₂₅ clusters can allow the fabrication of silica coating around the clusters via hydrolysis and condensation with tetraethylorthosilicate (TEOS).²³⁻²⁴

Here we report a direct method for the synthesis of Au₂₅ clusters with MPTS stabilizers. To the best of our knowledge, this is the first direct synthesis report of Au clusters using this ligand, as others have reported the synthesis of MPTS-protected Au₂₅ clusters via ligand exchange of polydisperse Au_nL_m clusters (where L is glutathione/ triphenylphosphine).¹⁷⁻¹⁸ The mobility of Au clusters on mesoporous silica supports under heat treatment was monitored by environmental *in situ* TEM analysis, which suggested that Brownian motion of smaller particles is responsible for initial sintering, while the growth of larger particles occurred via Ostwald ripening. Visual evidence is reported for the particle migration and coalescence mechanism under high-temperature heat treatments. The mobility of Au₂₅(MPTS)₁₈ clusters was lowered by fabricating overlayers of silica via secondary TEOS treatments. The resulting materials showed tremendous sinter-resistance, which was confirmed by EXAFS and *in situ* TEM analysis. However, at high temperatures, some growth in particle size was still observed, which is likely due to slow movement of particles on the support.

4.3. Materials and Methods

4.3.1. Materials

Hydrogen tetrachloroaurate(III) trihydrate (HAuCl₄·3H₂O; 99.9% on metal basis, Aldrich), (3-mercaptopropyl)trimethoxysilane(MPTS; 95%, Sigma-Aldrich), tetraoctylammonium bromide (TOAB; 98%, Aldrich), sodium borohydride (NaBH₄; 98%, EMD), tetraethylorthosilicate (TEOS, 98%, Aldrich), triblock copolymer Pluronic P123 (PEO₂₀PPO₇₀PEO₂₀), and hydrochloric acid (HCl; 36%, EMD) were used as received. Tetrahydrofuran (THF; high purity) and ethanol (100%) were purchased from EMD. Milli-Q water (H₂O) was used for synthesis.

4.3.2. Synthesis of Au₂₅(MPTS)₁₈ clusters

100 mg of HAuCl₄·3H₂O and 0.1649 g of TOAB (1.2 equiv.) were added to 20 mL dry THF. This was followed by the addition of MPTS (240 uL, 5 equiv.). Upon the addition of MPTS, the solution became colourless. The solution was then cooled by an ice bath, and then 0.0941 g of NaBH₄ (10 equiv.) in ethanol (10 mL) was added dropwise. The solution was stirred at room temperature for 4 days. The residue was removed by centrifugation and Au₂₅(MPTS)₁₈

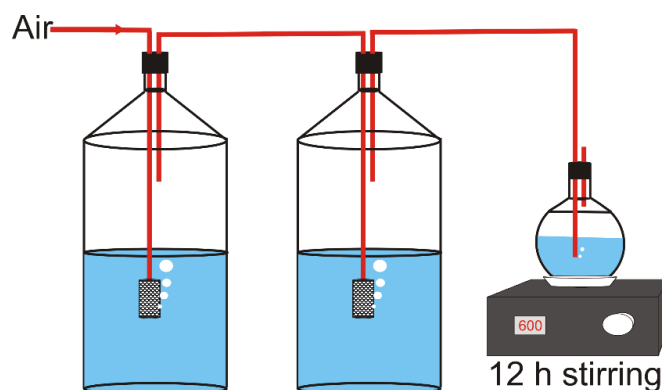
clusters remained in the supernatant THF solution. $\text{Au}_{25}(\text{MPTS})_{18}$ clusters in THF solution were used for impregnation on SBA-15.

4.3.3. Synthesis of SBA-15

SBA-15 was synthesized by the sol-gel and hydrothermal method.³⁶ In this procedure, 4.0 g of Pluronic 123 was dissolved in 120 g of 2.0 M HCl solution, followed by the addition of 8.5 g of TEOS. The resulting mixture was stirred for 20 h at 35 °C. The obtained gel was transferred into an autoclave and then kept in an oven at 80 °C for 12 h. The solid residue was washed with water several times and dried at 100 °C. Finally, the Pluronic 123 template was removed by calcination at 550 °C for 3 h under air. 10.0 mg of $\text{Au}_{25}(\text{MPTS})_{18}$ clusters in THF solution were deposited on 200.0 mg of SBA-15 by wet impregnation. For brevity, we refer to this catalyst as $\text{Au}_{25}(\text{MPTS})_{18}/\text{SBA-15}$. After immobilization, the catalyst was washed with water and THF several times. The resulting material was calcined at 250 °C, 450 °C, and 650 °C for 3 h.

4.3.4. Synthesis of thin overlayer on $\text{Au}_{25}(\text{MPTS})_{18}$ clusters on SBA-15.

The SBA-15 supported $\text{Au}_{25}(\text{MPTS})_{18}$ clusters (100 mg) were dispersed in 50 mL ethanol in a round-bottom flask, followed by the addition of 100 μl of TEOS. After this, air saturated with moisture was bubbled through the solution for a 12 h period while stirring the flask at 600 rpm, as shown in Scheme 4.1.³⁷ The air flow was maintained as 50 mL/min by mass flow controller. The solid was then collected by centrifugation and washed with ethanol and H_2O several times. For brevity, we refer to this catalyst as $\text{TEOS}/\text{Au}_{25}(\text{MPTS})_{18}/\text{SBA-15}$. The resulting material was calcined at 250 °C, 450 °C, and 650 °C for 3 h. For EXAFS analysis, materials were also calcined at 350 °C and 550 °C.



Scheme 4.1: Schematic representation of experimental setup to introduce moisture to the ethanolic TEOS solution for silica coating.

4.3.5. Characterization

UV-Vis absorption spectra of the Au₂₅(MPTS)₁₈ clusters were recorded using a Varian Cary 50 Bio UV-Vis spectrometer. Transmission Electron Microscopy (TEM) imaging was performed with a HT7700 TEM operating at 100 kV. Silica supported samples were dispersed in ethanol before drop-casting on a Cu TEM grid coated with carbon film. ImageJ software was used to calculate average particle sizes and standard deviations and create size distribution histograms.³⁸ The sintering behavior of the catalysts at various temperatures was monitored by a field emission HF3300 TEM instrument operating at 300 kV. An electron transparent silicon nitride grid was used for TEM analysis. The Au cluster sample was dispersed in ethanol and a thin film of the sample was deposited on the grid. An external heating device was attached to a heating coil in the middle of silicon nitride chip. The heating rate for the sample was 10 °C /s. The oxygen pressure was maintained at 1 Pa during TEM measurements. The gas was restricted near the specimen through pressure-controlled apertures, and a differential pumping design helped retain the vacuum in other parts of the column. Extended X-ray Absorption Fine Structure (EXAFS) spectroscopic analysis was performed at HXMA beamline 061D-1 (energy range 5–30 keV, resolution $1 \times 10^{-4} \Delta E/E$) at the Canadian Light Source. All data were collected in transmission mode. The energy for the Au-L₃ edge (11,919 eV) was selected by using a Si(111) double crystal monochromator with a Rh-coated 100 nm long KB mirror. Higher harmonics were removed by detuning the double crystal monochromator. Data fitting was carried out using the Demeter software package.³⁹ To fit the data, the amplitude reduction factor for Au data was fixed at 0.84, which was the value obtained from fitting of the Au foil data. Powder X-Ray diffraction data was collected using a Rigaku Ultima IV X-Ray diffractometer equipped with a Cu source (wavelength 1.5 Å).

4.4. Results and Discussion

Au₂₅(MPTS)₁₈ clusters in THF showed three distinct absorption peaks at 680 nm, 440 nm, and 400 nm, as shown in Figure 4.1a. These absorption bands in the UV-Vis region are due to HOMO-LUMO transitions and are similar to those seen in Au₂₅(SR)₁₈ clusters protected with other ligands such as phenylethanethiol, mercaptoundecanoic acid, and dodecanethiol.^{11,40-42} This UV-Vis spectrum is also in good agreement with the spectra of Au₂₅(MPTS)₁₈ clusters that were formed by a ligand exchanged method by Pradeep and coworkers.²³ Figure 4.1b shows the TEM image of the Au₂₅(MPTS)₁₈ clusters, and the average diameter of clusters was found to be 0.8 ± 0.2 nm, which is comparable to that of Au₂₅(SR)₁₈ clusters protected with other ligands and near the expected size for Au₂₅(SR)₁₈ clusters.⁴³

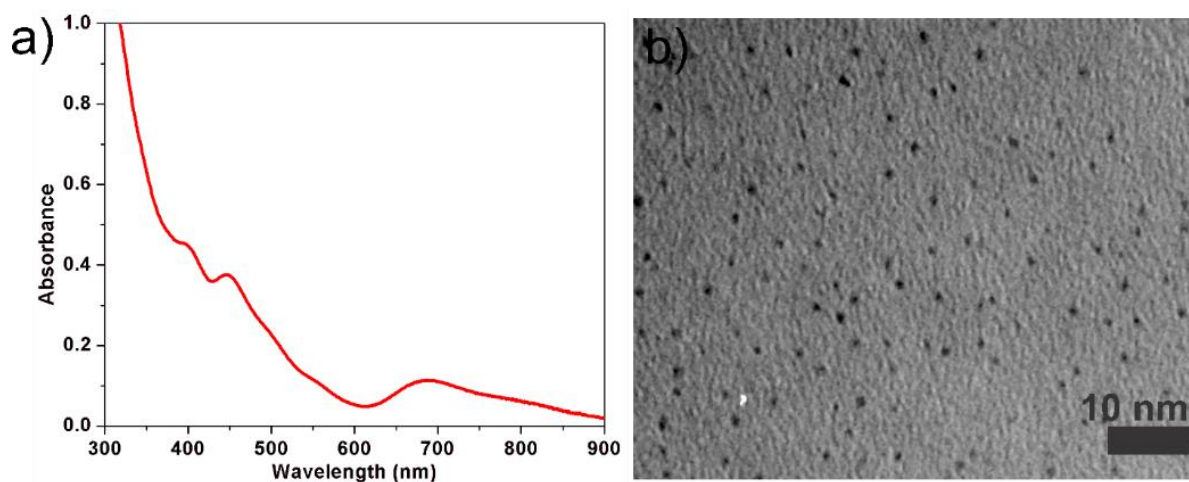


Figure 4.1: a) UV-Vis spectra and b) TEM image of $\text{Au}_{25}(\text{MPTS})_{18}$ clusters.

Au L_3 edge EXAFS analysis was further used to evaluate the basic structure of the $\text{Au}_{25}(\text{MPTS})_{18}$ clusters, and this analysis was performed in transmission mode on the HXMA beamline at the Canadian Light Source. Figure 4.2 shows the Au L_3 -edge k-space and R-space spectra of the TEOS-treated $\text{Au}_{25}(\text{MPTS})_{18}/\text{SBA-15}$ clusters before calcination. Previous X-ray crystallographic studies have shown that $\text{Au}_{25}(\text{SR})_{18}$ clusters have a core-shell morphology: the core consists of a 13-atom icosahedron, in which one central Au atom is surrounded by 12 Au atoms.^{40, 44-45} Twelve out of twenty faces of the icosahedron are covered by six staple motifs; each staple motif has S-Au-S-Au-S unit in which each S atom is directly attached to Au atoms. A multi-shell peak-fitting approach that was documented by the Zhang group was used to fit the data in which there are one Au-S and three Au-Au contributions.⁴⁶ Previously, our group used a similar multishell approach for the fitting of Au_{25} clusters protected with mercaptoundecanoic acid, hexanethiol, and phenylethanethiol.^{27, 47} The Au-S model that was derived from standard $\text{Au}_{25}(\text{SR})_{18}$ clusters was used to fit the Au-S contribution. After fitting the parameters for Au-S scattering, those values were fixed, followed by fitting the first shell coordination of all three Au-Au contributions. Based on the crystal structure of clusters, the coordination number of these three Au-Au contributions was fixed. Table 4.1 shows the EXAFS fitting parameters. The interatomic distance between Au and S atoms was 2.30(1) Å, which is consistent with the crystallographic data of other $\text{Au}_{25}(\text{SR})_{18}$ clusters (SR= phenylethanethiol).⁴⁰ The first Au-Au contribution, which appeared at 2.83(1) Å, is due to the distance from central Au atom to 12 surface atoms of the icosahedron core, and also some interactions between adjacent surface Au atoms. The second Au-Au contribution appeared at 3.09(9) Å and involves adjacent Au atoms on the surface of the icosahedron, while the third

contribution at 3.37(8) Å is due to surface-staple Au interactions. This fitting result was in good agreement with that of Au₂₅(SR)₁₈ clusters with other ligands.²⁸

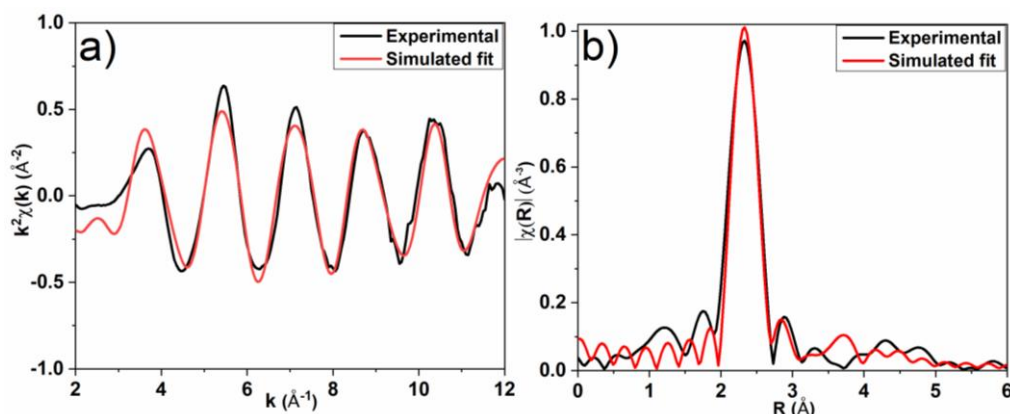


Figure 4.2: Au L₃ edge EXAFS fitting in a) k-space and b) R-space of as-synthesized TEOS-treated Au₂₅(MPTS)₁₈ clusters on SBA-15.

Table 4.1: EXAFS fitting parameters of as-synthesized TEOS-treated Au₂₅(MPTS)₁₈ clusters on SBA-15.

Bond	CN	R/Å	$\sigma^2 / \text{Å}^2$	E _o Shift(eV)	R (%)
Au-S	1.3	2.30(1)	0.0004(4)	8.4(9)	2.0
Au-Au(core)	1.44	2.83(1)	0.01(1)	8.4(9)	
Au-Au(surf)	1.92	3.09(9)	0.009(8)	8.4(9)	
Au-Au(staple)	2.88	3.37(8)	0.010(9)	8.4(9)	

Previously, several groups reported that MPTS ligands on Au clusters can facilitate the growth of silica overcoats around the clusters.²⁴ This can lead to strong interaction with the silica support, as well as helping to create further silica layers during hydrolysis with TEOS. It is well known that high concentrations of H₂O can lead to an increase in the hydrolysis rate, resulting in the formation of silica spheres.⁴⁸ Thus, water was slowly brought into the system in the gas phase (as shown in Scheme 4.1) to slow the rate of hydrolysis and condensation of the TEOS precursor, and thus allow for the generation of silica overlayers. It should be noted that we were not able to image the silica overlayers by TEM, which is likely due to the lack of contrast between SBA-15 and silica overlayer. However, calcination results shown below show the tremendous impact of such overlayers on sintering behavior. No significant change was

seen in the average particle size of $\text{Au}_{25}(\text{MPTS})_{18}$ clusters on SBA-15 before and after TEOS treatment, as they were measured to be 0.9 ± 0.3 nm and 1.0 ± 0.3 nm respectively.

To probe the thermal stability, $\text{Au}_{25}(\text{MPTS})_{18}$ clusters on SBA-15 before and after TEOS treatment were calcined at 250 °C, 450 °C, and 650 °C for 3 h in air and analyzed by TEM, as shown in Figure 4.3. Considerable sintering was observed in SBA-15-supported $\text{Au}_{25}(\text{MPTS})_{18}$ clusters in the absence of any silica overlayers, with Au particle sizes increasing to 3.9 ± 2.3 nm at 250 °C, 10.5 ± 3.3 nm at 450 °C, and 100.0 ± 27.4 nm at 650 °C, respectively. These results are consistent with work by Das and coworkers who found that $\text{Au}_{25}(\text{SR})_{18}$ clusters are not sufficiently stabilized by incorporating them into two-dimensional mesoporous silica templates alone.³¹ In contrast, TEOS-treated catalysts showed negligible size changes after heat-treatment at 250 °C, as shown in Figure 4.4. The average particle size for 250 °C-treated, 450 °C-treated and 650 °C-treated TEOS/ $\text{Au}_{25}(\text{MPTS})_{18}$ /SBA-15 samples were measured to be 1.4 ± 0.4 nm, 2.1 ± 0.8 nm and 3.2 ± 0.9 nm respectively. Even after high-temperature heat treatment, particles with 0.8 nm in size were still observed. It is clear that TEOS-treated clusters showed much improved stability toward sintering. These results indicate the formation of additional silica overlayers during TEOS treatment under a moisture atmosphere that provided significant thermal stability to the clusters.

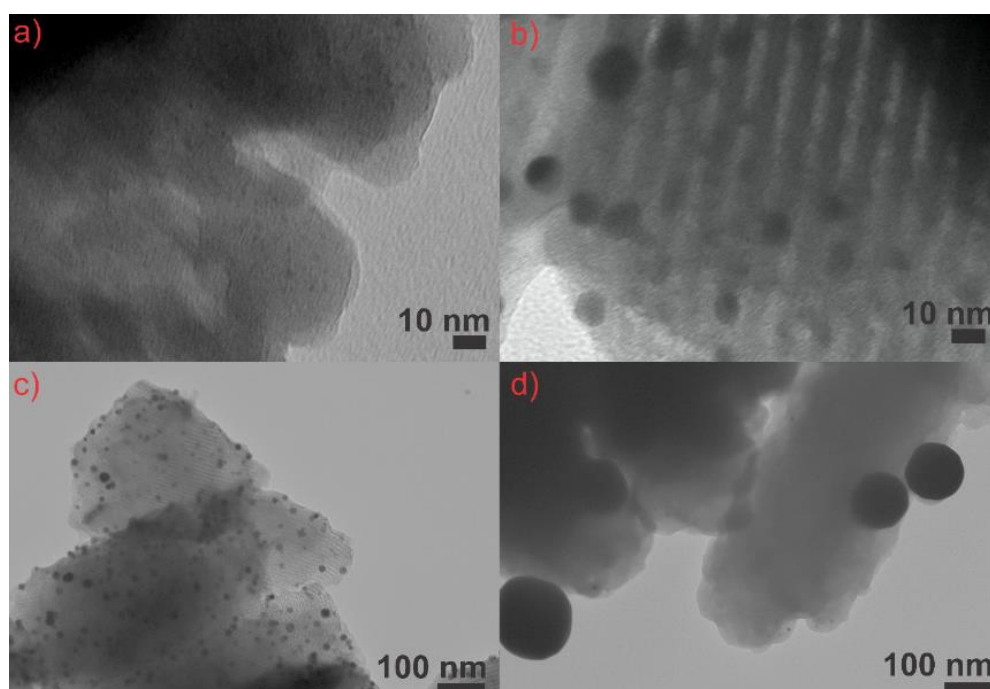


Figure 4.3: TEM images of $\text{Au}_{25}(\text{MPTS})_{18}$ /SBA-15, a) as-synthesized, b) calcined at 250 °C, c) 450 °C, and d) 650 °C for 3 h.

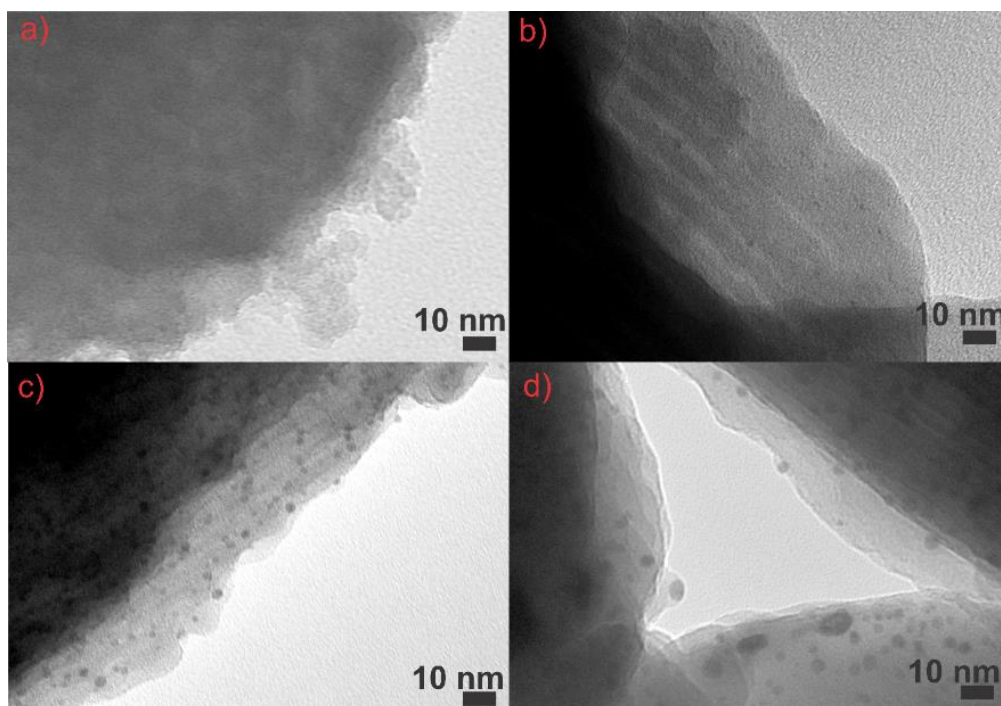


Figure 4.4: TEM images of TEOS/Au₂₅(MPTS)₁₈/SBA-15, a) as-synthesized, b) calcined at 250 °C, c) 450 °C, and d) 650 °C for 3 h.

Figure 4.5 shows the X-ray diffraction patterns of Au₂₅(MPTS)₁₈ clusters on SBA-15 calcined at different temperatures. For Au₂₅(MPTS)₁₈ clusters on SBA-15, a small broad peak due to fcc Au was seen after calcination at 250 °C, and this peak became sharper at 450 °C as other peaks due to fcc Au also emerged.⁴⁹ The average size of Au particles was calculated using the Scherrer equation and found to be 4.0 nm at 250 °C and 13.3 nm at 450 °C, which is consistent with TEM images above. Due to the presence of small Au clusters, as-synthesized TEOS/Au₂₅(MPTS)₁₈/SBA-15 systems did not show any characteristic X-ray diffraction pattern for the clusters.⁵⁰⁻⁵³ A broad peak was observed at 23° which is due to the X-ray diffraction pattern of amorphous silica.⁵⁴ After calcination at 250 °C, no significant change was observed. Further calcination at 450 °C resulted in the appearance of a broad peak at 38° which is characteristic of the (111) peak of fcc Au.⁵⁵ The 650 °C-treated sample showed a number of peaks consistent with fcc Au albeit with significant broadening, which implies the presence of very small crystallites.⁵⁶ Scherrer particle size analysis showed that the Au nanoparticles were an average size of 2.2 nm at 450 °C and 6.5 nm at 650 °C.

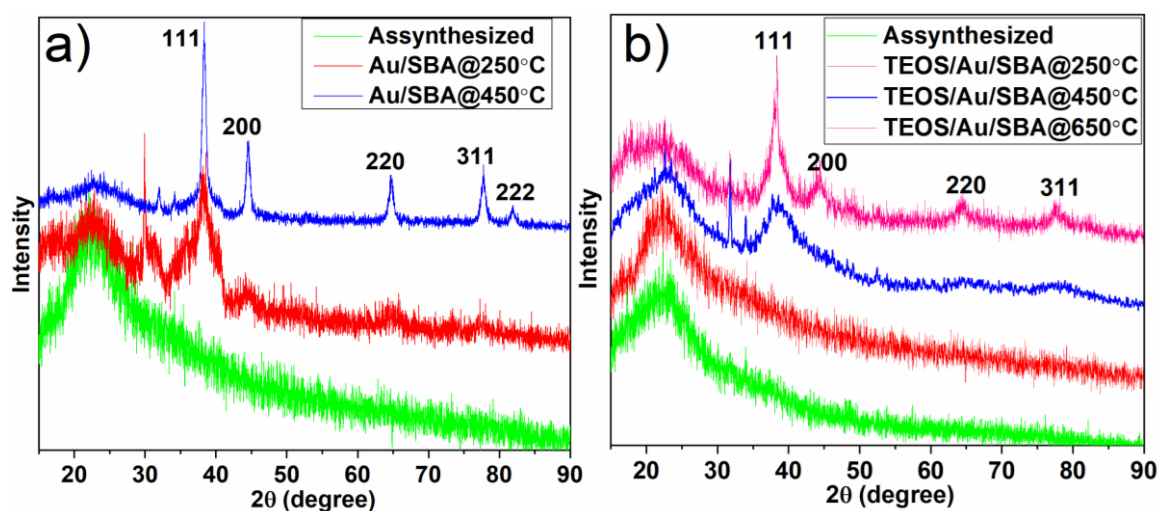


Figure 4.5: XRD spectra of a) $\text{Au}_{25}(\text{MPTS})_{18}/\text{SBA}$, and b) $\text{TEOS}/\text{Au}_{25}(\text{MPTS})_{18}/\text{SBA}$.

To further follow the thermal stability of $\text{Au}_{25}(\text{MPTS})_{18}$ clusters, Au- L_3 edge EXAFS analysis was also carried out after calcination of the clusters. Figure 4.6a and 4.6b show the Au- L_3 edge R-space of the untreated and TEOS-treated $\text{Au}_{25}(\text{MPTS})_{18}/\text{SBA}-15$ samples calcined at different temperatures, while fitted data are shown in Table 4.2. Figures 4.7 shows the Au- L_3 edge k-space and R-space EXAFS spectra and fits of untreated $\text{Au}_{25}(\text{MPTS})_{18}/\text{SBA}-15$ materials calcined at 250 °C and 650 °C. In all cases, the EXAFS results well agree with TEM particle size measurements. The EXAFS results strongly support that the $\text{TEOS}/\text{Au}_{25}(\text{MPTS})_{18}/\text{SBA}-15$ system shows excellent sinter-resistance upon calcination up to 550 °C, which is likely due to the formation of a silica coating around the clusters during the TEOS treatment. A major change in particle size was observed during 550-650 °C-thermal treatment which is like due to the deformation of pore walls. Rombi *et al.* reported that disruption of ordered pore structure of SBA-15 occurred under H_2/He -thermal treatments at 600 °C resulted in sintering of Au nanoparticles.⁵⁷ After calcination at 250 °C, the Au-S contribution of TEOS-treated $\text{Au}_{25}(\text{MPTS})_{18}$ clusters on SBA-15 was slightly reduced, and the Au-Au contribution was slightly increased, indicating that this is the transition temperature where the thiol ligands begin to be lost from the Au surface. Since the isolation of all three Au-Au contributions was not possible, the use of the previous Au_{25} model for fitting was not done. Thus, Au-S and Au-Au shells from Au_2S and Au fcc structural models were used for data fitting. The first shell coordination number for Au-S and Au-Au contributions were found to be 1.3(2) and 3.5(7), respectively. In contrast, greater removal of thiolate ligands was observed for untreated $\text{Au}_{25}(\text{MPTS})_{18}$ clusters that were calcined at 250 °C. At this temperature $\text{Au}_{25}(\text{MPTS})_{18}/\text{SBA}-15$ catalysts had a significantly lower Au-S CN, 0.7(2), while the Au-Au

CN for Au-Au increased to 7.0(9). These results for the untreated and treated samples are consistent with earlier TEM and XRD results that suggest that the TEOS-treated clusters are much more stable to calcination than the untreated system. Previous work has shown that ligands such as phenylethanethiol, mercaptoundecanoic acid, and hexanethiol begin to be lost at 150 °C and are completely removed from Au surfaces in Au clusters by 250 °C.^{7, 47, 58} Unlike other thiol ligands, the complete removal of MPTS ligands did not occur at 250 °C, which is likely due to the strong anchoring of the clusters to the SBA-15 support.³¹ The additional stability of the MPTS ligand that was observed in the TEOS/Au₂₅(MPTS)₁₈/SBA-15 system likely arises from the anchoring of the Au₂₅ clusters to the silica overlayers as well.

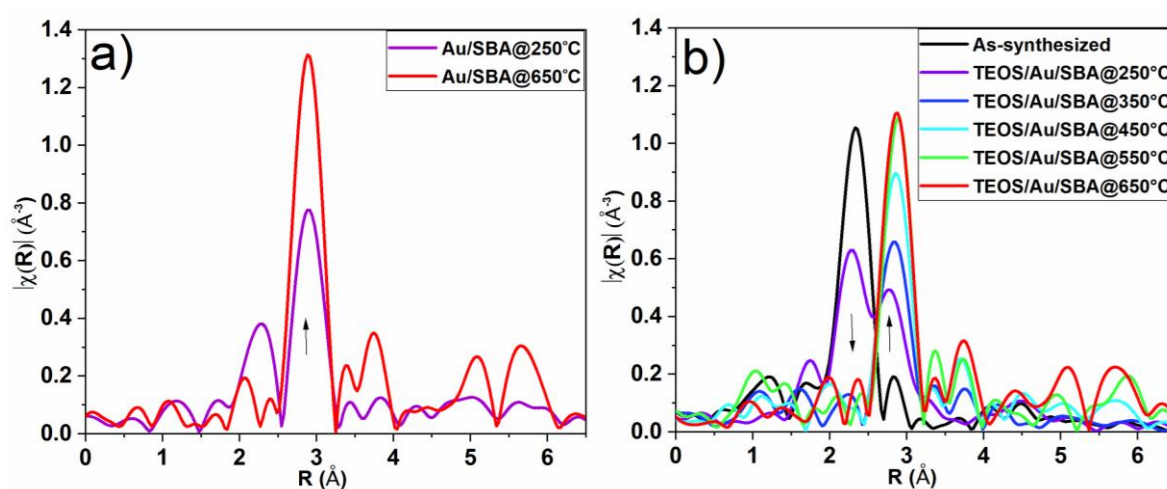


Figure 4.6: Au L₃-edge EXAFS fitting in phase corrected R-space of a) Au₂₅(MPTS)₁₈/SBA-15 calcined at 250 °C and 650 °C and b) TEOS/Au₂₅(MPTS)₁₈/ SBA-15 materials calcined at temperatures between 250 °C and 650 °C.

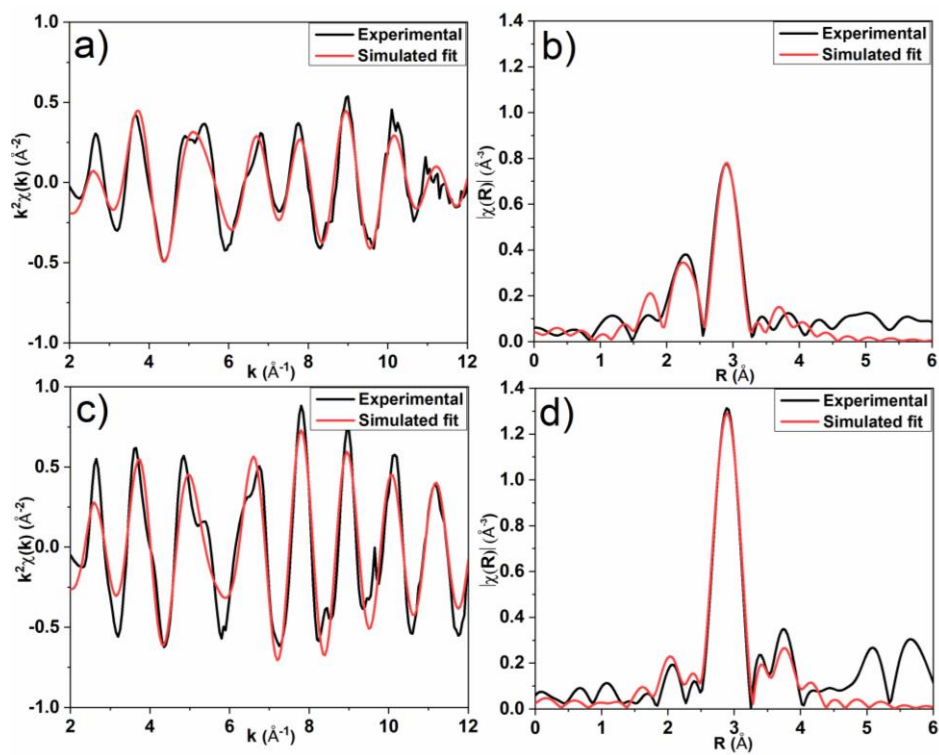


Figure 4.7: Au L₃-edge EXAFS fitting in phase-corrected k- (left) space and R- (right) space of Au₂₅(MPTS)₁₈/SBA calcined at a) & b) 250 °C, and c) & d) 650 °C.

Table 4.2: EXAFS fitting parameters of untreated and TEOS-treated Au₂₅(MPTS)₁₈/SBA-15 materials calcined at different temperatures.

Sample	Calcination T (°C)	Type	CN	R/Å	$\sigma^2 / \text{Å}^2$	E ₀ Shift(eV)	R (%)
Au/SBA-15	250 °C	Au-S	0.7(2)	2.28(1)	0.001(2)	4.8(8)	1.7
		Au-Au	7.0(9)	2.856(7)	0.008(1)		
	650 °C	Au-Au	12.0(5)	2.851(6)	0.0082(9)	4.7(6)	1.0
TEOS/Au/SBA-15	250 °C	Au-S	1.3(2)	2.293(1)	0.002(1)	5(2)	1.8
		Au-Au	3.5(7)	2.79(3)	0.013(5)		
	350 °C	Au-Au	7.0(1)	2.81296)	0.010(2)	3.4(5)	1.9
	450 °C	Au-Au	9.7(5)	2.838(5)	0.009(1)	4.0(5)	1.0
	550 °C	Au-Au	9.9(5)	2.848(6)	0.008(1)	5.2(6)	1.7
	650 °C	Au-Au	10.8(5)	2.852(6)	0.0072(7)	3.4(5)	1.9

Figure 4.8 shows the fitted Au-L₃ edge k-space and R-space EXAFS spectra of TEOS-treated Au₂₅(MPTS)₁₈/SBA-15 materials calcined at temperatures from 250 °C to 650 °C. The Au-S contribution was not observed in the TEOS/Au₂₅(MPTS)₁₈/SBA-15 sample after calcination at 350 °C. The absence of an Au-S contribution indicates that the complete removal of thiol ligands from the gold surface occurred after thermal treatment at 350 °C. The first shell coordination for Au-Au contribution was measured to be 7.0(1), which suggests the Au clusters have grown to nanoparticles with an average particle size of ~1.5 nm.^{55, 59-60} Marinkovic *et al.* theoretically calculated the average CN of cuboctahedron core of Au clusters that were 1.41 nm in diameter and found that the first shell CN is close to 7.8.⁶¹ Further calcination at 450 °C and 550 °C led to a slight increase in the average Au-Au CN, which was found to be 9.7(5) and 9.9(5), respectively. First shell coordination numbers of *ca.* 9.7 imply an average particle size of approximately 1.9-2.4 nm and an average CN 9.9 suggests that the size of the particles is in the range of 2.4-2.8 nm.⁶¹ In the case of 650 °C-treated catalysts, the average first shell CN was found to be 10.8(5), which indicates an average particle size of about 3-3.5 nm.⁶¹ Thus, EXAFS results indicate that some growth in particle size occurred after 650 °C treatment which is in good agreement with TEM results. In contrast, the average first shell coordination number of the uncoated Au₂₅(MPTS)₁₈/SBA-15 system after calcination at 650 °C was measured to be ~12, indicating the formation of bulk Au particles.

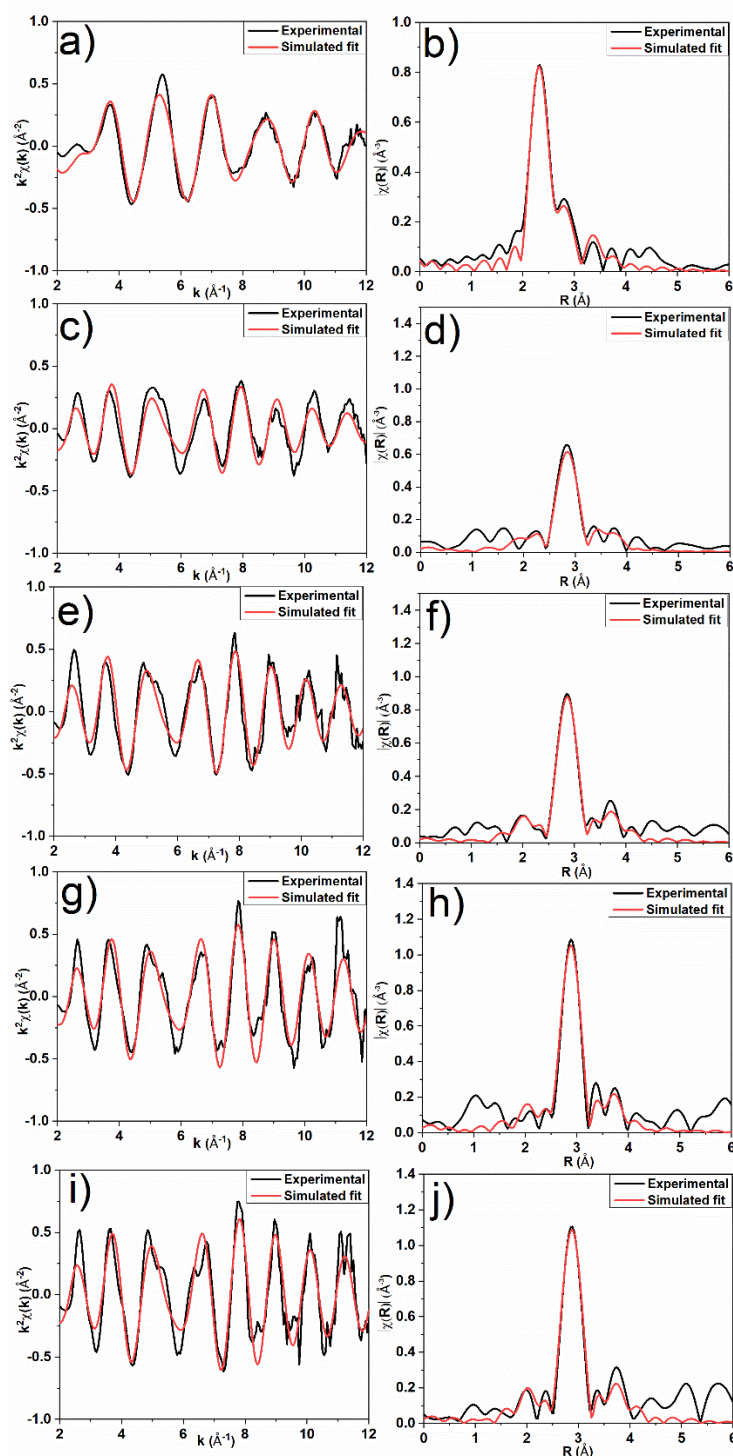


Figure 4.8: Au L₃ edge EXAFS fitting in phase corrected k- (left) and R-space (right) of TEOS/Au₂₅(MPTS)₁₈/SBA catalysts calcined at a) & b) 250 °C, c) & d) 350 °C, e) & f) 450 °C, g) & h) 550 °C, and i) & j) 650 °C. (The black line represents the experimental Fourier-transformed EXAFS spectra and the red line represents the simulated fit.)

To obtain a better understanding of the sintering process, both samples were heated *in situ* in a field emission TEM under a 1 Pa oxygen environment. This allowed for monitoring the structural and morphological changes that occurred during *in situ* heating. Samples were mounted on a silicon nitride window and heated up to 650 °C. The trajectory of Au particles at different temperatures was tracked by ImageJ software with an additional particle tracker plug-in software.⁶² We note that due to the small sizes of Au₂₅ clusters, it was unfortunately not possible to follow structural transformations at lower temperatures, but we were able to follow transformations of partly sintered particles at higher temperatures. Figure 4.9 shows *in situ* TEM heating images at 550 °C in which a 3.5 nm particle became mobile with a velocity of 0.2 nm/s at 550 °C. Figure 4.10 shows the sequence of *in situ* TEM heating images of Au₂₅(MPTS)₁₈ clusters on the SBA-15 support at 650 °C as a function of time. An example of Brownian motion of nanoparticle is indicated by the blue arrow in Figure 4.10. Increasing the temperature to 650 °C lead to an enhancement in the Brownian motion and the average velocity of a tracked Au nanoparticle with a diameter of 3.9 nm was measured to be 1.1 nm/s. A fraction of smaller Au particles showed significant mobility on the silica support, and this mobility resulted in coalescence. However, the growth of larger immobile particles (one of which is indicated by the red circle in Figure 4.10) also occurred at higher temperatures without noticeable collisions between particles, and the highlighted particle grew from 15.1 nm to 19.4 nm within 12 seconds which is likely due to the diffusion of atomic species. Thus it seems that small particles first move and coalesce into larger particles, followed by the further growth of larger particles by Ostwald ripening.

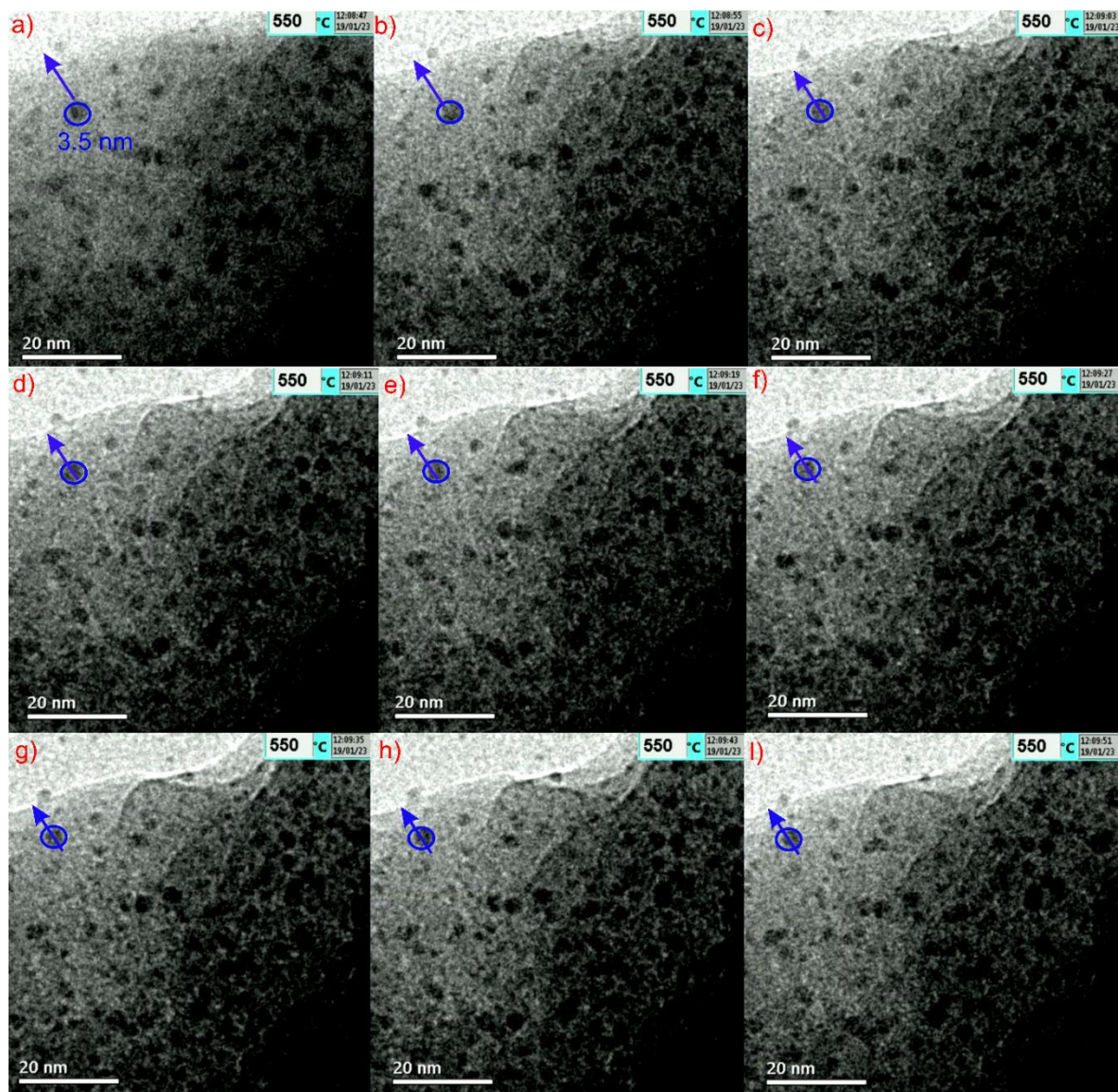


Figure 4.9: A sequence of *in situ* TEM heating images of Au₂₅(MPTS)₁₈ clusters on SBA-15 at 550 °C every 8 s. The trajectory of individual Au particles is indicated by blue line.

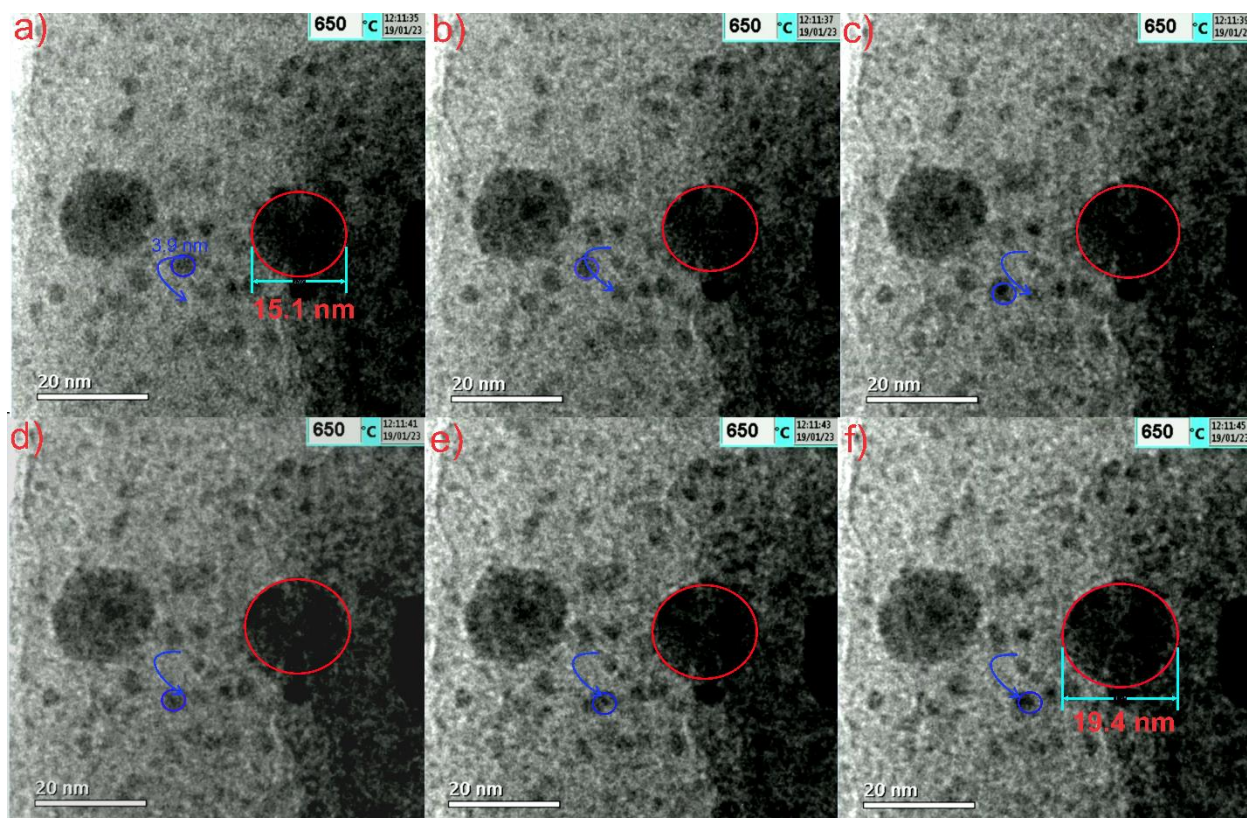


Figure 4.10: A sequence of *in situ* TEM heating images of the Au₂₅(MPTS)₁₈/SBA-15 sample were collected at 650 °C every 2 s. The trajectory of a Au particle (particle in a blue circle) is indicated by blue line, and the growth of a larger particle is shown by the red circle.

The sintering of clusters on the catalyst support is typically due to two mass transport mechanisms, Particle Migration and Coalescence (PMC) and Ostwald Ripening (OR).^{17, 63} The PMC mechanism involves the Brownian motion of particles on the catalyst support, followed by coalescence that leads to the growth in the size of the particles, whereas the OR mechanism refers to the growth of larger particles at the expense of smaller particles and is due to the diffusion of atoms or atomic species either on the surface of catalyst support or through the gas phase. Previous studies show that the PMC mechanism plays an important role when the size of the particles is less than 4 nm.⁶⁴⁻⁶⁵ Pan *et al.* demonstrated that PMC is responsible for sintering of monodisperse 2 nm Pt nanoparticles on alumina, whereas the OR mechanism becomes dominant when there is a discrepancy in the particle size.²⁰ Smaller particles typically have higher mobility than larger ones.⁶⁵ Baker *et al.* reported that the OR mechanism is more dominant in the case of larger particles due to lower mobility.⁶⁶

Cargnello *et al.* performed an *in situ* TEM technique to differentiate the contribution of PMC and OR mechanisms to the sintering of Pt nanoparticles on Al₂O₃ using monodispersed and polydispersed samples.²⁰ Samples with narrow size distributions (either 2.2 ± 0.4 nm or 4.4 ±

0.2 nm) were found to be more stable than mixed samples. They suggested that the OR mechanism can be eliminated via selection of particles with same size. Here particle growth due to OR should be ruled out when the particles are monodisperse, and thus PMC is most possible mechanism for the initial loss of monodispersity. As noted earlier, however, we were not able to satisfactorily follow sintering events at lower temperatures due to the small cluster size. At higher temperatures, Figures 4.9 and 4.10 show clear evidence for PMC and Ostwald Ripening process after some sintering has already occurred. *in situ* TEM imaging indicated that particle migration occurs for some smaller particles, while the growth of larger particles seems to occur due to the mass transport from smaller particles via the Ostwald ripening process.

Figure 4.11 shows the sequence of *in situ* TEM heating images of TEOS/Au₂₅(MPTS)₁₈/SBA-15 samples throughout a range of temperatures (50 °C to 650 °C). No significant change in particle size was observed until 550 °C. The velocity of the Au clusters was found to be negligible until 550 °C. However, 650 °C-treated samples showed minor sintering which is due to the particle migration and coalescence, perhaps triggered by the collapse of the silica pore structure at this temperature.^{57,67} Figure 4.12 shows *in situ* TEM heating images of TEOS/Au₂₅(MPTS)₁₈/SBA-15 samples at 650 °C. The velocity of the tracked particle was found to be much slower (0.1 nm/s) than that was seen for non-overcoated Au₂₅(MPTS)₁₈/SBA-15 samples at 550 °C and 650 °C, and it can be seen that two particles come together to form a larger particle. The result indicates that the mobility of Au particles could be mitigated by the fabrication of silica layers. Bore *et al.* reported that pore size and pore arrangements of support materials such as SBA-15 have a significant role in the sintering of Au nanoparticles.²² They noted that physical confinement of particles in SBA-15 with 1-D pore structures limits the migration of Au particles to the external silica surface, and the sintering of particles can be minimized by strengthening the thickness of the pore walls. In contrast, the migration of Au nanoparticles to the external surface of SBA-15 was observed, when Au nanoparticles are incorporated inside the 3-D pores. Both PMC and OR mechanisms were found to be responsible for nanoparticle sintering inside the 3D pores, while the OR mechanism dominated for nanoparticles trapped in 1D pores.

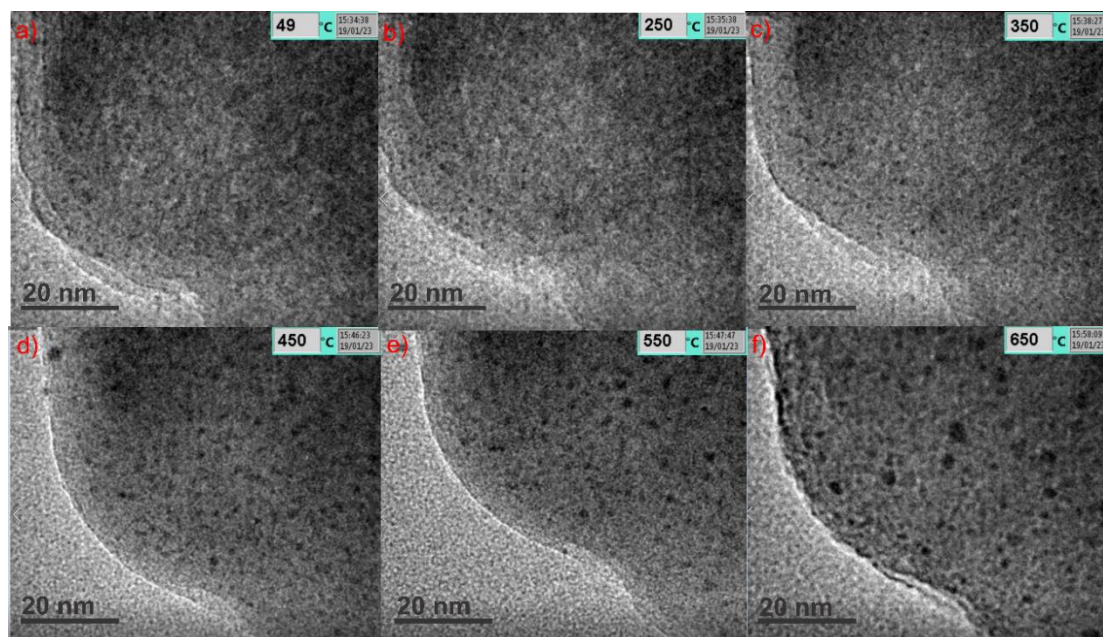


Figure 4.11: The sequence of *in situ* TEM heating images of TEOS/Au₂₅(MPTS)₁₈/SBA-15 samples at a) 50 °C, b) 250 °C, c) 350 °C, d) 450 °C, e) 550 °C, and f) 650 °C.

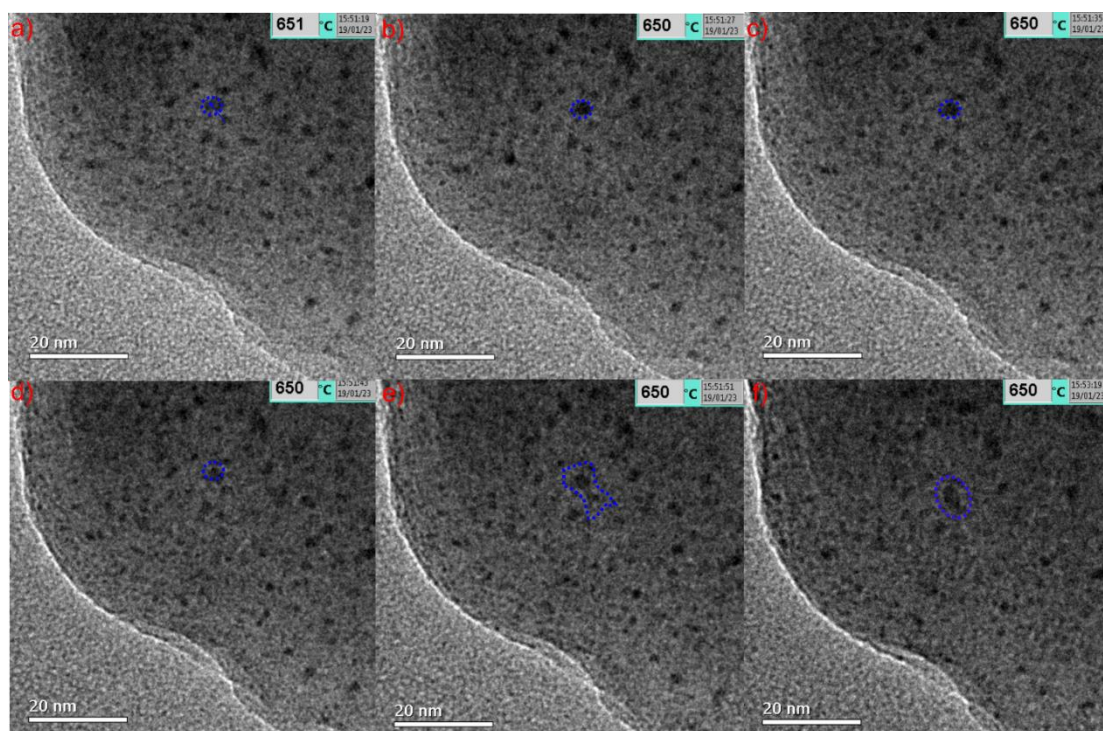


Figure 4.12: A sequence of *in situ* TEM heating TEOS/Au₂₅(MPTS)₁₈/SBA-15 at 650 °C n every 8 s (image f-after 88 s).

4.5. Conclusion

Au₂₅ clusters protected with 3-mercaptopropyltrimethoxysilane were synthesized by a direct synthesis method for the first time. Environmental *in situ* TEM analysis was used to monitor the sintering behavior of Au₂₅(MPTS)₁₈ clusters on the SBA-15 support. This analysis indicates that smaller particles migrate and coalesce into bigger particles, while the growth of even larger particles is likely due to the Ostwald Ripening. The particle migration and coalescence mechanism was observed to be the more dominant process under high-temperature heat treatment. TEOS-treated Au₂₅(MPTS)₁₈ clusters showed less mobility which is due to the additional silica overlayer formation around the clusters. The resulting materials showed strong sinter-resistance, which was confirmed by EXAFS and *in situ* TEM analysis. Our work indicates that both OR and PMC mechanisms can be suppressed by using monodisperse cluster materials and silica overcoating of clusters within mesoporous silica supports.

4.6. References

- (1) Haruta, M.; Yamada, N.; Kobayashi, T.; Iijima, S. Gold Catalysts Prepared by Coprecipitation for Low-Temperature Oxidation of Hydrogen and of Carbon Monoxide. *J. Catal.* **1989**, *115*, 301-309.
- (2) Herzing, A. A.; Kiely, C. J.; Carley, A. F.; Landon, P.; Hutchings, G. J. Identification of Active Gold Nanoclusters on Iron Oxide Supports for CO Oxidation. *Science* **2008**, *321*, 1331-1335.
- (3) Sudheeshkumar, V.; Sulaiman, K. O.; Scott, R. W. J. Activation of atom-precise clusters for catalysis. *Nanoscale Adv.* **2020**, *2*, 55-69.
- (4) Haruta, M. Size- and Support-Dependency in the Catalysis of Gold. *Catal. Today* **1997**, *36*, 153-166.
- (5) Nie, X.; Qian, H.; Ge, Q.; Xu, H.; Jin, R. CO Oxidation Catalyzed by Oxide-Supported Au₂₅(SR)₁₈ Nanoclusters and Identification of Perimeter Sites as Active Centers. *ACS Nano*. **2012**, *6*, 6014-6022.
- (6) Liu, Y.; Tsunoyama, H.; Akita, T.; Tsukuda, T. Efficient and selective epoxidation of styrene with TBHP catalyzed by Au₂₅ clusters on hydroxyapatite. *Chem. Commun.* **2010**, *46*, 550-552.
- (7) Zhu, Y.; Qian, H.; Jin, R. An Atomic-Level Strategy for Unraveling Gold Nanocatalysis from the Perspective of Au_n(SR)_m Nanoclusters. *Chem. Eur. J.* **2010**, *16*, 11455-11462.
- (8) Zhu, Y.; Qian, H.; Zhu, M.; Jin, R. Thiolate-Protected Au_n Nanoclusters as Catalysts for Selective Oxidation and Hydrogenation Processes. *Adv. Mater.* **2010**, *22*, 1915-1920.
- (9) Zhu, Y.; Qian, H.; Drake, B. A.; Jin, R. Atomically Precise Au₂₅(SR)₁₈ Nanoparticles as Catalysts for the Selective Hydrogenation of α,β -Unsaturated Ketones and Aldehydes. *Angew. Chem. Int. Edit.* **2010**, *49*, 1295-1298.
- (10) Hu, D.; Jin, S.; Shi, Y.; Wang, X.; Graff, R. W.; Liu, W.; Zhu, M.; Gao, H. Preparation of Hyperstar Polymers with Encapsulated Au₂₅(SR)₁₈ Clusters as Recyclable Catalysts for Nitrophenol Reduction. *Nanoscale* **2017**, *9*, 3629-3636.

- (11) Shivhare, A.; Ambrose, S. J.; Zhang, H.; Purves, R. W.; Scott, R. W. J. Stable and Recyclable Au₂₅ Clusters for the Reduction of 4-nitrophenol. *Chem. Commun.* **2013**, *49*, 276-278.
- (12) Yang, C.M.; Kalwei, M.; Schüth, F.; Chao, K.J. Gold Nanoparticles in SBA-15 Showing Catalytic Activity in CO Oxidation. *Appl. Catal. A: Gen.* **2003**, *254*, 289-296.
- (13) Hansen, T. W.; DeLaRiva, A. T.; Challa, S. R.; Datye, A. K. Sintering of Catalytic Nanoparticles: Particle Migration or Ostwald Ripening? *Acc. Chem. Res.* **2013**, *46*, 1720-1730.
- (14) Yang, F.; Chen, M. S.; Goodman, D. W. Sintering of Au Particles Supported on TiO₂(110) during CO Oxidation. *J. Phys. Chem. C* **2009**, *113*, 254-260.
- (15) Xu, Q.; Kharas, K. C.; Croley, B. J.; Datye, A. K. The sintering of Supported Pd Automotive Catalysts. *ChemCatChem* **2011**, *3*, 1004-1014.
- (16) Simonsen, S. B.; Chorkendorff, I.; Dahl, S.; Skoglundh, M.; Sehested, J.; Helveg, S. Direct Observations of Oxygen-induced Platinum Nanoparticle Ripening Studied by In Situ TEM. *J. Am. Chem. Soc.* **2010**, *132*, 7968-7975.
- (17) Ouyang, R.; Liu, J.-X.; Li, W. X. Atomistic Theory of Ostwald Ripening and Disintegration of Supported Metal Particles under Reaction Conditions. *J. Am. Chem. Soc.* **2013**, *135*, 1760-1771.
- (18) Wettergren, K.; Schweinberger, F. F.; Deiana, D.; Ridge, C. J.; Crampton, A. S.; Rötzer, M. D.; Hansen, T. W.; Zhdanov, V. P.; Heiz, U.; Langhammer, C. High Sintering Resistance of Size-Selected Platinum Cluster Catalysts by Suppressed Ostwald Ripening. *Nano Lett.* **2014**, *14*, 5803-5809.
- (19) Zhdanov, V. P.; Schweinberger, F. F.; Heiz, U.; Langhammer, C. Ostwald Ripening of Supported Pt Nanoclusters With Initial Size-Selected Distributions. *Chem. Phys. Lett.* **2015**, *631-632*, 21-25.
- (20) Zhang, S.; Cargnello, M.; Cai, W.; Murray, C. B.; Graham, G. W.; Pan, X. Revealing particle Growth Mechanisms by Combining High-Surface-Area Catalysts Made with Monodisperse Particles and Electron Microscopy Conducted at Atmospheric Pressure. *J. Catal.* **2016**, *337*, 240-247.

- (21) Baker, R. T. K. The Relationship Between Particle Motion on a Graphite Surface and Tammann Temperature. *J. Catal.* **1982**, *78*, 473-476.
- (22) Bore, M. T.; Pham, H. N.; Switzer, E. E.; Ward, T. L.; Fukuoka, A.; Datye, A. K. The Role of Pore Size and Structure on the Thermal Stability of Gold Nanoparticles within Mesoporous Silica. *J. Phys. Chem. B* **2005**, *109*, 2873-2880.
- (23) Habeeb Muhammed, M. A.; Pradeep, T. Au₂₅@SiO₂: Quantum Clusters of Gold Embedded in Silica. *Small* **2011**, *7*, 204-208.
- (24) Chen, H.; Liu, C.; Wang, M.; Zhang, C.; Li, G.; Wang, F. Thermally Robust Silica-Enclosed Au₂₅ Nanocluster and its Catalysis. *Chin. J. Catal.* **2016**, *37*, 1787-1793.
- (25) Galeano, C.; Güttel, R.; Paul, M.; Arnal, P.; Lu, A.-H.; Schüth, F. Yolk-Shell Gold Nanoparticles as Model Materials for Support-Effect Studies in Heterogeneous Catalysis: Au@C and Au@ZrO₂ for CO Oxidation as an Example. *Chem. Eur. J.* **2011**, *17*, 8434-8439.
- (26) Samanta, A.; Rajesh, T.; Nandini Devi, R. Confined Space Synthesis of Fully Alloyed and Sinter-Resistant AuPd Nanoparticles Encapsulated in Porous Silica. *J. Mater. Chem. A* **2014**, *2*, 4398-4405.
- (27) Sudheeshkumar, V.; Shivhare, A.; Scott, R. W. J. Synthesis of Sinter-Resistant Au@Silica Catalysts Derived from Au₂₅ Clusters. *Catal. Sci. Technol.* **2017**, *7*, 272-280.
- (28) Sudheeshkumar, V.; Lushington, A.; Sun, X.; Scott, R. W. J. Thermal Stability of Alumina-Overcoated Au₂₅ Clusters for Catalysis. *ACS Appl. Nano Mater.* **2018**, *1*, 6904-6911.
- (29) Luo, Y.; Fan, S.; Yu, W.; Wu, Z.; Cullen, D. A.; Liang, C.; Shi, J.; Su, C. Fabrication of Au₂₅(SG)₁₈-ZIF-8 Nanocomposites: A Facile Strategy to Position Au₂₅(SG)₁₈ Nanoclusters Inside and Outside ZIF-8. *Adv. Mater.* **2018**, *30*, 1-7.
- (30) Li, Z.; Ji, Y.; Cadigan, C.; Richards, R. M. Thermally Stable Gold/Alumina Aerogel Catalysts Prepared by a Simultaneous Synthesis Process for Solvent-Free Aerobic Benzyl Alcohol Oxidation. *Catal. Sci. Technol.* **2014**, *4*, 2520-2525.
- (31) Das, S.; Goswami, A.; Hesari, M.; Al-Sharab, J. F.; Mikmeková, E.; Maran, F.; Asefa, T. Reductive Deprotection of Monolayer Protected Nanoclusters: An Efficient Route to Supported Ultrasmall Au Nanocatalysts for Selective Oxidation. *Small* **2014**, *10*, 1473-1478.

- (32) García-Soto, M. J.; González-Ortega, O. Synthesis of Silica-Core Gold Nanoshells and Some Modifications/Variations. *Gold Bull.* **2016**, *49*, 111-131.
- (33) Vakarelski, I. U.; McNamee, C. E.; Higashitani, K. Deposition of Silica Nanoparticles on a Gold Surface via a Self-Assembled Monolayer of (3-mercaptopropyl)trimethoxysilane. *Colloid. Surf.. A.* **2007**, *295*, 16-20.
- (34) Tseng, J. Y.; Lin, M. H.; Chau, L. K. Preparation of Colloidal Gold Multilayers with 3-(mercaptopropyl)-trimethoxysilane as a Linker Molecule. *Colloid. Surf.. A* **2001**, *182*, 239-245.
- (35) Wu, P.; Bai, P.; Lei, Z.; Loh, K. P.; Zhao, X. S. Gold Nanoparticles Supported on Functionalized Mesoporous Silica for Selective Oxidation of Cyclohexane. *Micropor. Mesopor. Mat.* **2011**, *141*, 222-230.
- (36) Zhao, D.; Huo, Q.; Feng, J.; Chmelka, B. F.; Stucky, G. D. Nonionic Triblock and Star Diblock Copolymer and Oligomeric Surfactant Syntheses of Highly Ordered, Hydrothermally Stable, Mesoporous Silica Structures. *J. Am. Chem. Soc.* **1998**, *120*, 6024-6036.
- (37) Gangishetty, M. K.; Scott, R. W. J.; Kelly, T. L. Effect of Relative Humidity on Crystal Growth, Device Performance and Hysteresis in Planar Heterojunction Perovskite Solar Cells. *Nanoscale.* **2016**, *8*, 6300-6307.
- (38) Schneider, C. A.; Rasband, W. S.; Eliceiri, K. W. NIH Image to ImageJ: 25 years of image analysis. *Nat. Methods.* **2012**, *9*, 671-682.
- (39) Ravel, B.; Newville, M. ATHENA, ARTEMIS, HEPHAESTUS: Data Analysis for X-ray Absorption Spectroscopy using IFEFFIT. *J. Synchrotron Radiat.* **2005**, *12*, 537-541,.
- (40) Zhu, M.; Aikens, C. M.; Hollander, F. J.; Schatz, G. C.; Jin, R. Correlating the Crystal Structure of A Thiol-Protected Au₂₅ Cluster and Optical Properties. *J. Am. Chem. Soc.* **2008**, *130*, 5883-5885.
- (41) Shivhare, A.; Wang, L.; Scott, R. W. J. Isolation of Carboxylic Acid-Protected Au₂₅ Clusters Using a Borohydride Purification Strategy. *Langmuir* **2015**, *31*, 1835-1841.
- (42) Yao, H. On the Electronic Structures of Au₂₅(SR)₁₈ Clusters Studied by Magnetic Circular Dichroism Spectroscopy. *J. Phys. Chem. Lett.* **2012**, *3*, 1701-1706.

- (43) Yoskamtorn, T.; Yamazoe, S.; Takahata, R.; Nishigaki, J.-i.; Thivasasith, A.; Limtrakul, J.; Tsukuda, T. Thiolate-Mediated Selectivity Control in Aerobic Alcohol Oxidation by Porous Carbon-Supported Au₂₅ Clusters. *ACS Catal.* **2014**, *4*, 3696-3700.
- (44) Heaven, M. W.; Dass, A.; White, P. S.; Holt, K. M.; Murray, R. W. Crystal Structure of the Gold Nanoparticle [N(C₈H₁₇)₄][Au₂₅(SCH₂CH₂Ph)₁₈]. *J. Am. Chem. Soc.* **2008**, *130*, 3754-3755.
- (45) Dainese, T.; Antonello, S.; Gascón, J. A.; Pan, F.; Perera, N. V.; Ruzzi, M.; Venzo, A.; Zoleo, A.; Rissanen, K.; Maran, F. Au₂₅(SEt)₁₈, A Nearly Naked Thiolate-Protected Au₂₅ Cluster: Structural Analysis by Single Crystal X-ray Crystallography and Electron Nuclear Double Resonance. *ACS Nano.* **2014**, *8*, 3904-3912.
- (46) MacDonald, M. A.; Chevrier, D. M.; Zhang, P.; Qian, H.; Jin, R. The Structure and Bonding of Au₂₅(SR)₁₈ Nanoclusters from EXAFS: The Interplay of Metallic and Molecular Behavior. *J. Phys. Chem. C* **2011**, *115*, 15282-15287.
- (47) Shivhare, A.; Chevrier, D. M.; Purves, R. W.; Scott, R. W. J. Following the Thermal Activation of Au₂₅(SR)₁₈ Clusters for Catalysis by X-ray Absorption Spectroscopy. *J. Phys. Chem. C* **2013**, *117*, 20007-20016.
- (48) Park, S. K.; Kim, K. D.; Kim, H. T. Preparation of Silica Nanoparticles: Determination of the Optimal Synthesis Conditions for Small and Uniform Particles. *Colloid. Surf. A* **2002**, *197*, 7-17.
- (49) Xu, Z.; Hou, Y.; Sun, S. Magnetic Core/Shell Fe₃O₄/Au and Fe₃O₄/Au/Ag Nanoparticles with Tunable Plasmonic Properties. *J. Am. Chem. Soc.* **2007**, *129*, 8698-8699.
- (50) Ma, G.; Binder, A.; Chi, M.; Liu, C.; Jin, R.; Jiang, D.-e.; Fan, J.; Dai, S. Stabilizing Gold Clusters by Heterostructured Transition-Metal Oxide–Mesoporous Silica Supports for Enhanced Catalytic Activities for CO Oxidation. *Chem. Commun.* **2012**, *48*, 11413-11415.
- (51) Manju, C. K.; Chakraborty, I.; Pradeep, T. Highly Luminescent Monolayer Protected Ag₅₆Se₁₃S₁₅ clusters. *J. Mater. Chem. C* **2016**, *4*, 5572-5577.
- (52) Wu, Z.; MacDonald, M. A.; Chen, J.; Zhang, P.; Jin, R. Kinetic Control and Thermodynamic Selection in the Synthesis of Atomically Precise Gold Nanoclusters. *J. Am. Chem. Soc.* **2011**, *133*, 9670-9673.

- (53) Qian, H.; Jin, R. Controlling Nanoparticles with Atomic Precision: The Case of $\text{Au}_{144}(\text{SCH}_2\text{CH}_2\text{Ph})_{60}$. *Nano Lett.* **2009**, *9*, 4083-4087.
- (54) Sarawade, P. B.; Kim, J.-K.; Hilonga, A.; Kim, H. T. Recovery of High Surface Area Mesoporous Silica from Waste Hexafluorosilicic Acid (H_2SiF_6) of Fertilizer Industry. *J. Hazard. Mater.* **2010**, *173*, 576-580,.
- (55) Benfield, R. E. Mean Coordination Numbers and the Non-metal–Metal Transition in Clusters. *J. Chem. Soc., Faraday Trans.* **1992**, *88*, 1107-1110.
- (56) Carotenuto, G.; Nicolais, L. Size-Controlled Synthesis of Thiol-Derivatized Gold Clusters. *J. Mater. Chem.* **2003**, *13*, 1038-1041.
- (57) Rombi, E.; Cutrufello, M. G.; Cannas, C.; Casu, M.; Gazzoli, D.; Occhiuzzi, M.; Monaci, R.; Ferino, I. Modifications Induced by Pretreatments on Au/SBA-15 and their Influence on the Catalytic Activity for Low Temperature CO Oxidation. *Phys. Chem. Chem. Phys.* **2009**, *11*, 593-602.
- (58) Wu, Z.; Jiang, D. E.; Mann, A. K. P.; Mullins, D. R.; Qiao, Z. A.; Allard, L. F.; Zeng, C.; Jin, R.; Overbury, S. H. Thiolate Ligands as a Double-Edged Sword for CO Oxidation on CeO_2 Supported $\text{Au}_{25}(\text{SCH}_2\text{CH}_2\text{Ph})_{18}$ Nanoclusters. *J. Am. Chem. Soc.* **2014**, *136*, 6111-6122.
- (59) Fritsche, H. G.; Benfield, R. E. Exact Analytical Formulae for Mean Coordination Numbers in Clusters. *Z. Phys. D. Atom. Mol. Cl.* **1993**, *26*, 15-17.
- (60) Jentys, A. Estimation of Mean Size and Shape of Small Metal Particles by EXAFS. *Phys. Chem. Chem. Phys.* **1999**, *1*, 4059-4063.
- (61) Marinković N.S., K. S., and R. R. Adžić. Nanoparticle Size Evaluation of Catalysts by EXAFS: Advantages and Limitations. *Z. Mater.* **2016**, *57*, 101-109.
- (62) Schindelin, J.; Arganda, C. I.; Frise, E.; Kaynig, V.; Longair, M.; Pietzsch, T.; Preibisch, S.; Rueden, C.; Saalfeld, S.; Schmid, B.; Tinevez, J. Y.; White, D. J.; Hartenstein, V.; Eliceiri, K.; Tomancak, P.; Cardona, A. Fiji: an Open-Source Platform for Biological-Image Analysis. *Nat. Method.* **2012**, *9*, 676-682.
- (63) Wynblatt, P.; Gjostein, N. A. Particle Growth in Model Supported Metal Catalysts-I. Theory. *Acta. Metal. Mater.* **1976**, *24*, 1165-1174.

- (64) Harris, P. J. F.; Boyes, E. D.; Cairns, J. A. The Sintering of an Alumina-Supported Platinum Catalyst Studied by Transmission Electron Microscopy. *J. Catal.* **1983**, *82*, 127-146.
- (65) Wynblatt, P.; Gjostein, N. A. Supported Metal Crystallites. *Prog. Solid. State. Ch.* **1975**, *9*, 21-58.
- (66) Baker, R. T. K.; Thomas, C.; Thomas, R. B. Continuous Observation of the Particle Size Behavior of Platinum on Alumina. *J. Catal.* **1975**, *38*, 510-513.
- (67) Baker, J. B. L. A. R. T. Deformation of Ordered Mesoporous Silica Structures on Exposure to High Temperatures. *J. Nanomater.* **2011**, *3*, 1-7.

CHAPTER 5

Galvanic Synthesis of Ag-Pd Bimetallic Catalysts from Ag Clusters Dispersed in a Silica

This chapter describes a top-down approach for synthesizing ligand-free clusters. Thermally activated Ag clusters made via a top-down method were used for galvanic replacement reactions with Pd precursors. No activation process was needed after the synthesis of the catalyst as no stabilizers were on the surface of the clusters. *In situ* XAS Pd-L₃ edge analysis and XPS were employed to probe the reduction of Pd(II) to Pd(0), and showed that the Pd was reduced but not all the Ag was removed from the final sample. The catalytic activity of Ag-Pd@SiO₂ for 3-hexyne-1-ol hydrogenation reaction is also shown.

This chapter is based on a manuscript that will be submitted for publication in the near future. All the experimental work was done by me, and the first draft of the manuscript was written by myself.

5.1. Abstract

While bottom-up synthetic strategies for the formation of near-monodisperse clusters have attracted much attention, top-down synthetic strategies in which metals are dispersed into clusters can also be viable. In this study, we follow up previous work that showed the formation of Ag clusters dispersed in a silica matrix by breaking up larger triangular Ag nanoparticles upon calcination in air. In this study, AgPd bimetallic catalysts were synthesized via a galvanic replacement reaction of these thermally activated Ag clusters in a silica matrix. The galvanic reaction of the Ag clusters with Pd(II) salts was monitored by *in situ* XANES spectroscopy. Interestingly, extended X-ray absorption fine structure (EXAFS) spectroscopy and X-ray photoelectron spectroscopy (XPS) studies suggested that the majority of the Ag atoms are located on the surface of the resulting clusters and Pd atoms are in the core region. The catalytic activity for 3-hexyne-1-ol hydrogenation was investigated and the AgPd@SiO₂ catalysts showed superior selectivity for the selective hydrogenation to 3-hexene-1-ol.

5.2. Introduction

Design and fabrication of a ligand free-nanomaterials is a special area of interest in catalysis because that enables one to avoid activation processes. Generally, bottom-up and top-down approaches have been reported for the synthesis of nanoparticles.¹ In the bottom-up approach, nanostructures are synthesized via assembling atoms or molecules. The chemical reduction method is the most common and simple bottom-up approach for the synthesis of nanostructures that involves the reduction of metal salt using various reducing agents in the presence of capping agents. The presence of a capping agent blocks the active sites on the metal surface that often affects the activity and selectivity of catalysts.² Although it is possible to remove the capping agents through an activation process, this often leads to sintering and the subsequent deactivation of the catalyst.³ On the other hand, in top-down approaches nanostructures are fabricated by slicing or breaking apart a bulk material. Micro-patterning, pyrolysis, thermal decomposition, and milling are commonly used techniques for the top-down fabrication of metal nanostructures.⁴ Nanostructures synthesized via top-down approaches possess a definite advantage over chemically synthesized nanoparticles as they have a clean surface and can show uniform size distribution which is essential for catalysis. Despite these attractive features, several challenges such as the complexity of the synthetic procedure and

the use of sophisticated techniques limit the application of top-down approaches in nanoparticle synthesis.⁵

Thermal decomposition is most convenient and easiest top-down approach for nanoparticle synthesis.^{6,7} Wang *et al.* demonstrated a simple method for the synthesis of monodispersed spherical colloids from the low melting metals such as Pb, In, Sn, Cd, and Bi.⁸ By taking advantage of thermal decomposition of Bi metal, nanoparticles with diameters in the range of 100-600 nm are synthesized by emulsifying molten drops of Bi in boiling di(ethylene glycol) followed by quenching with cold ethanol. Jung *et al.* demonstrated that Ag nanoparticles with an average size of 6.2 ± 1.2 nm can be synthesized using Ag metal as a precursor in a ceramic heater by an evaporation–condensation process.⁹ Others have shown that the surface of Ag nanoparticles is easily oxidized to AgO_x during annealing in air.¹⁰⁻¹¹ However, AgO_x is thermodynamically unstable and dissociates into Ag and O_2 above ~ 300 °C. Previously our group synthesized Ag clusters with an average size of 2.3 ± 0.4 nm by the thermal decomposition of silica-encapsulated Ag nanotriangles in air.¹²

There has been significant interest in the synthesis of Ag nanostructures because they can serve as a sacrificial template for the synthesis of various bimetallic nanostructures via galvanic replacement. The driving force for galvanic reactions is the redox potential difference between two metal atoms, *i.e.* the metal with lower redox potential is typically replaced by another metal atom. Specifically, Ag ($E^{0/2} \text{Ag}^+$, $\text{Ag} = 0.79$ V) can be oxidized with metal salts of Au ($E^{0/2} \text{Au}^{3+}$, $\text{Au} = 1.49$ V), Pt ($E^{0/2} \text{Pt}^{2+}$, $\text{Pt} = 1.18$ V) and Pd ($E^{0/2} \text{Pd}^{2+}$, $\text{Pd} = 0.95$ V).¹³ A number of groups have synthesized AgPd, AgAu and AgPt bimetallic catalysts via galvanic reactions using Ag as sacrificial template.¹⁴⁻²⁰ This method enables the synthesis of a broad range of hollow and porous nanostructures from Ag templates with different morphologies that includes nanoboxes, nanoprisms, and nanocages.²¹⁻²³ Tedsree *et al.* synthesized a series of core-shell M@Pd catalysts (M=Ag, Au, Rh, Pt and Ru) and observed that Ag nanoparticles coated with a thin layer of Pd atoms are the most effective catalysts for H_2 production from formic acid decomposition.²⁴ The improvement in a catalytic activity that was seen in Ag@Pd catalysts is due to the electronic modification of the Pd shell by Ag core. AgPd bimetallic catalysts were found to be more active for 4-nitrophenol reduction reaction than their monometallic systems.²⁵ Pei *et al.* observed a significant improvement in selectivity for acetylene hydrogenation by alloying Pd with Ag.²⁶ Interestingly, Ag alloyed Pd-single catalysts showed higher activity and selectivity towards ethylene than the monometallic Pd/SiO₂ and Ag/SiO₂ catalysts. Previously our group reported the synthesis of Ag core-Pd shell catalysts by galvanic replacement of

polyvinylpyrrolidone stabilized Ag nanoparticles with K_2PdCl_4 .²⁷ While atom-precise Ag clusters can be made using thiolate stabilizers, activating such clusters for catalysis without sintering is very challenging.^{3, 28} Top-down strategies that create highly disperse Ag clusters without ligands on their surfaces which can then be used as templates for the formation of bimetallic nanoparticles are needed.

Herein we report a procedure to synthesize AgPd bimetallic catalysts from Ag@SiO₂ catalysts that are created by the thermal decomposition of larger Ag nanotriangles inside silica shells. The reduction of Pd(II) salts was monitored through using *in situ* Pd L₃-edge XANES using a liquid cell. XPS and EXAFS analysis provided clear evidence for the formation of bimetallic clusters. Low first shell coordination numbers of Ag in the EXAFS analysis suggested that Ag atoms are predominantly located on the surface of a Pd core. The catalytic activity for 3-hexyne-1-ol hydrogenation was investigated and the bimetallic AgPd@SiO₂ catalysts showed a superior selectivity to 3-hexene-1-ol compared to its monometallic counterparts.

5.3. Materials and Methods

5.3.1. Materials

Silver nitrate (AgNO₃, ≥99%, Sigma-Aldrich), (16-mercaptohexadecanoic acid (MHA, 95%, Sigma-Aldrich), trisodium citrate (96%, EMD), potassium tetrachloropalladate (II) (K_2PdCl_4 , 98%, Aldrich), 11-mercaptoundecanoic acid (MUA, 95%, Sigma-Aldrich), sodium borohydride (NaBH₄, 98%, Alfa Aesar), acetone (C₃H₆O, 99.5%, Fischer Scientific), o-phosphoric acid (H₃PO₄, 85%, Fischer Scientific), methylene chloride (CH₂Cl₂, 99.5%, Fischer Scientific), tetraethylorthosilicate (TEOS, 98%, Aldrich), hydrogen peroxide (H₂O₂, 30%, Fischer Scientific), poly(N-vinylpyrrolidone (PVP, 40.000g/mol, Alfa Aesar), and dimethylamine (DMA, 40%, Sigma-Aldrich) were used as received. Ammonia (30%), tetrahydrofuran (THF, high purity) and ethanol (100%) were purchased from EMD, Fisher Scientific and Commercial Alcohols, respectively. Eighteen MΩ · cm Milli-Q deionized water (Millipore, Bedford, MA) was used throughout.

5.3.2. Synthesis of Ag encapsulated with silica

The procedure for the synthesis of silica encapsulated Ag nanotriangles has been documented previously.¹² Briefly, AgNO₃ (500 μL, 50 mM), trisodium citrate (5 ml, 75 mM),

PVP (1 mL, 17.5 mM), and H₂O₂ (30%, 600 μL) were added to 248 mL of deionized water. Finally, NaBH₄ was added to the solution and the solution was stirred until it turned from yellow to blue. After this, the Ag nanotriangles were collected by centrifugation at 8500 rpm for 2.0 h. The Ag nanotriangles were then redispersed in 100 mL of deionized water, followed by the addition of ethanolic MHA (1.5 mL, 5.0 mM). After stirring for 10 min, MHA functionalized Ag triangles were collected by centrifugation (8500 rpm, 2.0 h). The Ag nanotriangles were then dispersed into an ethanolic TEOS solution (20 mL, 16 mM) and stirred for 2 min. To this solution, aqueous DMA (2 mL, 20 % w/v) was added and the resulting solution was stirred at 200 rpm for 12 h. The final material was removed from the solution by centrifuge and washed several times with water and ethanol. The resulting materials were dried in an oven at 100 °C followed by the calcination in a Lindberg/Blue M tube furnace at 650 °C in air for 15 min with a ramping rate of 10 °C/min. For brevity, the resulting Ag nanotriangles encapsulated with silica and calcined at 650 °C are designated as Ag@SiO₂. The metal loading was found to be 2.0 % by AAS analysis.

5.3.3. Synthesis of AgPd@SiO₂ bimetallic catalysts by galvanic exchange with Pd precursor

20 mg of Ag@SiO₂ (4.0×10^{-3} mmol) was dispersed in water followed by the addition of K₂PdCl₄ (200 μl, 0.020 M). The solution was stirred for 1 h. The resulting black coloured material was collected by centrifugation and washed with deionized water. The AgPd bimetallic catalyst (AgPd@SiO₂) was dried in an oven at 100 °C.

5.3.4. Synthesis of Pd@SiO₂ catalysts

Pd@SiO₂ catalysts were made using the following procedure.²⁹ K₂PdCl₄ (20 mg, 0.06 mmol) was dissolved in H₂O (2 mL). To this clear brown solution, acetone (10 mL) was added, which changed the solution color to a clear orange. Next, H₃PO₄ (250 μL) was added, followed by MUA (7 mg, 0.03 mmol). The solution was stirred for 5 min, then cooled in an ice bath. After cooling, a solution of NaBH₄ (23.2 mg, 0.613 mmol) in H₂O (1 mL) was added, and the solution immediately became black. After stirring for an additional 5 min, the ice bath was removed, and the solution was stirred at room temperature for 5 min. The acetone was removed by vacuum at room temperature and the solid black product was collected by centrifugation. The solid was washed with methylene chloride and water and left to dry at room temperature. The resulting Pd_m(MUA)_n clusters (10 mg) were dissolved in a minimal amount of tetrahydrofuran,

then diluted with ethanol (10 mL). This Pd_m(MUA)_n solution (0.25 mL) was added to a stirred solution of ethanol (10 mL) and TEOS (10 μL, 0.04 mmol). The solution was stirred for 1 min, then NH₄OH (1 mL) was added. The final solution was stirred for 6 h. The dark brown product was collected by centrifugation, then washed with H₂O and ethanol. The product was left to dry at room temperature. The dried Pd_m(MUA)_n@SiO₂ particles were calcined in air at 350 °C for 3 h. The catalyst was reduced by calcination at 250 °C under 5% H₂ in N₂ for 1 h to give Pd@SiO₂.

5.3.5. Characterization

Samples were analyzed by a Hitachi HT7700 TEM operating at 100 kV. All samples were dispersed in ethanol and drop casted on a Cu grid coated with carbon film. ImageJ software was used to measure the size of 100 particles for particle size distribution histograms.³⁰ The Brunauer–Emmett–Teller (BET) surface area and pore size distribution of the Ag@SiO₂ catalysts were performed on an ASAP 2010 Micrometrics instrument. Prior to the analysis, the catalyst was degassed under vacuum at 200 ± 2 °C and nitrogen adsorption analysis was conducted at -196 °C. Metal loading was analyzed by a Varian Spectra AA 55 Atomic Absorption Spectroscopy. UV-Vis spectra of Ag nanotriangles were recorded on a Varian Cary 50 Bio UV-Vis Spectrometer. Pd L₃ edge spectra was collected at the Soft X-ray Micro Characterization Beamline (SXRMB) at the Canadian Light Source. For *in situ* measurements, the Pd precursor (1 mL, 0.020 M) aqueous solution was sealed in a liquid cell (SPEX CertiPrep Disposable XRF X-Cell sample cups) and was covered with an Ultralene[®] thin film. The liquid cell was placed inside an aluminum chamber. A magnetic stirrer was used for stirring and all the measurements were carried out under He atmosphere. Extended X-ray Absorption Spectra Fine Structure (EXAFS) spectroscopic analysis was performed on the HXMA beamline 061D-1 (energy range 5-30 keV, resolution 1x10⁻⁴ ΔE/E) at the Canadian Light Source. All data was collected in fluorescence mode using a 32-element detector. The energy for the Ag K edge (25514 eV) and Pd K edge (24350 eV) was selected by using a Si monochromator. All samples were mixed with boron nitride and then pressed into pellets before analysis. Higher harmonics were removed by detuning the double crystal monochromator. Data analysis and EXAFS fitting were carried out using the Demeter software package.³¹ To fit the Ag and Pd data, an amplitude reduction factor was obtained from fitting of the corresponding metal foils. The amplitude reduction factor for both Pd and Ag were found to be 0.81. The coordination number of samples was determined by keeping this amplitude reduction factor fixed. All XPS measurements were

collected using a Kratos (Manchester, UK) system equipped with a 500 mm Rowland circle monochromated Al K- α (1486.6 eV) source and combined hemispherical analyzer (HSA) and spherical mirror analyzer (SMA). The largest spot size (hybrid slot setting) was used to collect the data, which is approximately a beam size of 300 x 700 microns. All survey scan spectra were collected in the 0-1200 binding energy range in 1 eV steps with a pass energy of 160 eV. High-resolution scans of multiple regions were conducted using 0.1 eV steps with a pass energy of 20 eV. An accelerating voltage of 15 keV and an emission current of 15 mA was used for the analysis. The operating vacuum pressure was less than 1×10^{-8} Torr. The spectra were referenced to a standard C 1s binding energy of 284.4 eV. All spectra were fitted using Casa XPS software.³² ^1H nuclear magnetic resonance (NMR) were recorded on a with a Bruker 500 MHz Avance spectrometer, with CDCl_3 as the solvent.

5.3.6. Catalytic activity for 3 hexyne-1-ol hydrogenation

Hydrogenation reactions were carried out in 50 mL round-bottom flask under H_2 atmosphere. 20 mg of the catalyst was dispersed in 5.0 mL water/ethanol (4:1) mixture and 100 μL of 3-hexyne-1-ol was added to start the reaction. The reaction mixture was stirred at room temperature for 3 h. Prior to the ^1H NMR analysis, the products were extracted from the reaction solution with 2 mL aliquots of CDCl_3 .

5.4. Results and Discussions

Figure 5.1 shows the UV-Vis absorption spectra of the Ag nanotriangles. The spectra shows three peaks, at 334 nm, 430 nm, and an intense peak centered at 538 nm that could be assigned to out-plane quadrupole resonances, in-plane quadrupole, and in-plane dipole resonance of the Ag nanotriangles, respectively.³³ Figure 5.3a shows a TEM image of the Ag nanotriangles, note that the nanotriangles are randomly oriented and thus some appear to be non-triangular in shape. The TEM image of as-synthesized Ag@SiO_2 (Figure 5.3b) indicates that Ag nanotriangles are encapsulated by a silica shell. The average Ag nanotriangle size is 19 ± 4 nm and silica shell thickness is 80 ± 10 nm. After calcination at 650 $^\circ\text{C}$, the Ag nanotriangles are fragmented into small particles, as shown in Figure 5.3c. The average Ag particle size in the resulting materials is 2.5 ± 0.5 nm. These results agree with previous work that investigated the thermal degradation of silica encapsulated Ag nanotriangles by *ex situ* TEM and EXAFS analysis.¹² It was proposed that atoms from tips and corners of Ag nanotriangles are easily oxidized to AgO_x during annealing in air. However, AgO_x is thermodynamically unstable at

higher temperatures and dissociates back into Ag and O₂ above ~300 °C.¹² Previous results suggested that the oxygen atmosphere has a crucial role in the fragmentation process, as no such dispersion of Ag was seen in inert atmosphere.

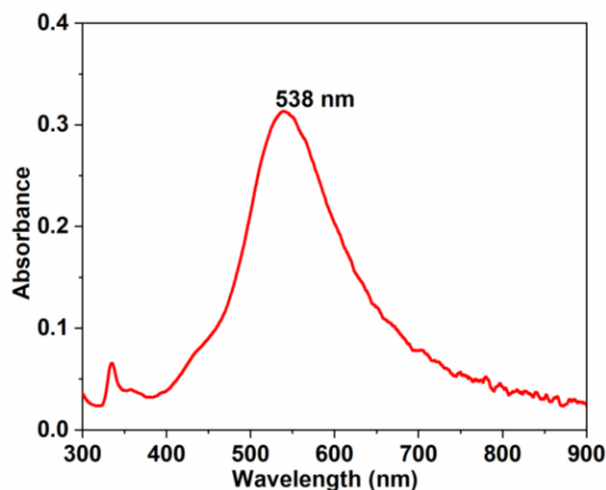


Figure 5.1: UV-Vis spectra of Ag Nanotriangles.

The porous nature of the Ag@SiO₂ materials was evaluated by nitrogen adsorption/desorption isotherm, which is shown in Figure 5.2. The BET surface area of the Ag@SiO₂ materials was found to be 97 m²/g and BJH desorption average pore width is 24.5 nm. The thermal treatment at 650 °C leads to the removal of protecting ligands and solvent, which leads to the disordered mesoporosity; similar results have been seen by other groups.³⁴⁻³⁶ The final porosity of the materials should allow the accessibility of Pd precursor to the silver atoms for the galvanic replacement reaction.

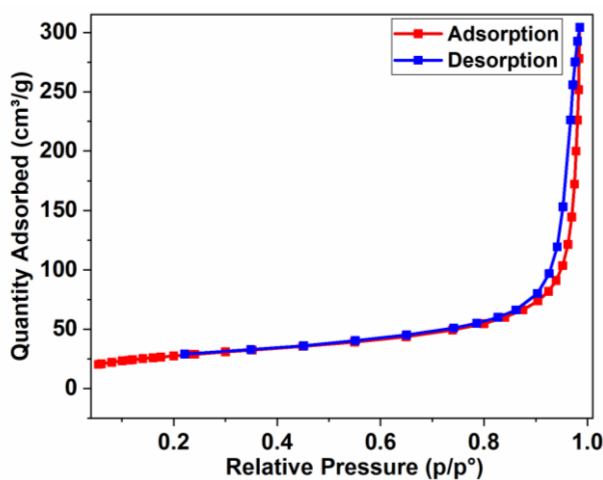


Figure 5.2: BET surface area of Ag@SiO₂ materials after calcination at 650 °C.

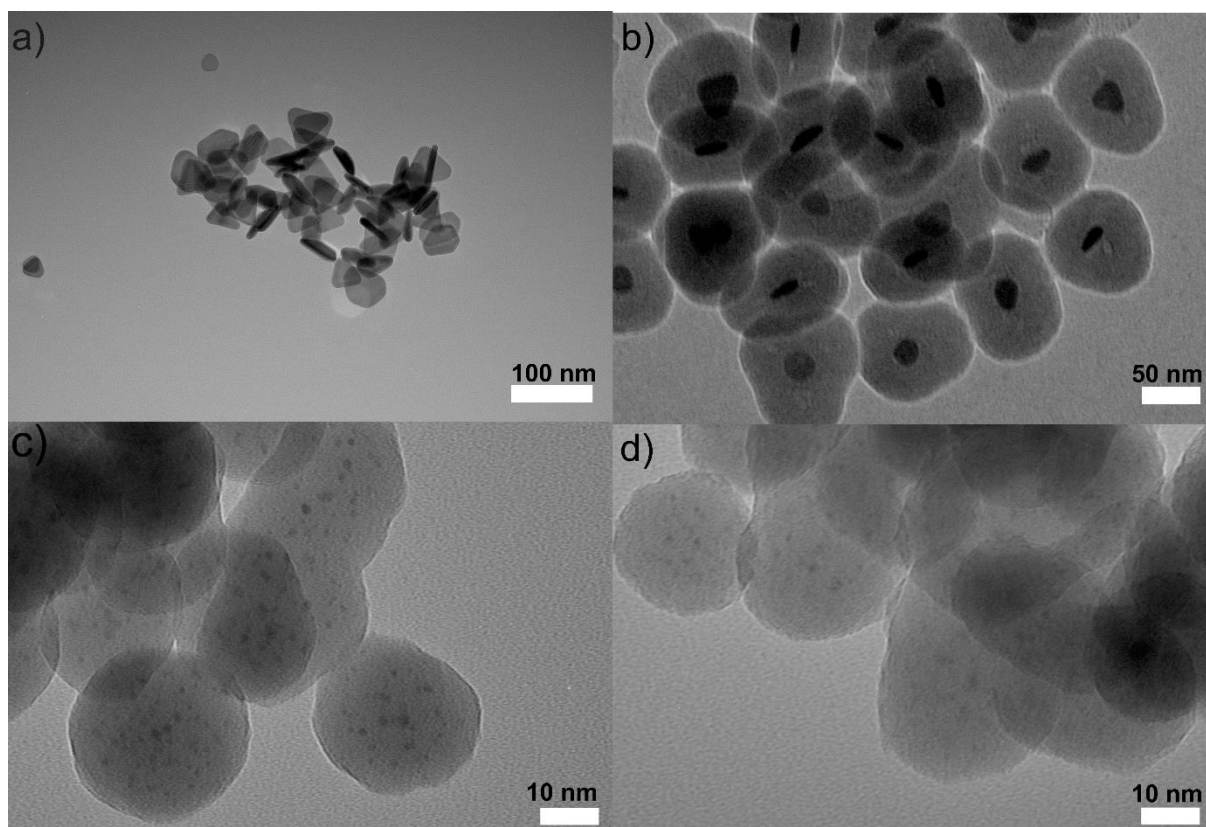


Figure 5.3: a) TEM image of a) as-synthesized Ag NPs, b) as-synthesized Ag@SiO₂, c) Ag@SiO₂ calcined at 650 °C, and d) Ag-Pd@SiO₂ sample after galvanic exchange.

The AgPd@silica catalysts were synthesized by redispersing the calcined Ag@SiO₂ sample and adding a Pd(II) salt in excess, which then underwent a galvanic replacement reaction. After the addition of K₂PdCl₄, the colour of the solution turned from yellow to black which is consistent with the reduction of the Pd salt. The complete replacement reaction of Ag with Pd precursor can be described as $2\text{Ag} + \text{Pd}^{2+} \rightarrow \text{Pd} + 2\text{Ag}^+$. A TEM image of the resulting AgPd@SiO₂ sample is shown in Figure 5.3d. The average particle size was measured to be 2.6 ± 1.3 nm. The final metal composition of Ag-Pd@silica samples was examined by AAS analysis which indicates the sample has 1.0% Pd and 0.1% Ag content. To compare the catalytic activity, Pd@SiO₂ materials were also made directly with a similar 1.0% metal loading which was confirmed by AAS analysis. The average particle size of Pd@SiO₂ catalysts was measured to be 2.2 ± 0.8 nm (see Chapter 6).

XPS was performed to probe the composition and chemical state of Ag and Pd in the silica matrix. Figure 5.4a shows the XPS spectrum of the Ag@SiO₂ starting material. The Ag 3d_{5/2} and Ag 3d_{3/2} peaks were seen at 368.3 eV and 374.3 eV. These values are in good agreement with reported values for metallic Ag.³⁷ Thus Ag clusters remain in the zerovalent state after the

calcination and the presence of oxidized Ag can be ruled out. The atom percentage of Ag as determined by XPS was reduced from 0.5% to 0.1% after the galvanic exchange with Pd. Figure 5.4b & c shows the XPS spectrum of the final Ag-Pd@SiO₂. The Ag 3d_{5/2} and Ag 3d_{3/2} peaks appear at 367.8 eV and 373.8 eV, respectively.³⁸ The Pd 3d XPS spectrum consists of Pd 3d_{5/2} and Pd 3d_{3/2} peaks at 334.5 eV and 339.8 eV corresponding to the binding energy of metallic Pd.⁴¹ The signal-to-noise for the Pd XPS is much poorer (despite the presence of significantly more Pd than Ag seen in AAS results), possibly due to a negligible amount of Pd on the surface of the particles.³⁹ The XPS results show evidence for the complete reduction of Pd²⁺ to zerovalent Pd oxidation state. The Ag 3d spectra are redshifted by 0.5 eV in comparison to that of pure Ag@SiO₂ catalysts, while the Pd 3d peaks also show a redshift by 0.5 eV which may be due to electronic AgPd interactions in the bimetallic clusters.⁴⁰⁻⁴² As Pd is more electronegative than Ag, charge transfer would be expected from Ag to Pd.⁴³ As a result, Ag would be expected to shift lower binding energy and Pd to higher binding energy. The negative shift of both Pd and Ag has previously been observed in the AgPd alloy system and was explained by Abrikosov *et al.* in terms of an inter-atomic charge redistribution due to valence electron distribution.⁴⁴

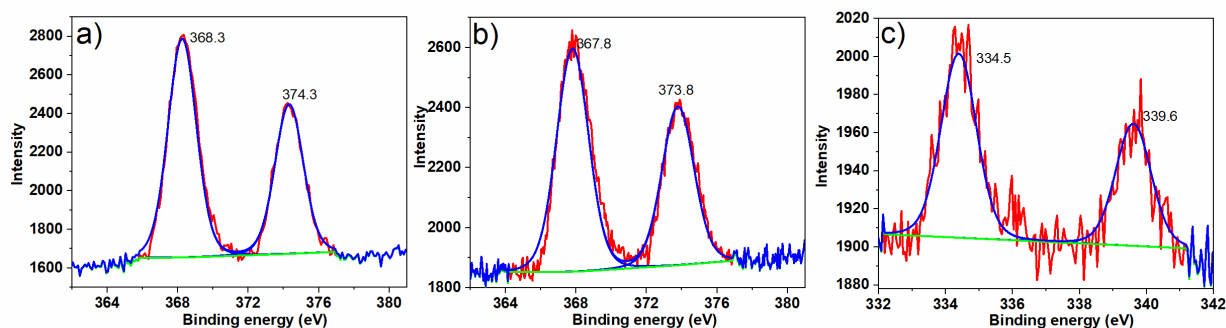


Figure 5.4: a) Ag 3d XPS spectra of Ag@SiO₂, b) Ag 3d XPS spectra of AgPd@SiO₂ and c) Pd 3d XPS spectra of AgPd@SiO₂.

XANES can be used for monitoring changes in the oxidation state of materials, whereas, the EXAFS technique provides information about the local structure of absorbing atom. In the XANES region, the white line intensity of the Pd L₃ edge spectra is directly related to the number of vacancies in the Pd 4d-band.⁴⁵ The Pd L₃ edge represents the 2p_{3/2} to 4d allowed transition which is sensitive to the oxidation state and vacancy change of the valence d band. *i.e.* the adsorption edge energy increases as the oxidation state of the metal increases. Hence a change in white line intensity reflects a change in the oxidation state of the Pd. The galvanic

reaction between K_2PdCl_4 and Ag clusters (Ag@SiO_2) was monitored by *in situ* XANES spectra at the Pd L_3 edge using a liquid cell set up for *in situ* XAS studies developed at the SXRMB beamline at the Canadian Light Source.⁴⁶ The *in situ* XAS spectra of the Pd salt solution before and after the addition of Ag@SiO_2 is shown in Figure 5.5. A prominent white line was observed for the K_2PdCl_4 solution which is an indication of the presence of Pd(II). After the addition of Ag@SiO_2 , the white line intensity at the Pd L_3 edge spectra decreased significantly, which is an indication of the reduction of Pd(II) to Pd(0). The final XANES spectrum closely resembles a Pd foil spectrum, thus suggesting that Pd is being fully reduced to the zerovalent state. This provides direct evidence for the galvanic reaction of K_2PdCl_4 with zerovalent Ag clusters.

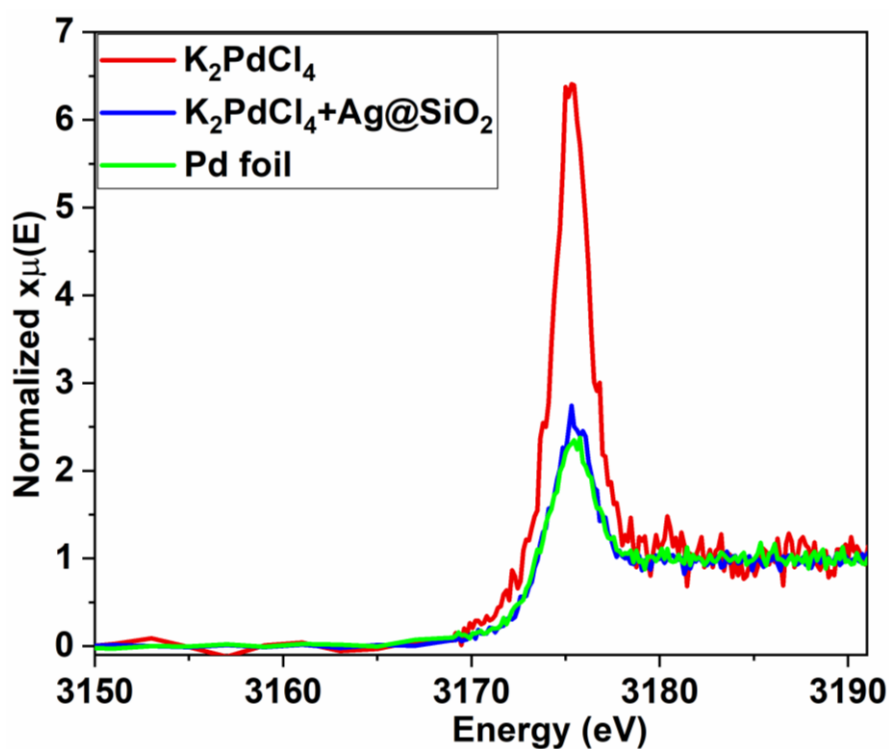


Figure 5.5: Pd L_3 -edge XANES spectra of K_2PdCl_4 before and after the addition of Ag@silica .

EXAFS analysis at both the Pd and Ag K edges was carried out in fluorescence mode on the Hard X-ray Microanalysis (HXMA) beamline at CLS. Figure 5.6 shows the Ag and Pd K edge EXAFS data in k -space for the AgPd@SiO_2 sample. The amplitude decreases for the AgPd@SiO_2 sample as compared to bulk Ag and Pd foil, respectively, suggesting that small clusters were formed that have a large fraction of atoms on the surface. The periodicity of the EXAFS oscillation pattern for AgPd@SiO_2 at both the Ag and Pd K edge was observed to be

slightly different than the respective foils which indicates the presence of bimetallic clusters. A face-centered cubic alloy model was used to fit Ag and Pd K edge data, and the fitting results at the k- and R-space are shown in Figure 5.7. Since Pd and Ag have similar atomic numbers, their backscattering and phase effects on the photoelectron wave is nearly identical, and thus it is very difficult to distinguish between these species around the central atom. Since the scattering of Ag-Ag and Ag-Pd are similar, general coordination numbers N_{Pd-M} and N_{Ag-M} were fit (whereas M is Ag or Pd). Black and red lines represent the experimental data and simulated EXAFS fit respectively. The EXAFS fit parameters that were obtained from 1st shell modeling are shown in Table 5.1. The modeled Ag-Ag distance of 2.83(1) Å is slightly shorter than the typical Ag-M distance in Ag foil (2.88 Å). Similarly, the Pd-M first shell distance of 2.799(9) Å is longer than typically seen for Pd foil (R=2.75 Å). These dissimilarities in interatomic distances are strong indicators of the presence of heteroatomic bonding in Ag-Pd catalysts.⁴⁷⁻⁴⁹ The average coordination number for the Ag-M and Pd-M shell was found to be 3.3(1) and 8.7(1) respectively. The low coordination number of Ag-M shell suggests that the majority of the Ag atoms are present on the Pd surface.^{50, 51} The CN of 3.3(1) for Ag-M contribution is likely due to the presence of Ag atoms on the edges or corners of the clusters. The presence of Ag atoms on the surface and Pd atoms in the core is also consistent with XPS analyses. By combining EXAFS, XPS and AAS results, it seems that the majority of the Ag atoms are located on the surface of the bimetallic clusters, while Pd atoms are predominantly in the core region.

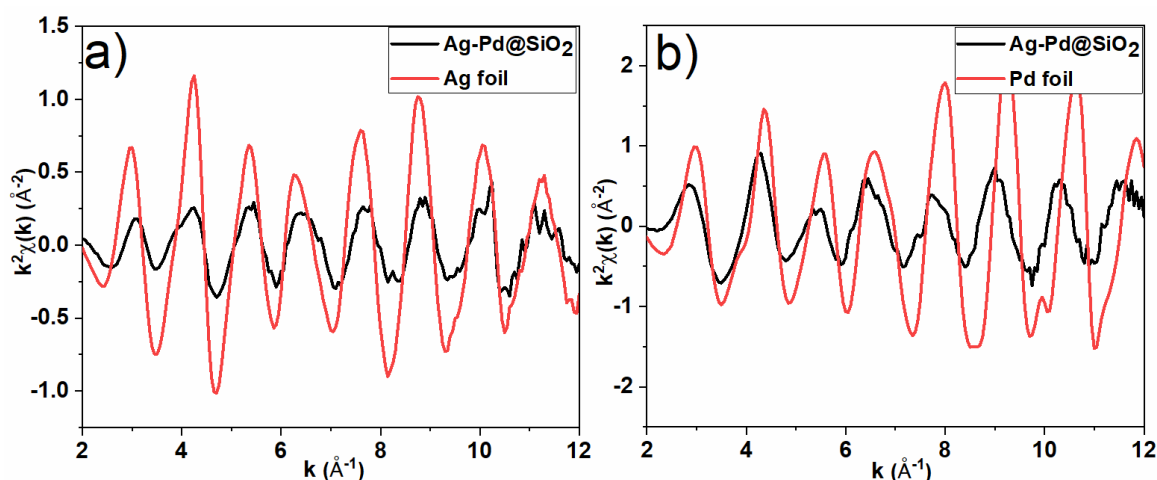
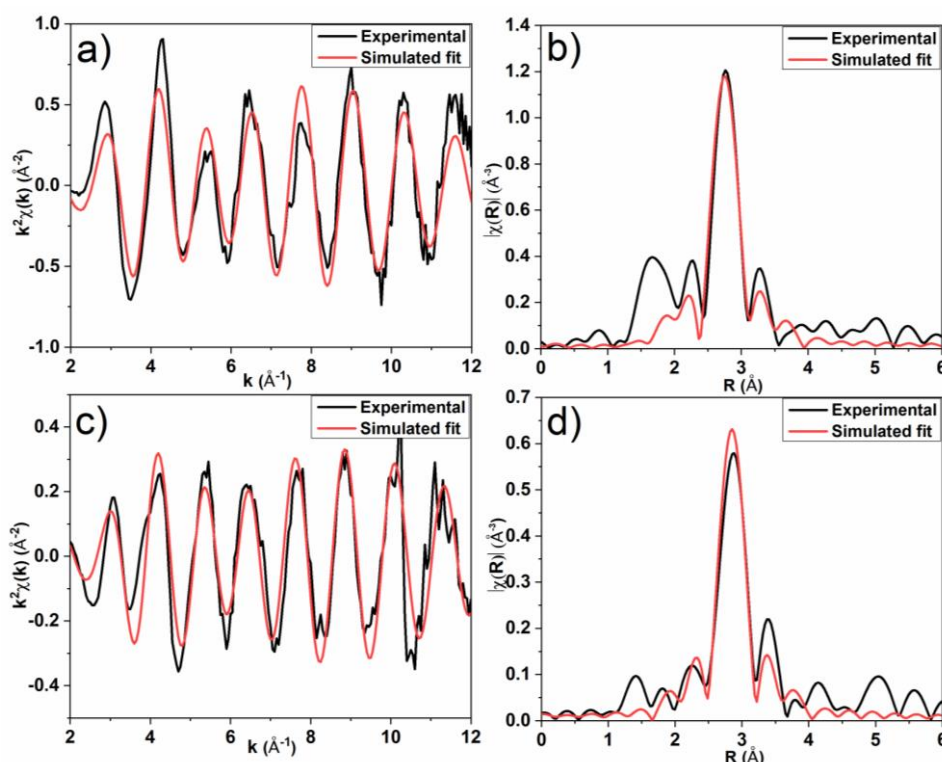


Figure 5.6: EXAFS data in k-space of AgPd@SiO₂ samples at a) the Ag K edge, and b) the Pd K edge.

Table 5.1: EXAFS fitting parameters of AgPd@SiO₂ catalyst.

	Type	CN	R/Å	σ^2 /Å ²	E _o Shift(eV)	R-factor (%)
Pd	Pd-M	8.7(9)	2.799(9)	0.009(1)	-2.2(8)	1.6
Ag	Ag-M	3.3(1)	2.83(1)	0.006(1)	-0.6(9)	1.7

**Figure 5.7:** EXAFS fitting data of AgPd@SiO₂, a) Pd K edge in k-space, b) Pd K edge in R-space, c) Ag K edge in k space, and d) Ag K edge in R space.

Pd catalysts are widely used for hydrogenation reactions, but when used for substrates such as of 3-hexyn-1-ol typically show poor selectivity to alkenes due to over-hydrogenation.⁵³ Active site isolation by addition of other metals is an efficient way to improve the selectivity to 3-hexen-1-ol.^{26,53,54} To analyze the catalytic activity and selectivity of the catalysts, the hydrogenation reaction of 3-hexyn-1-ol was evaluated over Ag@SiO₂, Pd@SiO₂, and Ag-Pd@SiO₂ catalysts, and results are shown in Table 5.2. No catalytic activity was observed using Ag@SiO₂. The activity was slightly higher in the case of the pure Pd@SiO₂ as compared to AgPd@SiO₂. However, the monometallic Pd@SiO₂ catalyst also promoted the over-hydrogenation and gave the undesired hexanol product. Interestingly, after the addition of Pd

to Ag@SiO₂, the catalyst became active for the hydrogenation reaction. A significant selectivity difference was observed for Pd@SiO₂ and AgPd@SiO₂ catalysts for the hydrogenation reaction. The promotional effect that was observed in AgPd catalysts is due to the synergetic effect of bimetallic AgPd nanoparticles for selective hydrogenations, as the presence of Ag atoms suppresses the full hydrogenation product and increases selectivity to 3-hexen-1-ol.⁵⁵ Mei *et al.* investigated the role of Ag on the Pd surface in selective hydrogenation of acetylene–ethylene mixtures over Pd and bimetallic PdAg alloy as model catalysts.⁵⁶ They found that the presence of Ag on the Pd surface weakens the binding strengths of all surface intermediates and therefore increases their rates of desorption as well as their rates of hydrogenation. Ag enhanced the desorption of ethylene and hydrogen from the catalyst surface and suppressed further hydrogenation. Mitsudome *et al.* reported that modification of Pd nanoparticles with Ag suppresses the over-hydrogenation of alkynes to alkanes.⁵⁷ They found that Ag-Pd core-shell structures are active for the semi-hydrogenation of 1-octyne under 1 bar H₂ at room temperature resulting in selectivity towards the alkene of 99%. The Pd core act as an H₂ source and the Ag shell served as the surface for the semi-hydrogenation of the alkyne resulting in a reduction of the intrinsically low alkene-selectivity of Pd by inhibiting the contact between Pd and the alkenes. Previously we investigated the selective hydrogenation of 3-hexyne-1-ol over AgPd catalysts synthesized via galvanic exchange reaction of Ag seed (3 nm) with K₂PdCl₄.²⁷ The catalytic activity and selectivity of catalysts with different Ag: Pd ratio was investigated and the catalysts with Ag: Pd ratios of 2:1 were found to be the most active catalysts, with high selectivity to *cis*-3-hexen-1-ol.

Table 5.2: The catalytic activity for 3-hexyne-1-ol hydrogenation reaction.

Catalysts	Ag: Pd ratio ^a	Conversion %	Selectivity %	
			3 hexen-1-ol	3 hexan-1-ol
Ag@SiO ₂	2.0:0.0	0.0	-	-
Ag-Pd@SiO ₂	0.1:1.0	43.0	90.7	9.3
Pd@SiO ₂	0.0:1.0	47.6	67.6	32.4

^a Ag: Pd ratio from AAS analysis. The 3-hexyne-1-ol hydrogenation reaction (100 μL) was performed at room temperature for 3 h over the 20 mg of the catalyst with 1.0% Pd loading.

5.5. Conclusions

AgPd bimetallic catalysts were prepared using a top-down thermally activated dispersion of large Ag nanoparticles, followed by galvanic replacement of Ag with Pd. *In situ* XANES spectroscopy showed that all Pd was reduced during the galvanic replacement of K₂PdCl₄ with

the Ag clusters. EXAFS spectroscopy and XPS studies suggested that the majority of the Ag atoms are located on the surface of the resulting bimetallic clusters and Pd atoms are in the core region. The catalytic activity for the 3-hexyn-1-ol hydrogenation reaction was investigated. AgPd catalysts derived from Ag@SiO₂ showed better selectivity to 3-hexen-1-ol than their monometallic counterparts, which indicates the isolation of active Pd sites suppresses the over-hydrogenation of 3-hexyn-1-ol.

5.6 References

- (1) Iqbal, P.; Preece, J. A.; Mendes, P. M.; Nanotechnology: The “Top-Down” and “Bottom-Up” Approaches. *Nanotechnol. Supramol. Chem.* **2012**, *6*, 1-12.
- (2) Nie, X.; Qian, H.; Ge, Q.; Xu, H.; Jin, R. CO Oxidation Catalyzed by Oxide-Supported Au₂₅(SR)₁₈ Nanoclusters and Identification of Perimeter Sites as Active Centers. *ACS Nano.* **2012**, *6*, 6014-6022.
- (3) Sudheeshkumar, V.; Sulaiman, K. O.; Scott, R. W. J. Activation of Atom-Precise clusters for Catalysis. *Nanoscale Adv.* **2020**, *2*, 55-69.
- (4) Pareek, V.; Bhargava, A.; Gupta, R.; Jain, N.; Panwar, J. Synthesis and Applications of Noble Metal Nanoparticles: A Review. *Adv. Sci. Eng. Med.* **2017**, *9*, 527-544,
- (5) Pelton, M.; Aizpurua, J.; Bryant, G. Metal-nanoparticle plasmonics. *Laser. Photonics Rev.* **2008**, *2*, 136-159.
- (6) Lee, D. K.; Kang, Y. S. Synthesis of Silver Nanocrystallites by a New Thermal Decomposition Method and Their Characterization. *ACS. Nano.* **2004**, *26*, 252-256.
- (7) Gharibshahi, L.; Saion, E.; Gharibshahi, E.; Shaari, A. H.; Matori, K. A. Structural and Optical Properties of Ag Nanoparticles Synthesized by Thermal Treatment Method. *Mater.* **2017**, *10*, 402-411.
- (8) Wang, Y.; Xia, Y. Bottom-Up and Top-Down Approaches to the Synthesis of Monodispersed Spherical Colloids of Low Melting-Point Metals. *Nano Lett.* **2004**, *4*, 2047-2050.
- (9) Jung, J. H.; Cheol Oh, H.; Soo Noh, H.; Ji, J. H.; Soo Kim, S. Metal Nanoparticle Generation Using a Small Ceramic Heater With a Local Heating Area. *J. Aerosol. Sci.* **2006**, *37*, 1662-1670.
- (10) Lei, Z. W.; Liu, M.; Ge, W.; Fu, Z. P.; Reinhardt, K.; Knize, R. J.; Lu, Y. Morphology and Optical Absorption Change of Ag/SiO₂ Core-Shell Nanoparticles Under Thermal Annealing. *Appl. Phys. Lett.* **2012**, *101*, 272-283.

- (11) Chatterjee, K.; Banerjee, S.; Chakravorty, D. Plasmon Resonance Shifts in Oxide-ated Silver Nanoparticles. *Phys. Rev. B* **2002**, *66*, 085421.
- (12) Gangishetty, M. K.; Scott, R. W. J.; Kelly, T. L. Thermal Degradation Mechanism of Triangular Ag@SiO₂ Nanoparticles. *Dalton Trans.* **2016**, *45*, 9827-9834.
- (13) Lide, D. R. CRC Handbook of Chemistry and Physics. **2005**.
- (14) Zhang, W.; Yang, J.; Lu, X. Tailoring Galvanic Replacement Reaction for the Preparation of Pt/Ag Bimetallic Hollow Nanostructures with Controlled Number of Voids. *ACS Nano* **2012**, *6*, 7397-7405.
- (15) Prevo, B. G.; Esakoff, S. A.; Mikhailovsky, A.; Zasadzinski, J. A. Scalable Routes to Gold Nanoshells with Tunable Sizes and Response to Near-Infrared Pulsed-Laser Irradiation. *Small* **2008**, *4*, 1183-1195.
- (16) da Silva, A. G. M.; Rodrigues, T. S.; Correia, V. G.; Alves, T. V.; Alves, R. S.; Ando, R. A.; Ornellas, F. R.; Wang, J.; Andrade, L. H.; Camargo, P. H. C. Plasmonic Nanorattles as Next-Generation Catalysts for Surface Plasmon Resonance-Mediated Oxidations Promoted by Activated Oxygen. *Angew. Chem. Inter. Edit.* **2016**, *55*, 7111-7115.
- (17) Rodrigues, T. S.; DaSilva, A. G. M.; De Moura, A. B. L.; Freitas, I. G.; Camargo, P. H. C. Rational Design of Plasmonic Catalysts: Matching the Surface Plasmon Resonance with Lamp Emission Spectra for Improved Performance in AgAu nanorings. *RSC Adv.* **2016**, *6*, 62286-62290.
- (18) da Silva, A. G. M.; Rodrigues, T. S.; Haigh, S. J.; Camargo, P. H. C. Galvanic Replacement Reaction: Recent Developments for Engineering Metal Nanostructures Towards Catalytic Applications. *Chem. Commun.* **2017**, *53*, 7135-7148.
- (19) Chen, J.; Wiley, B.; McLellan, J.; Xiong, Y.; Li, Z. Y.; Xia, Y. Optical Properties of Pd–Ag and Pt–Ag Nanoboxes Synthesized via Galvanic Replacement Reactions. *Nano Lett.* **2005**, *5*, 2058-2062.
- (20) Chen, A. N.; McClain, S. M.; House, S. D.; Yang, J. C.; Skrabalak, S. E. Mechanistic Study of Galvanic Replacement of Chemically Heterogeneous Templates. *Chem. Mater.* **2019**, *31*, 1344-1351.

- (21) Sutter, E.; Jungjohann, K.; Bliznakov, S.; Courty, A.; Maisonhaute, E.; Tenney, S.; Sutter, P. In situ Liquid-Cell Electron Microscopy of Silver–Palladium Galvanic Replacement Reactions on Silver Nanoparticles. *Nat. Commun.* **2014**, *5*, 4949-4958.
- (22) Lee, C. L.; Tseng, C. M.; Wu, R. B.; Wu, C. C.; Syu, S. C. Catalytic Characterization of Hollow Silver/Palladium Nanoparticles Synthesized by a Displacement Reaction. *Electrochim. Acta.* **2009**, *54*, 5544-5547.
- (23) Tsuji, M.; Kidera, T.; Yajima, A.; Hamasaki, M.; Hattori, M.; Tsuji, T.; Kawazumi, H. Synthesis of Ag–Au and Ag–Pd Alloy Triangular Hollow Nanoframes by Galvanic Replacement Reactions Without and With Post-Treatment using NaCl in an Aqueous Solution. *CrystEngComm.* **2014**, *16*, 2684-2691.
- (24) Tedsree, K.; Li, T.; Jones, S.; Chan, C. W. A.; Yu, K. M. K.; Bagot, P. A. J.; Marquis, E. A.; Smith, G. D. W.; Tsang, S. C. E. Hydrogen Production from Formic Acid Decomposition at Room Temperature using a Ag–Pd Core–Shell Nanocatalyst. *Nature Nanotechnol.* **2011**, *6*, 302-307.
- (25) Zhang, T.; Li, L.; Ye, Z.; Yang, Q.; Tian, Y.; Guo, X. Preparation and characterization of Ag–Pd Bimetallic Nano-Catalysts in Thermosensitive Microgel Nano-Reactor. *RSC Adv.* **2018**, *8*, 18252-18259.
- (26) Pei, G. X.; Liu, X. Y.; Wang, A.; Lee, A. F.; Isaacs, M. A.; Li, L.; Pan, X.; Yang, X.; Wang, X.; Tai, Z.; Wilson, K.; Zhang, T. Ag Alloyed Pd Single-Atom Catalysts for Efficient Selective Hydrogenation of Acetylene to Ethylene in Excess Ethylene. *ACS Catal.* **2015**, *5*, 3717-3725.
- (27) Calver, C. F.; Dash, P.; Scott, R. W. J. Selective Hydrogenations with Ag-Pd Catalysts Prepared by Galvanic Exchange Reactions. *ChemCatChem* **2011**, *3*, 695-697.
- (28) Sulaiman, K. O.; Sudheeshkumar, V.; Scott, R. W. J. Activation of Atomically Precise Silver Clusters on Carbon Supports for Styrene Oxidation Reactions. *RSC Adv.* **2019**, *9*, 28019-28027.
- (29) Cargnello, M.; Wieder, N. L.; Canton, P.; Montini, T.; Giambastiani, G.; Benedetti, A.; Gorte, R. J.; Fornasiero, P. A Versatile Approach to the Synthesis of Functionalized Thiol-Protected Palladium Nanoparticles. *Chem. Mater.* **2011**, *23*, 3961-3969.

- (30) Schneider, C. A.; Rasband, W. S.; Eliceiri, K. W. NIH Image to ImageJ: 25 years of image analysis. *Nat. Method.* **2012**, *9*, 671-682.
- (31) Ravel, B.; Newville, M. ATHENA, ARTEMIS, HEPHAESTUS: Data Analysis for X-ray Absorption Spectroscopy Using IFEFFIT. *J. Synchrotron. Radiat.* **2005**, *12*, 537-541.
- (32) Baltrusaitis, J.; Mendoza-Sanchez, B.; Fernandez, V.; Veenstra, R.; Dukstiene, N.; Roberts, A.; Fairley, N. Generalized Molybdenum Oxide Surface Chemical State XPS Determination via Informed Amorphous Sample Model. *Appl. Surf. Sci.* **2015**, *326*, 151-161.
- (33) Amirjani, A.; Fatmehsari, D. Synthesis of Silver Nanotriangles with Tunable Edge Length: a Promising Candidate for Light Harvesting Purposes within Visible and Near-Infrared Ranges. *Talanta.* **2018**, *176*, 242.
- (34) Zanganeh, N.; Guda, V. K.; Toghiani, H.; Keith, J. M. Sinter-Resistant and Highly Active Sub-5 nm Bimetallic Au-Cu Nanoparticle Catalysts Encapsulated in Silica for High-Temperature Carbon Monoxide Oxidation. *ACS Appl. Mater. Inter.* **2018**, *10*, 4776-4785.
- (35) Habibi, A. H.; Hayes, R. E.; Semagina, N. Bringing Attention to Metal (un)availability in Encapsulated Catalysts. *Catal. Sci. Technol.* **2018**, *8*, 798-805.
- (36) Kim, S.; Lee, D. W.; Lee, K. Y.; Cho, E. A. Effect of Pd Particle Size on the Direct Synthesis of Hydrogen Peroxide from Hydrogen and Oxygen over Pd Core-Porous SiO₂ Shell Catalysts. *Catal. Lett.* **2014**, *144*, 905-911.
- (37) Zhang, H.; Wang, G.; Chen, D.; Lv, X.; Li, J. Tuning Photoelectrochemical Performances of Ag-TiO₂ Nanocomposites via Reduction/Oxidation of Ag. *Chem. Mater.* **2008**, *20*, 6543-6549.
- (38) Wu, P.; Huang, Y.; Kang, L.; Wu, M.; Wang, Y. Multisource Synergistic Electrocatalytic Oxidation Effect of Strongly Coupled PdM (M = Sn, Pb)/N-doped Graphene Nanocomposite on Small Organic Molecules. *Sci. Rep.* **2015**, *5*, 14173-14185.
- (39) Vysakh, A. B.; Babu, C. L.; Vinod, C. P. Demonstration of Synergistic Catalysis in Au@Ni Bimetallic Core-Shell Nanostructures. *J. Phys. Chem. C.* **2015**, *119*, 8138-8146, DOI: 10.1021/jp5128089.

- (40) Slanac, D. A.; Hardin, W. G.; Johnston, K. P.; Stevenson, K. J. Atomic Ensemble and Electronic Effects in Ag-Rich AgPd Nanoalloy Catalysts for Oxygen Reduction in Alkaline Media. *J. Am. Chem. Soc.* **2012**, *134*, 9812-9819.
- (41) Sengar, S. K.; Mehta, B. R.; Govind. Size and Alloying Induced Shift in Core and Valence Bands of Pd-Ag and Pd-Cu Nanoparticles. *J. Appl. Phys.* **2014**, *115*, 1-9.
- (42) Semaltianos, N. G.; Chassagnon, R.; Moutarlier, V.; Blondeau-Patissier, V.; Assoul, M.; Monteil, G. Nanoparticles Alloying in Liquids: Laser-Ablation-Generated Ag or Pd Nanoparticles and Laser Irradiation-Induced AgPd Nanoparticle Alloying. *Nanotechnol.* **2017**, *28*, 1-8.
- (43) Alonso, J. A.; Girifalco, L. A. Electronegativity Scale for Metals. *Phys. Rev. B.* **1979**, *19*, 3889-3895.
- (44) Abrikosov, I. A.; Olovsson, W.; Johansson, B. Valence-Band Hybridization and Core Level Shifts in Random Ag-Pd Alloys. *Phys. Rev. Lett.* **2001**, *87*, 1-12.
- (45) Sham, T. K. L-Edge X-ray-Absorption Systematics of the Noble Metals Rh, Pd, and Ag and the Main-Group Metals In and Sn: A Study of the Unoccupied Density of States in 4d Elements. *Phys. Rev. B.* **1985**, *31*, 1888-1902.
- (46) Yao, Y.; Hu, Y.; Scott, R. W. J. Watching Iron Nanoparticles Rust: An in Situ X-ray Absorption Spectroscopic Study. *J. Phys. Chem. C.* **2014**, *118*, 22317-22324.
- (47) Navlani-García, M.; Mori, K.; Nozaki, A.; Kuwahara, Y.; Yamashita, H. Screening of Carbon-Supported PdAg Nanoparticles in the Hydrogen Production from Formic Acid. *Ind. Eng. Chem. Res.* **2016**, *55*, 7612-7620.
- (48) Verma, P.; Kuwahara, Y.; Mori, K.; Yamashita, H. Synthesis and Characterization of a Pd/Ag Bimetallic Nanocatalyst on SBA-15 Mesoporous Silica as a Plasmonic Catalyst. *J. Mater. Chem. A.* **2015**, *3*, 18889-18897.
- (49) Hu, C.; Mu, X.; Fan, J.; Ma, H.; Zhao, X.; Chen, G.; Zhou, Z.; Zheng, N. Interfacial Effects in PdAg Bimetallic Nanosheets for Selective Dehydrogenation of Formic Acid. *ChemNanoMat* **2016**, *2*, 28-32.
- (50) Chen, C. H.; Sarma, L. S.; Chen, J. M.; Shih, S. C.; Wang, G. R.; Liu, D. G.; Tang, M.T.; Lee, J. F.; Hwang, B. J. Architecture of Pd–Au Bimetallic Nanoparticles in Sodium Bis(2-

ethylhexyl)Sulfosuccinate Reverse Micelles as Investigated by X-ray Absorption Spectroscopy. *ACS Nano*. **2007**, *1*, 114-125.

(51) Duchesne, P. N.; Zhang, P. Element-Specific Analysis of the Growth Mechanism, Local Structure, and Electronic Properties of Pt Clusters Formed on Ag Nanoparticle Surfaces. *J. Phys. Chem. C*. **2014**, *118*, 21714-21721.

(52) Benavidez, A. D.; Burton, P. D.; Nogales, J. L.; Jenkins, A. R.; Ivanov, S. A.; Miller, J. T.; Karim, A. M.; Datye, A. K. Improved Selectivity of Carbon-Supported Palladium Catalysts for the Hydrogenation of Acetylene in Excess Ethylene. *Appl. Catal. A: Gen.* **2014**, *482*, 108-115.

(53) Zhou, H.; Yang, X.; Li, L.; Liu, X.; Huang, Y.; Pan, X.; Wang, A.; Li, J.; Zhang, T. PdZn Intermetallic Nanostructure with Pd–Zn–Pd Ensembles for Highly Active and Chemoselective Semi-Hydrogenation of Acetylene. *ACS Catal.* **2016**, *6*, 1054-1061.

(54) Osswald, J.; Giedigkeit, R.; Jentoft, R. E.; Armbrüster, M.; Girgsdies, F.; Kovnir, K.; Ressler, T.; Grin, Y.; Schlögl, R. Palladium–Gallium Intermetallic Compounds for the Selective Hydrogenation of Acetylene: Part I: Preparation and Structural Investigation Under Reaction Conditions. *J. Catal.* **2008**, *258*, 210-218.

(55) González, S.; Neyman, K. M.; Shaikhutdinov, S.; Freund, H. J.; Illas, F. On the Promoting Role of Ag in Selective Hydrogenation Reactions over Pd–Ag Bimetallic Catalysts: A Theoretical Study. *J. Phys. Chem. C*. **2007**, *111*, 6852-6856.

(56) Mei, D.; Neurock, M.; Smith, C. M. Hydrogenation of Acetylene–Ethylene Mixtures Over Pd and Pd–Ag alloys: First-principles-Based kinetic Monte Carlo Simulations. *J. Catal.* **2009**, *268*, 181-195.

(57) Mitsudome, T.; Urayama, T.; Yamazaki, K.; Maehara, Y.; Yamasaki, J.; Gohara, K.; Maeno, Z.; Mizugaki, T.; Jitsukawa, K.; Kaneda, K. Design of Core-Pd/Shell-Ag Nanocomposite Catalyst for Selective Semihydrogenation of Alkynes. *ACS Catal.* **2016**, *6*, 666-670.

CHAPTER 6

Activation of Silica Encapsulated Pd_m(MUA)_n

Clusters for Catalysis

This project focuses on the synthesis and activation of silica-encapsulated Pd_m(MUA)_n clusters. TEM and EXAFS are employed to understand the morphological and structural changes of the catalysts during the activation process. The thermal stability of Pd_m(MUA)_n clusters in a silica shell is compared with a control sample of Pd_m(MUA)_n clusters on silica spheres. The catalytic activity for methane combustion reaction and CO adsorption analysis are discussed.

Synthetic work on the clusters was done with the assistance of Miranda Lavier and Brianna Lukan. Catalytic activity studies were done by Dr. Jing Shen in collaboration with the laboratory of Dr. Natalia Semagina. This chapter is a manuscript that is in preparation for publication. The first draft of this manuscript was written by myself.

6.1. Abstract

Methane is the most abundant constituent of natural gas and it is difficult to fully oxidize without effective catalysts. Pd is recognized as the most efficient catalyst for the methane combustion reaction and typically shows increased activity at small particle sizes. However, few routes are available for the preparation of near-monodisperse Pd clusters for catalysis. Here we focused on the synthesis and activation of mercaptoundecanoic acid protected Pd clusters (1.1 ± 0.3 nm), and encapsulated them in a silica matrix using sol-gel chemistry. EXAFS analysis revealed that removal of thiolate ligands at 250 °C in air leads to the partial oxidation of Pd clusters and that the clusters are completely oxidized to PdO at 650 °C. TEM and CO chemisorption studies suggest that silica-coated Pd clusters are much more resistant to sintering than the control sample of Pd clusters on silica spheres. The activity studies over silica-coated and non-coated catalysts for the methane combustion reaction indicate the presence of the silica shell on the Pd clusters significantly improves the catalytic activity. Low activity at higher loading was explained by CO chemisorption analysis, which indicated that fewer sites were available for catalysis in the higher loading samples.

6.2. Introduction

Over the past several decades, Pd-based heterogeneous catalysts have received great attention because of their wide range of applications in catalysis. Pd based catalysts are widely used as an oxidation/reduction catalyst for reactions such as CO oxidation,¹ methane combustion,² aerobic alcohol oxidation,³ NO_x reduction,⁴ and hydrogenation of unsaturated alcohols.⁵ Pd is well known to catalyze oxidation reactions with high efficiency and can play a significant role in a three-way catalytic converters to minimize the contents of NO_x, CO, and unburned hydrocarbons in automobile emissions.⁶ Studies show that catalytic activity and selectivity of Pd nanoparticles often improve when the size of the particles is reduced to the nanoscale.⁷⁻⁹ However, few routes are available to synthesize highly monodisperse Pd clusters.¹⁰⁻¹³

While there has been tremendous progress in the synthesis of atom-precise Au and Ag systems,¹⁴⁻¹⁹ the synthesis of analogous thiolate protected Pd clusters has been challenging due to the formation of strong Pd-thiolate bonds and the possibility of the subsequent formation of PdS species.²⁰⁻²³ Cargnello *et al.* synthesized water-soluble Pd clusters with a size of 2 nm using mercaptoundecanoic acid (MUA) as a capping agent.¹² Gao *et al.* reported a modified

Brust method for the synthesis of $\text{Pd}_6(\text{SC}_{12}\text{H}_{26})_{12}$ clusters using PdCl_2 as a Pd source and NaBH_4 as a reducing agent in tetrahydrofuran.²⁴ Recently, Zhuang *et al.* successfully synthesized atom-precise, non-metallic $\text{Pd}_6(\text{C}_{12}\text{H}_{25}\text{S})_{11}$ clusters using Pd(II) acetylacetonate as a metal precursor and oleylamine as a solvent.¹³ A single-phase method has been reported for the synthesis of 4-tert-butylbenzenethiolate-protected Pd clusters with less than 20 Pd atoms.²⁵ Several studies show that stabilizing ligands on the active sites may block the accessibility of reactants, resulting in a change in the catalytic activity and selectivity of catalysts.¹⁴

Several stabilization strategies have been explored to overcome the limitations associated with the sintering of Pd nanoparticles and enhance the stability of precious metal nanoparticles.²⁶⁻²⁹ Encapsulation with porous metal oxides such as silica, titania, or zirconia is an efficient method to achieve high thermal stability.³⁰ Among the various metal oxides, silica is the most widely used material for the synthesis of core-shell catalysts because of its high thermal stability and chemical inertness. For example, Joo *et al.* demonstrated that a 17 nm overlayer of silica prevented the aggregation of 14 nm Pt nanoparticles and found to be stable during calcination up to 750 °C.³¹ Our group synthesized a core-shell catalyst by incorporating MUA-protected Au_{25} clusters into a silica matrix via sol-gel synthesis.³² The sintering of clusters could be mitigated by encapsulating them with a 40 nm silica shell. The size of the Au particles was maintained to be ~3 nm upon calcination at 650 °C for 3 h when they were inside the silica shell. Samanta *et al.* reported a procedure for the synthesis of highly sinter-resistant silica-encapsulated Pd catalysts using propylammonium-functionalized thiolate protected Pd clusters.³⁰ The removal of ligands at 350 °C lead to minor sintering and the average size of the particles was maintained even after calcination at 750 °C.

Here we synthesized MUA-protected Pd clusters, and encapsulated the $\text{Pd}_m(\text{MUA})_n$ clusters with silica using sol-gel chemistry. EXAFS analysis indicated that thermal treatment at 250 °C not only leads to the removal of ligands from the Pd surface but also leads to the oxidation of Pd. Upon calcination at 650 °C, the Pd clusters were found to be completely oxidized to PdO. The catalytic activity for the methane combustion reaction over the silica-coated and non-coated catalysts was investigated. A significant improvement in thermal stability and catalytic activity was observed when Pd clusters were confined in a silica shell. Uncoated Pd clusters were found to be deactivated after thermal treatment at 650 °C due to the loss of active surface area by sintering.

6.3. Materials and Methods

6.3.1. Materials

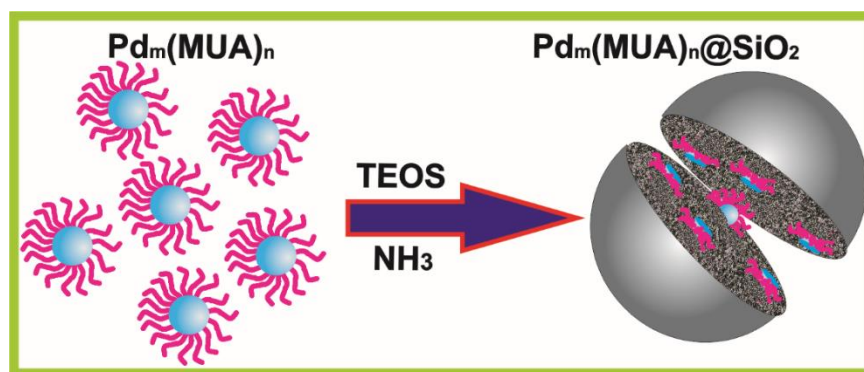
Potassium tetrachloropalladate (II) (K_2PdCl_4 , 98%, Aldrich), 11-mercaptoundecanoic acid (MUA, 95%, Sigma-Aldrich), sodium borohydride ($NaBH_4$, 98%, Alfa Aesar), acetone (99.5%, Fischer Scientific), o-phosphoric acid (H_3PO_4 , 85%, Fischer Scientific), methylene chloride (CH_2Cl_2 , 99.5%, Fischer Scientific), tetrahydrofuran (99.9%, OmniSolv), ethanol (95%, Commercial Alcohols), tetraethyl orthosilicate (98%, Aldrich), ammonium hydroxide (NH_4OH , 28.0-30.0%, EMD Millipore), and 2-propanol (99.5%, Fischer Scientific) were used as received. Milli-Q water was used for synthesis throughout.

6.3.2. Synthesis of $Pd_m(MUA)_n$ clusters

Pd clusters were synthesized following a procedure detailed by Cargnello *et al.*¹² Briefly, K_2PdCl_4 (20 mg, 0.060 mmol) was dissolved in H_2O (2 mL). To this clear brown solution, acetone (10 mL) was added, which changed the solution color to a clear orange. Next, H_3PO_4 (250 μ L) was added, followed by MUA (7.0 mg, 0.030 mmol). The solution was stirred for 5 min, then cooled in an ice bath. After cooling, a solution of $NaBH_4$ (23.2 mg, 0.613 mmol) in H_2O (1 mL) was added. The solution immediately became black upon the addition of $NaBH_4$ solution. After stirring for an additional 5 min, the ice bath was removed, and the solution was stirred at room temperature for 5 min. The acetone was removed by vacuum at room temperature and the solid black product was collected by centrifugation. The solid was washed with CH_2Cl_2 and water and left to dry at room temperature.

6.3.3. Synthesis of silica-encapsulated $Pd_m(MUA)_n$ clusters

The silica encapsulation synthesis strategy is shown in Scheme 6.1. $Pd_m(MUA)_n$ clusters (10 mg) were dissolved in THF (1 ml), then diluted with ethanol (10 mL). This $Pd_m(MUA)_n$ solution (10 mL) was added to a stirred solution of ethanol (10 mL) and TEOS (500 μ L). The solution was stirred for 2 min, then NH_4OH (1 mL) was added. The solution was stirred for 12 h. Silica encapsulated $Pd_m(MUA)_n$ clusters (0.2738 g) were collected by centrifugation, then washed with H_2O and ethanol. The product was left to dry at room temperature. The dried $Pd_m(MUA)_n@SiO_2$ particles were calcined at 250 °C and 650 °C for 3 h at a heating rate 10 °C min^{-1} to give $Pd@SiO_2$.



Scheme 6.1: Silica encapsulation of $\text{Pd}_m(\text{MUA})_n$ clusters.

6.3.4. Synthesis of $\text{Pd}_m(\text{MUA})_n$ clusters on silica spheres (control sample)

The $\text{Pd}_m(\text{MUA})_n$ clusters (10 mg) dissolved in THF (1 mL) and diluted to 10 ml with ethanol. SiO_2 spheres (0.2728 g) were added to this solution and stirred for 12 h at room temperature, followed by drying at 100 °C to remove the water.³² Pd/SiO_2 was then calcined at 650 °C in air for 3 h; the heating rate was 10 °C min^{-1} . Metal loading on both $\text{Pd}@/\text{SiO}_2$ and Pd/SiO_2 were found to be 2.2 % wt% Pd by AAS.

6.3.5. Characterization

UV-Vis absorption spectra of the $\text{Pd}_m(\text{MUA})_n$ clusters was collected by a Varian Cary 50 Bio UV-Vis Spectrometer. Images of the $\text{Pd}_m(\text{MUA})_n$ clusters were collected by a HT7700 TEM operating at 100 kV. ImageJ software was used to measure the size of 100 clusters for cluster size distribution histograms.³³ Extended X-ray Absorption Spectra Fine Structure (EXAFS) spectroscopic analysis was performed on the HXMA beamline 061D-1 (energy range 5-30 keV, resolution $1 \times 10^{-4} \Delta E/E$) at the Canadian Light Source. All data were collected in transmission mode. The energy for the Pd-K edge (24350 eV) was selected by using a Si (111) double crystal monochromator with a Rh-coated 100 nm long KB mirror. The double crystal monochromator was used to remove higher harmonics. Data analysis and EXAFS fitting were carried out using the Demeter software package.³³ An amplitude reduction factor of 0.86 was obtained from fitting Pd foil. The EXAFS fitting parameters of samples were determined by keeping this amplitude reduction factor fixed. The fitting of the data was done over the range 1.3-3.8 Å (R space) and 2.5-13.5 Å (k space), which includes three shells, and modelling results are shown in Table 6.1. Thermal gravimetric analysis (TGA) was performed using a TA Instruments TGA Q5000IR under air flow. For the analysis, $\text{Pd}_m(\text{MUA})_n$ clusters were heated from 25 to 500 °C with a heating rate of 10 °C /min. The Brunauer–Emmett–Teller (BET) surface area and pore size distribution of the $\text{Pd}@/\text{SiO}_2$ catalysts were performed on an ASAP 2010 Micrometrics instrument. Prior to the analysis, the catalyst was degassed under vacuum

at 200 ± 2 °C and nitrogen adsorption analysis was conducted at -196 °C. An AutoChem 2920HP instrument equipped with a quartz U-tube reactor and a thermal conductivity detector (TCD) was used for CO chemisorption analysis. Prior to the analysis, the catalyst was reduced under 10% H₂/Ar (25 mL min⁻¹) flow at 350 °C for 1 h. Metal loadings were analyzed by a Varian Spectra AA 55 Atomic Absorption Spectroscope.

6.3.6. Catalytic activity for the methane combustion reaction

The catalytic activity of Pd@SiO₂ calcined at 650 °C for 3 h was tested for the methane combustion reaction. The catalytic test was performed in a 20" long tubular reactor with an inner diameter of 3/8". The catalyst bed with 1.2 mg Pd loading was packed in the middle of the tubular reactor and layers of quartz wool were used at both ends of the catalyst bed. Gases, 10 % (CH₄/N₂) and extra dry air were used for the catalysis. The feed rate for methane and air was maintained to be 8.5 ml/min and 201 ml/min respectively which was controlled by mass flow controllers (Matheson and MKS). Approximately 4000 ppm of methane was used for the catalytic activity studies and the corresponding gas hourly space value was calculated between 586 000–592 000 L STP per h per kg catalyst. The GHSV was defined as a total flow rate (214 mL min⁻¹, STP) per the weight of the catalyst in kg used in the reactor.

6.4. Results and Discussion

A UV-Vis absorption spectra of Pd_m(MUA)_n clusters is shown in Figure 6.1a, which shows a featureless absorption in the visible region and a steep rise in the lower wavelength which indicates the reduction of Pd(II) to Pd(0) and the formation of very small Pd colloids.³⁴ TEM images of the as-synthesized clusters before and after silica encapsulation are shown in Figures 6.2a and 6.2b. The average particle size of the Pd clusters in the Pd_m(MUA)_n and Pd_m(MUA)_n@SiO₂ samples were measured to be 1.1 ± 0.3 nm and 1.3 ± 0.4 nm respectively. After encapsulation, a slightly larger size was seen, which is likely an artifact due to the inability to focus on small clusters in a three-dimensional silica sphere. After calcination at 250 °C, the average size of the particles was measured to be 2.2 ± 0.8 nm, which is shown in Figure 6.2c. A little growth in the particle size was seen in the calcined sample which is likely due to the agglomeration of multiple clusters in the single silica matrix. A major weight loss was observed at a temperature range of 150-250 °C in the TGA analysis (Figure 6.1b) which indicated that clusters begin to lose thiol ligands at 150 °C and that these ligands are completely removed at 250 °C.³³ The removal of thiolate ligands from the Pd surface at 250 °C was

confirmed by EXAFS analysis below. Figure 6.2d shows the TEM images Pd@SiO₂ after calcination at 650 °C. Upon calcination, a great number of clusters aggregated, and the size of the particles inside the silica sphere increased to 4.9 ± 2.6 nm.

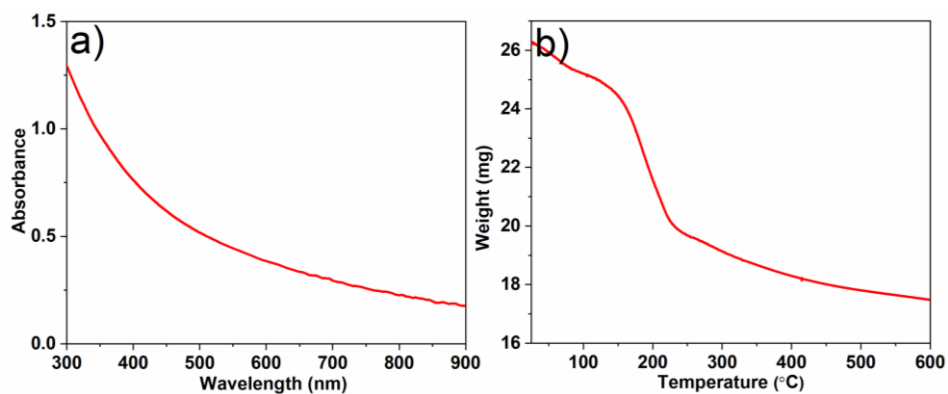


Figure 6.1: a) UV-Vis spectra of Pd_m(MUA)_n clusters, and b) TGA plot of Pd_m(MUA)_n clusters.

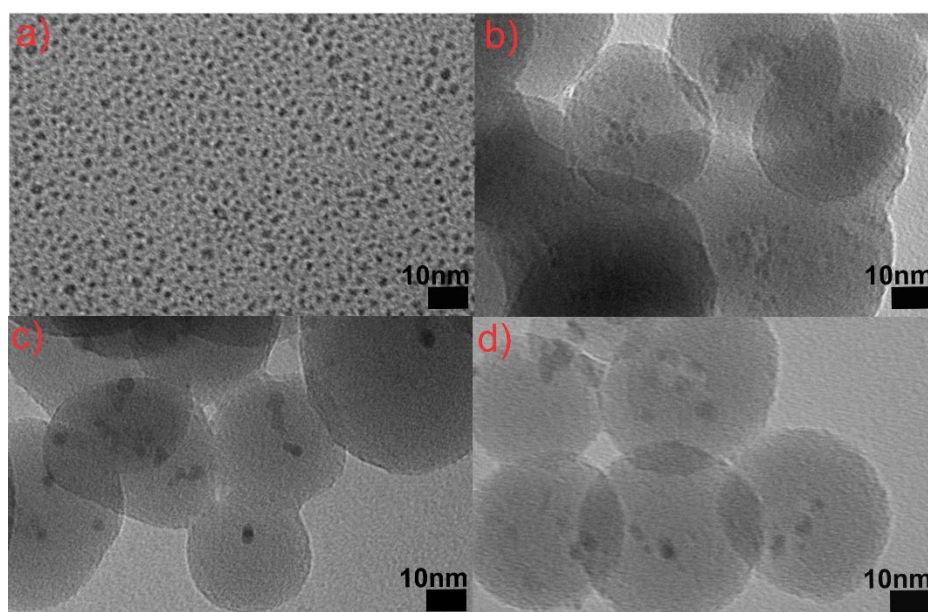


Figure 6.2: a) TEM image of Pd_m(MUA)_n clusters, b) as-synthesized Pd(MUA)_n@SiO₂, c) Pd@SiO₂ calcined at 250 °C, and d) Pd@SiO₂ calcined at 650 °C.

Figure 6.3 shows the TEM images of the Pd clusters deposited on silica spheres. The average size of the as-synthesized Pd clusters was measured to be 1.1 ± 0.3 nm. After calcination at 250 °C and 650 °C, it is clearly evident that clusters on the silica spheres are not stable and agglomerated to form larger particles. The average particle size was measured to be 3.9 ± 2.0 nm and 5.3 ± 9.2 nm upon calcination at 250 °C and 650 °C, respectively. Previously our group

found that Au₂₅ clusters are much more sinter resistant when they are in a silica shell, while significant sintering is observed on the non-coated samples (Au₂₅ clusters on the silica sphere).³² Park *et al.* carried out similar studies of larger 4 nm Pd nanoparticles.²⁷ Significant improvement in thermal stability and activity for CO oxidation reactions was observed for the silica-coated sample, while the non-coated samples showed tremendous sintering and poor activity.

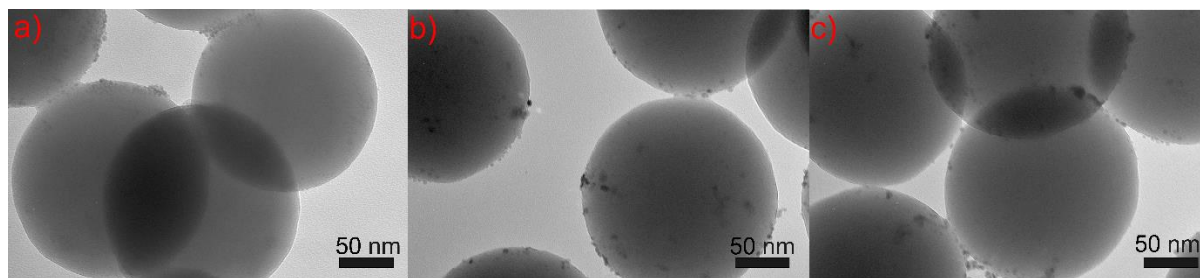


Figure 6.3: TEM images of a) as-synthesized Pd/SiO₂ samples, and b) calcined at 250 °C, and c) calcined at 650 °C.

The mesoporous nature of the Pd@SiO₂ catalyst calcined at 250 °C was confirmed by nitrogen adsorption/desorption isotherm which is shown in Figure 6.4. The Pd@SiO₂ catalysts exhibit a type IV adsorption isotherm and the BET surface area of the catalyst was measured to be 100 m²/g.³⁵ The pore size distribution of the catalysts was measured from the BJH desorption plot and the pore size was found to be 21 nm. We believe that removal of protecting ligands and solvent leads to disordered mesoporosity.

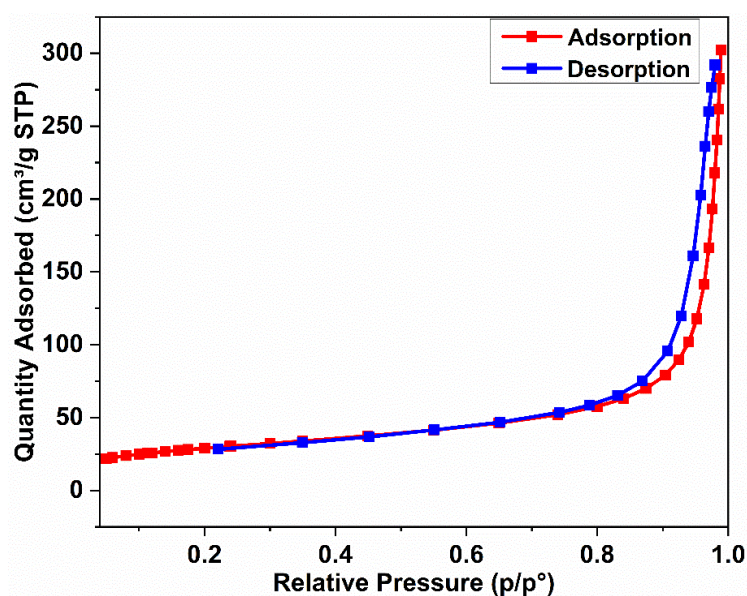


Figure 6.4: BET surface area analysis of silica encapsulated Pd_m(MUA)_n clusters.

The $\text{Pd}_m(\text{MUA})_n@ \text{SiO}_2$ materials as-synthesized and calcined at different temperatures (250 °C and 650 °C) were also analyzed by EXAFS spectroscopy at the Pd K edge. Figure 6.5 shows EXAFS plots in R-space for these samples; there is a large change in the speciation of the Pd clusters upon calcination. Figure 6.6 shows the Pd-K edge EXAFS in k-space and phase-corrected R-space of the as-synthesized $\text{Pd}_m(\text{MUA})_n@ \text{SiO}_2$ and calcined at 250 °C. The black line represents the experimental Fourier transformed EXAFS spectra and the red line represents the simulated fit. Since as synthesized samples showed Pd-S and Pd-Pd contributions, Pd-S and Pd-Pd paths from PdS and fcc Pd structures were used for EXAFS data fitting. The experimental fit parameters are shown in Table 6.1. The modelled Pd-S and Pd-Pd bond lengths were found to be 2.29(1) Å and 2.78(1) Å, respectively, which are consistent with literature values.³⁶ The low Pd-Pd CN of 2.6(3) is indicative of the presence of very small zerovalent Pd clusters. Overall, the EXAFS data is consistent with the presence of small thiolate stabilized Pd clusters which are capped by thiolate ligands. After calcination at 250 °C, the Pd-S contribution was not observed, which gives a clear indication of the removal of thiol ligands from the Pd surface. This result is in good agreement with the TGA result. First shell contributions from Pd-Pd and Pd-O were fit using fcc Pd and PdO models, respectively. Pd was found to be partially oxidized, and Pd-O scattering was observed at 1.96(2) Å.³⁷ Another peak was found to be at 2.737(6) Å which is due to the metallic Pd-Pd contribution.³⁸ The small growth in the Pd-Pd CN is consistent with mild sintering as seen via TEM.

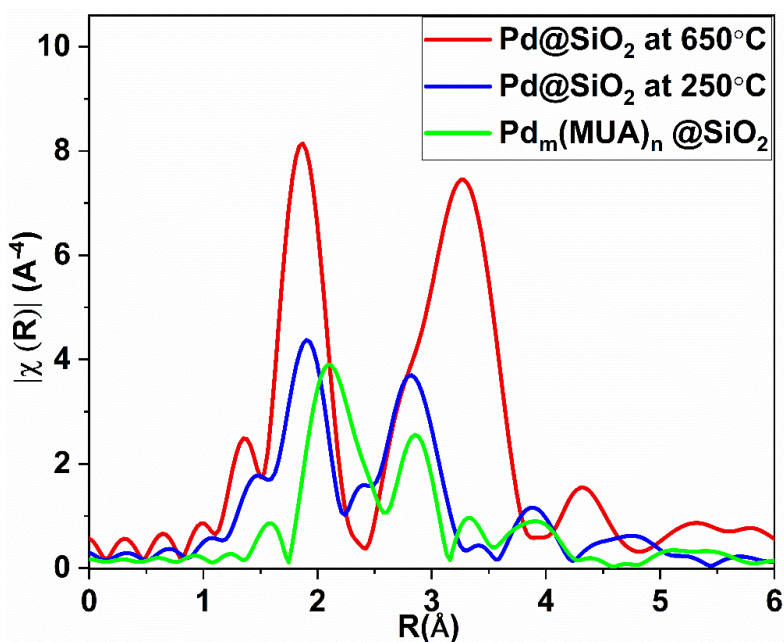


Figure 6.5: Pd K-edge EXAFS spectra in R-space of $\text{Pd}_m(\text{MUA})_n@ \text{SiO}_2$ catalysts calcined at different temperatures.

Table 6.1: EXAFS fitting parameters Pd_m(MUA)_n@SiO₂ materials as synthesized and calcined at different temperatures.

Catalyst	Type	CN	R/Å	σ²/Å²	E₀ Shift (eV)	R (%)
As synthesized	Pd-S	2.3(2)	2.29(1)	0.009(4)	1.0(8)	1.1
	Pd-Pd	2.6(3)	2.78(1)	0.009(3)	1.0(8)	
Calcined at 250 °C	Pd-O	1.7(6)	1.96(2)	0.007(5)	1.2(9)	1.8
	Pd-Pd	4.1(5)	2.737(6)	0.006(1)	1.2(9)	
Calcined at 650 °C	Pd-O	3.8(3)	2.018(6)	0.0016(8)	2.5(9)	1.1
	Pd-Pd1	3.6(7)	3.047(8)	0.005(1)	2.5(9)	
	Pd-Pd2	6.2(5)	3.428(7)	0.005(2)	2.5(9)	

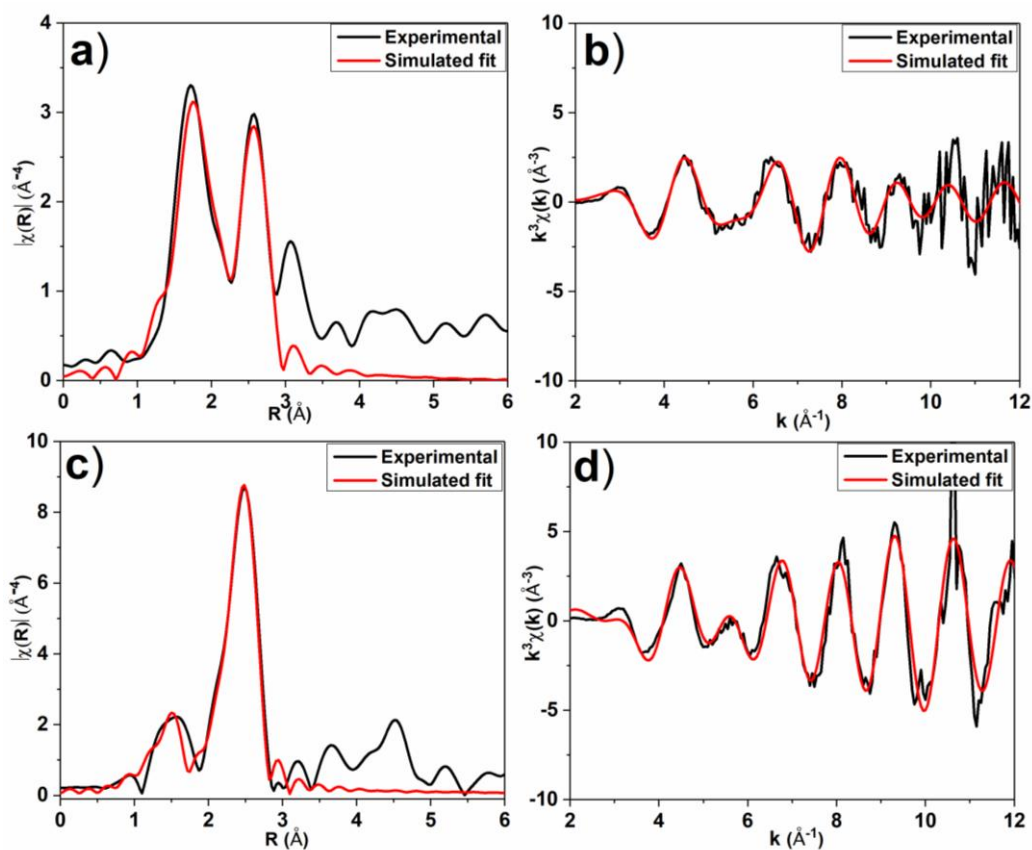


Figure 6.6: Pd K-edge EXAFS fitting data of Pd_m(MUA)_n@SiO₂ in a) R-space, and b) k-space. Pd K-edge EXAFS fitting data of Pd_m(MUA)_n@SiO₂ calcined at 250 °C in c) R-space, and d) k-space.

Figure 6.7 shows the EXAFS k-space and phase-corrected R-space of the Pd@SiO₂ catalysts calcined at 650 °C. After calcination at 650 °C for 3 h, three prominent peaks were observed in the R-space EXAFS data at distance 2.018(6) Å, 3.047(8) Å, and 3.428(7) Å. Since the EXAFS spectra was found to be similar to the spectrum of bulk PdO, a Pd-O model was used to fit the data. Three scattering paths, Pd-O, Pd-Pd, and Pd-Pd, were used. In the PdO crystal structure (Figure 6.7a), Pd atoms are surrounded by four O atoms located at a distance $R_1 = 2.0194$ Å from the central Pd. The second shell is composed of four Pd atoms at a distance $R_2 = 3.036$ Å, and the third shell is composed of eight Pd atoms at a distance $R_3 = 3.4209$ Å. The three peaks observed at distance 2.018(6) Å, 3.047(8) Å, and 3.428(7) Å represent the contribution from first, second and third shells respectively. The Pd-O bond distance of 2.018(6) Å is consistent with that of PdO.³⁹ The coordination numbers for all three shells was observed to be less than the theoretical value, which is consistent with the presence of small PdO particles. The conversion of Pd to PdO at 650 °C is in good agreement with the literature.⁴⁰

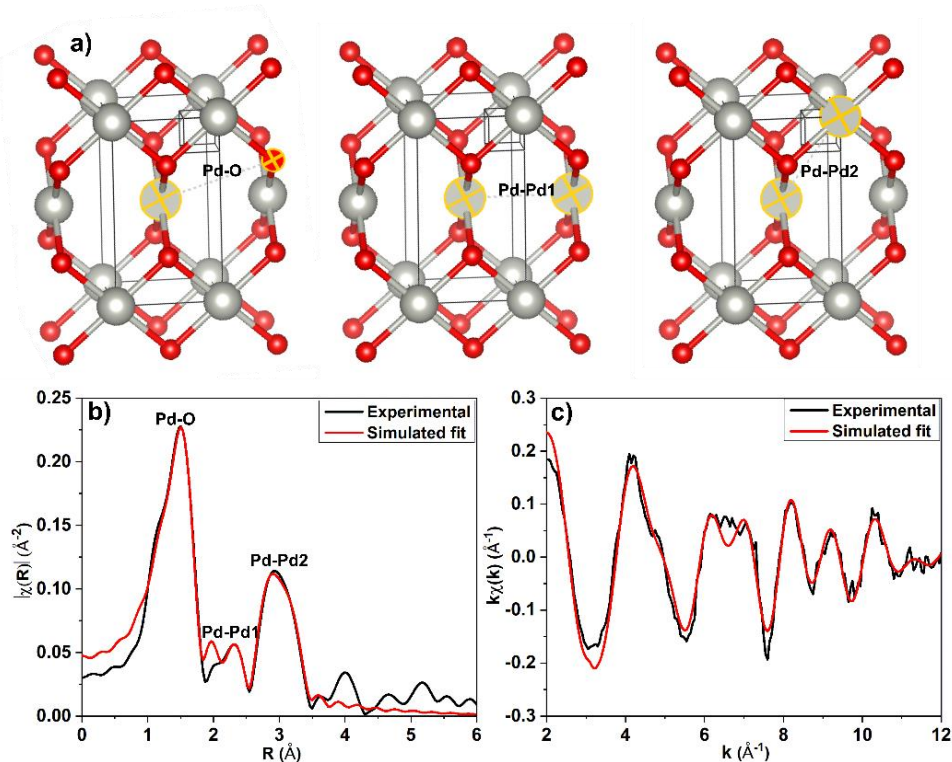


Figure 6.7: a) Unit cell of Pd-O, grey and red circles represent Pd and O, respectively, and Pd K-edge EXAFS spectra in b) R-space and c) k-space of Pd@SiO₂ catalysts calcined at 650 °C.

Figure 6.8 shows the methane oxidation plots as a function of temperature over Pd@SiO₂ catalysts that were calcined at 650 °C. Methane starts to be oxidized over these catalysts at 450 °C and showed maximum activity (31%) at 550 °C. The moderate activity is likely due to the inaccessibility of the Pd active sites through the silica shell. Interestingly, the Pd clusters were found to be completely deactivated when they are deposited on the silica sphere; showed only a 3% methane conversion at 550 °C. This difference is likely due to the much greater sintering seen in the control samples. Previously Habibi *et al.* observed similar conversions over nonporous silica encapsulated Pd nanoparticle catalysts with 7.1 % loading (Pd wt%) and surface area 70 m² g⁻¹.⁴¹ They studied the effect of the porous nature of a silica shell around the 8 nm Pd nanoparticles on the methane combustion reaction. The Pd catalysts with a nonporous shell showed a conversion 28% at 550 °C whereas a significant improvement in conversion was seen in the porous silica-encapsulated catalysts.

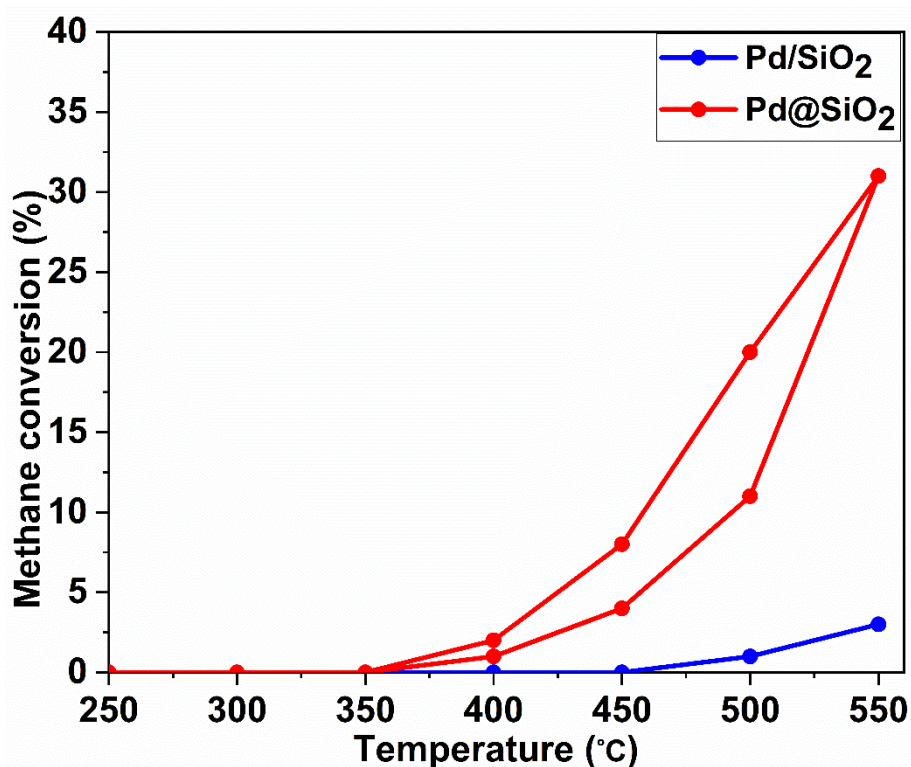


Figure 6.8: Methane combustion reaction over Pd@SiO₂ and Pd/SiO₂ catalysts.

CO chemisorption analyses were done to probe the relative availability of Pd sites in the catalysts. Both catalysts were reduced under H₂ flow prior to the chemisorption analysis. Dispersion data from CO chemisorption measurements are summarized in Table 6.2. The average size of the particle, as determined from chemisorption analysis, was calculated to be 47.8 nm. This large discrepancy in size from that measured from TEM and EXAFS data indicates that a large amount of the Pd seems to be inaccessible for CO (and thus for catalysis as well) in these systems. Both TEM and CO chemisorption data suggest severe agglomeration of Pd clusters occurred on the silica sphere during the activation process. The Pd dispersion of Pd/SiO₂ was measured to be 1.9 %, which yielded a calculated particle size of 56.9 nm. The CO chemisorption data also strengthen the claim that catalytic deactivation after the activation process is due to the loss of active surface area due to the sintering.

Table 6.2: CO chemisorption analysis and catalytic activity for methane combustion reaction of 0.5-Pd@SiO₂ and 2.0-Pd@SiO₂ catalysts calcined at 650 °C.

Sample	Pd dispersion (%)	Particle size from CO chemisorption	Particle size from TEM	CH₄ conversion at 550 °C (%)
Pd@SiO ₂	2.4	47.8 nm	4.9 ± 2.6 nm	31
Pd/SiO ₂	1.9	56.9 nm	9.3 ± 5.2 nm	3

6.5. Conclusion

In summary, we synthesized silica encapsulated Pd_m(MUA)_n clusters, followed by calcination to give Pd particles dispersed inside silica spheres. EXAFS results revealed that the complete removal of thiolate ligands from the Pd surface occurred under thermal treatment at 250 °C in air that facilitates the partial oxidation of Pd atoms. Upon calcination at 650 °C for 3 h under air, the Pd clusters were found to be completely oxidized to PdO. The catalytic activity for the methane combustion reaction over Pd@SiO₂ and Pd/SiO₂ catalysts calcined at 650 °C was investigated. The Pd@SiO₂ catalysts showed 31% conversion at 550 °C for the methane combustion reaction while complete deactivation was observed in control sample.

6.6. References

- (1) Murata, K.; Eleeda, E.; Ohyama, J.; Yamamoto, Y.; Arai, S.; Satsuma, A. Identification of Active Sites in CO Oxidation over a Pd/Al₂O₃ Catalyst. *Phys. Chem. Chem. Phys.* 2019, *21*, 18128-18137.
- (2) Schwartz, W. R.; Ciuparu, D.; Pfefferle, L. D. Combustion of Methane over Palladium-Based Catalysts: Catalytic Deactivation and Role of the Support. *J. Phys. Chem. C.* 2012, *116*, 8587-8593.
- (3) Parlett, C. M. A.; Bruce, D. W.; Hondow, N. S.; Lee, A. F.; Wilson, K. Support-Enhanced Selective Aerobic Alcohol Oxidation over Pd/Mesoporous Silicas. *ACS Catal.* 2011, *1*, 636-640.
- (4) Zhou, S.; Varughese, B.; Eichhorn, B.; Jackson, G.; McIlwrath, K. Pt–Cu Core–Shell and Alloy Nanoparticles for Heterogeneous NO_x Reduction: Anomalous Stability and Reactivity of a Core–Shell Nanostructure. *Angew. Chem. Int. Edit.* 2005, *44*, 4539-4543.
- (5) Bhattacharjee, S.; Dotzauer, D. M.; Bruening, M. L. Selectivity as a Function of Nanoparticle Size in the Catalytic Hydrogenation of Unsaturated Alcohols. *J. Am. Chem. Soc.* 2009, *131*, 3601-3610.
- (6) Farrauto, R. J.; Heck, R. M. Catalytic Converters: State of the Art and Perspectives. *Catal. Today.* 1999, *51*, 351-360.
- (7) Tardy, B.; Noupa, C.; Leclercq, C.; Bertolini, J. C.; Hoareau, A.; Treilleux, M.; Faure, J. P.; Nihoul, G. Catalytic Hydrogenation of 1,3-butadiene on Pd Particles Evaporated on Carbonaceous Supports: Particle Size Effect. *J. Catal.* 1991, *129*, 1-11.
- (8) Dal Santo, V.; Gallo, A.; Naldoni, A.; Sordelli, L. Selective Butadiene Hydrogenation by Pd Nanoparticles Deposited onto Nano-sized Oxide Supports by CVD of Pd-Hexafluoroacetylacetonate. *Inorg. Chim. Acta.* 2012, *380*, 216-222.
- (9) Jiang, F.; Cai, J.; Liu, B.; Xu, Y.; Liu, X. Particle Size Effects in the Selective Hydrogenation of Cinnamaldehyde over Supported Palladium Catalysts. *RSC Adv.* 2016, *6*, 75541-75551.

- (10) Li, X.; Goh, T. W.; Xiao, C.; Stanton, A. L. D.; Pei, Y.; Jain, P. K.; Huang, W. Synthesis of Monodisperse Palladium Nanoclusters Using Metal–Organic Frameworks as Sacrificial Templates. *ChemNanoMat*. 2016, 2, 810-815.
- (11) Quiros, I.; Yamada, M.; Kubo, K.; Mizutani, J.; Kurihara, M.; Nishihara, H. Preparation of Alkanethiolate-Protected Palladium Nanoparticles and Their Size Dependence on Synthetic Conditions. *Langmuir* 2002, 18, 1413-1418.
- (12) Cargnello, M.; Wieder, N. L.; Canton, P.; Montini, T.; Giambastiani, G.; Benedetti, A.; Gorte, R. J.; Fornasiero, P. A Versatile Approach to the Synthesis of Functionalized Thiol-Protected Palladium Nanoparticles. *Chem.Mater.* 2011, 23, 3961-3969.
- (13) Zhuang, Z.; Yang, Q.; Chen, W. One-Step Rapid and Facile Synthesis of Subnanometer-Sized Pd₆(C₁₂H₂₅S)₁₁ Clusters with Ultra-High Catalytic Activity for 4-Nitrophenol Reduction. *ACS Sustain. Chem. Eng.* 2019, 7, 2916-2923.
- (14) Sudheeshkumar, V.; Sulaiman, K. O.; Scott, R. W. J. Activation of Atom-Precise Clusters for Catalysis. *Nanoscale Adv.* 2020, 2, 55-69.
- (15) Yan, J.; Teo, B. K.; Zheng, N. Surface Chemistry of Atomically Precise Coinage–Metal Nanoclusters: From Structural Control to Surface Reactivity and Catalysis. *Acc. Chem. Res.* 2018, 51, 3084-3093.
- (16) Du, Y.; Sheng, H.; Astruc, D.; Zhu, M. Atomically Precise Noble Metal Nanoclusters as Efficient Catalysts: A Bridge between Structure and Properties. *Chem. Rev.* 2020, 120, 526-622.
- (17) Qian, H.; Zhu, M.; Wu, Z.; Jin, R. Quantum Sized Gold Nanoclusters with Atomic Precision. *Acc. Chem. Res.* 2012, 45, 1470-1479.
- (18) Jin, R.; Zeng, C.; Zhou, M.; Chen, Y. Atomically Precise Colloidal Metal Nanoclusters and Nanoparticles: Fundamentals and Opportunities. *Chem. Rev.* 2016, 116, 10346-10413.
- (19) Li, G.; Jin, R. Atomically Precise Gold Nanoclusters as New Model Catalysts. *Acc. Chem. Res.* 2013, 46, 1749-1758.
- (20) Corthey, G.; Rubert, A. A.; Picone, A. L.; Casillas, G.; Giovanetti, L. J.; Ramallo-López, J. M.; Zelaya, E.; Benitez, G. A.; Requejo, F. G.; José-Yacamán, M.; Salvarezza, R. C.;

Fonticelli, M. H. New Insights into the Chemistry of Thiolate-Protected Palladium Nanoparticles. *J. Phys. Chem. C*. 2012, *116*, 9830-9837.

(21) Das, J. K.; Das, N. Mercaptoundecanoic Acid Capped Palladium Nanoparticles in a SAPO-34 Membrane: A Solution for Enhancement of H₂/CO₂ Separation Efficiency. *ACS Appl. Mater. Inter.* 2014, *6*, 20717-20728.

(22) Lu, C. H.; Chang, F. C. Polyhedral Oligomeric Silsesquioxane-Encapsulating Amorphous Palladium Nanoclusters as Catalysts for Heck Reactions. *ACS Catal.* 2011, *1*, 481-488, .

(23) Moreno, M.; Ibañez, F. J.; Jasinski, J. B.; Zamborini, F. P. Hydrogen Reactivity of Palladium Nanoparticles Coated with Mixed Monolayers of Alkyl Thiols and Alkyl Amines for Sensing and Catalysis Applications. *J. Am. Chem. Soc.* 2011, *133*, 4389-4397.

(24) Gao, X.; Chen, W. Highly stable and efficient Pd₆(SR)₁₂ cluster catalysts for the hydrogen and oxygen evolution reactions. *Chem. Commun.* 2017, *53*, 9733-9736..

(25) Zhao, S.; Zhang, H.; House, S. D.; Jin, R.; Yang, J. C.; Jin, R. Ultrasmall Palladium Nanoclusters as Effective Catalyst for Oxygen Reduction Reaction. *ChemElectroChem* 2016, *3*, 1225-1229.

(26) Forman, A. J.; Park, J. N.; Tang, W.; Hu, Y. S.; Stucky, G. D.; McFarland, E. W. Silica-Encapsulated Pd Nanoparticles as a Regenerable and Sintering-Resistant Catalyst. *ChemCatChem* 2010, *2*, 1318-1324.

(27) Park, J. N.; Forman, A. J.; Tang, W.; Cheng, J.; Hu, Y. S.; Lin, H.; McFarland, E. W. Highly Active and Sinter-Resistant Pd-Nanoparticle Catalysts Encapsulated in Silica. *Small*. 2008, *4*, 1694-1697.

(28) Wang, N.; Sun, Q.; Bai, R.; Li, X.; Guo, G.; Yu, J. In Situ Confinement of Ultrasmall Pd Clusters within Nanosized Silicalite-1 Zeolite for Highly Efficient Catalysis of Hydrogen Generation. *J. Am. Chem. Soc.* 2016, *138*, 7484-7487.

(29) Feng, H.; Lu, J.; Stair, P. C.; Elam, J. W. Alumina Over-coating on Pd Nanoparticle Catalysts by Atomic Layer Deposition: Enhanced Stability and Reactivity. *Catal. Lett.* 2011, *141*, 512-517.

(30) Samanta, A.; Devi, R. N. Pd Ultra-Small Clusters as Precursors for Silica-Encapsulated Pd Nanoreactors: Highly Sinter-Resistant Catalysts. *ChemCatChem* 2013, *5*, 1911-1916.

- (31) Joo, S. H.; Park, J. Y.; Tsung, C. K.; Yamada, Y.; Yang, P.; Somorjai, G. A. Thermally Stable Pt/Mesoporous Silica Core–Shell Nanocatalysts for High-Temperature Reactions. *Nat. Mater.* 2009, 8, 126-131.
- (32) Sudheeshkumar, V.; Shivhare, A.; Scott, R. W. J. Synthesis of Sinter-Resistant Au@silica Catalysts Derived from Au₂₅ Clusters. *Catal. Sci. Technol.* 2017, 7, 272-280.
- (33) Liu, X.; Atwater, M.; Wang, J.; Huo, Q. Extinction Coefficient of Gold Nanoparticles with Different Sizes and Different Capping Ligands. *Colloid. Surface. B.* 2007, 58, 3-7.
- (34) Farrag, M.; Mohamed, R. A. Ecotoxicity of ~1nm Silver and Palladium Nanoclusters Protected by l-Glutathione on the Microbial Growth under Light and Dark Conditions. *J. Photochem. Photobio. A.* 2016, 330, 117-125.
- (35) Hong, E.; Kim, C.; Lim, D. H.; Cho, H. J.; Shin, C. H. Catalytic Methane Combustion over Pd/ZrO₂ Catalysts: Effects of Crystalline Structure and Textural Properties. *Appl. Catal. B: Environ.* 2018, 232, 544-552.
- (36) Murayama, H.; Ichikuni, N.; Negishi, Y.; Nagata, T.; Tsukuda, T. EXAFS Study on Interfacial Structure between Pd Cluster and n-octadecanethiolate Monolayer: Formation of Mixed Pd–S Interlayer. *Chem. Phys. Lett.* 2003, 376, 26-32.
- (37) Keresszegi, C.; Grunwaldt, J. D.; Mallat, T.; Baiker, A. In situ EXAFS Study on the Oxidation State of Pd/Al₂O₃ and Bi–Pd/Al₂O₃ During the Liquid-phase Oxidation of 1-phenylethanol. *J. Catal.* 2004, 222, 268-280.
- (38) Matsubayashi, N.; Yasuda, H.; Imamura, M.; Yoshimura, Y. EXAFS study on Pd–Pt Catalyst Supported on USY Zeolite. *Catal. Today.* 1998, 45, 375-380.
- (39) Yoshida, H.; Nakajima, T.; Yazawa, Y.; Hattori, T. Support Effect on Methane Combustion over Palladium Catalysts. *Appl. Catal. B: Environ.* 2007, 71, 70-79.
- (40) Xiong, H.; Lester, K.; Ressler, T.; Schlögl, R.; Allard, L. F.; Datye, A. K. Metastable Pd ↔ PdO Structures During High Temperature Methane Oxidation. *Catal. Lett.* 2017, 147, 1095-1103.
- (41) Habibi, A. H.; Hayes, R. E.; Semagina, N. Bringing Attention to Metal (un)Availability in Encapsulated Catalysts. *Catal. Sci. Technol.* 2018, 8, 798-805.

CHAPTER 7

Conclusions

7.1. Summary and Conclusions

This thesis investigated several strategies for minimizing the sintering of thiolate-protected Au and Pd cluster catalysts during the activation process of high-temperature calcinations. Chapter 2 described a strategy for the isolation of Au₂₅(MUA)₁₈ (MUA = mercaptoundecanoic acid) clusters in a silica matrix via silica sol-gel chemistry. The silica-encapsulated clusters showed a significant sinter-resistance upon calcination and grew from *ca.* 1.1 nm ± 0.3 nm to 2.2 nm ± 1.0 nm and 3.2 ± 2.0 nm after calcination at 250 °C and 650 °C for 3 h, respectively. The average particle size measured by TEM is in good agreement with EXAFS results. The average coordination number of the calcined sample (650 °C) was measured to be 10.5(6) indicated the size of the particle is ~3 nm. The slight growth in particle size was seen in encapsulated catalysts which is due to aggregation of multiple clusters in some of the silica spheres. Control samples of Au₂₅(MUA)₁₈ clusters decorated on the top of silica colloids showed tremendous sintering upon calcination with average particles sizes of 3.2 ± 1.7 nm and 15.5 ± 10.0 nm seen at similar calcination temperatures of 250 °C and 650 °C, respectively. Catalytic activity studies for 4-nitrophenol reduction and styrene oxidation reactions suggested that active sites on the Au surface are accessible through the mesopores in the 40 nm silica shell and catalytic activity was almost preserved after the calcination at 650 °C, whereas catalyst deactivation was observed in the non-encapsulated sample. However, mass transfer issues were identified in the final encapsulated clusters, though turnover numbers for styrene oxidation adjusted for the number of surface metal atoms suggested that encapsulated catalysts calcined at 650 °C were less hindered by mass transfer issues, potentially because all thiolate by-products were removed by this temperature.

From the previous study, I understood that the thickness of the metal oxide shell plays a significant role in the catalysis. My next focus was to control the thickness of the shell around the clusters and optimize the number of layers of metal oxide to protect the clusters towards sintering. Atomic layer deposition offers an efficient route for depositing highly uniform and conformal films. In Chapter 3, the nature of the ligand on Au clusters on the effectiveness of ALD overlayer growth was studied, along with the effect of the number of alumina layers on the thermal stability of Au₂₅(SR)₁₈ clusters. 10 cycles of alumina ALD overlayers were

deposited on Au₂₅(SR)₁₈ clusters protected with two different ligands (mercaptoundecanoic acid and dodecanethiol), and dramatically improved thermal stability of clusters was seen for clusters which had surface carboxylic acid groups. This is likely due to the fact that the trimethylaluminum ALD precursor can anchor to surface carboxylate groups, leading to ALD overlayers on top of clusters in that system, while for dodecanethiolate stabilized clusters, ALD growth can only occur around the clusters. To study the effect of thickness of the alumina layers on thermal stability, catalysts were synthesized by 5, 10, and 20 cycles of alumina deposition over Au₂₅(MUA)₁₈ clusters predeposited on alumina supports. Au₂₅(MUA)₁₈ clusters stabilized by 20 cycles of alumina overcoats were much more sinter-resistant than the 10 and 5 cycle coated clusters. The average particle size of 20 cycle alumina-overcoated Au₂₅(MUA)₁₈ clusters calcined at 250 °C and 650 °C was found to be 1.8 ± 0.5 nm and 2.4 ± 0.9 nm respectively.

In Chapter 4, the driving force for agglomeration of Au₂₅ clusters on a mesoporous silica support was investigated using environmental *in situ* TEM analysis. To improve the metal-support interaction, 3-mercaptopropyltrimethoxysilane was used as a stabilizing ligand for Au₂₅ synthesis. These supported clusters were calcined at various temperatures (250 °C, 450 °C, and 650 °C) under air for 3 h and analyzed by TEM and EXAFS. A significant growth in the particle size was observed in 450 °C and 650 °C treated-Au₂₅(MPTS)₁₈/SBA-15 samples. The *in situ* heating experiment was performed under oxygen (1 Pa) atmosphere in a specialized TEM cell that enabled direct observation of Au₂₅(MPTS)₁₈ clusters on the mesoporous silica SBA-15 support. At the earlier stage of heating, the driving force for sintering is likely due to the particle migration and coalescence mechanism. It is found that smaller particles migrate and coalesce into bigger particles, while the growth of even larger particles is likely due to the Ostwald Ripening. The mobility of nanoparticles increases as the calcination temperature increases and the speed of mobile Au particles was measured to be 0.2 nm/s and 1.1 nm/s at temperatures of 550 °C and 650 °C respectively. To reduce the mobility, Au₂₅(MPTS)₁₈/SBA-15 was treated with TEOS precursor in humid conditions to create silica overlayers on the clusters. In the silica-overcoated samples, the speed of the mobile Au particles was found to be 0.1 nm/s at 650 °C, which was much smaller than that was seen in the non-coated sample. The result strongly suggested that the additional TEOS overcoating treatment helped to mitigate the mobility of the Au clusters. However, small growth of particle size was still observed at higher temperatures.

Chapters 2, 3, and 4 mainly describe the bottom-up approach for the thiolate-stabilized $\text{Au}_{25}(\text{SR})_{18}$ cluster synthesis. In Chapter 5, a top-down approach was used to synthesize a ligand-free catalyst that did not need to be activated for catalysis. Ag nanotriangles encapsulated in silica were broken down into small Ag clusters via a high-temperature calcination step. Subsequently, Ag-Pd bimetallic catalysts were synthesized using the ligand-free Ag clusters as a sacrificial template for galvanic replacement of Pd. The reduction of Pd^{2+} to Pd^0 was monitored using *in situ* Pd L_3 edge XANES spectra. XPS and EXAFS analysis provided clear evidence for the formation of bimetallic AgPd particles with high Pd loadings. The low coordination number of Ag by EXAFS analysis suggested that the remaining Ag atoms are dispersed on the surface of the Pd core. The catalytic activity for 3-hexyne-1-ol hydrogenation was investigated and the bimetallic Ag-Pd@ SiO_2 catalysts showed a superior selectivity for the selective hydrogenation to 3-hexene-1-ol.

In Chapter 6, silica encapsulated $\text{Pd}_n(\text{MUA})_m$ clusters were synthesized and the structural changes of the Pd clusters were monitored during the activation process. EXAFS results indicated that removal of thiolate ligands at 250 °C in air leads to the partial oxidation of Pd clusters and that the clusters are completely oxidized to PdO at 650 °C. To study the effectiveness of the silica coating around the Pd clusters, the catalytic activity and thermal stability were compared with non-coated catalysts. The encapsulated Pd clusters showed much better activity for methane activation compared to the un-encapsulated clusters.

Finally, the major findings of this thesis are summarized as follows: first, that metal oxide coatings over catalytic metal clusters can be helpful to mitigate sintering, presumably by slowing down the particle migration and coalescence mechanism. Since the overlayers can limit catalysis due to mass transfer challenges, coating with thinner layers is highly desirable to enhance the catalytic performance. Second, the nature of the stabilizing ligand on the clusters has a significant role in the effectiveness of metal oxide coating. Finally, I established that thermal degradation behavior of Ag metal can be utilized to fabricate ligand-free metal clusters that enable to avoid the need for a secondary activation process.

7.2. Future outlook

Encapsulation with metal oxide shells is a straightforward way of stabilizing metal nanoparticles towards sintering. In Chapters 2 and 3, a protective metal oxide shell was shown to substantially enhance the thermal stability of $\text{Au}_{25}(\text{SR})_{18}$ clusters. The encapsulated catalysts

were found to be more sinter-resistant than non-encapsulated catalysts. One of the important challenges of encapsulation is the mass transfer issue associated with the silica shell that needs to be addressed. The enhanced thermal stability of the encapsulated metal clusters is at the cost of their catalytic activity, owing to the blocking of active sites and delayed mass transfer as compared to that of the pristine metal clusters. It is highly desirable to synthesize a sinter-resistant catalyst while minimizing the mass transfer issue associated with the protective shell. Wang *et al.* have shown that encapsulation with hollow nanostructures is suitable for improving mass transfer.¹ That is, if the shell can be made very thin it should not limit the mass transfer of reactants and products.² Only a few attempts have been made to control the sintering of metal clusters by growing a hollow shell of metal oxide and other materials.³⁻⁴ To date, encapsulation of atom-precise clusters with a hollow shell has not been reported.

7.2.1. Synthesis of metal clusters encapsulated within hollow silica spheres

The insertion of metals clusters in a yolk-shell structured material is of special interest since this method offers an efficient way to minimize the mass transfer issue associated with the shell while protecting against agglomeration. Many groups have shown that large hollow space between the shell and catalytic sites are suitable to minimize sintering while preventing surface blockage associated with a dense shell around the nanoparticles.⁵⁻⁶ A general strategy for the synthesis of yolk-shell catalysts is an encapsulation of metal core with double shells of different materials, followed by selective etching of the inner shell.⁷ For example, Zhan *et al.* demonstrated that unwanted ligands can be converted to mesoporous carbon shells via an efficient thermal annealing strategy.⁸ By annealing at 500 °C under nitrogen atmosphere, the protecting ligands, octadec-9-enylamine, on the Au nanoparticle were carbonized to a carbon shell that offers partial encapsulation, and this can be an efficient way of significantly slowing down the sintering of clusters and maintaining the exposure of active sites. Inspired by this work, below I lay out a possible procedure to synthesize Au catalysts encapsulated with a hollow silica shell.

Encapsulation of metal clusters with carbon shells can be carried out using a reported procedure used for larger nanoparticles.⁹⁻¹⁰ Briefly, an aqueous solution of Au₂₅(MUA)₁₈ clusters can be added to triblock copolymer EO₁₀₆PO₇₀EO₁₀₆ (F127) in H₂O with stirring to form a clear solution. As a first step, the concentration of F127 will be optimized. Then the solution can be placed in a sealed autoclave and maintained at 100 °C for 1 h. The metal cluster encapsulated with a carbon shell can be collected by centrifugation. In the next step, silica

shells can be deposited on the carbon shell via sol-gel polymerization of TEOS in a basic medium. Finally, the hollow shell can be obtained by the thermal removal of the carbon shell at 550 °C in air. The thickness of the silica shell can be controlled by changing the concentration of TEOS, base, and reaction time.¹¹ The effect of thickness on the catalytic activity could be studied by tuning the thickness of the silica shell. Both TEM and EXAFS analyses can be used to study the thermal stability of the catalysts before and after calcinations at various temperatures. Methane combustion and CO oxidation reactions could be used as model reactions to study the catalytic activity of these materials.

7.2.2. Synthesis of ligand-free catalysts via a top-down approach

A bottom-up approach especially chemical reduction method is the most common and simple method for the synthesis of metal clusters.¹² This method involves the reduction of a metal precursor using reducing agents in the presence of stabilizing ligands. The major challenge associated with the chemical reduction method is the requirement of stabilizing ligands to control the nucleation process and inhibit further particle agglomeration. Since stabilizing ligands block the active sites on the metal surface, an activation process is required, which leads to the deactivation of the catalyst.¹³ As the top-down approach offers an efficient route to synthesize catalysts with a clean surface, the activation process can be eliminated, which addresses the sintering issue during activation.

AuAg@SiO₂ and PtAg@SiO₂ catalysts can be synthesized via galvanic replacement of corresponding metal precursors using the procedure that was mentioned in Chapter 5. Since Au and Pt also have higher redox potentials than silver metal, Ag clusters can also be replaced with Au and Pt.¹³ Silica encapsulated Ag clusters can be synthesized as reported by Gangishetty *et al.*¹⁴ As proof of concept, I looked to make both AuAg and PtAg clusters using this method. For the AuAg system, 20 mg of a Ag@SiO₂ material (made as described in Chapter 5, with 3.7×10^{-6} moles of Ag) was dispersed in ethanol, followed by the addition of HAuCl₄ (3 equiv.). After 1 h stirring, the Au-Ag@SiO₂ sample was collected by centrifugation. Pt-Ag@SiO₂ catalysts can similarly be synthesized by adding H₂PtCl₄ (2 eq.) to Ag@SiO₂.

The as-synthesized proof-of-concept Au-Ag@SiO₂ sample was characterized by TEM and analysis. The average size of the clusters was measured to be 2.5 ± 0.3 nm which is shown in Figure 7.1. In the XPS spectra, two peaks were identified at 84.3 eV and 87.9 eV which correspond to the Au 4f_{7/2} and 4f_{5/2} spin-orbit peaks for the metallic Au.¹⁵ In future work,

samples could be characterized by XAS at the Au L₃ and Ag K edge to study the structure of the bimetallic nanomaterials. PtAg@SiO₂ catalysts could similarly be characterized by TEM, EXAFS, and XPS analysis.

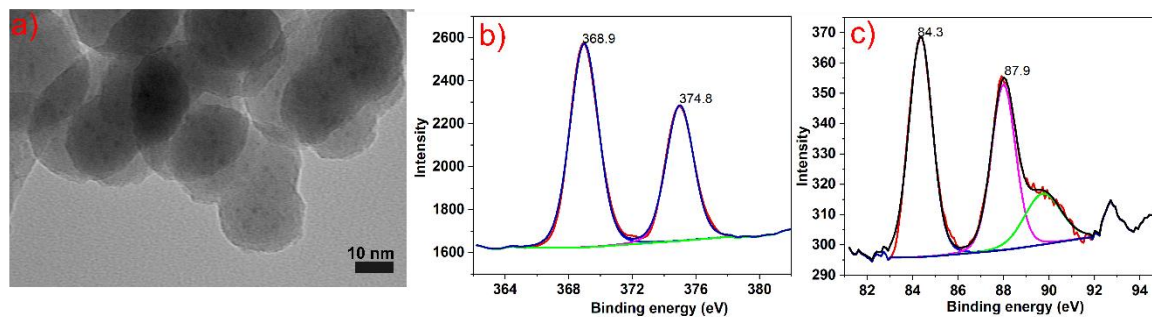


Figure 7.1: a) TEM image of a) as-synthesized Au-Ag@SiO₂ b) Ag 3d XPS spectra of Au-Ag@SiO₂ and c) Au 4f spectra of Au-Ag@SiO₂.

7.3. References

- (1) Wang, S.; Zhang, M.; Zhang, W. Yolk–Shell Catalyst of Single Au Nanoparticle Encapsulated within Hollow Mesoporous Silica Microspheres. *ACS Catal.* 2011, *1*, 207-211.
- (2) Kim, M.; Park, J. C.; Kim, A.; Park, K. H.; Song, H. Porosity Control of Pd@SiO₂ Yolk–Shell Nanocatalysts by the Formation of Nickel Phyllosilicate and Its Influence on Suzuki Coupling Reactions. *Langmuir.* 2012, *28*, 6441-6447.
- (3) Qiao, Z. A.; Zhang, P.; Chai, S.H.; Chi, M.; Veith, G. M.; Gallego, N. C.; Kidder, M.; Dai, S. Lab-in-a-Shell: Encapsulating Metal Clusters for Size Sieving Catalysis. *J. Am. Chem. Soc.* 2014, *136*, 11260-11263.
- (4) Sousa-Castillo, A.; Gauthier, M.; Arenal, R.; Pérez-Lorenzo, M.; Correa-Duarte, M. A. Engineering Microencapsulation of Highly Catalytic Gold Nanoclusters for an Extreme Thermal Stability. *Nanoscale.* 2015, *7*, 20584-20592.
- (5) Liu, J.; Qiao, S. Z.; Chen, J. S.; Lou, X. W. D.; Xing, X.; Lu, G. Q. M. Yolk/Shell Nanoparticles: New Platforms for Nanoreactors, Drug Delivery and Lithium-Ion Batteries. *Chem. Commun.* 2011, *47*, 12578-12591.
- (6) Titirici, M. M.; Antonietti, M.; Thomas, A. A Generalized Synthesis of Metal Oxide Hollow Spheres Using a Hydrothermal Approach. *Chem. Mater.* 2006, *18*, 3808-3812, .
- (7) Arnal, P. M.; Comotti, M.; Schüth, F. High-Temperature-Stable Catalysts by Hollow Sphere Encapsulation. *Angew. Chem. Int. Edit.* 2006, *45*, 8224-8227.
- (8) Zhan, W.; Shu, Y.; Sheng, Y.; Zhu, H.; Guo, Y.; Wang, L.; Guo, Y.; Zhang, J.; Lu, G.; Dai, S. Surfactant-Assisted Stabilization of Au Colloids on Solids for Heterogeneous Catalysis. *Angew. Chem. Int. Edit.* 2017, *56*, 4494-4498.
- (9) Sun, X.; Li, Y. Colloidal Carbon Spheres and Their Core/Shell Structures with Noble-Metal Nanoparticles. *Angew. Chem. Int. Edit.* 2004, *43*, 597-601.
- (10) Liu, J.; Hartono, S. B.; Jin, Y. G.; Li, Z.; Lu, G. Q.; Qiao, S. Z. A Facile Vesicle Template Route to Multi-Shelled Mesoporous Silica Hollow Nanospheres. *J. Mater. Chem.* 2010, *20* , 4595-4601.

- (11) Kobayashi, Y.; Inose, H.; Nakagawa, T.; Gonda, K.; Takeda, M.; Ohuchi, N.; Kasuya, A. Control of Shell Thickness in Silica-Coating of Au Nanoparticles and their X-ray Imaging properties. *J. Colloid. Interf. Sc.* 2011, 358, 329-333.
- (12) Iqbal, P.; Preece, J. A.; Mendes, P. M.; Nanotechnology: The “Top-Down” and “Bottom-Up” Approaches. *Nanotechnol. Supramol. Chem.* 2012, 6, 1-12
- (13) Sudheeshkumar, V.; Sulaiman, K. O.; Scott, R. W. J. Activation of Atom-Precise Clusters for Catalysis. *Nanoscale Adv.* 2020, 2, 55-69.
- (14) Gangishetty, M. K.; Scott, R. W. J.; Kelly, T. L. Thermal Degradation Mechanism of Triangular Ag@SiO₂ Nanoparticles. *Dalton Trans.* 2016, 45, 9827-9834.
- (15) Zwijnenburg, A.; Goossens, A.; Sloof, W. G.; Crajé, M. W. J.; van der Kraan, A. M.; Jos de Jongh, L.; Makkee, M.; Moulijn, J. A. XPS and Mössbauer Characterization of Au/TiO₂ Propene Epoxidation Catalysts. *J. Phys. Chem. B* 2002, 106, 9853-9862.